

UNIVERSITÉ DE NANTES
UFR SCIENCES ET TECHNIQUES

ÉCOLE DOCTORALE
MOLECULES, MATIERES ET MATERIAUX EN PAYS DE LOIRE (3MPL)

Année 2012

N° attribué par la bibliothèque



Tunable luminescence of doped $\text{MAl}_2\text{Si}_2\text{O}_8$ aluminosilicates (M= Ca, Sr, Ba)

THÈSE DE DOCTORAT
Discipline : Science des Matériaux
Spécialité : **Physico-chimie du solide**

*Présentée
et soutenue publiquement par*

Wubin DAI

Le 24 octobre 2012, devant le jury ci-dessous

- Président OUVRARD Guy, *Professeur des Universités – Univ. de Nantes, Nantes*
- Rapporteurs CHANE CHING Jean-Yves, *Directeur de Recherche - CIRIMAT, Toulouse*
ZAMBON Daniel, *Professeur des Universités – Univ. Blaise Pascal, Clermont-Ferrand*
- Examinateurs BRAULT Hélène, *Maître de Conférences - Univ. de Nantes, Nantes*
JOBIC Stéphane, *Directeur de Recherche - IMN, Nantes*
ZHANG Xianghua, *Directeur de Recherche – ISCR, Rennes*
- Invité DENIARD Philippe, *Directeur de Recherche – IMN, Nantes*

*Directeur de thèse : Stéphane Jobic
Co-encadrants : Hélène Brault et Philippe Deniard*

UNIVERSITÉ DE NANTES
UFR SCIENCES ET TECHNIQUES

ÉCOLE DOCTORALE
MOLECULES, MATIERES ET MATERIAUX EN PAYS DE LOIRE (3MPL)

Année 2012

N° attribué par la bibliothèque



Tunable luminescence of doped $\text{MAl}_2\text{Si}_2\text{O}_8$ aluminosilicates (M= Ca, Sr, Ba)

THÈSE DE DOCTORAT
Discipline : Science des Matériaux
Spécialité : **Physico-chimie du solide**

*Présentée
et soutenue publiquement par*

Wubin DAI

Le 24 octobre 2012, devant le jury ci-dessous

- Président OUVRARD Guy, *Professeur des Universités – Univ. de Nantes, Nantes*
- Rapporteurs CHANE CHING Jean-Yves, *Directeur de Recherche - CIRIMAT, Toulouse*
ZAMBON Daniel, *Professeur des Universités – Univ. Blaise Pascal, Clermont-Ferrand*
- Examinateurs BRAULT Hélène, *Maître de Conférences - Univ. de Nantes, Nantes*
JOBIC Stéphane, *Directeur de Recherche - IMN, Nantes*
ZHANG Xianghua, *Directeur de Recherche – ISCR, Rennes*
- Invité DENIARD Philippe, *Directeur de Recherche – IMN, Nantes*

*Directeur de thèse : Stéphane Jobic
Co-encadrants : Hélène Brault et Philippe Deniard*

Contents

Acknowledgments.....	1
Résumé de la Thèse en Français	3
Chapitre I : Introduction.....	4
1. Généralité	4
2. L'Etat de l'art.....	7
3. Les aspects fondamentaux sur la luminescence et les LEDs blanches	11
Chapitre II: Etude du transfert d'énergie entre cations Eu ²⁺ et cations Eu ³⁺ dans les matériaux MAl ₂ Si ₂ O ₈ (M = Ca, Sr, Ba) dopé avec Eu et préparés à l'air	18
1. Introduction	18
2. Description des structures MAl ₂ Si ₂ O ₈ (M = Ca ; Sr et Ba).....	20
3. Propriétés optiques des échantillons MAl ₂ Si ₂ O ₈ (M = Ca ; Sr et Ba) dopés par Eu ²⁺ sous atmosphère réductrice	21
4. Propriétés optiques MAl ₂ Si ₂ O ₈ dopés par Eu ²⁺ et synthétisés sous air.....	24
5. Stabilisation des ions Eu ³⁺ dans les matrices MASO (M = Ca, Sr, Ba)	26
7. Mécanisme de réduction des ions Eu ³⁺ en Eu ²⁺ dans les matrices MASO (M = Ca, Sr, Ba).....	27
8. Transfert d'énergie Eu ²⁺ -Eu ³⁺ dans les matrices MASO (M = Ca, Sr, Ba)	30
9. Conclusion du chapitre II	33
Chapitre III: Caractérisation optique de matériaux M _{1-y-3x/2} Al ₂ Si ₂ O ₈ : xCe ³⁺ , yMn ²⁺ (M = Ca, Sr).....	34
1. Introduction	34
2. Fluorescence des composés MASO (M = Ca, Sr) dopés Ce ³⁺	35
3. Fluorescence des composés MASO (M = Ca, Sr) dopés Mn ²⁺	38
4. Transfert d'énergie entre Ce ³⁺ et Mn ²⁺ dans les matrices CASO et SASO	39
5. Conclusion du chapitre III.....	40
Conclusion générale	42
Chapter I : Introduction	45
1. Introduction	46
2. State of the art	48
3. Fundamental aspects on luminescence and phosphors-converted white LEDs	56
3.1. Background on luminescence.....	56
3.2. CIE chromaticity coordinates and color temperature.....	64
References	69
Chapter II : Investigation of the Energy Transfer Between Eu²⁺ and Eu³⁺ in Eu-doped MAl₂Si₂O₈ (M = Ca, Sr, Ba) Materials Prepared in Air.....	73
1. Introduction	74
2. Experimental part	76
2.1. Synthesis process.....	76
2.2 Optical measurements	77
2.3. Structural characterization.....	77
2.4. Description of MAl ₂ Si ₂ O ₈ structures.....	78
3. Optical properties of MASO:Eu ²⁺ in reducing atmosphere	80
3.1. Ca _{1-x} Al ₂ Si ₂ O ₈ :xEu ²⁺	82
3.2. Sr _{1-x} Al ₂ Si ₂ O ₈ :xEu ²⁺	88

3.3. $\text{Ba}_{1-x}\text{Al}_2\text{Si}_2\text{O}_8:\text{xEu}^{2+}$	92
3.4. Comparison between Eu^{2+} -doped CASO, SASO and BASO synthesized in reducing atmosphere	95
4. Optical properties of MASO: $\text{Eu}^{3+}/\text{Eu}^{2+}$ materials prepared in air	97
4.1. CASO: $\text{Eu}^{2+}/\text{Eu}^{3+}$	98
4.2. SASO: $\text{Eu}^{2+}/\text{Eu}^{3+}$	107
4.3. BASO: $\text{Eu}^{2+}/(\text{Eu}^{3+})$	113
5. Stabilization of Eu^{3+} ions higher in CASO and SASO than in BASO	116
6. The Eu^{3+} to Eu^{2+} reduction mechanism in MASO ($M = \text{Ca}$ to Ba) host lattice and the ET from Eu^{2+} to Eu^{3+}	119
6.1. The mechanism of the abnormal reduction of Eu^{3+} to Eu^{2+} in MASO	119
6.2. The mechanism of ET from Eu^{2+} to Eu^{3+} in the MASO	124
Concluding remarks.....	134
References	135
Chapter III : Optical characterization of $\text{M}_{1-y-3x/2}\text{Al}_2\text{Si}_2\text{O}_8: x\text{Ce}^{3+}, y\text{Mn}^{2+}$ ($M = \text{Ca, Sr}$) with efficient energy transfers for generation of white-light-emitting diodes	137
1. Introduction	138
2. Experimental section	139
2.1. Synthesis and optical measurements	139
2.2. Structure characterization.....	139
3. Fluorescence of MASO doped with Ce^{3+}	141
3.1. Fluorescence of $\text{C}_{1-3x/2}\text{ASO}: x\text{Ce}^{3+}$ ($x = 0.1\%$ to 25%).....	141
3.2 Fluorescence of $\text{S}_{1-3x/2}\text{ASO}: x\text{Ce}^{3+}$ ($x = 0.1\%$ to 25%)	148
3.3 Comparison of CASO: $x\text{Ce}^{3+}$ and SASO: $x\text{Ce}^{3+}$ fluorescences	155
4. Fluorescence of MASO doped with Mn^{2+}	156
4.1. Fluorescence of $\text{C}_{1-x}\text{ASO}: x\text{Mn}^{2+}$ ($x = 0.5\%$ to 15%)	156
4.2. Fluorescence of $\text{S}_{1-x}\text{ASO}: x\text{Mn}^{2+}$ ($x = 0.5\%$ to 15%)	158
5. The mechanism of the ET from Ce^{3+} to Mn^{2+} in the CASO and SASO matrixes	159
5.1. Energy transfer from Ce^{3+} to Mn^{2+} in CASO matrix	159
5.2. Energy transfer from Ce^{3+} to Mn^{2+} in SASO matrix	169
6. The CIE chromaticity coordinates of the phosphors for CASO and SASO (co)-doped with Ce^{3+} and Mn^{2+}	177
6.1. CIE chromaticity properties of Ce^{3+} and/or Mn^{2+} (co)doped in CASO matrix	177
6.2. CIE chromaticity properties of Ce^{3+} and/or Mn^{2+} (co)doped phosphors in SASO matrix	180
Concluding remarks.....	183
References	184
General conclusion	187
Annexes	189
Appendix 1	191
Appendix 2	195
Appendix 3	197
Appendix 4	201

Acknowledgments

First and foremost, I would like to express my sincerest appreciation to my research and thesis advisor, Prof. Dr. Stéphane JOBIC. I thank him greatly with regards for his patience and encouragements that carried me on through the tough times, for his insights and suggestions that helped to shape my research skills, for his help in administrative matters related to my residence in Nantes. I own him lots of gratitude for having me shown this way of research and kindly thanks for the tolerance, commitment and understanding. Besides, of being an excellent supervisor, Dr. JOBIC is always cheerful and humor and as close as a good friend to me.

Many thanks and regards to my co-advisors Dr. Hélène BRAULT and Dr. Philippe DENIARD for sharing their knowledge and efforts with me throughout my dissertation. I am grateful to them for their careful and critical reading of my thesis and invaluable suggestions, for their fruitful discussions and positive criticism. Their comments and advices not only helped me to improve my research skills but also led me to go deeper insights into further research.

It was my honor to study and work in the MIOPS group, IMN, Nantes University. I am thankful to all the group members and all the laboratory staffs for their great help and friendship throughout the entire process. I would like to pronounce my special thanks to Dr. Florian MASSUYEAU for his advice and help, and also for teaching me operating the instruments and preparing the samples. I would also special thanks to Dr. Catherine GUILLOT for teaching me how to perform an EDX measurement.

The financial supports from Chinese Scholarship Council (CSC) are also acknowledged very much (N⁰: 2009615018).

Finally, I would like to thank my family. I wish to express my deepest and most heartfelt gratitude to my parents for their endless love. I am grateful to my sister and brother for their love and support. My special thanks go to my girlfriend Yifeng Lei for always being there for me with great love and support during my stay in Nantes University. This thesis can not have been done without them.

Résumé de la Thèse en Français

Chapitre I : Introduction

Ce chapitre va présenter au lecteur le contexte de la thèse. Il donnera également un bref "Etat de l'Art" dédié à l'éclairage et un résumé des concepts majeurs qui gouvernent la luminescence.

1. Généralité

Aujourd'hui, les gens se rendent compte que les combustibles fossiles sont de plus en rares ce qui crée une prise de conscience des questions environnementales (les changements climatiques par exemple). Par conséquent, il est temps d'économiser l'énergie. Approximativement, 20% de la consommation d'électricité mondiale est utilisée à ce jour uniquement pour l'éclairage. En outre, la demande d'énergie toujours croissante couplée à l'augmentation régulière de la population rend d'une importance primordiale la découverte de nouvelles sources de lumière qui pourraient offrir des avantages en termes de consommation d'énergie électrique, d'efficacité lumineuse, de maintenance, de fiabilité, de durée de vie, de protection de l'environnement, etc. Pour résoudre les problèmes de réchauffement de la planète, le développement des actions d'économie d'énergie est donc devenu urgent. Dans ce contexte, les diodes électroluminescentes blanches (LED blanche) à haute efficacité reçoivent une forte motivation avec l'espoir de remplacer les lampes conventionnelles et les lampes fluorescentes pour les applications d'éclairage dans un proche avenir. En effet, les lampes à incandescence, et par conséquent les lampes fluorescentes, dominent toujours le marché de l'éclairage, mais leur position est de plus en plus contestée par l'émergence du concept d'éclairage de dispositifs tout solide en raison de la disponibilité récente des LEDs blanches à haute efficacité. Malheureusement, les LEDs les plus lumineuses ont généralement une qualité mauvaise chromatique ainsi qu'un faible flux d'émission. Donc, des solutions à ces inconvénients doivent être proposées afin de conquérir le marché global de l'éclairage.

Seul un nombre très limité de phosphores peut actuellement remplir les exigences minimales pour les applications "LEDs à lumière blanche". Par conséquent, il est urgent de donner une forte impulsion à explorer de nouveaux matériaux luminescents avec des propriétés améliorées (soit un rendement de conversion supérieur à 90%, une durée de vie

d'environ 100.000 heures, une stabilité thermique jusqu'à 150 ° C, etc.) et remplissant les contraintes environnementales dans l'objectif d'une utilisation pour des diodes blanches tout inorganique. Dans ce contexte, beaucoup de travaux sont dédiés à travers le monde à la recherche de nouveaux phosphores rouges, verts et bleus, ou à l'amélioration des performances des phosphores préexistants (c'est-à-dire, les phosphores couramment utilisés pour des applications connexes). Ce n'est pas du tout le but de cette thèse de se concentrer sur un matériau luminescent avec une bande d'émission étroite centrée à une longueur d'onde donnée. En revanche, mes travaux visent exclusivement à l'élaboration d'une prochaine génération de lumière blanche basée sur l'association d'une diode émettant dans l'UV et d'un matériau photoluminescent inorganique émettant une lumière blanche sous excitation UV. Ce dernier doit présenter une émission recouvrant toute la région visible du spectre électromagnétique, et doit mimer autant que possible la lumière naturelle pour atteindre, une fois déposé sur la "puce-UV", un haut indice de rendu de couleur (IRC). Rappelons que l'IRC n'est pas une quantité physique, mais une caractéristique qualitative de la lumière. Meilleur est le rendu de couleur, plus les objets éclairés en lumière artificielle présentent leur coloration authentique, à savoir leur couleur observée à la lumière du jour. Les objets semblent donc naturels lorsque l'IRC est égal à 100. Les valeurs des IRCs sont typiquement de 90, 80 et 75 pour une source incandescente, une lumière fluorescente, et les LEDs blanches, respectivement. A ce jour, la façon de produire de la lumière blanche décrite ci-dessus (juxtaposition d'une diode UV et d'un luminophore blanc) n'a presque jamais été explorée et mérite de plus amples investigations. Remarquons que si un IRC élevé est attendu pour les applications "haute gamme", un phosphore blanc monophasé avec un "faible" IRC (~ 70) pourrait aussi être intéressant pour des applications "bas de gamme" très prometteuses comme la signalisation automobile en plein jour.

A ce stade, rappelons très brièvement le contexte géopolitique dans le monde entier relatif à l'innovation sur l'éclairage LED. Il est intéressant de remarquer que les pays asiatiques, en particulier le Japon et Taiwan, adoptent une politique agressive pour trouver des utilisations pratiques pour les LEDs blanches. En parallèle, le gouvernement américain a financé un programme de 470 millions de dollars pour fabriquer en 2011 les LEDs blanches avec une efficacité de 120 lm / W. Dans le même temps, les fabricants de semi-conducteurs et les fabricants des appareils d'éclairage primaire en Amérique et en Allemagne établissent ou ont établi des entreprises à risque (GELcore, LumiLeds, Osram Opto, CREE Lighting) afin de

poursuivre les recherches et le développement sur les technologies et les applications d'éclairage à LED blanche. Jusqu'à présent, nous pouvons regretter la faible implication (par rapport aux autres pays industrialisés) de l'industrie française et la faiblesse des soutiens financiers pour les recherches fondamentales consacrées aux nouveaux phosphores pour les applications LEDs, même si les institutions publiques (CNRS, CEA ...) concentrent avec succès leur attention sur les puces-LEDs émettant dans l'ultraviolet et/ou le visible. Pourtant, il existe une véritable opportunité pour les entreprises françaises à relever les défis des marchés futurs et de développer un l'éclairage LED peu consommateur d'énergie en couplant un dispositif LED ou un phosphore inorganique blanc. Au cours de la dernière décennie, l'attention a été dirigée principalement vers le développement des dispositifs organiques. Malheureusement, ces dispositifs souffrent d'une durée de vie opérationnelle limitée en grande partie à cause de la nature organique même des composants. C'est la raison pour laquelle nous nous concentrerons ici sur les phosphores inorganiques émettant de la lumière blanche. Mon travail se focalisera uniquement sur la partie "phosphores", c'est à dire la synthèse et la caractérisation de phosphores émettant une lumière blanche. Aucun assemblage de "phosphores + Puce de LEDs" n'est présenté ici.

Notons que le matériau désiré qui convertira le rayonnement UV en rayonnement visible (down conversion) peut aussi présenter les applications potentielles dans des domaines autres que de l'éclairage. Par exemple, l'efficacité de dispositifs photovoltaïques basés sur Si, CIGS ou CuInSe_2 pourrait être sensiblement améliorée après un dépôt d'un tel phosphore blanc à leur surface, ce dernier transformant une partie de la lumière UV incidente non utilisable en lumière visible avec une section efficace d'absorption supérieure. Cela pourrait être considéré comme un remède complémentaire aux processus de "up-conversion" et de "down-conversion" classiques proposés pour remodeler la lumière incidente et pour l'adapter à la capacité d'absorption réelle de la cellule solaire (conversion des radiations inutiles en celles efficaces pour l'effet photovoltaïque). En vertu de ces considérations, les matériaux luminescents développés pourraient favoriser un meilleur rendement de conversion lumière/électricité.

2. L'Etat de l'art

Les lampes LEDs ont de nombreux avantages par rapport aux méthodes d'éclairage traditionnelles et peuvent vraiment être considérées comme une percée dans l'industrie de l'éclairage. En effet, depuis les années soixante où elles ont été introduites comme simples voyants de signalisation, un long chemin a été parcouru. Aujourd'hui, "l'éclairage tout solide" a déjà pénétré le marché avec une grande variété d'applications de niche (par exemple, les feux stop dans le domaine de l'automobile, les feux de circulation, les écrans à cristaux liquides, les téléphone portables, les lampes de poche et toutes sortes de projecteurs). Parallèlement, les LEDs deviennent compétitives par rapport aux lampes incandescentes et fluorescentes pour les applications d'éclairage. Pour information, le succès des LEDs a été récemment illustré par leur incorporation à l'extérieur du Stade Olympique National et du Piscine d'Eau Cube de Pékin lors des Jeux Olympiques de 2008 (plus de 750, 000 LEDs utilisées). La **Figure 1-1** montre clairement cette tendance d'évolution naturelle. Notamment, l'efficacité lumineuse des WLEDs (white LEDs) est prévue pour approcher ~ 200 lumens / Watt d'ici à l'année 2020, ce qui serait de beaucoup supérieure à celle des lampes à incandescence et fluorescentes. En effet, au cours des dernières années, les matériaux luminescents ont été considérés comme des composants technologiquement importants et clefs pour la fonctionnalité et le succès de nombreux systèmes de l'éclairage et d'affichage. De plus, comme on peut voir sur la **Figure 1-2**, le coût pour la lumière blanche générée à partir de LEDs est considérablement à la baisse. A partir des observations ci-dessus, il peut être conclu sans ambiguïté que les LEDs basées sur l'éclairage à l'état solide seront la prochaine génération de sources de lumière domestiques.

En plus d'un rendement élevé et d'une longue durée de vie, les LEDs fournissent d'autres avantages comme une consommation d'énergie faible. Selon différentes sources, il est prévu que l'éclairage LED réduira d'environ 50% la consommation d'énergie mondiale pour l'éclairage d'ici 2025 ! Néanmoins, une telle évolution ne peut être accomplie que si des LEDs peu coûteuses sont mises à notre disposition. Notons que outre les économies d'énergie, l'utilisation de LEDs peut s'accompagner de plusieurs avantages comme une bonne résistance aux vibrations et aux chocs, l'absence d'émissions dans le domaine ultraviolet, une grande compatibilité avec les impératifs environnementaux (par exemple, pas de mercure contrairement aux lampes fluocompactes), une faible taille de la source de lumière, un temps

de réponse à l'allumage court, un rendement élevé dans les conditions de basse température... Bien sûr, ces avantages évidents vont de paire avec certains inconvénients. Notamment, les LEDs sont actuellement encore trop chères par rapport aux technologies d'éclairages conventionnels. En outre, une température excessive ou des conditions de fonctionnement inappropriées réduisent considérablement à la fois l'efficacité et la durée de vie. Par ailleurs, le spectre optique de LEDs blanches fabriquées diffère significativement de celui du corps noir (source produisant un spectre continu), c'est-à-dire que l'indice de rendu de couleur (IRC) est significativement inférieur à 100% (généralement autour de 70%). Par conséquent, la couleur des objets est perçue différemment sous l'éclairage de LEDs blanches par rapport aux sources incandescentes et la lumière du jour. En particulier, l'éclairage des LEDs blanches est actuellement souvent caractérisé par une émission de rouge déficiente, conduisant à une couleur bleu-blanc.

Aujourd'hui, plusieurs approches ont été exploitées pour produire la lumière blanche basée sur l'utilisation de LEDs. Juste pour indication, elles sont listées ci-dessous :

- La lumière produite à partir de "puces LEDs" est monochromatique par nature. Ainsi, la génération de lumière blanche demande une combinaison de multi-puces qui peut être réalisée par l'association de diodes émettant de façon individuelle dans le rouge, le vert et le bleu (**Figure 1-3a**). Dans ce cas, un contrôle complexe et coûteux du dispositif d'éclairage est nécessaire pour aboutir au bon dosage de rouge, de vert et de bleu et pour contrecarrer de façon instantanée les modifications des caractéristiques optiques de chaque composant suite à un changement de température ou un vieillissement prématûr par exemple. Ceci explique le coût élevé de ces systèmes, beaucoup trop élevé pour répondre au marché de l'éclairage de façon générale, et ce même si des rendements élevés sont atteints avec une large gamme de températures de couleur (la température de couleur (K) d'une lumière est la température qu'un corps noir doit avoir pour présenter des caractéristiques optiques similaires à la source de lumière réelle). Les températures de couleur élevées (4000 K et plus) sont considérées comme des couleurs "froides", les températures de couleur faibles (2700-3000 K) comme les couleurs chaudes).

- Alternativement, comme introduit dans les années 1990s par la société Nichia, la lumière blanche peut être obtenue en recouvrant une puce bleu (GaN ou InGaN émettant à 460 nm) avec un phosphore grenat d'yttrium aluminium (YAG: Ce³⁺) dopé au cérium pour convertir une partie de la lumière bleue émise en une lumière jaune (**Figure 1-3b et Schéma 1-1**). S'en suit un coût de fabrication plus faible que précédemment, mais l'IRC est modeste (inférieur à 80) en raison de l'absence d'une contribution rouge au spectre d'émission (température de couleur en 7000 K et 8000K selon l'épaisseur de la couche). Par conséquent, du fait de leur couleur trop bleutée, ces dispositifs sont actuellement commercialisés principalement pour du rétro-éclairage pour l'affichage à cristaux liquides, les lampes de poche, les lampes de bureau et les illuminations décoratives. Une solution alternative consiste à combiner d'une "puce" bleue avec un phosphore vert et un phosphore rouge (**Figure 1-3c**). Malheureusement, les matériaux luminescents rouges pouvant être efficacement pompés par LEDs émettant dans le bleu sont encore très rares. C'est pourquoi la recherche de nouveaux phosphores rouges qui remplissent cette condition pour les applications LEDs donne lieu actuellement à de nombreuses études. Le **Tableau 1-1** rassemble les phosphores qui sont commercialisés lors d'un dépôt sur des "chip" bleus.

- Une troisième approche pour générer une lumière blanche consiste à combiner une puce émettant dans l'UV (par exemple, In_xGa_{1-x}N avec λ_{ex} variant de 360 nm à 480 nm selon x commercialisé par Nichia, Toyoda Gosei, Cris, Philips, Séoul semi-conducteurs et Osram) avec des phosphores excitables par UV émettant dans le rouge, le vert, et le bleu en proportions contrôlées (**Figure 1-3d**) (voir le **Tableau 1-2** pour une liste des phosphores potentiels). Il est alors attendu une série d'avantages comme un IRC élevé (> 80), une température de couleur chaude, etc. Néanmoins, le problème majeur à ce jour reste l'absence de rendements élevés et la faible qualité spectrale des phosphores. Par ailleurs, la stabilité de chaque phosphore n'est pas assez élevée, et leurs produits de décomposition peuvent être vus, dans certains cas, comme nuisibles à l'environnement. De plus, il reste difficile de mélanger et de déposer les films uniformes ce qui entraîne des variations de couleurs indésirables. En plus de ces inconvénients, il faut ajouter la réabsorption forte de la lumière bleue par les phosphores rouge et verts. C'est cependant une solution qui est retenue par les industriels actuellement.

Basées sur ces observations, l'élaboration d'une phase inorganique excitable sous UV et émettant de la lumière blanche à elle seule grâce au principe de transfert d'énergie entre un sensibilisateur et un activateur (par exemple) apparaît comme une solution potentielle pour générer une lumière blanche chaude d'une manière beaucoup plus simple et moins coûteuse. Cela permettrait de résoudre en une seule fois les difficultés associées aux durées de vie différentes des phosphores et à la complexité de mélanger des phosphores R, G, B de façon homogène. Mon travail a été consacré à la recherche d'un tel phosphore idéal. Le matériau (idéal) doit présenter une émission variant de 400 nm à 800 nm sous excitation UV et mimer le spectre de la lumière solaire autant que possible avec les paramètres chromatique CIE (x,y) proches de 1/3, 1/3 (0.35,0.35 pour une température de couleur de 4800K-voir **Figure 1-4**), avec un rendement quantique élevé et une grande stabilité thermique.

Pour résumer, l'objectif de ma thèse était de gagner en simplicité dans la mise en place des LEDs blanches via la synthèse d'un seul phosphore approprié qui réponde à certains critères comme une efficacité élevée dans la conversion de lumière, une haute température de "quenching" thermique (supérieur à ~ 150 °C), etc. Ce matériau doit être suffisamment souple pour accepter des changements de composition. Notamment, les dopants et co-dopants doivent pouvoir être introduits dans les proportions appropriées afin d'ajuster le point de couleur (c'est-à-dire, les paramètres CIE(x, y)). Le phosphore doit présenter une émission large qui s'étend sur l'ensemble du spectre visible. Les matériaux préparés ont systématiquement été caractérisés d'un point de vue structural et optique, et les différentes possibilités à notre disposition pour moduler les propriétés optiques ont été identifiées par l'étude des matériaux d'une série complète. Nous avons concentré notre attention en particulier sur les réseaux hôte d'alumino-silicate $\text{MAl}_2\text{Si}_2\text{O}_8$ (M = Ca, Sr, Ba) avec pour dopants l'euroium avec ses degrés d'oxydation II et III (Eu^{2+} et/ou Eu^{3+}), le cérium (Ce^{3+}) et des éléments de transition comme le manganèse (Mn^{2+}) comme activateurs. Formellement, ce type de matériaux hôtes offre souvent l'avantage de contenir différents sites cristallographiques alcalino-terreux où les ions luminescents peuvent être hébergés (*nota bene*: l'existence de plusieurs sites atomiques où les activateurs peuvent se positionner n'est pas une condition nécessaire pour atteindre un phosphore blanc, mais peut aider). Comme les propriétés optiques dépendent fortement de l'environnement cristallographique, l'objectif est alors de contrôler l'insertion d'éléments luminescents dans les matériaux, afin de contrôler leur absorption et émission. Ce point est particulièrement pertinent pour les ions Eu^{2+} et Ce^{3+} pour

lesquels les transitions optiques sont basées sur les transitions 4f-5d présentant des bandes larges d'absorption et d'émission situées respectivement dans la gamme de spectre du proche-UV et du visible.,

3. Les aspects fondamentaux sur la luminescence et les LEDs blanches

3.1. Contexte

3.1.1 Principes

Un matériau luminescent, également appelé phosphore, peut être défini comme un matériau qui peut absorber l'énergie et la restituer, totalement ou partiellement, par une émission de lumière. L'énergie peut être fournie de différentes manières qui conduisent à différents types de luminescence, soit la cathodoluminescence (l'excitation via un faisceau d'électrons), l'électroluminescence (l'application d'une tension électrique), la triboluminescence (par exemple, l'utilisation de la pression ou le broyage comme stimulus), etc. Plus précisément, la luminescence est appelé photoluminescence (PL) lorsque l'émission de lumière résulte d'un phénomène d'absorption de lumière. Dans la suite, je vais me concentrer uniquement sur ce dernier type de luminescence. Notons qu'au contraire de l'incandescence, la photoluminescence aura toujours lieu à basse température. Le phénomène peut être affecté par la température, mais son origine n'est pas la température.

Dans la plupart des cas, la PL provient des éléments chimiques (par exemple, les éléments Terres Rares) introduits dans un réseau hôte comme dopants. Sous photo-excitation (voir **Figure 1-5**), les dopants transitent de leur état fondamental à leur état excité, et libèrent l'énergie via une émission de lumière sous la forme d'un rayonnement ultraviolet, visible, ou infrarouge. La lumière émise ne sera jamais plus énergétique que la lumière utilisée pour déclencher l'absorption à cause de phénomènes de relaxation. Ce retour radiatif peut être en concurrence avec un processus non-radiatif, le retour de l'état excité à l'état fondamental étant alors assuré par un don d'énergie au réseau hôte avec l'activation de phonons, c'est à dire sous

la forme de chaleur. Il est évident que les processus non-radiatifs doivent être réduits au maximum pour développer les matériaux luminescents hautement efficaces.

Quand les activateurs ont une faible propension à absorber la lumière, l'utilisation de sensibilisateurs peut être décidée. Ils sont introduits dans les réseaux d'accueil comme codopants pour capturer de manière plus intense la lumière incidente et transférer son énergie indirectement aux activateurs. Ces derniers sont ensuite promus de leur état fondamental à leur état excité, tandis que les sensibilisateurs retournent à leur état fondamental sans l'émission de lumière. La **Figure 1-6** schématise un tel processus. Dans certains cas extrêmes, l'énergie peut être directement absorbée par la matrice. Par conséquent, le réseau hôte transfère son énergie absorbée à l'activateur comme un sensibilisateur normal. Remarquons également que le centre luminescent peut jouer le rôle à la fois d'activateur et de sensibilisateur dans certains phosphores.

De manière générale, le processus de la photoluminescence d'un centre luminescent peut être brièvement résumé par les étapes suivantes. Tout d'abord, l'absorption de l'énergie a lieu avec la promotion d'un électron d'un état fondamental à un état excité (temps demandé $\sim 10^{-15}$ s). Deuxièmement, la relaxation de l'état excité vers sa configuration fondamentale se produit et cède de la chaleur au réseau (via les phonons) (temps demandé $\sim 10^{-13}$ s). À la fin, la lumière est émise par l'activateur excité avec un temps de décroissance dépendant de la nature de la transition électronique. Les transitions interdites (par exemple les transitions d-d et f-f avec différents élans de spin dans les états fondamental et excité) conduiront à des bandes d'émission étroites (la largeur spectrale typiquement de quelques nm), tandis que les transitions autorisées (par exemple les transitions d à f, les transferts de charge) sont caractérisées par une bande large. En première approximation, nous pouvons avancer que plus la transition électronique est autorisée, plus l'émission est large et intense. En fait, la forme de l'émission et le déplacement d'énergie (le déplacement de Stokes) entre l'absorption et l'émission peut être prédite en considérant la nature des liaisons chimiques dans laquelle l'activateur est impliqué, et les distances interatomiques d'équilibre entre l'activateur et ses ligands dans les états fondamental et excité. On peut considérer la **Figure 1-7**. Un tel schéma montre l'évolution de l'énergie potentielle E du centre absorbant (généralement un cation) par rapport à R qui est définie comme la distance entre ce centre et ses voisins atomiques dans la matrice. L'activateur est supposé être à une localisation fixe, tandis que les ligands

périphériques peuvent osciller autour de leur position d'équilibre (voir la **Figure 1-8** pour une représentation schématique d'un activateur coordonné à quatre ligands avec un environnement chimique carré). Nous considérons ici un mode d'étirement symétrique, mais le raisonnement peut être très facilement extrapolé à tous les modèles vibratoires.

En **Figure 1-7**, les courbes paraboliques g et e représentent l'état fondamental et excité, R_0 et R'_0 représentent les distances métal-ligand à l'équilibre dans l'état fondamental et excité, respectivement. La forme parabolique des courbes g et e est due au fait qu'une vibration harmonique est supposée, ce qui apparaît comme une approximation acceptable pour les déviations légères. Dans l'état fondamental (même pour l'état excité), la force de rappel subie par les ligands peut être écrite par l'**équation (1-1)**:

$$F = -k(R-R_0) \quad (1-1)$$

où k est une constante (la constante de ressort), R_0 est la position d'équilibre et R représente la distance d'équilibre pendant la vibration. Puis, l'énergie potentielle (E) associée à un tel vibrateur est donnée par l'**équation (1-2)**:

$$E = \frac{1}{2} k(R-R_0)^2 \quad (1-2)$$

Cette équation explique la forme parabolique du diagramme configurationnel. Les lignes solides horizontales dans les configurations fondamentale et excitée correspondent aux états de vibration, deux états de phonons successifs étant séparés par des énergies $\hbar\omega_g$ et $\hbar\omega_e$ dans les états fondamental et excité, respectivement. Les bandes d'absorption et d'émission sont représentées par des flèches verticales avec une énergie associée E_a et E_b ($E_a \geq E_b$), respectivement. La différence (E_a-E_b) est appelée le déplacement de Stokes et sa valeur dépendra fortement de la différence R'_0-R_0 , à savoir le changement de covalence de la liaison activateur-ligand entre l'état fondamental et l'état excité. S_e et S_g , les facteurs de Huang-Rhys dans les états g et e , donnent le nombre moyen de phonons impliqués dans l'absorption et l'émission. Nous noterons ici, que dans une première approximation, la courbure des courbes paraboliques dans les états fondamental et excité et les fréquences des phonons dans les deux états électroniques peuvent être considérées comme identiques. Cela signifie qu'aucun changement n'est induit dans la nature de la constante k et du mode de vibration sous

l'excitation. Bien sûr, une telle approximation n'est pas réaliste, mais suffisante pour rendre compte des phénomènes impliqués dans la PL.

A partir de la **Figure 1-7**, expliquons l'origine de quelques-uns des retours non radiatifs présentés en **Figure 1-9**. La **Figure 1-9a** est typiquement représentative d'une transition électronique permise, soit une transition $4f \rightarrow 5d$ par exemple. La nature de la liaison chimique est très différente dans l'état fondamental et l'état excité grâce au dépeuplement du bloc $4f^n$ d'un lanthanide au bénéfice des orbitales $5d$ qui interagissent fortement avec leur environnement (au contraire des orbitales f). Sous excitation, un électron promu de g à e (par exemple de l'orbitale f à d), relaxe vers l'état inférieur de l'état e et émet un photon. Néanmoins, si la température est suffisamment élevée, un 'quenching' en température peut se produire en raison de l'intersection des deux paraboles. Typiquement, la température va activer les phonons favorisant les états de haute énergie qui peuvent déclencher le retour non-radiatif à l'état fondamental. La **Figure 1-9b** est caractéristique des transitions interdites $f-f$. À première vue, les états excités et fondamentaux peuvent être superposés verticalement. Aucun 'quenching' thermique n'est, a priori, attendu parce qu'aucun croisement de paraboles n'est possible. En fait, le processus non-radiatif, appelé relaxation multi-phonon, peut néanmoins avoir lieu si certaines conditions sont présentes. C'est le cas si la différence d'énergie (ΔE) entre les états fondamentaux et excités est inférieure à 5-10 fois l'énergie des phonons ($\Delta E < 5-10 \hbar w$). Par ailleurs, si la température augmente, la relaxation multi-phonon sera favorisée grâce à la population des niveaux des phonons à l'énergie plus élevée. Enfin, la **Figure 1-9c** rassemble en une seule figure les deux schémas précédents. L'activateur est excité par une transition permise $g \rightarrow e'$ (la transition $d-d$ avec $\Delta S = 0$ ou le transfert de charge d'anion - cation). Ensuite, le système relaxe non radiativement si la température est "très" élevée ou transite vers une configuration excitée e avant de retourner à l'état fondamental avec l'émission de lumière. La transition $e' \rightarrow g$ est alors définitivement éteinte au bénéfice de la transition $e \rightarrow g$. Typiquement, une telle situation se produit pour $\text{Al}_2\text{O}_3: \text{Cr}^{3+}$, où les différentes étapes d'excitation et d'émission peuvent se résumer comme ci-dessous: i) l'excitation $^4\text{A}_2 \rightarrow ^4\text{T}_2$ ($\Delta S = 0$), ii) la relaxation $^4\text{T}_2 \rightarrow ^2\text{E}$, et iii) l'émission $^2\text{E} \rightarrow ^4\text{A}_2$. Un schéma similaire est aussi proposé pour les réseaux hôtes contenant Eu^{3+} .

3.1.2 Le transfert d'énergie (TE)

Il est bien connu que le transfert d'énergie (**Figure 1-6**) entre les ions peut jouer un rôle important pour générer l'émission blanche et pour adapter les caractéristiques d'émission à la demande (déplacement d'une couleur froide à une couleur chaude, par exemple). Le TE entre un sensibilisateur (S) et un activateur (A) peut s'exprimer par l'**équation (1-3)**:



où l'état excité a été marqué par un astérisque. Mettons l'accent sur le fait que A peut également jouer le rôle de S vers les activateurs de la même espèce. Le TE de S à A peut avoir lieu via des transferts radiatifs (i.e. l'absorption par A de l'émission de S), ou par des transferts non-radiatifs résonnantes. Le premier cas obéit à la théorie décrite brièvement ci-dessus (les phénomènes d'absorption / émission classiques). Ce deuxième cas est un peu plus complexe et les principes fondamentaux seront décrits ici très brièvement. Les discussions seront limitées au strict minimum pour introduire les discussions des chapitres II et III.

D'un point de vue physique, le processus TE non-radiatif est basé sur les interactions d'échange (le recouvrement entre les orbitales des atomes S et A) et les interactions multipolaires (principalement dipôle-dipôle) électriques (ou magnétiques). Quelle que soit l'interaction, l'efficacité de TE dépendra du degré de chevauchement entre les spectres d'émission de S et les spectres d'excitation de A et de la distance R séparant A de S. En pratique, le taux de transfert de S à A est exprimé par l'**équation (1-4)**:

$$P_{SA} = \frac{2\pi}{\hbar} | \langle S, A^* | H_{SA} | S^*, A \rangle |^2 \times \int g_S(E) g_A(E) dE \quad (1-4)$$

où $g_S(E)$ et $g_A(E)$ sont toutes des fonctions normalisées du centre S et A (l'émission et l'absorption, respectivement), H_{SA} est l'interaction Hamiltonien, $|S^*, A\rangle$ et $|S, A^*\rangle$ sont les configurations électroniques dans les états initiaux (avant le transfert) et finaux (après le

transfert), respectivement. En fait, l'intégrale représente le chevauchement spectral entre l'émission de S et de l'absorption de A (partie hachurée sur la **Figure 1-10**).

Le type d'interaction (H_{SA}), dépendant fortement de la distance entre S et A, détermine le taux de TE. En particulier, pour les interactions dipôle-dipôle, dipôle-quadrupôle et quadrupôle-quadrupôle, la probabilité de transfert est inversement proportionnelle à R^6 , R^8 et R^{10} , respectivement (R: la distance entre S et A). Pour l'interaction d'échange, la dépendance en distance est exponentielle. Par conséquent, le TE de S à A peut être efficace pour les valeurs de R jusqu'à environ 30 Å pour les transitions permises dipolaires électriques (les transitions $4f \rightarrow 5d$ par exemple). Si les transitions sont interdites, le transfert peut avoir lieu seulement via l'interaction d'échange et les valeurs de R inférieures à ~ 10 Å sont alors requises. Dans les chapitres II et III, nous discutons de l'origine de TE et mettons en évidence leurs intérêts pour modifier les caractéristiques optiques de nos matériaux.

3.2 Les coordonnées chromatiques CIE et la température de couleur

Une couleur est caractérisée par ses paramètres chromatiques CIE (x, y). Selon la Commission Internationale de l'Eclairage (CIE), chaque couleur en colorimétrie peut être décomposée en trois coordonnées associées à trois fonctions concordant aux couleurs comme décrit dans la **Figure 1-11**. Ces trois courbes sont destinées à correspondre à la sensibilité de trois capteurs de couleur des yeux d'humains. Puis, les valeurs trichromatiques CIE (XYZ) peuvent être calculées selon les **équations (1-5)** ci-dessous:

$$\begin{aligned} X &= \int \Phi(\lambda) \bar{x}(\lambda) d\lambda \\ Y &= \int \Phi(\lambda) \bar{y}(\lambda) d\lambda \\ Z &= \int \Phi(\lambda) \bar{z}(\lambda) d\lambda \end{aligned} \quad (1-5)$$

où l'intégration est effectuée sur toute la gamme visible du spectre électromagnétique et $\Phi(\lambda)$ est le spectre d'émission du phosphore à l'étude. Comme le concept de couleur peut être divisé en deux parties, la luminosité et la chromaticité (un matériau blanc et un matériau gris

ont la même couleur (blanche), mais une luminosité différente), l'espace colorimétrique CIE (XYZ) peut être remplacé par l'espace colorimétrique CIE (xyY) où Y mesure la luminosité et le (x, y) mesure la chromaticité qui donne lieu le diagramme de chromaticité donné dans la **Figure 1-12** avec les valeurs calculées par les **équations (1-6)**:

$$\begin{aligned} x &= X / X + Y + Z \\ y &= Y / X + Y + Z \quad (1-6) \\ z &= Z / X + Y + Z = 1 - x - y \end{aligned}$$

Un phosphore idéal avec une luminescence blanche sera associé au point $x = y = 1/3$ du diagramme de chromaticité. Bien sûr, les phosphores bleus, verts, jaunes, oranges ou rouges seront attribués à un point spécifique du diagramme. Une lumière monochromatique correspondra au point situé à la périphérie du diagramme, appelé spectrum locus.

La température de couleur (CT) est un autre terme important couramment utilisé pour qualifier un phosphore. D'après le **Tableau 1-3**, il apparaît qu'une CT de 1850K, 3000K, 5400K et 6500K correspondrait approximativement à la flamme d'une bougie, une ampoule à incandescence ou une ampoule blanche fluorescente compacte, un flash électronique et la lumière du jour, respectivement (voir Tableau 1-3 pour plus d'information). Généralement, les températures de couleur supérieure à 5000K sont classés comme des couleurs froides (c'est-à-dire, blanc bleuté), tandis que les températures de couleur blanche autour de 3000K sont appelées couleurs chaudes (blanc jaunâtre à blanc rougeâtre). Juste pour souligner l'importance de la CT, la **Figure 1-13** rassemble les photographies de la même pièce sous les différents éclairages.

Chapitre II: Etude du transfert d'énergie entre cations Eu^{2+} et cations Eu^{3+} dans les matériaux $MAl_2Si_2O_8$ ($M = Ca, Sr, Ba$) dopé avec Eu et préparés à l'air

Les matériaux $MAl_2Si_2O_8$ dopés avec Eu^{2+} ($M = Ca, Sr, Ba$) préparés sous atmosphère réductrice font état d'une luminescence blanche-bleuâtre sous l'excitation UV. Ainsi, nous avons décidé d'enquêter sur la synthèse de ces composés synthétisés sous air pour favoriser la coexistence des cations Eu^{2+} et Eu^{3+} afin d'atteindre une couleur plus chaude, les cations Eu^{3+} donnant lieu naturellement à des émissions orange au rouge.

1. Introduction

Grâce à leurs propriétés luminescentes, les recherches approfondies ont été consacrées aux matériaux dopés avec Eu^{2+} . Dans ce cadre, les aluminates, les silicates, les aluminosilicates ont reçu beaucoup d'attentions et certains d'entre eux donnent lieu aujourd'hui à des applications importantes dans le domaine des écrans plasma et de l'éclairage (par exemple $BaMgAl_{10}O_{17}: Eu^{2+}$, $MAl_2O_4: Eu^{2+}$ ($M = Ca, Sr, Ba$), $CaMgSi_2O_6: Eu^{2+}$, etc.). Il est bien connu que la fluorescence des cations Eu^{2+} s'exprime normalement par une émission large dont la position peut varier dans une large gamme de longueurs d'onde allant de l'ultraviolet au jaune (et même le rouge) en fonction de l'intensité du champ cristallin généré par les ligands environnents, ces derniers impactant l'éclatement du bloc d en fonction de leur charge, de leur taille, de leur nombre, etc. La fluorescence de Eu^{2+} est souvent associée avec une transition permise du bloc 5d vers le bloc 4f qui est une transition $4f^65d^1 \rightarrow 4f^7$ dont la position en énergie peut être réglée à souhait via le choix approprié du réseau hôte. Les matériaux dopés avec des cations Eu^{3+} sont également largement étudiés, notamment dans les matrices oxydes, borates, phosphates et sulfures. Au contraire des cations Eu^{2+} , l'émission de ce genre d'ions est communément constituée de bandes étroites (transitions f-f) localisées dans le rouge et/ou l'orange. Les cations Eu^{3+} sont très utiles pour des applications dans le domaine

de l'éclairage et l'industrie d'affichage (la TV couleur par exemple). Les spectres d'émission des cations Eu³⁺ sont principalement associés à des transitions du niveau excité ⁵D₀ aux états fondamentaux ⁷F_j (j = 0 à 6). De plus, les probabilités de transition ⁵D₀ → ⁷F_j dépendent fortement de la symétrie du site occupé par l'activateur dans le réseau hôte. Ainsi, dans un site sans symétrie d'inversion, un cation Eu³⁺ présentera préférentiellement la transition électrique-dipôle hypersensible forcé ⁵D₀ → ⁷F₂ avec émission à une longueur d'onde d'environ 610 nm. En revanche, la transition permise magnétique-dipolaire ⁵D₀ → ⁷F₁ autour de 590 nm est généralement exacerbée pour des cations Eu³⁺ situés sur un site avec centre d'inversion. Ainsi, à l'opposé des cations Eu²⁺, les activateurs Eu³⁺ génèrent les luminescences qui ne dépendent pas (ou presque pas) du réseau hôte.

Avant de décrire mes travaux sur les aluminosilicates dopés avec Eu, je tiens à mettre l'accent sur le fait que les matériaux MAl₂Si₂O₈ dopés avec Eu²⁺ (M = Ca, Sr, Ba) ont déjà été étudiés à Nantes. Ainsi, F. Clabau a caractérisé les propriétés optiques de ces matériaux au cours de sa thèse et a mis en évidence leur longue luminescence persistante blanche. Pour plus d'informations, la phosphorescence dans ces composés est liée à une photooxydation des cations Eu²⁺ en Eu³⁺ sous l'irradiation, avec piégeage des électrons photogénérés sur les défauts positifs, à savoir des défauts construits sur des lacunes d'atomes d'oxygène. Ces électrons sont libérés à température ambiante et se recombinent sur les sites Eu³⁺ photo-ionisés avec une émission de lumière. F. Clabau a également démontré que, sur la base de mesures spectroscopiques de Mössbauer, une faible quantité résiduelle de cations Eu³⁺ est systématiquement présente dans les échantillons préparés, même si ceux-ci ont été synthétisés sous une atmosphère réductrice. Dans le contexte actuel, cela suggère que le ratio Eu²⁺/Eu³⁺ peut être contrôlé via les conditions de synthèse.

Sous l'excitation UV, les composés MAl₂Si₂O₈: Eu²⁺ émettent une lumière bleue-blanche avec les coordonnées chromatiques CIE à température ambiante de (0,17, 0,12), (0,16, 0,09) et (0,16, 0,11) pour M = Ca, Sr et Ba, respectivement. Bien sûr, ces valeurs peuvent paraître bien loin des valeurs cibles de l'ordre de (0,35, 0,35). Cependant, les propriétés optiques peuvent être modifiées significativement en jouant sur la composition chimique. Sur cette base, Yang et al. a démontré par exemple que les matériaux (Ca_{0,99-n}Eu_{0,01}Mn_n)Al₂Si₂O₈ peuvent conduire à la génération de lumière blanche sous excitation ultraviolette. Ces

matériaux présenteraient même selon les auteurs un réel potentiel comme phosphore pour diode inorganique émettant dans le blanc. La comparaison des caractéristiques chromatiques de ces séries de matériaux avec celles de diodes à base de YAG: Ce commerciale (Nichia Co., Japon) excitées par une lumière monochromatique bleu de 467 nm a conduit à des résultats assez probants. Ainsi, les coordonnées CIE sont (0,30, 0,29) et (0,33, 0,32) pour les compositions $(\text{Ca}_{0.79}\text{Eu}_{0.01}\text{Mn}_{0.20})\text{Al}_2\text{Si}_2\text{O}_8$ et $(\text{Ca}_{0.74}\text{Eu}_{0.01}\text{Mn}_{0.25})\text{Al}_2\text{Si}_2\text{O}_8$, respectivement excités dans NUV, à comparer avec (0,31, 0,27) pour le YAG: Ce recouvert sur un LED-chip GaN! A cet instant, la question essentielle concerne la possibilité de régler les coefficients chromatiques des matériaux $\text{MAl}_2\text{Si}_2\text{O}_8$ dopés avec Eu par rapport au ratio $\text{Eu}^{2+} / \text{Eu}^{3+}$.

À notre connaissance, la réduction de cations Eu^{3+} en cations Eu^{2+} à l'air a déjà été observée dans des composés, tels que les chlorures, les oxydes, les sulfures métalliques, sous une forme cristallisée ou plus fréquemment sous une forme vitreuse. Pour cette étude, nous sommes les premiers à étudier les propriétés de photoluminescence des composés $\text{MAl}_2\text{Si}_2\text{O}_8$ dopés avec Eu synthétisés à l'air où coexistent des valences mixtes $\text{Eu}^{2+} / \text{Eu}^{3+}$ avec transferts d'énergie possibles (TE) du Eu^{2+} vers Eu^{3+} . Formellement, avant toute caractérisation, la coexistence des deux types d'états pour l'europium (c'est-à-dire, Eu^{2+} et Eu^{3+}) dans nos matériaux préparés dans l'air peuvent être soupçonnés sur la simple base de photographies de composés excités à deux longueurs d'onde différentes, nommément 254 nm et 365 nm avec une lampe UV labosi Fisher Bioblock (**Figure 2-1**). Les luminescences rouges et blanches sont attribuées aux cations Eu^{3+} et Eu^{2+} , respectivement.

2. Description des structures $\text{MAl}_2\text{Si}_2\text{O}_8$ (M = Ca ; Sr et Ba)

Des études thermodynamiques ont montré que la structure des feldspath de formulation MASO est stable. Chaque composé est construit sur un réseau tridimensionnel de tétraèdres AlO_4 et SiO_4 qui s'enchaînent par les sommets de manière régulière de manière à ce que chaque tétraèdre de SiO_4 soient entouré de quatre tétraèdres d'aluminium et vice versa. Pour chaque composé, différentes variétés allotropiques existent. Le feldspath $\text{CaAl}_2\text{Si}_2\text{O}_8$ existe sous trois formes, triclinique (P-1), orthorhombique ou hexagonale (P63/mcm), parmi lesquelles la variété triclinique anorthite serait la seule phase stable. L'aluminosilicate $\text{SrAl}_2\text{Si}_2\text{O}_8$ présente quasiment les quatre mêmes formes cristallographiques. La variété

celsian (I2/c) est ici la forme stable de la température ambiante jusqu'à la température de fusion (1650°C), tandis que la variété slawsonite (P21/a) n'a encore jamais pu être synthétisée. La variété β -hexacelsian (P6/mmm) peut être obtenue par une trempe de la phase liquide, et la variété α - hexacelsian (Immm) apparaît sous certaines conditions lors du refroidissement. Le feldspath BaAl₂Si₂O₈, quant à lui, existe sous quatre formes cristallographiques, dont deux variétés naturelles toutes deux monocliniques. La variété la plus abondante, appelée celsian (I2/c), est la forme thermodynamiquement stable de la température ambiante jusqu'à 1590°C. La variété paracelsian (P2₁/a) n'a encore jamais pu être synthétisée. La variété synthétique hexagonale β -hexacelsian (P6₃/mcm) est stable de 1590°C jusqu'à la température de fusion (1760°C), et métastable sous 1590°C. Elle se transforme en variété orthorhombique α -hexacelsian (Immm) lors du refroidissement sous 300°C.

Dans les conditions de synthèse utilisées lors de cette thèse, nous avons obtenu la phase CaAl₂Si₂O₈ sous sa forme anorthite (P-1) dans laquelle l'ion Ca²⁺ occupe quatre sites cristallographiques. Trois de ces sites présentent une coordinence 7 et le dernier possède une coordinence 6. Pour le composé SrAl₂Si₂O₈, nous avons stabilisé la variété celsian (I2/c) pour laquelle l'ion alcalino-terreux Sr²⁺ ne se place que dans un seul site cristallographique de coordinence 9. La phase obtenue de BaAl₂Si₂O₈ est aussi une phase celsian où l'ion Ba²⁺ est présent en coordinence 9.

Des études antérieures, déjà menées au sein du groupe, ont montré que ces matrices étaient de très bonnes matrices hôtes pour générer des matériaux luminescents par dopage d'ions terres rares (Eu²⁺, Ce³⁺ ...). Par ailleurs, il a été démontré que ces ions terres rares se plaçaient préférentiellement sur les sites cristallographiques des ions alcalino-terreux.

3. Propriétés optiques des échantillons $MAl_2Si_2O_8$ ($M = Ca ; Sr$ et Ba) dopés par Eu²⁺ sous atmosphère réductrice

La matrice CASO dopé Eu²⁺ a été, dans un premier temps, étudiées. Les spectres d'émission de ces matériaux, enregistrés pour à une longueur d'onde d'excitation de 420 nm, présentent une large bande d'émission centrée en 440 nm. Cette bande d'émission est associée à la transition 4f⁶5d¹ \rightarrow 4f⁷ (⁸S_{7/2}) de l'ion Eu²⁺ et le maximum de la bande varie entre 420 et

475 nm lorsque la concentration en Eu^{2+} varie de 0 à 50%. L'important élargissement de la bande d'émission vient du caractère permis de la transition $5d \rightarrow 4f$ mais aussi de la présence de quatre sites cristallographiques de l'ion Ca^{2+} qui engendre autant de sites d'accueil potentiel pour l'europium. L'augmentation de la quantité d'europium conduit à un décalage du maximum de la bande d'émission vers les hautes longueurs d'onde qui peut être expliqué par un possible transfert d'énergie entre des ions europium placé dans différents sites cristallographiques.

Dans une étude précédente, des mesures Mössbauer avaient permis de montrer la présence d'ions Eu^{3+} résiduels issus du précurseur utilisé lors de la synthèse, soit Eu_2O_3 . Par conséquent, afin de vérifier si nos échantillons présentent également des traces d' Eu^{3+} , des spectres d'émission ont été enregistrés à une longueur d'onde d'excitation de 611 nm, qui correspond à la longueur d'onde caractéristique de lion Eu^{3+} . Le spectre, représenté en **Figure 2-9**, révèle en effet la présence de raies fines situées à 393 et 463 nm et caractéristiques de l'ion Eu^{3+} .

La même étude a été réalisée sur la matrice $\text{SrAl}_2\text{Si}_2\text{O}_8$ pour laquelle on observe une bande d'émission variant de 404 à 437 nm pour une concentration en europium variant de 0 à 15%. Le fait marquant pour ce composé est le fait que la bande d'émission ne présente pas un profil symétrique alors que la structure cristallographique ne possède qu'un site d'accueil pour l'ion europium. Cette légère asymétrie suppose donc la présence d'autres environnements pour l'ion Sr^{2+} (coordinence de surface ?). De la même manière que pour le composé $\text{CaAl}_2\text{Si}_2\text{O}_8$, les spectres d'émission, enregistrés à 611 nm, révèlent la présence d'ions Eu^{3+} dans la structure.

Pour la matrice BASO ($\text{BaAl}_2\text{Si}_2\text{O}_8$), les spectres d'émission caractéristique de l'ion Eu^{2+} présentent une large bande centrée à 440 nm et dont le maximum n'est pas modifié avec la concentration en ions europium. En revanche, contrairement aux deux autres matrices, le composé BASO ne présente pas de traces résiduelles d'ions Eu^{3+} .

La comparaison des spectres d'excitation des composés MASO dopés Eu^{3+} révèle une certaine similarité entre les matériaux. Il est cependant possible d'observer en **Figure 2-17** une tendance régulière allant de CASO à SASO et à BASO, à savoir que les bandes

d'excitation se décalent progressivement vers les hautes énergies quand on passe de la matrice CASO à la matrice BASO. A première vue, ce phénomène est en complet accord avec la diminution de la covalence de la liaison Eu-O lorsque l'on passe de la matrice CASO à la matrice BASO. En effet, plus la taille de l'ion alcalino-terreux est petite et plus l'éclatement des orbitales d de l'euroium dû au champ cristallin est important et plus l'énergie nécessaire à la promotion d'un électron de l'orbitale 4f vers l'orbitale 5d est faible. Notons que ce modèle simple permet d'expliquer le blue-shift observé dans l'hypothèse où le barycentre des orbitales d de l'euroium ainsi que la position en énergie des orbitales f ne sont pas affectées par le changement de matrice.

Contrairement aux spectres d'excitation, l'évolution de la bande d'émission de l'ion Eu^{2+} , lorsque l'on passe de la matrice SASO à la matrice BASO, est loin d'être régulière. Comme on peut le voir sur la **Figure 2-17**, le maximum d'émission est situé à 425 nm pour la matrice CASO, à 404 nm pour la matrice SASO et à 440 nm pour la matrice BASO. De manière générale, plus la coordinence du site est élevée et plus le champ cristallin est faible, cela se traduit par une plus faible longueur d'onde d'émission (énergie plus élevée). Parallèlement, pour une même coordinence, l'éclatement (ou levée de dégénérescence) du bloc d'orbitales 5d diminue lorsque la taille de l'ion alcalino-terreux augmente. Ainsi, l'émission de l'ion Eu^{2+} devrait être décalée vers les plus courtes longueurs d'onde lorsque le rayon ionique du cation M^{3+} augmente, c'est-à-dire selon la séquence $\text{Ca} < \text{Sr} < \text{Ba}$. En se basant sur cet argument, il est possible d'expliquer le blue-shift observé entre les matrices CASO et SASO. Au contraire, l'émission à plus grande longueur d'onde de la matrice BASO reste inexpliquée. Cependant, on peut observer que le décalage de Stokes est beaucoup plus important pour BASO (1.11 eV) que pour CASO (0.96 eV) et SASO (0.86 eV). Par définition, le décalage de Stokes est associé à la modification des distances d'équilibre Eu-O. Etant donné que cette distance est plus courte à l'état excité qu'à l'état fondamental (cf diagramme configurationnel) pour l'ion Eu^{2+} , il est possible de suggérer que les ions Eu^{2+} placés sur les sites du baryum peuvent gagner en stabilité à l'état excité par rapport au site du strontium (**Figure 2-19**).

Pour deux des trois matrices alumino-silicates étudiées lors de cette thèse, nous avons vu que malgré l'utilisation d'une atmosphère réductrice lors de la synthèse, il reste des traces d'ions Eu^{3+} . L'étude approfondies des spectres optiques enregistrés a démontré la présence

d'une superposition entre la bande d'émission de l'ion Eu^{2+} et la bande d'excitation de l'ion Eu^{3+} , suggérant la présence d'un possible transfert d'énergie entre Eu^{2+} et Eu^{3+} .

4. Propriétés optiques $\text{MAl}_2\text{Si}_2\text{O}_8$ dopés par Eu^{2+} et synthétisés sous air

Dans cette partie, nous nous sommes principalement orientés sur l'étude des matériaux synthétisés sous air à partir du précurseur Eu_2O_3 . Dans ces conditions, on imagine facilement que la quantité d'ions Eu^{3+} sera plus conséquente. De plus, la substitution d'ion alcalino-terreux par un ion trivalent, en l'occurrence Eu^{3+} , aura des répercussions non négligeables sur le matériau. On peut citer, par exemple, la présence de lacunes cationiques pour compenser l'équilibre des charges mais aussi la création de distorsions locales au sein de la structure cristallographique. Ainsi, lors de la synthèse, il est possible de considérer deux formulations, à savoir $\text{M}_{1-3x/2}\text{Eu}_x\text{Al}_2\text{Si}_2\text{O}_8$ et $\text{M}_{1-x}\text{Eu}_x\text{Al}_2\text{Si}_2\text{O}_{8+0.5x}$. Ces deux formules supposent évidemment que tous les atomes d'euroium sont complètement oxydés en Eu^{3+} . Concernant ces deux formulations, d'un côté, nous envisageons que les défauts créés par le dopage par Eu^{3+} soient des lacunes cationiques (deux ions Eu^{3+} remplacent trois cations M^{2+}) et de l'autre côté, nous supposons que des atomes d'oxygène interstitiels apparaissent pour contrebalancer le déficit de charge lorsque l'on substitue M^{2+} par Eu^{3+} . Bien que deux séries de composition ont été rigoureusement synthétisées, il s'avère que les échantillons finaux ne correspondent pas totalement à ce qui était attendu de par la présence conjoint d'ions Eu^{3+} et d'ions Eu^{2+} , comme nous allons l'expliquer par la suite.

Dans un premier temps, la matrice CASO dopé Eu synthétisée pour air a été caractérisée d'un point de vue optique. Sur les **Figures 2-21a** et **2-21b** sont représentés les spectres d'excitation (longueur d'onde d'émission de 425 nm) et d'émission (longueur d'onde d'excitation de 320 nm) des échantillons CASO :Eu obtenus sous air. Le spectre d'excitation présente une large bande caractéristique de la transition $4f \rightarrow 5d$ centrée à 320 nm avec l'apparition d'un épaulement situé à 287 nm. Sur le spectre d'émission, il est possible d'observer la transition typique de l'ion Eu^{2+} située autour de 425 nm. De ce fait, nous pouvons conclure quant à la présence d'ions Eu^{2+} dans les échantillons même lorsque ceux-ci sont synthétisés sous air, qui par comparaison au mélange Ar/H_2 peut être considérée comme une atmosphère oxydante. A partir des **Figures 2-21a** et **2-21b**, il est frappant de noter que

l'intensité de l'émission associée à Eu²⁺ commence à diminuer pour un taux de dopant de 2%. Notons que cette valeur incluse aussi bien les ions Eu³⁺ que les ions Eu²⁺, ce qui signifie que la quantité en ions Eu²⁺ est encore plus faible. Ainsi, la quantité réelle d'ions Eu²⁺ est inférieure à 2%, ce qui est aussi inférieur la concentration de « quenching » de 7% obtenues dans les conditions réductrices. Cette diminution de l'intensité de la bande d'émission peut être expliquée par la présence d'un transfert d'énergie entre Eu²⁺ et Eu³⁺.

L'étude des propriétés optiques de l'ion Eu³⁺ placé dans la matrice CASO a également été menée. Il est à noter ici, que comme les électrons de valence de l'ion Eu³⁺ sont écrantés par les électrons des orbitales 5s et 5p, les transitions 4f-4f de l'ion ne sont que faiblement affectées par le champ cristallin. Sur la **Figure 2-23**, il est possible d'observer les différentes raies d'excitation caractéristiques de l'ion Eu³⁺ ainsi que la présence d'une bande de transfert de charge O²⁻ → Eu³⁺ située dans le domaine ultra-violet. Sur le spectre d'excitation, il est possible de trouver la bande d'excitation à 320 nm associée à l'ion Eu²⁺ qui se superpose légèrement avec la bande de transfert de charge. On trouve aussi les différentes transitions f-f centrées à 361 nm, 382 nm, 393 nm, 413 nm, 463 nm, 530 nm et 576 nm que l'on peut attribuer aux transitions ⁷F₀ → ⁵D₄, ⁷F₀ → ⁵L₇, ⁷F₀ → ⁵L₀, ⁷F₀ → ⁵D₃, ⁷F₀ → ⁵D₂, ⁷F₀ → ⁵D₁ et ⁷F₀ → ⁵D₀, respectivement. Des spectres d'émission ont été enregistrés aux longueurs d'onde d'excitation des deux principales transitions de l'ion Eu³⁺. Il s'avère que plus la concentration totale en ions europium (Eu²⁺ et Eu³⁺) augmente et plus l'intensité des différentes raies d'émission s'accroît. Par ailleurs, lorsque la longueur d'onde d'excitation correspond à la bande de transfert de charge, on observe une intense bande d'émission associée à l'ion Eu²⁺ ainsi que les raies d'émission de l'ion Eu³⁺. Les mêmes observations ont pu également être faites pour la matrice SASO.

En revanche, dans le cas de la matrice BASO, les raies d'émissions caractéristiques des ions Eu³⁺ sont très faibles voire inexistantes, ce qui laisse supposer que, malgré un caractère oxydant lors de la synthèse, tous les ions Eu³⁺ introduits ont été réduite en ions Eu²⁺.

5. Stabilisation des ions Eu^{3+} dans les matrices MASO ($\text{M} = \text{Ca, Sr, Ba}$)

Lorsque les ions Eu^{2+} et/ou Eu^{3+} sont intégrées dans les réseaux hôte MASO, l'ion Eu pourrait être situé, au premier coup d'œil, dans tous les sites cationiques, c'est à dire les sites des ions alcalino-terreux M^{2+} mais aussi sur les sites des ions Al^{3+} et Si^{4+} , plus petits. De toute évidence, pour des raisons géométriques (à savoir la taille et la coordinence des sites), il est impossible pour ion europium puisse être placé dans les sites tétraédriques des ions Al^{3+} et Si^{4+} . Comme les lanthanides ont la propension à migrer vers les sites AE, comment pouvons-nous expliquer la capacité des matériaux MASO à stabiliser les deux degrés d'oxydation de leuropium, Eu^{2+} et Eu^{3+} , lorsque les matériaux sont préparés sous air? Communément, selon l'étude menée sur $\text{BaAlO}_4:\text{Eu}$, $\text{NaCaPO}_4:\text{Eu}$... quatre conditions sont nécessaires pour favoriser la réduction de Eu^{3+} en Eu^{2+} dans des matrices inorganique préparées sous atmosphère non réductrice avec des précurseurs contenant Eu^{3+} . Ils sont énumérés ci-dessous :

- 1) absence d'ions oxydants dans le réseau hôte
- 2) le dopant ion Eu^{3+} doit remplacer un cation divalent, soit un ion alcalino-terreux M^{2+}
- 3) le cation substitué est supposé avoir un rayon similaire à celui de l'ion Eu^{2+}
- 4) le réseau hôte doit être construit sur des groupes d'anions tétraédriques tels que SiO_4 , BO_4 , PO_4 , ou AlO_4 .

Dans le cas des matériaux MASO, les quatre critères sont remplis. Par conséquent, le processus de réduction de l'ion Eu^{3+} en Eu^{2+} peut se produire dans ces matrices aluminosilicates. De manière évidente, le degré de conversion dépendra fortement de la nature de lalcalino-terreux, et en particulier de l'écart de taille entre les rayons de Eu^{2+} , Eu^{3+} et les cations M^{2+} .

Comme mentionné précédemment, le spectre d'émission associé aux ions Eu^{3+} ont une intensité de plus en plus faible allant de CASO à BASO. Ce résultat signifie que l'existence de Eu^{3+} dans la matrice MASO est beaucoup plus difficile à stabiliser pour les phase au baryum que pour celles au Ca lorsque la synthèse s'effectue sous air. On peut expliquer cette tendance en prenant en considération la différence, en pourcentage, entre le rayon de M^{2+} , Eu^{2+} et Eu^{3+} . Normalement, il est bien admis que la différence de rayon ionique entre les ions introduits et

ceux substitués ne doit pas dépasser $\pm 30\%$. La différence, exprimée en pourcentage, peut être calculée par l'équation suivante (2-2):

$$D_r = 100 \times [R_m(CN) - R_d(CN)] / R_m(CN) \quad (2-2)$$

où Dr est la différence de rayon exprimée en pourcentage, CN représente la coordinence, Rm(CN) est le rayon du cation hôte (M^{2+}) et Rd(CN) est le rayon ionique du dopant (Eu^{2+} et Eu^{3+}). Les calculs de la différence de rayon exprimée en pourcentage pour les trois matrices MASO sont résumés dans le **Tableau 2-4**.

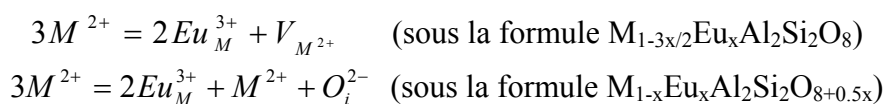
A partir du **tableau 2-4**, on peut voir que la valeur Dr entre le M^{2+} et Eu^{3+} augmente de façon significative d'environ 5% (Ca^{2+} - Eu^{3+}) à 24% (Ba^{2+} - Eu^{3+}), valeur proche de la limite de 30%. Cela suffit à expliquer pourquoi l'état trivalent de l'europtium est beaucoup plus difficile à stabiliser dans BASO que dans les matrices SASO et CASO. En outre, les différences entre le rayon M^{2+} et Eu^{2+} sont loin en-dessous de la limite en particulier pour la matrice SASO (0,76% contre 30%). Ceci suggère que l'ion Eu^{2+} est, *a priori*, stable dans les trois matériaux MASO. Cependant, pour la matrice SASO, en raison de la différence de rayon entre Sr^{2+} et Eu^{3+} qui n'est pas si élevée (14,50%), nous pouvons dire qu'il y a une quantité non négligeable d'ions Eu^{3+} dans la matrice. Quant à la matrice CASO, dans les deux différents sites cristallographiques ($CN = 6$ et 7), on peut avancer qu'il y aura une quantité beaucoup plus importante d'ions Eu^{3+} dans cette matrice car la valeur Dr entre Ca^{2+} et Eu^{3+} est beaucoup plus petite que celle entre Ca^{2+} et Eu^{2+} . À l'opposé, pour la matrice BASO, presque tous les ions Eu^{3+} sont susceptibles de se réduire en Eu^{2+} pour les mêmes raisons. Basé sur ces observations, on peut comprendre aisément le comportement optique (ratio Eu^{2+} / Eu^{3+}) dans la série MASO allant de Ca à Ba.

7. Mécanisme de réduction des ions Eu^{3+} en Eu^{2+} dans les matrices MASO ($M = Ca, Sr, Ba$)

Communément, il est bien accepté au sein de la communauté que la stabilisation des cations Eu^{2+} est provoquée par l'utilisation de conditions réductrices, tandis que les ions Eu^{3+} sont naturellement stabilisés sous air ou sous oxygène pur. A partir de ce postulat, il est souvent conclu que la synthèse sou air mènera systématiquement à la stabilisation des cations

Eu^{3+} uniquement, tandis que l'utilisation d'une atmosphère Ar/H₂ entraînera la réduction systématique des ions Eu^{3+} en Eu^{2+} .

En principe, la réduction des cations Eu^{3+} en Eu^{2+} nécessite le transfert d'électrons à partir d'éléments chimiques du réseau hôte vers la terre rare. Dans les matrices MASO, aucun élément ne peut être réduit. Ainsi, on peut se demander d'où les électrons viennent et comment ils sont transférés vers les ions Eu^{3+} ions situés dans la matrice MASO. D'un point de vue chimique, lorsque le dopant est ajouté à la place de l'alcalino-terreux dans l'état divalent (Eu^{2+}), la compensation de charge dans le réseau global MASO est remplie par une substitution une à une ($\text{M}^{2+}-\text{Eu}^{2+}$). En revanche, pour les cations Eu^{3+} placés sur les sites M^{2+} , la compensation de charge nécessite un changement dans la composition du réseau hôte, par l'apparition de lacunes cationiques ou des atomes d'oxygène dans les sites interstitiels. Ces deux types de réarrangements de charge peuvent être schématisés comme suit:



Considérons le premier cas que nous avons privilégié, à savoir la création de lacunes cationiques. Une lacune d'alcalino-terreux avec deux charges négatives sont générées ainsi que deux défauts de substitution avec une charge +1. Dans une certaine mesure, on peut considérer une lacune (avec deux charges négatives) comme donneur d'électrons et de même, les deux défauts positifs comme accepteurs d'électrons. En conséquence, par agitation thermique, les charges négatives des défauts lacunaires seraient transférées à l' Eu^{3+} pour le réduire en Eu^{2+} . L'ensemble du processus peut être exprimé par l'équation suivante (2-3):

$$2[Eu_M]^\bullet + [V_M]'' = 2[Eu_M]^x + [V_M]^x \quad (2-3)$$

En tenant compte de ce modèle, très utilisé dans la communauté des matériaux vitreux, on peut supposer que si d'autres lacunes sont créées, alors la quantité d'ions Eu^{3+} sera plus importante, par conséquent leur propension à être réduit à l'état divalent (Eu^{2+}) sera également renforcée. Sur la base de ce postulat, on comprend aisément que, pour les mêmes concentrations de dopant Eu, il y a plus de lacunes cationiques dans le composé présentant le formule $M_{1-3x/2}\text{Eu}_x\text{Al}_2\text{Si}_2\text{O}_8$ que pour la formule $M_{1-x}\text{Eu}_x\text{Al}_2\text{Si}_2\text{O}_{8+0.5x}$. Par conséquent, on

s'attend à ce que les cations Eu^{2+} soient plus stabilisés dans les composés $\text{M}_{1-3x/2}\text{Eu}_x\text{Al}_2\text{Si}_2\text{O}_8$ que dans les composés $\text{M}_{1-x}\text{Eu}_x\text{Al}_2\text{Si}_2\text{O}_{8+0,5x}$ pour une même concentration d'europtium. (voir les **figures 2-21 et 2-30**).

Pour confirmer l'hypothèse selon laquelle une augmentation de lacunes cationiques dans le réseau faciliterait la réduction de Eu^{3+} en Eu^{2+} , nous avons préparé une série de matériaux avec différents codopants dans la série CASO et analysé leurs propriétés optiques. Les codopants choisis étaient K^+ , La^{3+} et Zr^{4+} . Les matériaux ont été préparés dans les mêmes conditions qu'énoncées précédemment pour CASO: $\text{Eu}^{2+}/\text{Eu}^{3+}$. Les précurseurs utilisés sont K_2CO_3 , La_2O_3 et ZrO_2 pour K, La et Zr respectivement. Dans ce contexte, nous avons préparé les composés $\text{Ca}_{0.90}\text{Eu}_{0.05}\text{K}_{0.05}\text{Al}_2\text{Si}_2\text{O}_8$ (0 par Eu atome), $\text{Ca}_{0.85}\text{Eu}_{0.05}\text{La}_{0.05}\text{Al}_2\text{Si}_2\text{O}_8$ (1 par atome Eu), $\text{Ca}_{0.825}\text{Eu}_{0.05}\text{Zr}_{0.05}\text{Al}_2\text{Si}_2\text{O}_8$ (1,5 pour Eu atome) que nous avons comparés à $\text{Ca}_{0.925}\text{Eu}_{0.05}\text{Al}_2\text{Si}_2\text{O}_8$ (0,5 par atome Eu). Comme $r(\text{K}^+) = 1,37 \text{ \AA}$ lorsque le CN = 6 et $1,38 \text{ \AA}$ lorsque le CN = 7, $r(\text{La}^{3+}) = 1,032 \text{ \AA}$, lorsque le CN = 6 et $1,10 \text{ \AA}$ lorsque le CN = 7, $r(\text{Zr}^{4+}) = 0,72 \text{ \AA}$ lorsque le CN = 6 et $0,78 \text{ \AA}$ lorsque le CN = 7, ces ions sont susceptibles de remplacer les ions Ca^{2+} dans la matrice CASO pour des raisons stériques. En **Figure 2-38** sont représentés les spectres de photoluminescence des quatre matériaux pour une longueur d'onde d'excitation de 393 nm. Par ailleurs, dans le **Tableau 2-5** est regroupée l'évolution du rapport d'intensité entre l'émission de l'ion Eu^{2+} et celle de l'ion Eu^{3+} en fonction de la quantité de lacunes cationiques créées. Dans ce tableau R est défini comme étant le rapport du nombre d'électrons effectifs sur les défauts (s charge négative nette sur les défauts) et le nombre d'ions Eu^{3+} susceptibles d'être réduits.

D'après la **figure 2-38**, il apparaît évident que l'intensité de la transition $4f \rightarrow 5d$ de l'ion Eu^{2+} augmente selon la séquence $\text{K} < \text{Ca} < \text{La} < \text{Zr}$. La tendance inverse est observée pour l'évolution de l'intensité de la transition $4f \rightarrow 4f$ de l'ion Eu^{3+} . Ainsi, selon les résultats présentés dans le **tableau 2-5**, l'augmentation de la valeur de R favorise la réduction de l'ion Eu^{3+} en Eu^{2+} . Ainsi selon la séquence $\text{K}^+ < \text{Ca}^{2+} < \text{La}^{3+} < \text{Zr}^{4+}$, la quantité initiale d'ions Eu^{3+} qui subit une réduction augmente.

Par ailleurs, les spectres de PLE et PL de ces quatre échantillons ont été également enregistrés pour une longueur d'onde d'émission de 420 nm et une longueur d'onde

d'excitation de 320 nm (valeurs typiques des transitions permises pour Eu^{2+} dans la matrice CASO) comme le montre la **Figure 2-39**. Pour un taux fixe de dopant ($x = 5\%$), l'intensité d'excitation et d'émission d' Eu^{2+} augmente lorsque de plus en plus de lacunes cationiques sont créées. Ces résultats confirment en outre que plus la charge du co-dopant est élevée, plus il y a de lacunes cationiques et plus le degré de réductibilité des cations Eu^{3+} est important, tout cela ayant pour conséquence une augmentation du rapport $\text{Eu}^{2+}/\text{Eu}^{3+}$.

8. Transfert d'énergie Eu^{2+} - Eu^{3+} dans les matrices MASO (M = Ca, Sr, Ba)

Sur la base des résultats expérimentaux précédents, le diagramme des niveaux d'énergie des ions Eu^{2+} et Eu^{3+} et le chemin possible pour réaliser le transfert d'énergie entre Eu^{2+} et Eu^{3+} sont schématisés sur la **Figure 2-43**. Dans cette étude, nous avons mesuré les propriétés de fluorescence des ions Eu^{3+} correspondant aux transitions entre le niveau fondamental $^5\text{D}_0$ et les niveaux excités $^7\text{F}_J$ niveaux, sous une excitation correspondant à la transition $^7\text{F}_0 \rightarrow ^5\text{D}_2$. Comme déjà observé, la fluorescence est associée à la relaxation non radiative de l'ion excité Eu^{3+} vers le niveau fondamental $^5\text{D}_0$ et à la transition radiative vers les niveaux $^7\text{F}_J$. En outre, comme on peut le voir en **Figure 2-43**, le spectre d'émission de l'ion Eu^{2+} ($4\text{f}^65\text{d}^1$ (eg) $\rightarrow ^4\text{F}_7$) se superpose avec les spectres d'excitation de l'ion Eu^{3+} ($^7\text{F}_J \rightarrow ^5\text{D}_4$, $^5\text{D}_3$ jusqu'à $^5\text{D}_0$). Ainsi, le transfert d'énergie des ions Eu^{2+} vers Eu^{3+} peut être considéré comme suit: le niveau excité de l'ion Eu^{2+} relaxe partiellement vers le niveau fondamental $^8\text{S}_{7/2}$, et la partie restante de l'énergie sert à exciter les ions Eu^{3+} .

Le transfert d'énergie ne peut se produire que s'il y a chevauchement entre le spectre d'émission du sensibilisateur (Eu^{2+} dans ce cas présent) et le spectre d'excitation de l'activateur (Eu^{3+}). Une telle condition est respectée pour CASO et SASO comme on peut le voir en **Figures 2-44** et **2-45**. Rappelons que pour BASO, nous n'avons pas décelé la présence de cations Eu^{3+} . Par conséquent, le transfert d'énergie doit se faire via des interactions multipolaires. La question était donc de savoir si nous pouvons prouver la présence de ces transferts. En **Figure 2-44** sont représentés les spectres d'excitation pour CASO : Eu préparé sous air et sous un mélange Ar/H_2 (5%), respectivement. L'émission relative aux ions Eu^{2+} située à environ 425 nm est déclenchée par l'excitation de CASO: Eu à 287 et 320 nm. De toute évidence, le spectre d'excitation de la CASO: Eu $^{2+}$ /Eu $^{3+}$ enregistré à 611 nm, soit la

longueur d'onde caractéristique des transitions f-f de Eu³⁺, met en évidence la présence d'un pic à 320 nm. Par conséquent, nous pouvons conclure que l'on peut induire une émission de Eu³⁺ via l'excitation de Eu²⁺, ce implique un transfert d'énergie des ions Eu²⁺ vers les ions Eu³⁺. Cet argument est également soutenu par l'enregistrement du spectre d'excitation du composé CASO: Eu préparé sous atmosphère réductrice (contenant une faible quantité de cations Eu³⁺) pour une longueur d'onde d'émission égale à 611 nm. Pour SASO: Eu, le même raisonnement peut être appliqué (voir **Figure 2-45a**). Une autre indication d'un possible transfert d'énergie Eu²⁺ → Eu³⁺ dans les matrices CASO et SASO concerne l'évolution des spectres d'émission à 393 nm (**Figures 2-46** et **2-47** respectivement) où l'intensité de la transition 4f-5f de l'ion Eu²⁺ diminue au profit des transition 4f-4f de l'ion Eu³⁺ lorsque la concentration en europium augmente. Par ailleurs, la variation du temps de décroissance pour les matériaux CASO: Eu²⁺ / Eu³⁺ est en total accord avec la présence d'un transfert d'énergie.

En règle générale, l'efficacité du transfert d'énergie du sensibilisateur (Eu²⁺) vers l'activateur (Eu³⁺) peut être exprimée par l'équation suivante (2-4) :

$$\eta_T = 1 - \frac{I_s}{I_{s0}} \approx 1 - \frac{\tau_s}{\tau_{s0}} \quad (2-4)$$

où τ_s et τ_{s0} sont les temps de vie du sensibilisateur (Eu²⁺) en présence et en l'absence de l'activateur (Eu³⁺), respectivement. Ici, τ_{s0} est le temps de décroissance intrinsèque de l'émission de Eu²⁺ lorsque CASO est dopé seulement par Eu²⁺, à savoir 0,65 ms. Le nombre τ_s est le temps de décroissance du sensibilisateur (Eu²⁺) en présence d'un activateur (Eu³⁺), c'est à dire le temps de décroissance de l'émission des ions Eu²⁺ dans les échantillons préparés à l'air. Les valeurs recueillies sont présentées dans le **tableau 2-6**. Ainsi, l'efficacité du transfert d'énergie des ions Eu²⁺ vers Eu³⁺ dans le réseau hôte CASO est calculée pour les échantillons dans les différentes formules (**figure 2-49**). On peut alors observer que l'efficacité η_T augmente progressivement avec la concentration en europium. En outre, η_T est systématiquement plus élevé pour la formule C_{1-3x/2}Eu_xASO que pour C_{1-x}Eu_xASO_{8+0,5x} pour une valeur x donnée.

Le mécanisme de résonance du transfert d'énergie peut être constitué de deux types: 1) une interaction d'échange et 2) une interaction multipolaire. On sait que si le transfert d'énergie appartient à l'interaction d'échange, la distance critique entre le sensibilisateur et l'activateur doit être inférieure à 5 Å. Dans notre cas, la distance critique entre Eu^{2+} et Eu^{3+} est égale à 14,64 et 13.87 Å dans les deux différentes formules, respectivement. Par conséquent, le mécanisme de transfert d'énergie devrait correspondre à une interaction multipolaire. En outre, le mécanisme de transfert d'énergie entre Eu^{2+} et Eu^{3+} pour les composés de formule $\text{C}_{1-3x/2}\text{Eu}_x\text{ASO}$ et ceux de formule $\text{C}_{1-x}\text{Eu}_x\text{ASO}_{8+0,5x}$ est contrôlé par des interactions électriques de type multipoles-multipoles. D'après la théorie de Dexter, le mécanisme de transfert d'énergie obéit à l'équation suivante :

$$\frac{\tau_{S0}}{\tau_S} \propto C^{\alpha/3} \quad (2-5)$$

où τ_{S0} et τ_S sont les temps de déclin de luminescence des cations Eu^{2+} en l'absence et en présence d'ions Eu^{3+} , respectivement. C est la concentration totale d'ions Eu^{2+} et Eu^{3+} . Le paramètre α est égal à 6, 8 et 10 correspondant à une interaction de type dipôle-dipôle, dipôle-quadrupôle et quadrupôle-quadrupôle, respectivement. Les courbes représentant le rapport τ_{S0}/τ_S en fonction de $C^{\alpha/3}$ sont reportées en **figure 2-50a** ($\alpha = 6$), **2-50b** ($\alpha = 8$), **2-50c** ($\alpha = 10$) et **Figure 2-51a** ($\alpha = 6$), **2-51b** ($\alpha = 8$), le **2-51c** ($\alpha = 10$), pour les matériaux de composition $\text{C}_{1-3x/2}\text{Eu}_x\text{ASO}$ et $\text{C}_{1-x}\text{Eu}_x\text{ASO}_{8+0,5x}$, respectivement.

Comme le montrent les **figures 2-50a** et **2-51b**, ces courbes indiquent que le transfert d'énergie des ions Eu^{2+} vers Eu^{3+} se produit plutôt selon un mécanisme dipôle-dipôle pour les matériaux présentant la formule $\text{C}_{1-3x/2}\text{Eu}_x\text{ASO}$ et un mécanisme dipôle-quadrupôle pour la formule $\text{C}_{1-x}\text{Eu}_x\text{ASO}_{8+0,5x}$. Par conséquent, l'interaction électrique dipôle-dipôle prédomine dans le mécanisme de transfert d'énergie entre les ions Eu^{2+} et Eu^{3+} dans la formule $\text{C}_{1-3x/2}\text{Eu}_x\text{ASO}$ et un mécanisme dipôle-quadrupôle prédomine dans les matériaux $\text{C}_{1-x}\text{Eu}_x\text{ASO}_{8+0,5x}$. A ce stade, nous ne comprenons pas bien pourquoi le mécanisme dipôle-quadrupôle n'est pas obtenu pour les deux groupes d'échantillons comme on pourrait s'attendre.

9. Conclusion du chapitre II

En résumé, nous avons démontré la possibilité de "co-doper" les réseaux hôtes d'aluminosilicates $MAl_2Si_2O_8$ ($M = Ca, Sr, Ba$) avec à la fois des cations Eu^{3+} et Eu^{2+} via les réactions à l'état solide à haute température dans l'air avec a priori possibilité de contrôler la concentration de chacune des espèces. Les phases $MAl_2Si_2O_8$ dopées seulement avec Eu^{2+} doivent être préparées sous atmosphère réduite. Ces matériaux contiennent néanmoins une très faible concentration des cations Eu^{3+} résiduels (du moins pour les dérivés au Ca et au Sr) et présentent une luminescence bleutée blanche centrée à environ 425 nm, 404 nm et 440 nm pour M allant de Ca à Sr et Ba, respectivement. L'évolution irrégulière de la longueur d'onde d'émission depuis CASO à SASO et BASO pourrait être attribuée à une modification de l'environnement chimique local des cations Eu^{2+} une fois excités dans le réseau hôte de BASO.

Pour les matériaux préparés à l'air, les cations Eu^{2+} et Eu^{3+} coexistent, au moins pour les dérivés de Ca et Sr. Pour les phases BASO, il semble assez difficile de stabiliser la forme Eu^{3+} plus oxydée principalement en raison de la différence de rayon entre l'alcalino-terreux et la Terre Rare. En plus, la concentration d' Eu^{2+} au détriment des cations Eu^{3+} peut être privilégiée par le codopage avec les cations M^{4+} (Zr^{4+} par exemple). Cela pourrait ouvrir la porte à la synthèse à l'air de phosphores contenant Eu^{2+} dans un futur proche.

Comme prévu, la position et la forme des bandes d'émission Eu^{3+} ne sont pas influencées par la nature de réseau hôte. Pour les compositions CASO et SASO, les émissions les plus intenses sont autour de 611nm et peuvent être sensibilisés par le TE depuis Eu^{2+} . Elles conduisent à l'addition d'une contribution rouge à celle bleuâtre observée seulement pour les matériaux dopées avec Eu^{2+} . Nous prendrons dans le futur appui sur cette observation pour générer de nouveaux phosphores à l'air avec un contrôle des paramètres CIE (x, y) via un contrôle du rapport Eu^{2+}/Eu^{3+} et ainsi régler les émissions blanches pour passer d'une couleur froide à une couleur chaude ou *vice versa*.

Chapitre III: Caractérisation optique de matériaux $\text{M}_{1-y-3x/2}\text{Al}_2\text{Si}_2\text{O}_8$: $x\text{Ce}^{3+}, y\text{Mn}^{2+}$ ($\text{M} = \text{Ca, Sr}$)

Parmi les matériaux dopés avec les ions de terres rares, les phosphores activés par Ce^{3+} ont été largement appliquées dans le domaine de l'éclairage, l'affichage, et la scintillation. Ici nous avons spécifiquement étudié la capacité des cations de Ce^{3+} à transférer de l'énergie aux cations Mn^{2+} pour passer d'une lumière froide à une lumière chaude.

1. Introduction

En raison de ses propriétés spectroscopiques versatiles, l'ion Ce^{3+} a été utilisé comme activateur mais également comme sensibilisateur (forte section efficace d'absorption) dans les divers matrices hôtes. Comme les cations Eu^{2+} , les ions Ce^{3+} sont caractérisés par des transitions électroniques autorisées qui ont lieu entre les orbitaux 4f et 5d. Comme prévu, les propriétés optiques sont fortement affectées par la force du champ cristallin de la matrice hôte et l'émission peut prendre forme dans les domaines UV et visible. De la même manière, les matériaux luminescents dopés avec Mn^{2+} sont connus pour toujours présenter des émissions à large bande localisées entre 500 à 700 nm selon leur champ cristallin. Pour rappel, les cations Mn^{2+} présentent une configuration $3d^5$ avec un état fondamental $6A^1$. Généralement, les phosphores activés par Mn^{2+} sont divisés en deux catégories : ceux avec une émission verte et ceux avec une émission jaune ou rouge. Dans un environnement octaédrique (champ cristallin fort), l'émission est généralement située à une longueur d'onde plus grande que dans un environnement tétraédrique (champ cristallin faible). Dans de nombreux cas, l'émission provient de niveau $4T_1$ (4G), qui se déplace vers les énergies plus bas pour une intensité de champ de cristal plus élevée. Bien que ces matériaux luminescents dopés de Mn^{2+} puissent être les bons candidats pour les phosphores émettant du vert au rouge, leur inconvénient est que les transitions d'ions Mn^{2+} d-d sont a priori interdites, et que les ions sont donc difficiles à

exciter. Ye et al. et Kim et al. ont observé des transferts d'énergie non radiatifs efficaces de Eu²⁺ à Mn²⁺ dans BaMg₂Si₂O₇ et Ba₃MgSi₂O₈, respectivement, où Mn²⁺ présente des émissions rouges. On peut donc imaginer aisément par analogie que les ions Ce³⁺ pourraient aussi être des sensibilisateurs efficaces pour les activateurs de Mn²⁺ lorsqu'ils sont placés dans une matrice commune. Jusqu'à maintenant, Ce³⁺ a été étudié dans quelques hôtes codopées par Mn²⁺, tels que MgSiN₂, BaAl₂O₄ et Ca₉Y(PO₄)₇ afin d'améliorer l'intensité des émissions de Mn²⁺. A notre connaissance, les propriétés de luminescence de MAI₂Si₂O₈: Ce³⁺, Mn²⁺ n'ont pas encore été rapportées dans la littérature. Dans cette étude, nous avons rapporté sur un phosphore émettant une lumière blanche avec l'émission accordable, soit MAI₂Si₂O₈: Ce³⁺, Mn²⁺ (ci-après abrégé en MASO: Ce, Mn). Nous avons systématiquement étudié le mécanisme de TE entre Ce³⁺ et Mn²⁺ basé sur l'évolution des intensités d'émission par rapport aux taux de dopage.

2. Fluorescence des composés MASO (M = Ca, Sr) dopés Ce³⁺

La **Figure 3-3** montre le spectre d'excitation des composés C_{1-3x/2}ASO: xCe³⁺ (x = 1% et 10%) enregistrés à 356 nm qui correspond à la principale bande d'émission de l'ion Ce³⁺. Le spectre d'excitation est composé de deux bandes situées à 250 nm et 294 nm qui correspondent aux transitions du niveau fondamental 4f (²F_{5/2}) vers le bloc 5d séparé en plusieurs composantes en raison de l'éclatement dû au champ de ligand (le niveau ²F_{7/2} de l'ion Ce³⁺ ne peut pas être occupé à la température ambiante et, de ce fait, ne peut pas être pris en considération à cause de l'importante séparation spin-orbite (~ 1860 cm⁻¹ = 231 meV ≈ 0,25 eV) par rapport à l'agitation thermique (26 meV)). Les bandes d'absorption sont assez larges, ce qui empêche de distinguer les différentes transitions 4f → 5d des deux types de sites cristallographiques proposés par la structure CASO.

Les spectres d'émission des composés C_{1-3x/2}ASO: xCe³⁺ sont illustrés en **Figure 3-4**. Les spectres d'émission sont constitués de deux larges bandes situées à 356 et 430 nm, respectivement. On peut également remarquer un léger épaulement autour de 340 nm qui disparaît progressivement avec l'augmentation de la teneur en cérium. Comme Ce³⁺ peut occuper deux types de sites dans le cristal, au moins deux types d'émissions doivent être observées. En outre, chaque ion Ce³⁺ devrait conduire à deux bandes d'émission séparées par environ 0,25 eV due au couplage spin-orbite de l'état fondamental 4f¹ de Ce³⁺ (transitions 5d

$\rightarrow ^2\text{F}_{5/2}$ et $5\text{d} \rightarrow ^2\text{F}_{7/2}$). A ce stade, compte tenu de l'effet du champ cristallin, on peut soupçonner que les ions Ce^{3+} qui sont placés sur les sites de coordinence 7 donneront lieu à des bandes à faible longueur d'onde (340 nm), tandis que les cations Ce^{3+} en coordinence 6 devraient conduire à une bande d'émission à plus grande longueur d'onde (356 nm).

Comme deux bandes d'émission larges sont observées au lieu des quatre bandes attendues (une pour chaque site + un dédoublement de chaque bande dû au couplage spin-orbite), nous avons effectué une décomposition des spectres d'émission) l'aide de fonctions gaussiennes. Les décompositions ont été effectuées pour tous les échantillons et pour les deux longueurs d'excitation. Sur la **Figure 3-6** et la **Figure 3-7** sont reportés un exemple de déconvolution pour les spectres d'émission relatifs à l'échantillon dopé par 9% Ce^{3+} ($\lambda_{\text{exc}} = 294$ nm et $\lambda_{\text{exc}} = 250$ nm, respectivement).

Les déconvolutions ont pu être réalisées en utilisant cinq bandes pour CASO: Ce^{3+} quelle que soit la longueur d'onde d'excitation. Ces bandes sont situées à 3,79 eV (327 nm), 3,52 eV (352 nm), 3,49 eV (355 nm), 3,27 eV (379 nm) et 2,96 eV (430 nm) pour $\lambda_{\text{ex}} = 294$ nm et à 3,75 eV (331 nm), 3,52 eV (352 nm), 3,46 eV (358 nm), 3,22 eV (385 nm) et 2,91 eV (426 nm) pour $\lambda_{\text{ex}} = 250$ nm (**Figures 3-6 et 3-7**). Les émissions situées à 3,79 eV (3,75 eV pour $\lambda_{\text{ex}} = 250$ nm) et 3,49 eV (3,52 eV pour $\lambda_{\text{ex}} = 250$ nm) peuvent être associées à la présence de Ce^{3+} dans un type de sites cristallographiques, tandis que les émissions à 3,52 eV (3,46 eV pour $\lambda_{\text{ex}} = 250$ nm) et 3,27 eV (3,22 eV pour $\lambda_{\text{ex}} = 250$ nm) correspondent aux autres sites (autre coordinence). Si on se reporte à la théorie du champ cristallin, il est souvent reporté que plus la coordination est élevée, plus la longueur d'onde de l'émission est faible en raison d'une faible levée de dégénérescence. Par conséquent, les pics d'émission à 3,79 eV (327 nm) et 3,49 eV (355 nm) peuvent être attribués à la coordinence 7, tandis que les pics à 3,52 eV (352 nm) et 3,27 eV (379 nm) doivent correspondre à la coordinence 6. Cependant, cette hypothèse doit être tempérée par l'existence de certains contre-exemples.

Maintenant, il est intéressant de constater que des pics supplémentaires situés à $\sim 2,96$ eV (430 nm) ont été toujours observés quelles que soient les concentrations en Ce^{3+} dans la matrice CASO et les longueurs d'onde d'excitation. Ce type de bandes ne peut pas provenir de

la transition de l'ion Ce^{3+} dans la matrice CASO parce que: 1) toutes les quatre sites cristallographiques différents de l'ion Ca^{2+} sont occupés par Ce^{3+} et les bandes d'émission sont toutes situées dans la plage de 300 à 380 nm, 2) la plus petite différence d'énergie entre la bande d'émission de 2,96 eV et le Ce1 (3,27 eV, 3,52 eV) est beaucoup plus grande que 0,25 eV ($\sim 0,31$ eV). Cela signifie que ce groupe ne peut pas provenir de la transition issue de séparation spin-orbite de l'état fondamental de Ce^{3+} . De plus, comme précédemment étudié dans la littérature, la bande d'émission d'ions Eu^{2+} placé dans la matrice CASO est situé à ~ 425 nm. Toutefois, cette possible pollution par l'ion Eu^{2+} peut également être exclue parce que le temps de décroissance de la bande d'émission à 430 nm est égale à 22 ns ce qui n'est pas caractéristique de l'ion Eu^{2+} et ne correspond pas du tout à le temps de décroissance de 0,65 ms mesuré dans CASO: Eu^{2+} (voir chapitre II). Remarquons à ce stade que les synthèses ont été également réalisées dans de nouveaux creusets d'alumine avec des précurseurs de haute pureté et elles ont systématiquement conduits à des matériaux présentant cette bande d'émission large à environ 430 nm.

En fait, en raison de la différence de charge entre Ce^{3+} et Eu^{2+} et pour maintenir l'équilibre de charge, deux ions Ce^{3+} sont nécessaires pour compenser trois ions Ca^{2+} . Par conséquent, une lacune cationique ace deux charges négatives et deux défauts positifs seront créés lorsque deux Ce^{3+} cations seront introduits dans le réseau hôte à la place d'ions Ca^{2+} selon l'équation (3-2):



Ainsi, nous pouvons penser que cette bande d'émission large à environ 420 nm est due à des niveaux perturbés de lacunes situées au voisinage de $\text{Ce}_{\text{Ca}}^{\bullet}$. De cette façon, il peut aussi expliquer que la force d'une telle bande devrait augmenter naturellement avec la concentration de cérium dans la matrice CASO (par création de plus de lacunes), ce qui est observé sur la **Figure 3-4**.

En outre, nous pouvons vérifier cette hypothèse par le dopage de la matrice CASO avec La^{3+} , La^{3+} et K^+ et Ce^{3+} et K^+ (**Figure 3-9**). Pour des raisons stériques ($r(\text{K}^+) = 1,38$ Å et 1,46 Å, $r(\text{La}^{3+}) = 1,03$ Å et 1,10 Å lorsque CN = 6 et 7, respectivement) tous les dopants occupent

les sites du calcium. Le spectre d'émission du réseau CASO non dopé a également été mesuré à $\lambda_{\text{ex}} = 294$ nm. Aucune bande d'émission du réseau hôte n'est observée, ce qui indique clairement que la bande supplémentaire (420 nm) ne peut pas provenir de la matrice CASO elle-même. Lorsque seuls les ions La^{3+} sont introduits, on peut voir un unique pic d'émission aux alentours de 430 nm. Ainsi, cette bande peut être associée sans aucun doute à des défauts car les ions La^{3+} ne peuvent pas conduire à des émissions. De la même manière, lors du codopage Ce^{3+} avec K^+ ($2\text{Ca}^{2+} \rightarrow \text{Ce}^{3+} + \text{K}^+$), le pic d'émission à environ 430 nm tend à disparaître. Cela confirme définitivement que le pic situé autour de 430 nm provient des défauts lacunaires ($V_{\text{Ca}}^{\text{II}}$).

La même étude a été réalisée sur la matrice $\text{SrAl}_2\text{Si}_2\text{O}_8$ et les mêmes conclusions ont été faites.

3. Fluorescence des composés MASO (M = Ca, Sr) dopés Mn^{2+}

Pour les composés CASO dopés Mn^{2+} , le spectre d'excitation est constitué de plusieurs bandes faibles dans les régions UV et visible. Ces bandes sont attribuées aux transitions interdites par le spin entre les électrons des orbitales 3d^5 . Comme les transitions d-d de Mn^{2+} sont interdites en spin et en parité, ces transitions sont difficiles à exciter et, par conséquent les intensités sont très faibles. Selon le diagramme Orgel pour l'ion Mn^{2+} , le spectre d'excitation est constitué de plusieurs bandes centrées à ~ 339 , 353 , 403 , 416 , et 470 nm qui correspondent aux transitions de l'état fondamental de ${}^6\text{A}_1$ (${}^6\text{S}$) vers les sous-niveaux ${}^4\text{E}$ (${}^4\text{D}$), ${}^4\text{T}_2$ (${}^4\text{D}$), $[{}^4\text{A}_1$ (${}^4\text{G}$), ${}^4\text{E}$ (${}^4\text{G}$)], ${}^4\text{T}_2$ (${}^4\text{G}$) et ${}^4\text{T}_1$ (${}^4\text{G}$), respectivement. En outre, la large bande d'émission intense centrée à ~ 568 nm est attribuée à la transition interdite de spin ${}^4\text{T}_1$ (${}^4\text{G}$) \rightarrow ${}^6\text{A}_1$ (${}^6\text{S}$) de Mn^{2+} .

De la même façon pour la matrice SASO, le spectre d'émission de l'ion Mn^{2+} est composé de plusieurs bandes d'émission situées à ~ 334 , 346 , 401 , 416 et 445 nm et associées aux transitions énoncées précédemment.

4. Transfert d'énergie entre Ce³⁺ et Mn²⁺ dans les matrices CASO et SASO

La **Figure 3-21** montre le recouvrement spectral entre le spectre d'émission de Ce³⁺ ($\lambda_{\text{ex}} = 294 \text{ nm}$) et le spectre d'excitation de Mn²⁺ ($\lambda_{\text{em}} = 568 \text{ nm}$) dopés dans la matrice CASO. La comparaison de ces deux spectres pour les deux composés C_{0.865}ASO: 9% Ce³⁺ et C_{0.91}ASO: 9% Mn²⁺ révèle une superposition entre les bandes d'émission de Ce³⁺ et la base de la bande de "défaut" et la bande principale d'excitation de Mn²⁺. Par conséquent, on peut supposer que le transfert d'énergie de l'ion Ce³⁺ et "défauts" vers les ions Mn²⁺ peut se produire à travers un phénomène résonant. Jusqu'à maintenant, ce genre de transfert d'énergie entre Ce³⁺ et Mn²⁺ a également été observé chez d'autres matrices hôtes, comme dans les silicates d'alcalino-terreux de type glasérite, des fluorures, des nanocristaux de phosphate ou encore des sulfures ... Il n'y a pas d'étude reportée dans la littérature sur l'utilisation de Mn²⁺ et Ce³⁺ en tant que co-dopants pour améliorer la luminescence de matrices MASO (M = Ca, Sr).

La **Figure 3-23** illustre les spectres d'émission des échantillons luminophores préparés avec une concentration fixe Ce³⁺ (9%, la concentration critique de Ce³⁺ dopé dans CASO) et différentes concentrations en Mn²⁺ (0 à 15%). Les échantillons ont été excités à 294 nm, ce qui correspond à la bande d'excitation principale de CASO: Ce, Mn. Le spectre d'émission couvre presque toute la région visible pour les CASO: Ce, Mn comparé aux échantillons CASO: Ce et CASO: Mn. De plus, les intensités relatives de ces trois émissions peuvent être modulées pour former une lumière blanche pure dans une seule matrice en ajustant simplement les concentrations des activateurs et en utilisant le phénomène de transfert d'énergie. Cette lumière blanche obtenue permettrait une fabrication facile de lumière avec une parfaite stabilité et une reproductibilité des couleurs. Comme on peut le voir dans l'onglet de la **Figure 3-23**, l'intensité de l'émission de Ce³⁺ diminue de façon monotone avec l'augmentation de la teneur en Mn²⁺, tandis que l'intensité d'émission de Mn²⁺ atteint un maximum à environ 9% de Mn²⁺ avant de décroître. Notons ici que l'intensité des bandes provenant de la bande d'émission des lacunes et située à ~ 430 nm diminue également lorsque le taux de Mn²⁺ augmente. Ce phénomène indique que le transfert d'énergie se produit également à partir de ces bandes vers les ions Mn²⁺.

De la même manière que pour le chapitre MASO :Eu sous air, l'efficacité du transfert d'énergie été calculée entre Ce³⁺ et Mn²⁺. Comme le montre la **Figure 3-25**, l'efficacité du

transfert d'énergie augmente lorsque la concentration en Mn^{2+} augmente. Toutefois, l'efficacité du transfert évolue moins rapidement à fortes concentrations de Mn^{2+} . Ceci indique que la quantité d'énergie qui peut être transférée de Ce^{3+} à Mn^{2+} est progressivement restreinte par la grande concentration en Mn^{2+} .

A partir de la théorie de Dexter, le mécanisme de transfert d'énergie a été mis en évidence par le tracé du rapport I_{S0}/I_S en fonction de $C^{\alpha/3}$ où C correspond à la concentration en Mn^{2+} . Au regard de la **Figure 3-26**, il a été montré que le mécanisme dipole-dipole caractérisait le transfert d'énergie entre le Ce^{3+} et Mn^{2+} dans la matrice CASO. De la même façon, le suivi de l'évolution de l'intensité de la bande relative aux défauts et de la bande d'émission du manganèse a permis de conclure également à un mécanisme dipole-dipole.

De la même façon, l'étude a été menée sur la matrice SASO qui, bien que le transfert d'énergie est beaucoup moins intense, présente un transfert d'énergie entre Ce^{3+} et Mn^{2+} ainsi qu'entre les lacunes cationiques et les ions Mn^{2+} .

5. Conclusion du chapitre III

En conclusion, les phosphores aluminosilicatés $\text{MAl}_2\text{Si}_2\text{O}_8$ (M = Ca, Sr) co-dopés avec Ce^{3+} et Mn^{2+} aux couleurs ajustables ont été préparés par la méthode céramique traditionnelle, et leurs propriétés de luminescence ont été étudiées en détails. Les spectres de photoluminescence (PL) montrent que les phosphores MASO: Ce^{3+} présentent de fortes bandes d'émissions dans le bleu associées à des transitions permises intrasites du bas du bloc 4d du Ce^{3+} vers les états ${}^2\text{F}_{5/2}$ et ${}^2\text{F}_{7/2}$. A température ambiante, les concentrations critiques en céryum dans les matrices CASO et SASO sont estimés à environ 9% et 7%. Systématiquement, les émissions de céryum sont accompagnées par une large bande supplémentaire située à ~ 430 nm et ~ 400 nm pour les réseaux d'accueil CASO et SASO, respectivement. Cette bande serait associée à la présence de lacunes d'alcalinoterreux qui apparaissent lors des substitutions $\text{M}^{2+}/\text{Ce}^{3+}$ selon la réaction formelle: $3\text{M}^{2+} \rightarrow 2\text{Ce}_M^{\bullet} + V_M^{/\!/}$. L'intensité de ces bandes diminue fortement lorsque les matériaux CASO: Ce et SASO: Ce sont co-dopés avec

un métal alcalin ($2M^{2+} \rightarrow Ce_M^{\bullet} + Li_M^{\dot{}}_M$) , le codopage ayant pour effet de diminuer (voire d'annihiler) le nombre de lacunes cationiques ($V_M^{/\!/}$).

Parallèlement, l'examen des spectres de PL de MASO: Ce³⁺, Mn²⁺ a clairement démontré qu'il est possible d'exciter les cations Mn²⁺ par transfert d'énergie résonant Ce³⁺ → Mn²⁺ mais également "défaut" $V_M^{/\!/} \rightarrow Mn^{2+}$. Ceci conduit à l'addition d'une contribution jaune à la luminescence nominale bleue de MASO: Ce. Donc, via le choix propre des quantités de céryum et de manganèse, il est possible de régler la couleur des phosphores préparés à "souhait". La couleur d'émission des phosphores obtenus peut facilement être modulée du bleu au blanc en ajustant les quantités de Ce³⁺ et Mn²⁺. Dans ce contexte, il convient de mentionner que les compositions comme C_{0.85}ASO: 0.09Ce³⁺, 0.015Mn²⁺ (0,3176, 0,3242) et S_{0.85}ASO: 0.07Ce³⁺, 0.045Mn²⁺ (0.3362, 0.3442) sont assez proches de la couleur blanche prévue (1/3,1/3). Cependant, on peut regretter que la substitution de Mn²⁺ renforce la composante jaune plutôt que rouge, cette dernière étant préférée pour générer la lumière blanche chaude. Dans tous les cas, avant toute application dans des dispositifs UV-LEDs, le comportement des matériaux CASO: Ce, Mn et SASO: Ce, Mn devra être testée en température et le rendement quantique interne devra également être déterminé.

Conclusion générale

Le coefficient CIE (x, y) des matériaux $\text{MAl}_2\text{Si}_2\text{O}_8$ dopés avec Eu^{2+} et Ce^{3+} peut être influencé par l'insertion des cations de Eu^{3+} et Mn^{2+} dans le réseau hôte grâce à l'apparition des transferts d'énergie. Cela change la luminescence depuis blanche bleutée à blanche et rose ou jaune selon la concentration dans les dopants et codopants. De toute évidence, il témoigne que les spectres d'émission peuvent presque être adaptés à souhait via l'insertion des activateurs appropriés. Néanmoins, avant toutes applications de ces matériaux, des tests doivent être initiés concernant la stabilité de leurs propriétés optiques en température et leur capacité à générer les couleurs avec une grande efficacité (le rendement quantique externe).

Pour MASO (M = Ca, Sr) dopé avec Ce, un pic lié aux défauts est systématiquement observé. Plus précisément, cette bande d'émission, plus large que ceux associés aux transitions $\text{Ce}^{3+}-5d \rightarrow 4f$ et situé à la longueur d'onde plus grande, est liée à l'existence de lacunes d'alcalinoterreux nécessaire pour respecter l'équilibre de charges (c'est-à-dire, $3\text{M}^{2+} \rightarrow 2\text{Ce}_M^\bullet + V_M^{\parallel\parallel}$). L'intensité de cette bande peut être modulée et sa contribution presque anéantie quand les métaux alcalins sont utilisés comme codopants (c'est-à-dire, $2\text{M}^{2+} \rightarrow \text{Ce}_M^\bullet + A_M'$ avec A = K par exemple). Néanmoins, cette bande peut également présenter une certain intérêt car elle prend forme dans le visible et qu'elle peut servir de tremplin pour le transfert d'énergie des sensibilisateurs (par exemple Ce^{3+}) aux activateurs (par exemple Mn^{2+}). Selon les spectres de luminescence désirée, cette bande de "défaut" devra être privilégiée ou annulé.

Un point important de mes recherches concerne aussi la stabilisation possible des cations Eu^{2+} dans les aluminosilicates lorsque les matériaux sont préparés dans l'air. Normalement, les espèces Eu^{3+} devraient être formées dans les conditions oxydantes, tandis que la stabilisation des cations Eu^{2+} demande les conditions réductrices. En fait, la substitution des cations Eu^{3+} pour les alcalino-terreux (M) dans l'air déclenche la formation de lacunes $V_M^{\parallel\parallel}$ qui jouent le rôle de donneur d'électrons vers les défauts. Plus la concentration de $V_M^{\parallel\parallel}$ est importante, plus la réduction de Eu^{3+} vers Eu^{2+} est facile. Par conséquent, le codopage avec les éléments chimiques tétravalents (des éléments de transition, par exemple) peut beaucoup aider pour

augmenter la concentration des cations Eu^{2+} au détriment des ions Eu^{3+} . Pour être sûre, nous allons profiter des avantages de cette observation dans l'avenir pour préparer de nouveaux matériaux.

Jusqu'à présent, nos études se sont focalisées uniquement sur les réseaux d'accueil $\text{MAl}_2\text{Si}_2\text{O}_8$. Pourtant de nombreux composés pourraient conduire à de la luminescence blanche. Dans ce contexte, les matériaux $\text{M}_{13-x}\text{Al}_{22-2x}\text{Si}_{10-x}\text{O}_{66}$ ($\text{M} = \text{Sr}, \text{Ba}$) dopés avec Eu^{2+} ou Ce^{3+} et codopés avec des éléments de transition, semblent appropriés pour générer à terme une lumière blanche chaude. Formellement, la similarité déjà forte entre le spectre d'émission de $\text{Ba}_{10.4}\text{Sr}_{2.6}\text{Al}_{22}\text{Si}_{10}\text{O}_{66}$: Eu1% et celui d'un dispositif lumière LED YAG: Ce-GaN, est frappante et suggère que le codopage pourrait considérablement améliorer l'indice de rendu chromatique. Dans le cas présent, le codopage devra être testé pour les différentes compositions de Sr/Ba. Beaucoup de dispositifs aluminosilicates pourraient également être étudiés.

Chapter I : Introduction

This chapter will introduce the reader to the context of the thesis. Will be also given a brief “State of the Art” dedicated to lighting, and also a summary of the major concepts that govern luminescence.

1. Introduction

People nowadays are realizing that fossil fuels are overused and becoming scarce what create an awareness of environmental issues (i.e. climate changes) [1]. Therefore, it is time for sparing energy. Approximately, 20% of global electricity consumption is used only for illumination [2, 3]. Moreover, the ever-increasing energy demand coupled with regular population growth makes of prime importance the discovery of new light sources that could offer benefits in term of electrical energy consumption, luminous efficiency, maintenance, reliability, lifetime, environmental protection, etc. To address issues of global warming, promotion of energy-saving actions has become an urgent duty. In this context, high efficiency white light emitting diodes (white LEDs, WLEDs) are receiving a strong incentive with the expectation to replace conventional and fluorescent lamps for general lighting application in the near future [1, 2, 4]. Indeed, incandescent lamps and subsequently fluorescent lamps still dominate the lighting market but their positions are more and more contested by the emergence of solid state lighting concept owing to the recent availability of high efficiency white LEDs [3, 5]. Unfortunately, the highest brightness LEDs generally show a poor chromatic quality and a low emission flux [1, 3, 6]. Thus, remedies to these drawbacks have to be proposed to conquer the overall light market.

Actually, only a very limited number of phosphors can fulfil nowadays the minimum requirements for white-light LED applications [1, 7]. Therefore, a strong impulse to explore new, environmentally compatible phosphors with improved properties (i.e. a conversion yield higher than 90%, a lifetime of about 100,000 hours, a thermal stability up to 150°C, etc), is extremely urgent for using in reliable "all inorganic white LED light sources". In this context, a lot of investigations are dedicated around the world to the quest of new red [8, 9], green [2] and blue [10, 11] phosphors, or to the improvement of the performances of the pre-existing phosphors (i.e. phosphors commonly used for side applications) [12]. This is not the aim of the present proposal at all to focus on luminescent material with a narrow emission band centred at a given wavelength. In contrast, this thesis aims exclusively at the development of a next generation of LED sources based on the association of a near UV-LED chip with an innovative inorganic single phase white emitting phosphor. This latter should exhibit an emission ranging over the whole visible region of the electromagnetic spectrum, and should mimic as much as possible the natural light to achieve, once proceeded on UV-chip, a high

colour rendering index (CRI) [13, 14] *. So far, this way of producing white light has almost never been explored and deserved some investigations. Let notice that if a high CRI is expected for "high-market" applications, a single phase white phosphor with a relative "low" CRI (~70) could also be of interest for down-market applications with huge volumes (e.g. automotive daylight signalisation).

At this stage, let us remind very briefly the geopolitical context of worldwide innovation on LED lighting. It is worth noticing that Asian area, in particular Japan and Taiwan, adopt an aggressive politics to study practical uses for white LEDs (see [15, 16] for instance). In parallel, US government funded a \$470 million program to manufacture white LEDs with an efficacy of 120 lm/W on 2011 [17]. At the same time, semiconductor manufacturers and primary light fixture manufacturers in America and Germany establish or have established joint ventures (GELcore, LumiLeds, Osram Opto, CREE Lighting) [18, 19] pursue researches and developments on white LED lighting technologies and applications. Till now, we may regret the low implication (compared with other industrial countries) of the French industry and the weakness of the financial supports for basic researches devoted to new down-conversion phosphors for LED applications even if public institutions (CNRS, CEA...) focus with success their attentions on LED-chips emitting in the UV-vis range. Indeed, there exists a true opportunity for French companies to take up the challenges of tomorrow's markets and to develop business on LED lighting (business is the sense of elaboration and manufacturing of LED devices based on the couple LED-chip + inorganic phosphor(s)).** My work will focus only on the "phosphors" part, which are including the synthesis process and the characterization of single phase white emitting phosphor. No assembly of "led chip + phosphors" is reported here.

* Colour rendering is not a physical quantity but a qualitative characteristic of light. The more spectral colours that are contained in light, the better the colour rendering is, since an increase in the spectral colour proportion makes the illuminated objects appear more natural. The colour rendering quality of a lamp is given by the color rendering index (CRI). Objects appear most natural when the CRI equal to 100. CRI values are typically 90, 80 and 75 for the incandescent source, fluorescent light, and white LEDs, respectively.

** During the past decade, considerable attention has been directed to the development of organic white light emitting devices. Unfortunately, these devices suffer from limited operational lifetimes due in part to the organic nature of their components. This is the reason why we focus here on inorganic white light emitting phosphors.

As an aside, let us mention that the desired material which down convert (or more precisely down fold) UV light into visible light might could also present potential applications in domains distinguishable from white lighting. For instance, the solar cell efficiency of Si, CIGS or CuInSe_2 - based photovoltaic devices could be significantly enhanced after deposition of such a white phosphor at their surface by partially curing their incomplete absorption of the UV incident light [20, 21]. This could be viewed as a complement remedy to "classical" up-conversion and down-conversion processes proposed to remodel the impinging light and to adapt it to the real absorbing capacity of the solar cell (conversion of useless radiations into efficient ones for the photovoltaic effect). Under these considerations, it could favour higher light/electricity conversion yield.

2. State of the art

It is a common sense that LED lamps have many advantages over traditional lighting methods and can really be considered as a breakthrough in lighting industry [4, 11, 22, 23]. Indeed, since the sixties of the last century when they were invented as simple indicator lamps [24], a long way has been paved. Nowadays, solid-state lighting technology has already penetrated the market in a variety of niche applications (e.g. automobile brake lights [25], traffic signals [26], liquid crystal displays [27], mobile backlights [28], flashlights [29] and all manner of architectural spotlights [30]) and LEDs become competitive with incandescent and fluorescent lamps for lighting applications. **Figure 1-1** clearly evidences the natural evolution trend. Namely, the luminous efficiency of WLEDs is expected to approach $\sim 200 \text{ lm/W}$ by the year of 2020 which would be much higher than that of incandescent lamps and fluorescent lamps [3, 32]. Indeed, over the past few years, phosphors have been considered as technologically important and key components of the functionality and success of many lighting and display systems. For instance, the recent success of using LEDs was illustrated by their incorporation (more than 750, 000 LEDs) on the exterior of the Beijing's National Olympic stadium and water cube swimming facilities [31]. Furthermore, as one can see in **Figure 1-2**, the cost for white light generated based on LEDs is declining dramatically and continuously. Based on the observations above, it can be indicated without ambiguity that LEDs based on solid state lightening (SSL) would be the next generation of domestic light sources.

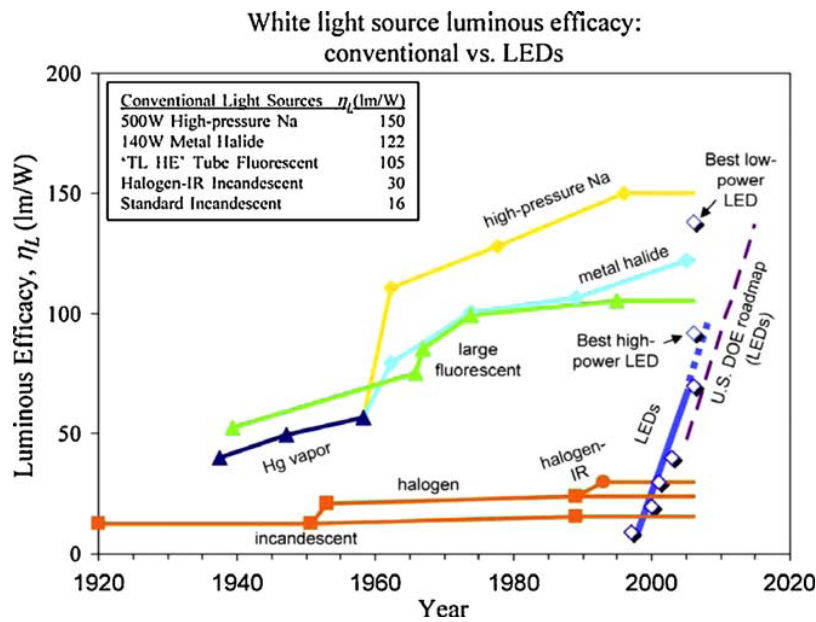


Figure 1-1. Evolution of luminous efficacy of white light sources. Commercially available high-power LED performance is indicated by the points along the solid blue curve (after [3])

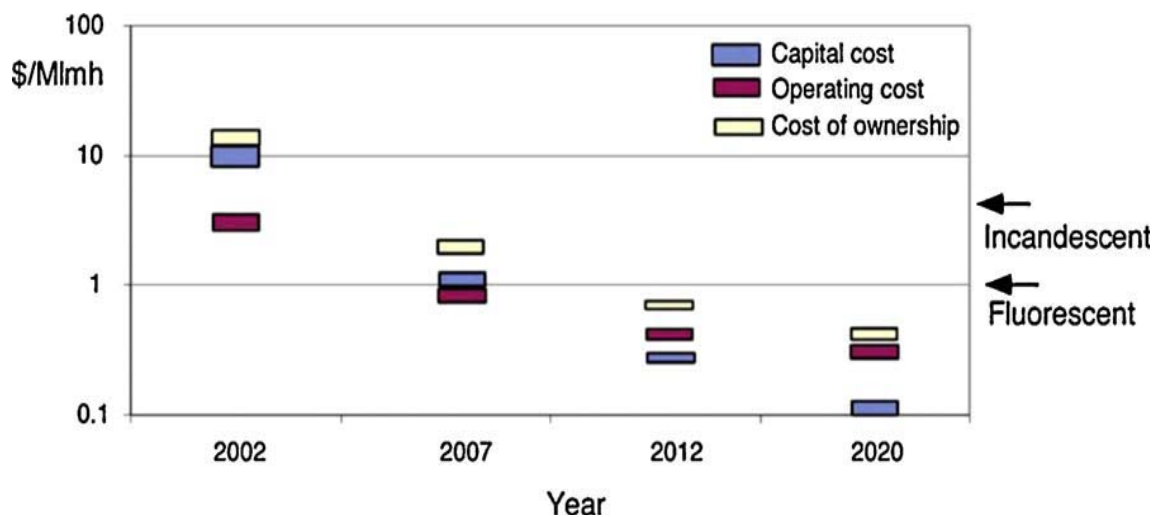


Figure 1-2. Projected cost of light. Arrows show the present cost of ownership for incandescent and fluorescent lighting (after [3])

Besides high efficiency and long lifetime, LEDs provide various other advantages such as low energy consumption*, high resistance to vibrations and shocks (all-solid-state devices without any gases or filaments), no infrared or ultraviolet emissions, environmental compatibility (e.g. mercury free system in contrast to Hg gas-discharge fluorescent lamps), small size of the light source, short response time, high efficiency in low temperature conditions... [33, 34] Of course, these clear advantages go along with some drawbacks. Namely, LEDs are currently still too expensive when compared to conventional lighting technologies [17]. In addition, excessive temperature or inappropriate operating conditions dramatically reduce both efficiency and lifetime. Moreover, the spectrum of manufactured white LEDs differs significantly from the black body radiator (a source producing a continuous spectrum), i.e. the CIE color rendering index (CRI) is significantly lower than 100% (usually around 70%). Consequently, the color of objects is perceived differently under white-LED illumination [35]. In particular, white LED lighting is currently often characterized by a marked deficient red emission in the visible region, leading to a bluish-white color [6, 9] (*vide infra*).

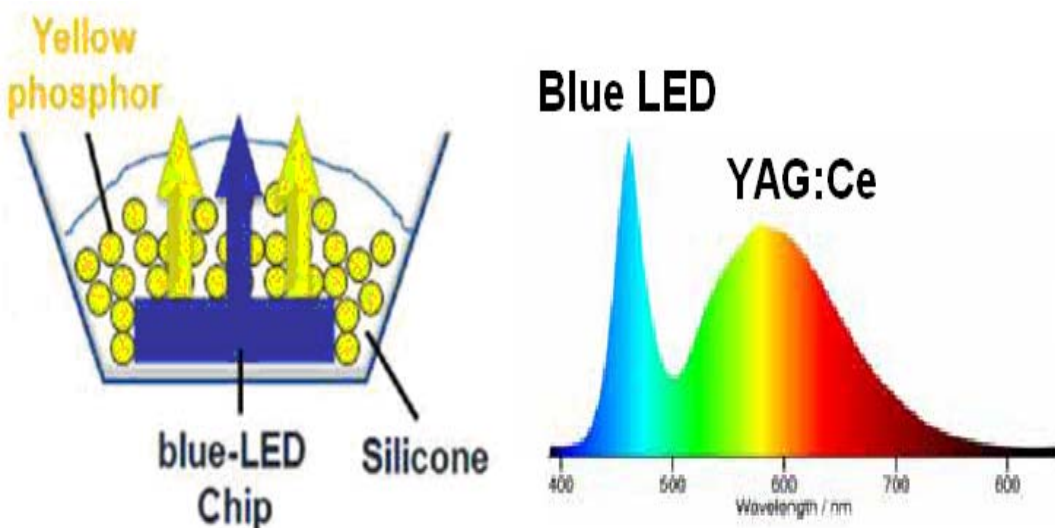
Nowadays, several approaches have been exploited to generate white light based on LEDs. Just for indication, they are listed below:

- Light produced from LED chips is monochromatic by nature. Then, generating white light requests a multi-chip combination which can be realized by mixing individual red-green-blue (RGB) emitting diodes (**Figure 1-3a**). In this case, complex and expensive drive and control circuitry are required for balancing the RGB output over operational lifetime due to the respective thermal dependency and time-evolution of each LED. This explains the high cost of such systems, much too high to address the general lighting market even though high efficiencies are reached and a large range of colour temperature ** may be achieved.

* According to different sources, it is expected that solid state lighting will reduce by about 50% the global energy consumption for lighting by 2025! Nevertheless, such an evolution may be accomplished only if energy-efficient and inexpensive white-LED are at our disposal. This implies that some progresses still have to be realized...

** The colour temperature (K) of a light is the temperature that a black body must have such that the colour of its emitted light matches with that of the real light source. High colour temperatures (4000 K and more) are considered as "cold" colours, low colour temperatures (2700–3000 K) as warm colours.

- Alternatively, as early introduced in the nineties of the last century by Nichia company (Japan), white light is obtained by covering a blue GaN or InGaN chip emitting at 460 nm with cerium doped yttrium aluminium garnet (YAG: Ce³⁺) phosphor to down convert a portion of the emitted blue light into a wide band yellow light (**Figure 1-3b** and **Scheme 1-1**). In this way the manufacturing cost is lower, but the CRI is poor (lower than 80) due to the serious scarcity of red light and the colour temperature ranges from 7000 to 8000 K depending on the thickness of the phosphor layer. Therefore, due to their too much bluish colour, they are actually mainly commercialised for backlight unit for liquid crystal display, flashlights, desk lamps and decorative illuminations. However, higher CRI and lower colour temperatures are expected for daily lighting. An alternative solution consists in combining a blue chip with a green phosphor and a red phosphor (**Figure 1-3c**). Unfortunately, red-emitting phosphors that can be efficiently pumped by UV-blue LEDs are still very scarce. This is the reason why the quest of new red phosphors which fulfil the requisite for LED applications gives rise currently to many investigations.



Scheme 1-1. Schematic structure of dichromatic phosphor convert—WLEDs (after [36]). Case of a blue LED chip recovered by a yellow phosphor

Table 1-1 gathers phosphors which are commercialized and can be used with blue led chips.

Table 1- 1. Examples of WLEDs that incorporate blue-LEDs excitable phosphors (after [1])

LED	phosphor	chemical composition	emission characteristics *			
			Intensity	width	durability	thermal quenching
Blue LED	green phosphor	$\text{Y}_3(\text{Al,Ga})_5\text{O}_{12}:\text{Ce}$	Δ	broad	√	Δ
		$\text{SrGa}_2\text{S}_4:\text{Eu}$	√	middle	x	x
		$(\text{Ba,Sr})_2\text{SiO}_4:\text{Eu}$	√	middle	Δ	Δ
		$\text{Ca}_3\text{Sc}_2\text{Si}_3\text{O}_{12}:\text{Ce}$	√	broad	√	√
		$\text{CaSc}_2\text{O}_4:\text{Ce}$	√	broad	√	√
		β-sialon:Eu	√	middle	√	√
		$(\text{Sr,Ba})\text{Si}_2\text{O}_2\text{N}_2:\text{Eu}$	√	middle	Δ	√
		$\text{Ba}_3\text{Si}_6\text{O}_{12}\text{N}_2:\text{Eu}$	Δ	middle	Δ	Δ
yellow phosphor	yellow phosphor	$(\text{Y,Gd})_3\text{Al}_5\text{O}_{12}:\text{Ce}$	√	broad	√	Δ
		$\text{Tb}_3\text{Al}_5\text{O}_{12}:\text{Ce}$	Δ	broad	√	Δ
		$\text{CaGa}_2\text{S}_4:\text{Eu}$	√	middle	x	x
		$(\text{Sr,Ca,Ba})_2\text{SiO}_4:\text{Eu}$	√	broad	√	Δ
		Ca-α-sialon:Eu	√	middle	√	√
red phosphor	red phosphor	$(\text{Sr,Ca})\text{S}:\text{Eu}$	√	broad	x	x
		$(\text{Ca,Sr})_2\text{Si}_5\text{N}_8:\text{Eu}$	√	broad	Δ	Δ
		$\text{CaAlSiN}_3:\text{Eu}$	√	broad	√	√
		$(\text{Sr,Ba})_2\text{SiO}_5:\text{Eu}$	√	broad	x	√
		$\text{K}_2\text{SiF}_6:\text{Mn}$	√	narrow	√	√

*: √ : good, Δ :medium, x :bad.

- A third approach to generate white light consists in combining a near-UV chip (e.g. $\text{In}_x\text{Ga}_{1-x}\text{N}$ with λ_{ex} from 360 to 480 nm versus x commercialized by Nichia, Toyoda Gosei, Cree, Philips, Seoul semi-conductors and Osram for instance) with UV excitable red, green, blue emitting phosphors in controlled proportions (**Figure 1-3d**) (see **Table 1-2** for a list of potential phosphors, *vide infra*). This is expected to own a series of advantages such as a high CRI (> 80), a warm color temperature, and a high tolerance towards the chip (i.e. the excitation wavelength). Nevertheless, the major problem to address so far remains the lack of high yield and high color quality phosphors. The stability of each phosphor is not high enough, not equal and their decomposition products may be viewed in some cases as harmful to environment [37]. In addition, it remains difficult to mix and deposit uniform films which disadvantageously results in undesired visible color variations [38]. To these drawbacks, we must add the strong re-absorption of the emitted blue light by the red and the green phosphors. This is, however, the solution which is retained by industrials nowadays.

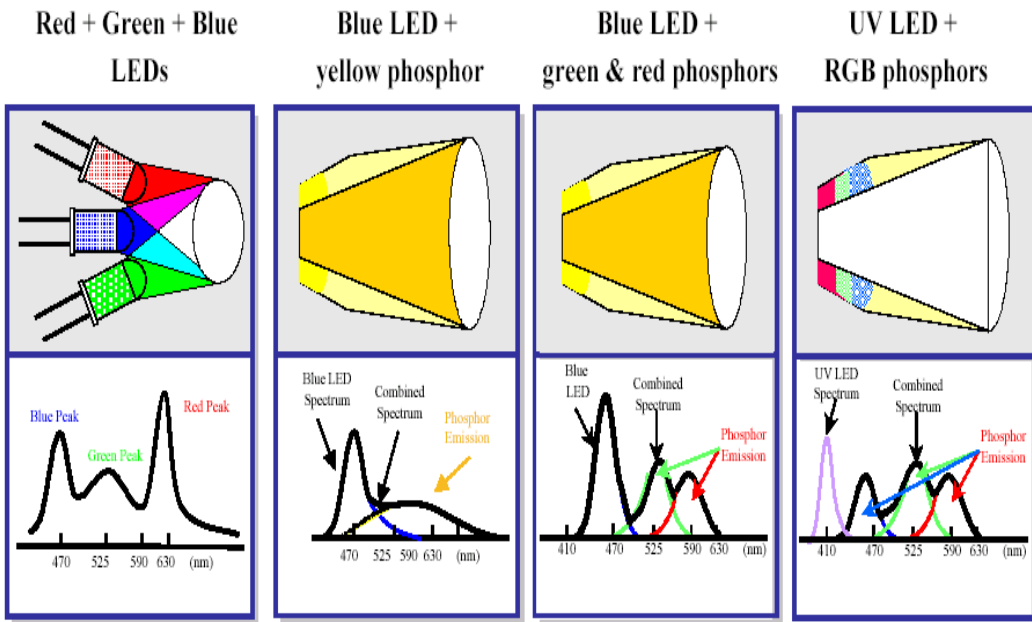


Figure 1-3. Schematic representation of different LED devices (Image Philips-Lumileds, after [3, 39]) (Fig. 1a to 1d: from the left to the right)

Table I- 2. Examples of WLEDs that incorporate UV-LEDs excitable phosphors (after [1])

LED	phosphor	Chemical composition	emission characteristics *			
			intensity	width	durability	thermal quenching
violet LED	blue phosphor	(Sr,Ca, $\text{Ba},\text{Mg})_{10}(\text{PO}_4)_6\text{Cl}_2:\text{Eu}$	✓	Narrow	✓	Δ
		(Ba,Sr) $\text{MgAl}_{10}\text{O}_{17}:\text{Eu}$	✓	middle	✓	✓
		(Sr,Ba) $_3\text{MgSi}_2\text{O}_8:\text{Eu}$	✓	narrow	Δ	Δ
	green phosphor	SrGa ₂ Si ₄ :Eu	✓	middle	x	x
		β-sialon:Eu	✓	middle	✓	✓
		SrSi ₂ O ₂ N ₂ :Eu	✓	middle	✓	✓
		Ba ₃ Si ₆ O ₁₂ N ₂ :Eu	✓	middle	✓	✓
		SrAl ₂ O ₄ :Eu	✓	narrow	✓	✓
		BaMgAl ₁₀ O ₁₇ :Eu,Mn	Δ	broad	Δ	Δ
red phosphor	(Sr,Ca)S:Eu (Ca,Sr) ₂ Si ₅ N ₈ :Eu CaAlSiN ₃ :Eu La ₂ O ₂ S:Eu 3.5MgO·0.5MgF ₂ ·GeO ₂ :Mn	(Sr,Ca)S:Eu	✓	broad	x	x
		(Ca,Sr) ₂ Si ₅ N ₈ :Eu	Δ	broad	Δ	Δ
		CaAlSiN ₃ :Eu	✓	broad	✓	✓
		La ₂ O ₂ S:Eu	Δ	narrow	Δ	Δ
		3.5MgO·0.5MgF ₂ ·GeO ₂ :Mn	Δ	narrow	✓	✓
		(Sr,Ca, $\text{Ba},\text{Mg})_{10}(\text{PO}_4)_6\text{Cl}_2:\text{Eu},\text{Mn}$	Δ	broad	✓	✓
		Ba ₃ MgSi ₂ O ₈ :Eu,Mn	✓	broad	Δ	Δ

*: ✓ : good, Δ :medium, x :bad.

Based on these observations, developing a single phase white emitting inorganic phosphor using the principle of energy transfer (ET) from a sensitizer to an activator in a single host lattice for UV LEDs appears as a potential solution to generate warm white light in a much easier way and at a lower cost. This would solve in once troubles associated with the different life times of phosphors and the complexity of the R,G,B phosphors mixture. My work was supposed to be devoted to the quest of such an ideal phosphor. The (ideal) material

should exhibit an emission ranging from 400 nm to 800 nm under UV excitation which mimics the solar light spectrum as much as possible with chromatic CIE (x, y) parameters near to 1/3, 1/3 (0.35, 0.35 for a color temperature of 4800K- see **figure 1-4**), a high quantum yield and a high thermal stability.

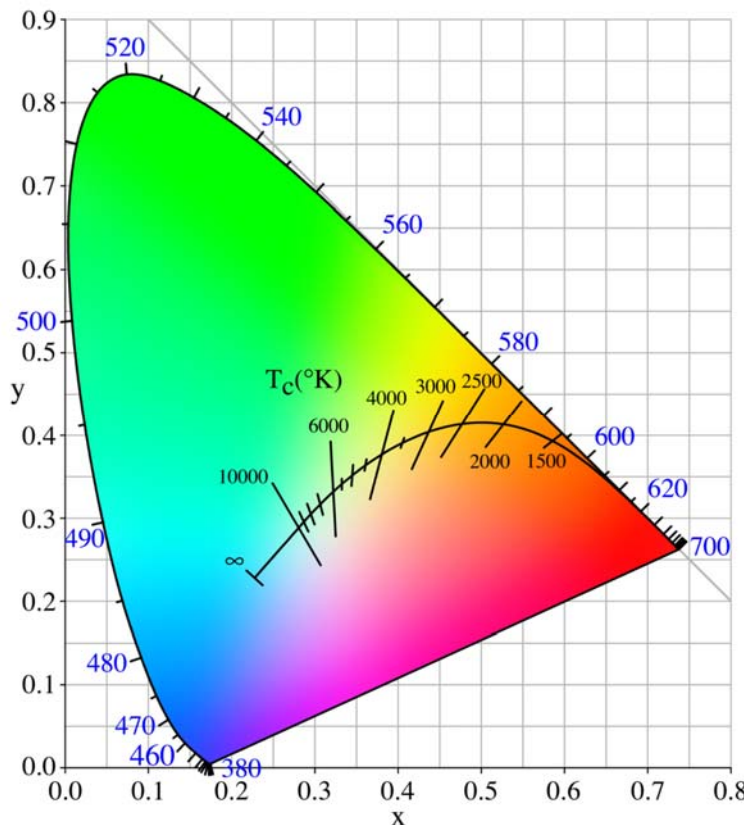


Figure 1-4. Black body colours shown on the chromaticity diagram (for indication: candle flame $\sim 1900\text{ K}$; 100W Halogen $\sim 3000\text{K}$; warm white fluorescent = 2700-3200 K; sunlight (noon, summer and mid-latitudes) $\sim 5400\text{ K}$; daylight fluorescent $\sim 6300\text{K}$, cool white fluorescent $\sim 6500\text{K}$).

CIE $x=0.31, y=0.33$; Colour temperature = 6500K

CIE $x=0.33, y=0.33$; Colour temperature = 5500K

CIE $x=0.35, y=0.35$; Colour temperature = 4800K

CIE $x=0.39, y=0.42$; Colour temperature = 3200K

To sum up, my aim is to gain in simplicity in the setting-up of UV white LEDs via the synthesis of only one appropriate phosphor which meets criteria as high efficiency in light conversion, high thermal quenching temperature (higher than $\sim 150^\circ\text{C}$), etc. This material should be flexible enough to accept changes in composition. Namely, dopants and co-dopants should be introduced in appropriate proportions to adjust the colour point (i.e. changing the CIE (x, y) parameters). The phosphor should present a broad emission (without valley if

possible) which extends on the whole range of the visible spectrum to give rise to a light color between sunlight and warm white light with high CRIs. The target CIE point is near (0.35, 0.35) with a color temperature of about 4800K. In the following, prepared material will be systematically structurally and optically characterized, and the different levers at our disposal to tune optical properties will be identified via the investigation of full series of materials. For this thesis, we will focus our attention in particular on the $\text{MAl}_2\text{Si}_2\text{O}_8$ alumino-silicate host lattices ($\text{M} = \text{Ca, Sr, Ba}$) and (co-) doped with different charge states of Eu (Eu^{2+} and/or Eu^{3+}), Ce^{3+} and transition elements (e.g. Mn) as activators. Formally, this type of host materials often offer the advantage to contain various alkaline earth crystallographic sites where the luminescent ions can be housed (*nota bene*: the existence of several atomic sites where the activators may lie is not a requisite to achieve a single phase white phosphors, but may help). As the optical properties depend strongly on the crystallographic environment, the goal is then to control the insertion of luminescent elements in the materials, in order to manage their absorption and emission. This point is specifically relevant for the Eu^{2+} and Ce^{3+} for which optical transitions are based on 4f-5d transitions exhibiting absorption and emission broad bands located in the near-UV and the visible spectral range, respectively.

3. Fundamental aspects on luminescence and phosphors-converted white LEDs

3.1. Background on luminescence

Many textbooks are dedicated to luminescence in inorganic materials (see for instance [34, 40-42]). I just remind here the major principles of luminescence, a topic I was not familiar with before my coming to Nantes.

3.1.1. Principles

A luminescent material, also called phosphor, can be defined as a material which can absorb energy and restitute it totally or partially, via an emission of light. Energy can be furnished through different ways that leads to different types of luminescence, i.e. cathodoluminescence (CL, excitation via an electron beam) [43-45], electroluminescence (EL, application of an electric voltage) [46, 47], triboluminescence (TL, for instance, use of

pressure or grinding as a stimulus) [48, 49] etc... More specifically, when light emission results from a light absorption phenomenon, luminescence is labeled photoluminescence (PL) [40, 41]. In the following, I will focus only on this latter. Let us notice that in contrast with incandescence, PL occurs in ambient conditions and even at very low temperature. The phenomenon may be impacted by temperature but its origin is not temperature [41].

In most cases, PL arises from chemical elements (e.g. Rare Earth elements) introduced in a host lattice as dopants [3, 40, 41]. Under photo-excitation (see **Figure 1-5**), the dopants transit from their ground-state to their excited state, and release energy via emission of light under the form of ultraviolet, visible, or infrared radiations. Emitted light will be never more energetic than the light used to trigger absorption due to relaxation phenomena (see below). Therefore, this radiative return competes with a non-radiative process. The return from the excited states to the ground state being then ensured via energy donation to the host lattice with the activation of phonons, i.e. under the form of heat [40-42]. Obviously, it is evident that non-radiative processes have to be minimized to develop high efficient luminescent materials.

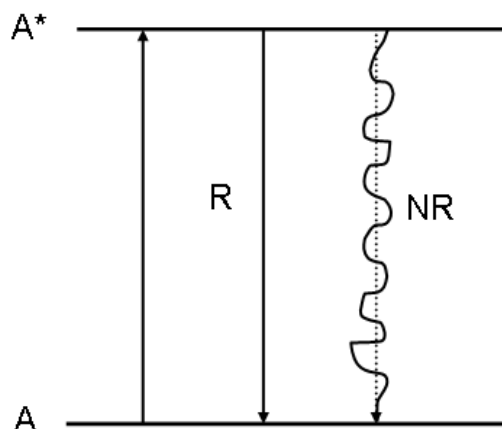


Figure 1-5. Schematic energy levels scheme of the luminescent activator. The asterisk indicates the excited state, R the radiative return and NR the non-radiative return to the ground state via activation of phonons (heat release to the host lattice), after[41]

When activators have a low propensity to absorb light, the use of sensitizer can be inserted in the host lattices as co-dopants to capture more intensively the impinging light and to transfer its energy indirectly to the activators. In principle, these latter are then promoted from their ground state to their excited state while the former return to their ground state without light emission. **Figure 1-6** schematizes such a process. In some extreme cases, the energy can be directly absorbed by the matrix [9, 41]. Therefore, the host lattice itself transfers its absorbed energy to activator as a regular sensitizer. Let notice that a luminescent center may play both the role of activator and sensitizer in some phosphors.

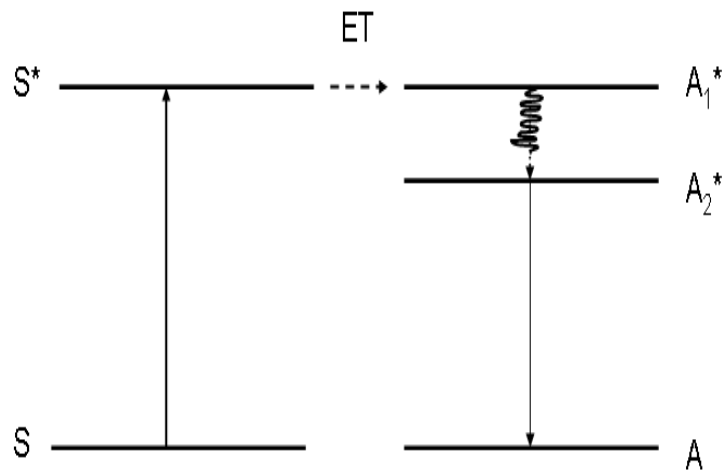


Figure 1-6. Energy transfer from S (sensitizer) to A (activator). The $S \rightarrow S^*$ transition is the absorption (or excitation), the $A_2^* \rightarrow A$ transition is the emission. The level A_1^* populated by energy transfer (ET), decays nonradiatively to the slightly lower A_2^* level via emission of phonons, after [41]

Generally speaking, the process of the PL at a luminescent center can be briefly summarized by the following steps [3, 34, 41]. First, absorption of energy takes place with promotion of an electron from a ground state to an excited state (requested time $\sim 10^{-15}\text{s}$). Second, relaxation of the excited state towards its lowest configuration occurs by giving up heat to the lattice (via phonons) (requested time $\sim 10^{-13}\text{s}$). At the end, light is emitted by the excited activator with a decay time depending on the nature of the electronic transition at work. Forbidden transitions (e.g. d-d and f-f transitions with different spin momentums in the ground and excited states) will conduct to sharp emission bands (spectral width typically a few nm) [50, 51], while allowed transitions (e.g. d to f transitions, charge transfers) are characterized by broad band [24, 52]. In a very first approximation, the more allowed the electronic transition, the larger and the more intense the emission. In fact, the form of the emission and the energy shift (Stokes shift) between the absorption and the emission can be

predicted considering the nature of the chemical bonds in which the activator is implied, and the equilibrium interatomic distances between the activator and its ligands in the ground and excited states. At this stage, let us consider the **Figure 1-7**. Such a scheme displays the evolution of the potential energy E of the absorbing center (commonly a cation) versus R which is defined as the distance between this center and its atomic neighbors in the matrix. The activator is supposed at a fixed location while the peripheral ligands can oscillate around their equilibrium position [3, 34, 41] (see **Figure 1-8** for a schematic representation of an activator coordinated to four ligands in a square chemical environment). We consider here a symmetrical stretching mode but the reasoning can be very easily extrapolated to any vibrational models.

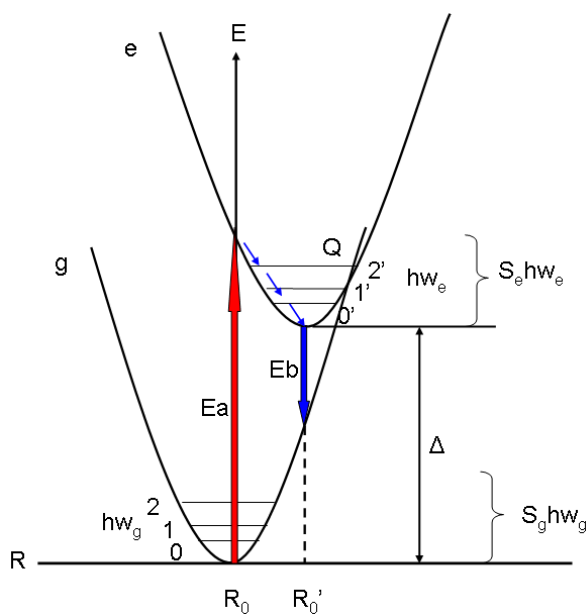


Figure 1-7. Configurational coordinate diagram. The ground state (g) has the equilibrium distance R_0 , the vibrational states $v = 0, 1, 2$ are shown. The excited state (e) has the equilibrium distance R_0' , the vibrational state $v' = 0, 1, 2$ are also shown. The parabola offset is defined $\Delta R = R_0' - R_0$.

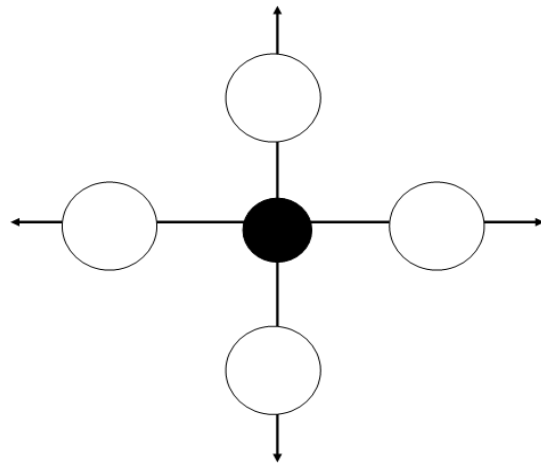


Figure1-8. Symmetrical stretching vibration model of a square-planar complex. The ligands (open circles) move in phase from and towards the central metal ion, after [41]

In **Figure1-7**, g and e parabolic curves represent the ground and excited states, R_0 and R_0' stands for the metal-ligand distances at the equilibrium in the ground and excited states, respectively. The parabolic form of the g and e curves is due to the fact that a harmonic vibration is supposed, what appears as an acceptable approximation for slight deviations. In the ground state (idem for the excited state), the restoring force undergoes by the ligands can be written by the **Equation (1-1)**:

$$F = -k(R-R_0) \quad (1-1)$$

where k is constant (spring constant), R_0 is the equilibrium position and R stands for the distance during the vibration. Then, the potential energy (E) associated with such a vibrator is given by the **Equation (1-2)**:

$$E = \frac{1}{2} k(R-R_0)^2 \quad (1-2)$$

what explains the parabolic shape of the configurational diagram [41]. The horizontal solid lines in the ground and excited configurations correspond to the vibrational states, two successive phonon states being separated by the $\hbar\omega_g$ and $\hbar\omega_e$ energies in the ground and excited states, respectively. The absorption and emission bands are represented by vertical arrows with an associated energy E_a and E_b ($E_a \geq E_b$) respectively. The difference ($E_a - E_b$) is called Stokes and its value will strongly depend on the difference $R_0' - R_0$, which is defined as

the change in the strength of the activator-ligands bonds once electrons are promoted in the excited state. The value difference between the two configuration curves g and e, labeled Δ , stands for the energy of the zero phonon line, i.e. a transition from the e-state to the g-state which involves no phonon excited state. S_e and S_g , the Huang-Rhys factors in the g and e states give the mean number of phonons involved in the absorption and the emission [34]. Note here that in a first approximation, the curvature of the parabolic curves in the ground and excited states and the phonon frequencies in the two electronic states are considered as identical. This means that no change is induced in the nature of the k constant and vibrational mode under excitation. Of course, such an approximation is not realistic but sufficient to account for PL by hand.

Based on **Figure 1-7**, let us explain the origin of some of the non-radiative returns displayed in **Figure 1-9**. **Figure 1-9a** is typically representative of an allowed electronic transition, i.e. a $4f \rightarrow 5d$ transition for instance. The nature of the chemical bond is quite different in the ground state and the excited state due to the depletion of the $4f^n$ block of a lanthanide at the benefit of 4d orbitals which strongly interact with their surroundings in contrast with the f orbitals [53, 54]. Under excitation, an electron is promoted from g to e (e.g. f to d orbital), relax to lower state of the e state and emit a photon. Nevertheless, if temperature is high enough, a temperature quenching may occur due to the crossing of the two parabolas. Namely, temperature will activate phonons favoring high energy states which can trigger non-radiative return to the ground state. **Figure 1-9b** is characteristic of forbidden f-f transitions. At first glance, the excited and ground states can be superposed vertically and temperature quenching is, a priori, not expected because no cross relaxation is possible. In fact, non-radiative process, called multi-phonon relaxation, can take place if certain conditions are suited [41, 42], that is if the energy difference (ΔE) between the ground and excited states is lower than 5-10 times the phonon energy ($\Delta E < 5-10 \hbar w$). If temperature increases, multiphonon relaxation will be favored due to the population of higher-energy phonon levels. At the end, **Figure 1-9c** gathers in one the two previous schemes. Namely, the activator is excited via an allowed $g \rightarrow e'$ transition (d-d transition with $\Delta S = 0$ or anion – cation charge transfer). Then the system relaxes non-radiatively if temperature is “very” high or transits towards an e excited configuration before returning to the ground state with light emission. Then, the $e' \rightarrow g$ transition is definitely quenched at the benefit of the $e \rightarrow g$ one. Typically, such situation occurs for $\text{Al}_2\text{O}_3:\text{Cr}^{3+}$ where the different excitation and emission

steps can be summed up as followed: i) ${}^4\text{A}_2 \rightarrow {}^4\text{T}_2$ excitation ($\Delta S = 0$), ii) ${}^4\text{T}_2 \rightarrow {}^2\text{E}$ relaxation, and iii) ${}^2\text{E} \rightarrow {}^4\text{A}_2$ emission [55]. A similar scheme is proposed also for Eu^{3+} containing hosts lattices [56].

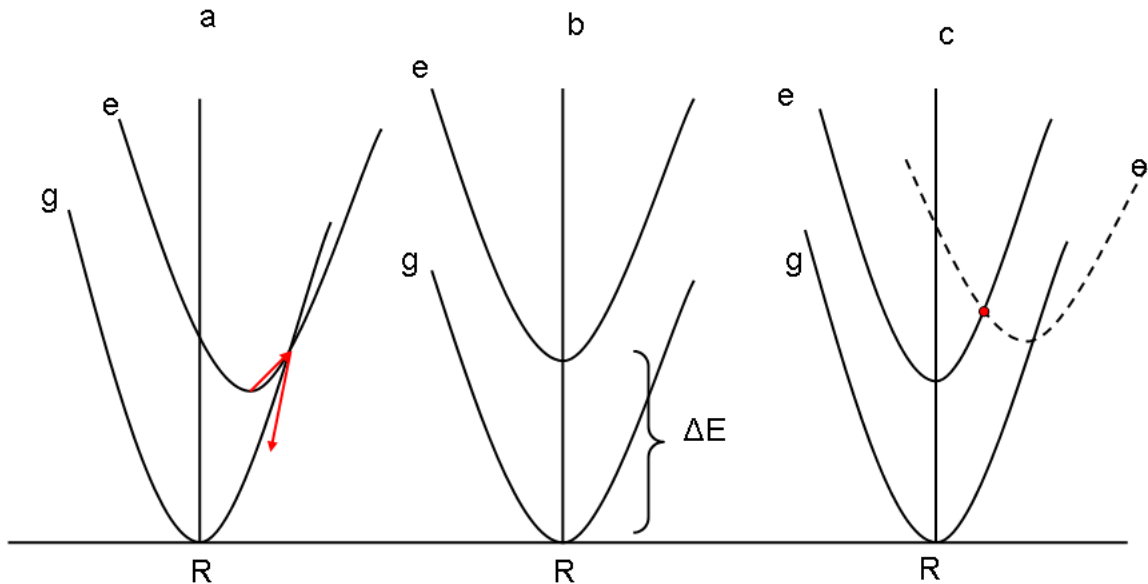


Figure 1-9. Configurational coordinate diagrams illustrating nonradiative transitions for isolated luminescent center. The ground state parabola is indicated by g , the excited state parabolas by e and e' . Non radiative is associated with temperature quenching in (a), multiphonon relaxation in (b) and cross relaxation in (c), after [41, 42]

3.1.2 Energy transfer (ET)

It is well-known that ET (Figure 1-6) between ions can play an important role to generate white emission and to adapt emission characteristics to requisites (shift from a cold color to a warm one for instance) [34, 40, 41, 57, 58]. The ET between a sensitizer (S) and an activator (A) can be expressed by the **Equation (1-3)**:



where the excited state is highlighted by a asterisk. Let put the emphasis on the fact that A may also play the role of S towards activators of the same species. ET from S to A may occur via resonant radiative transfers (i.e. absorption by A from the emission of S), or via resonant

non-radiative transfers. The former obey to the theory briefly described above (classical absorption/emission phenomena). The latter are a little more intricate and fundamentals will be very briefly described here. Discussions will be limited to the strict minimum to introduce the discussions in chapters II and III.

From a physical point of view, the non-radiative ET process is based on exchange interactions (overlap between the orbitals of the *S* and *A* atoms) and electric (or magnetic) multipolar (mainly dipole-dipole) interactions. Whatever the interaction at work, the efficiency of the ET will depend on the degree of overlap between the emission spectra of *S* and excitation spectra of *A* and the distance *R* separating *A* from *S* [34, 41, 42]. In practice, the transfer rate from *S* to *A* is expressed by the **Equation (1-4)**:

$$P_{SA} = \frac{2\pi}{\hbar} | \langle S, A^* | H_{SA} | S^*, A \rangle |^2 \times \int g_S(E) g_A(E) dE \quad (1-4)$$

where $g_S(E)$ and $g_A(E)$ are all the normalized optical line shape function of centre *S* and *A* (emission and absorption, respectively), H_{SA} is the interaction Hamiltonian and $|S^*, A\rangle$ and $|S, A^*\rangle$ are the electronic configuration in the initial (before transfer) and final (after transfer) states, respectively. In fact, the integral represents the spectral overlap between the emission of *S* and the absorption of *A* (hatched part in **Figure 1-10**).

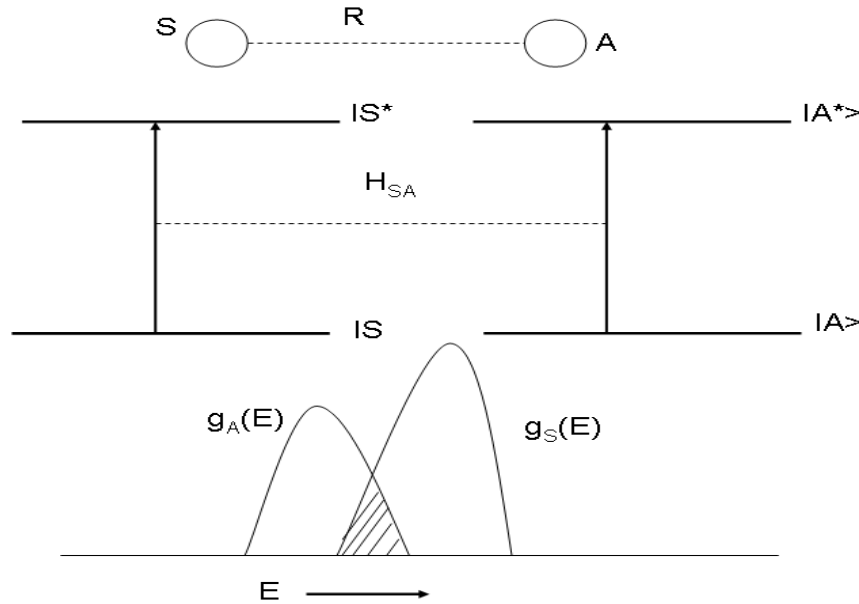


Figure1-10. ET between the S and A centers and illustration of Eq. (2). The two centers are at a distance R (top). The energy level schemes and the interaction H_{SA} are given in the middle. The spectral overlap is illustrated at the bottom (hatched part), reproduced from literature [41]

The type of interaction (H_{SA}), strongly dependant of distance between S and A, determines the ET rate [34, 41]. Specifically, for dipole-dipole, dipole-quadrupole, and quadrupole-quadrupole interactions, the transfer probability is inversely proportional to R^6 , R^8 and R^{10} , respectively (R : distance between S and A). For exchange interaction, the distance dependence is exponential. Consequently, S to A ET may be efficient for R values up to around 30 Å for allowed electric dipole transitions (4f → 5d transitions for instance). If the transitions are forbidden, only transfer can occur via exchange interaction and R values lower than ~ 10 Å are then requested. In chapter II and III, we will discuss the origin of the ET and highlight their interests to modify the optical characteristics of our materials.

3.2. CIE chromaticity coordinates and color temperature

A color is characterized by its CIE (x, y) chromatic parameters. Namely, according to the Commission Internationale de l'Eclairage(CIE) [59, 60], each color can be decomposed in three coordinates associated to three color-matching functions $\bar{x}(\lambda)$, $\bar{y}(\lambda)$, $\bar{z}(\lambda)$ as depicted in **Figure1-11**. These three curves are intended to correspond to the sensitivity of three color sensors of human eyes. Then, the CIE (XYZ) tristimulus values can be calculated by the following **Equations (1-5)**:

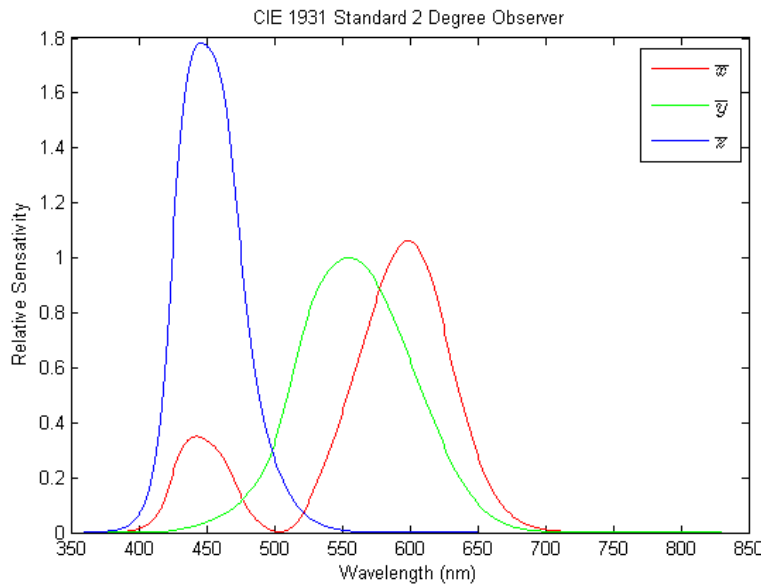


Figure 1-11. The CIE standard observer color matching functions, after [61]

$$\begin{aligned} X &= \int \Phi(\lambda) \bar{x}(\lambda) d\lambda \\ Y &= \int \Phi(\lambda) \bar{y}(\lambda) d\lambda \\ Z &= \int \Phi(\lambda) \bar{z}(\lambda) d\lambda \end{aligned} \quad (1-5)$$

where integration is performed over the entire visible range of the electromagnetic spectrum and $\Phi(\lambda)$ is the emission spectrum of the phosphor under consideration. As the concept of color can be divided into two parts, brightness and chromaticity *, the CIE (XYZ) color space can be replaced by the CIE (xyY) color space where Y measures the brightness and the (x,y) is the chromaticity that gives rise to the chromaticity diagram given in **Figure 1-12** with the values calculated from **Equations (1-6)**:

* a white material and a grey one have the same color (white) but different brightness.

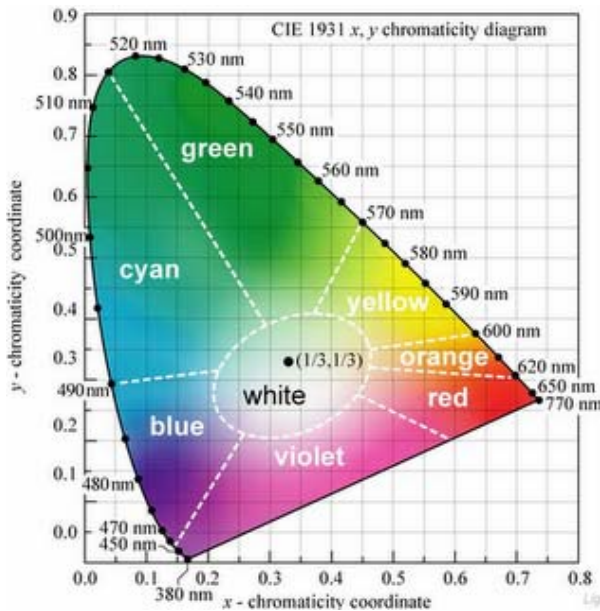


Figure 1-12. The CIE 1931 color space chromaticity diagram. The outer curved boundary is the spectral (or monochromatic) locus, with wavelengths shown in nanometers, after [62]

$$\begin{aligned} x &= X / (X + Y + Z) \\ y &= Y / (X + Y + Z) \\ z &= Z / (X + Y + Z) = 1 - x - y \end{aligned} \quad (1-6)$$

Indeed, an ideal phosphor with a white luminescence will be associated to a point at $x = y = 1/3$ of the chromaticity diagram. Of course, blue, green, yellow, orange or red phosphors will be assigned to a point in the specific colored regions of the diagram. For a specific monochromatic light, the associated point will be located at the periphery of the diagram, called spectral locus.

Color temperature (CT) is another important term commonly used to qualify a phosphor [63, 64]. CT of a light source is defined as the temperature (in Kelvin) at which an ideal black-body radiator has to be brought to mimic the color (not the emission spectrum) of the aforementioned light. Based on **Table 1-3**, it appears that for a CT of 1850K, 3000K, and 6500K would correspond approximately to a candle flame, a incandescent light bulb or a white compact fluorescent light bulb, and daylight, respectively (see **Table 1-3** for more indication). Commonly, CT higher than 5000K are classified as cool colors (i.e. bluish white), while color temperatures around 3000K are called warm colors (yellowish white to reddish

white). Just to highlight the importance of CT, **Figure 1-13** gathers photograph of the same room under different lightings (CT).

Table1- 3. *The color temperature of the radiator sources, after [65, 66]*

Color temperature	Sources
1,700K	Match flame
1,850K	Candle flame, sunset / sunrise
2,700 – 3, 300K	Incandescent light bulb
3,000K	Cool white, soft white compact fluorescent light bulb
3,200K	Studio lamps, photofloods, etc
3,350K	Studio “CP” light
4,100-4,150K	Moonlight, xenon arc lamp
5,000K	Horizon daylight, fluorescent light tubes or cool white / daylight compact fluorescent light bulb
5,500-6,000K	Vertical daylight, electronic flash
6,500K	Daylight, overcast
6,500-9,300K	LCD or CRT screen

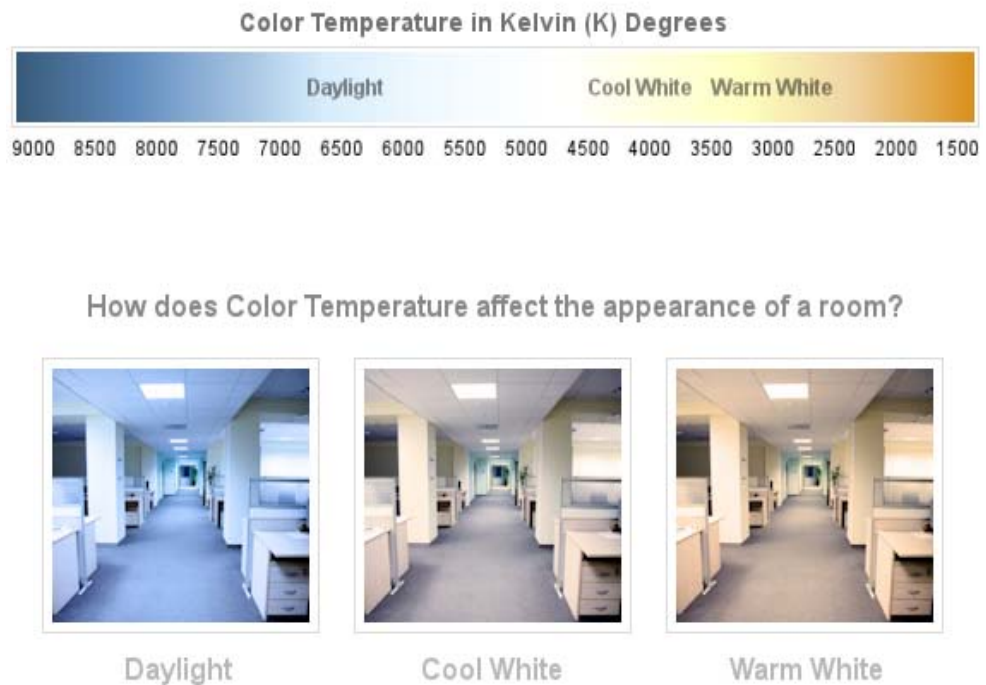


Figure 1-13. Color temperature comparison in the same office

References

1. C.C. Lin and R.-S. Liu, *The Journal of Physical Chemistry Letters* **2** (2011) (11), p. 1268.
2. W.J. Park, Y.H. Song and D.H. Yoon, *Materials Science and Engineering: B* **173** (2010), p. 76.
3. S. Ye, F. Xiao, Y.X. Pan, Y.Y. Ma and Q.Y. Zhang, *Materials Science and Engineering: R: Reports* **71** (2010) (1), p. 1.
4. S. Ye, Z.-S. Liu, X.-T. Wang, J.-G. Wang, L.-X. Wang and X.-P. Jing, *Journal of Luminescence* **129** (2009) (1), p. 50.
5. M. Rattier, H. Benisty, R.P. Stanley, J.F. Carlin, R. Houdre, U. Oesterle, C.J.M. Smith, C. Weisbuch and T.F. Krauss, *Selected Topics in Quantum Electronics, IEEE Journal of* **8** (2002) (2), p. 238.
6. C.-H. Huang, W.-R. Liu and T.-M. Chen, *The Journal of Physical Chemistry C* **114** (2010) (43), p. 18698.
7. P.F. Smet, A.B. Parmentier and D. Poelman, *Journal of The Electrochemical Society* **158** (2011) (6), p. R37.
8. G. Jia, K. Liu, Y. Zheng, Y. Song and H. You, *Crystal Growth & Design* **9** (2009) (8), p. 3702.
9. C.-C. Wu, K.-B. Chen, C.-S. Lee, T.-M. Chen and B.-M. Cheng, *Chemistry of Materials* **19** (2007) (13), p. 3278.
10. W.B. Im, Y.-I. Kim, J.H. Kang and D.Y. Jeon, *Solid State Communications* **134** (2005) (11), p. 717.
11. K.Y. Jung, J.H. Kim and Y.C. Kang, *Journal of Luminescence* **129** (2009) (6), p. 615.
12. J. Wang, S. Wang and Q. Su, *Journal of Materials Chemistry* **14** (2004) (16), p. 2569.
13. X. Guo and K.W. Houser, *Lighting Research and Technology* **36** (2004) (3), p. 183.
14. M.J. Flannagan and B. Schoettle, *LED Headlamps: Glare and Color Rendering*, University of Michigan Transportation Research Institute (2003).
15. *Compound semiconductor*, Franklin Pub. (2004).
16. C.W. Wessner, T. National Research Council . Steering Committee for Government-Industry Partnerships for the Development of New, T. National Research Council . Board on Science and P. Economic, *Partnerships for Solid-State Lighting: Report of a Workshop*, National Academy Press (2002).
17. T. Taguchi, *IEEJ Transactions on Electrical and Electronic Engineering* **3** (2008) (1), p. 21.
18. R. Szweda, *Gallium Nitride and Related Bandgap Materials and Devices* (2), Elsevier Science, Amsterdam (2000), pp. 193-293.
19. R. Szweda, *III-Vs Review* **15** (2002) (3), p. 40.
20. V.S. Saji, I.-H. Choi and C.-W. Lee, *Solar Energy* **85** (2011) (11), p. 2666.
21. E. Klampaftis, D. Ross, S. Seyrling, A.N. Tiwari and B.S. Richards, *Solar Energy Materials and Solar Cells* **101** (2012) (0), p. 62.
22. H. Ju, X. Su, S. Xu, Y. Zhang, D. Deng, S. Zhao, H. Wang, B. Wang and L. Sun, *Materials Letters* **63** (2009) (15), p. 1275.
23. Y.Q. Li, A.C.A. Delsing, G. de With and H.T. Hintzen, *Chemistry of Materials* **17** (2005) (12), p. 3242.
24. M. Zhang, J. Wang, W. Ding, Q. Zhang and Q. Su, *Optical Materials* **30** (2007) (4), p. 571.
25. A.V. Ortega and I.N. da Silva, *Applied Soft Computing* **6** (2005) (1), p. 18.

26. D. Vazquez-Molina, A. A Alvarez Fernandez-Balbuena, E. Bernaba and J. Alda, *Displays* **28** (2007), p. 167.
27. J.-C. Liou and F.-G. Tseng, *Displays* **30** (2009), p. 148.
28. Y. Cong, B. Li, S. Yue, Y. Liu, W. Li and X.-j. Wang, *The Journal of Physical Chemistry C* **113** (2008) (2), p. 493.
29. A.B. Ellis, K.J. Nordell, T.F. Kuech, S.A. Stockman, G.C. Lisensky and S.M. Condren, *Journal of Chemical Education* **78** (2001) (8), p. 1033.
30. H.C. Box, *Set Lighting Technician's Handbook (Fourth Edition)*, Focal Press, Boston, pp. 227-249.
31. M. Slovick., A bit of gloom, but no doom, at NEDA conference, *Electronic Products Mag.* (2009), pp. 51-52.
32. S.C. Allen and A.J. Steckl, *Applied Physics Letters* **92** (2008) (14), p. 143309.
33. X. Piao, K.-i. Machida, T. Horikawa, H. Hanzawa, Y. Shimomura and N. Kijima, *Chemistry of Materials* **19** (2007) (18), p. 4592.
34. C.Ronda, *Luminescence:From theory to applications*, WILEY-VCH (2008).
35. P.J. Bouma, *Physical aspects of colour: an introduction to the scientific study of colour stimuli and colour sensations*, Eindhoven: Philips Gloeilampenfabrieken (Philips Industries) Technical and Scientific Literature Dept. (1948).
36. Y.Q. Li, Structure and Luminescence Properties of Novel Rare-earth Doped Silicon Nitride Based Materials, Universiteit Eindhoven (2005).
37. W. Ding, J. Wang, M. Zhang, Q. Zhang and Q. Su, *Journal of Solid State Chemistry* **179** (2006) (11), p. 3582.
38. H.V.D. S. Nizamoglu, *Nanotechnology* **18** (2007), p. 405702.
39. J.C.B. D.A. Steigerwald, D. Collins, R.M. Fletcher, M.O. Holcomb, M.J. Ludowise, P.S. Martin, S.L. Rudaz, *IEEE, J. Sel. Top. Quant* **8** (2002), p. 310.
40. W.M.Y.S. Shionoya, *Phosphor Handbook*, CRC Press (1999).
41. B.C.G. G.Blass, Editor, *Luminescent materials*, Springer-Verlag (1994).
42. M.A. Omary, H.H. Patterson and L. Editor-in-Chief:Â John, *Encyclopedia of Spectroscopy and Spectrometry (Second Edition)*, Academic Press, Oxford (1999), pp. 1372-1391.
43. C.E. Norman, *Microscopy and Analysis* **88** (2002), p. 9.
44. Z. Liu, M. Stevens-Kalceff and H. Riesen, *The Journal of Physical Chemistry C* **116** (2012) (14), p. 8322.
45. R.N. Kniseley, F.C. Laabs and V.A. Fassel, *Analytical Chemistry* **41** (1969) (1), p. 50.
46. F. Chen, Z. Bian and C. Huang, *Journal of Rare Earths* **27** (2009) (3), p. 345.
47. W. Gao, T.-k. Li, Y. Ono and S.-T. Hsu, *Journal of Rare Earths* **24** (2006) (6), p. 673.
48. X.-F. Chen, C.-Y. Duan, X.-H. Zhu, X.-Z. You, S. Shanmuga Sundara Raj, H.-K. Fun and J. Wu, *Materials Chemistry and Physics* **72** (2001) (1), p. 11.
49. X.-L. Li, Y. Zheng, J.-L. Zuo, Y. Song and X.-Z. You, *Polyhedron* **26** (2007) (18), p. 5257.
50. Y.-C. Chang, C.-H. Liang, S.-A. Yan and Y.-S. Chang, *The Journal of Physical Chemistry C* **114** (2010) (8), p. 3645.
51. A.L. M. Katsnelson, *Journal of Physics: Condensed Matter* **22** (2010), p. 382201.
52. W. Chen, H. Liang, B. Han, J. Zhong and Q. Su, *The Journal of Physical Chemistry C* **113** (2009) (39), p. 17194.
53. M.O.K. N.E. Brese, *Acta Cryst* **B47** (1991), p. 192.
54. I.D. Brown, *Acta Cryst* **B48** (1992), p. 553.
55. A.P. Vink and A. Meijerink, *Spectrochimica Acta Part A: Molecular and Biomolecular Spectroscopy* **54** (1998) (11), p. 1755.

56. G. Seeta Rama Raju, H.C. Jung, J.Y. Park, B.K. Moon, R. Balakrishnaiah, J.H. Jeong and J.H. Kim, *Sensors and Actuators B: Chemical* **146** (2010) (1), p. 395.
57. C.-H. Huang, T.-W. Kuo and T.-M. Chen, *ACS Applied Materials & Interfaces* **2** (2010) (5), p. 1395.
58. K.Y. Jung and J.H. Kim, *Journal of Luminescence* **128** (2008) (12), p. 2004.
59. G.C. K. Bright, *The Colour, Light and Contrast Manual: Designing and Managing Inclusive Built Environments*, Wiley-Blackwell (2009).
60. M.R.P. R. W. G. Hunt, *Measuring Colour, 4th Edition*, Wiley-Blackwell (2011).
61. S.K. Shevell and O.S.o. America, *The Science of Color*, Elsevier (2003).
62. R.G. Kuehni, *Color Space and Its Divisions: Color Order from Antiquity to the Present*, Wiley-Blackwell (2003).
63. F.P. Miller, A.F. Vandome and J. McBrewster, *Color Temperature: Visible Spectrum, Chromaticity, Black Body, Kelvin, Planck's Law, Wien's Displacement Law, Luminous Efficacy, Over-illumination, Brightness Temperature, Effective Temperature*, Alphascript Publishing (2009).
64. J. Anderson, *Shooting Movies Without Shooting Yourself in the Foot*, Focal Press, Boston (2012), pp. 277-278.
65. H.G.W. Harding, *Proceedings of the Physical Society. Section B* **63** (1950), p. 685.
66. N. Salvaggio, *Basic Photographic Materials and Processes, 3rd Edition* Focal Press (2008).

Chapter II : Investigation of the Energy Transfer Between Eu²⁺ and Eu³⁺ in Eu-doped MAl₂Si₂O₈ (M = Ca, Sr, Ba) Materials

Prepared in Air

Eu²⁺ doped MAl₂Si₂O₈ materials (M= Ca, Sr, Ba) prepared under reducing atmosphere evidence a white-bluish luminescence under UV excitation. Therefore, we decided to investigate the synthesis of these compounds under air to favor co-existence of Eu²⁺ and Eu³⁺ cations and achieve a warmer color. Normally, Eu³⁺ cations are giving rise naturally to line emission spectra which the color is between orange and red emissions.

1. Introduction

Due to their luminescent properties, extensive investigations have been devoted to Eu^{2+} -doped luminescent materials [1-10]. In that framework, aluminates, silicates, aluminosilicates received much attention and some of them give rise now to major applications in plasma display panels or white lighting (e.g. $BaMgAl_{10}O_{17}:Eu^{2+}$ [6], $MAl_2O_4:Eu^{2+}$ ($M = Ca, Sr, Ba$) [2, 8-10], $CaMgSi_2O_6:Eu^{2+}$ [7], etc). It is well-known that the fluorescence of Eu^{2+} normally expresses a broad emission which can vary in a large wavelength region ranging from ultraviolet to yellow (and even red) according to the crystal field strength generated by the surrounding ligands, what depends on their charges, their size, their number, etc. Actually, the fluorescence of Eu^{2+} is commonly associated with an allowed transition from the 5d block towards the 4f block, which is specific of a $4f^65d^1 \rightarrow 4f^7$ transition and can be tuned at wish via the proper choice of the host lattice [3]. Eu^{3+} doped materials are also widely investigated in oxides [11, 12], borates [13], phosphates [14], sulfides [15], etc. In contrast with Eu^{2+} cations, emissions of this kind of ion is normally made up of line bands in the longer wavelength region (red or orange luminescences) which, in turn, are very useful for application in lighting and display industry (e.g. color TV) [14]. Considering from the view of energy levels, the line emission spectra of Eu^{3+} are mainly associated with transitions from the excited 5D_0 level to the ground states 7F_j ($j = 0$ to 6) within the 4f⁶ configurations [16]. Furthermore, the transition probabilities of the line emission spectra of Eu^{3+} from 5D_0 to the different ground states 7F_j would strongly depend on the symmetry of the site occupied by the activator in the host lattice [4, 17]. Namely, at a site without inversion symmetry, Eu^{3+} will exhibit the hypersensitive forced electric-dipole $^5D_0 \rightarrow ^7F_2$ transition with emission wavelengths of about 610 nm. In contrast, the allowed magnetic-dipole $^5D_0 \rightarrow ^7F_1$ transition is strongest and usually observed at around 590 nm from Eu^{3+} located at a site with inversion symmetry. Thus, at the opposite of Eu^{2+} cations, Eu^{3+} activators yield luminescence which are not dependent (or almost not dependent) of the host lattice [18, 19].

Prior to description of my studies on Eu-doped aluminosilicates, I would like to put the emphasis on the fact that Eu^{2+} -doped $MAl_2Si_2O_8$ materials ($M = Ca, Sr, Ba$) have been already investigated in Nantes. Indeed, F. Clabau characterized the optical properties of these materials during his thesis and evidenced their white persistent luminescence [3]. For information, in these compounds phosphorescence is related to a photooxydation of Eu^{2+} into

Eu³⁺ cations under irradiation, with trapping of the photogenerated electrons on positive defects, i.e. defects built upon oxygen vacancies. These electrons are released at room temperature and recombine at the photo-ionized Eu³⁺ site with emission of light. F. Clabau also demonstrated, on the basis of Mössbauer spectroscopy measurements that a slight residual amount of Eu³⁺ cations were systematically present in the prepared samples, even if they were synthesized under reducing atmosphere. In the present context, this suggests that the Eu²⁺/Eu³⁺ ratio may be controlled via the synthetic conditions.

Under UV excitation, MAl₂Si₂O₈:Eu²⁺ compounds emit a blue-white light with CIE chromatic coordinates at room temperature of (0.17, 0.12), (0.16, 0.09) and (0.16, 0.11) for M= Ca, Sr and Ba, respectively. For sure, these values may appear to be far away from the target values of about (0.35, 0.35) [20]. However, optical properties can be significantly changed by playing with the chemical composition. On this basis, Yang et al. [21] demonstrated that the (Ca_{0.99-n}Eu_{0.01}Mn_n)Al₂Si₂O₈ materials can be systematically tailored to generate white light under ultraviolet and that these materials even exhibit the potential to act really as a white-emitting phosphor for ultraviolet LEDs. The comparison of the chromaticity characteristics of this series of materials with those of the simulated white light generated from commercial YAG:Ce (Nichia Co., Japan) excited with a monochromatic blue light of 467 nm led to quite similar results [22, 23]. Actually, the CIE coordinates were found to be (0.30, 0.29) and (0.33, 0.32) for (Ca_{0.79}Eu_{0.01}Mn_{0.20})Al₂Si₂O₈ and (Ca_{0.74}Eu_{0.01}Mn_{0.25})Al₂Si₂O₈, respectively excited in NUV to compare with (0.31, 0.27) for the YAG:Ce coated on a GaN LED-chip! At this stage, the question to address concerns the possibility to tune the chromatic coefficients of Eu doped MAl₂Si₂O₈ materials versus the Eu²⁺/Eu³⁺ ratio.

To our knowledge, the transformation of Eu³⁺ into Eu²⁺ phenomenon in air have been already found in many compounds, such as mixed metal chlorides [24], oxides [10], sulphides [15], under a well crystallized form or as glasses [25, 26]. For this study, we are the first to report on the photoluminescence properties of the Eu-doped MAl₂Si₂O₈ compounds synthesized in air with the existence of Eu²⁺/Eu³⁺ mixed valence and the possible energy transfer (ET) from Eu²⁺ towards Eu³⁺. Formally, before any characterization, the co-existence of these two kinds of states for europium (i.e. Eu²⁺ and Eu³⁺) in our materials prepared in air can be suspected only on the basis of photographs of the compounds excited at two different

wavelengths, namely 254 nm and 365 nm with a Fisher Bioblock labosi UV lamp (**Figure 2-1**). Red and white luminescences are assigned to Eu^{3+} and Eu^{2+} cations, respectively. Based on these observations, we embarked on the characterization of the $MAl_2Si_2O_8:Eu$ systems prepared in air.

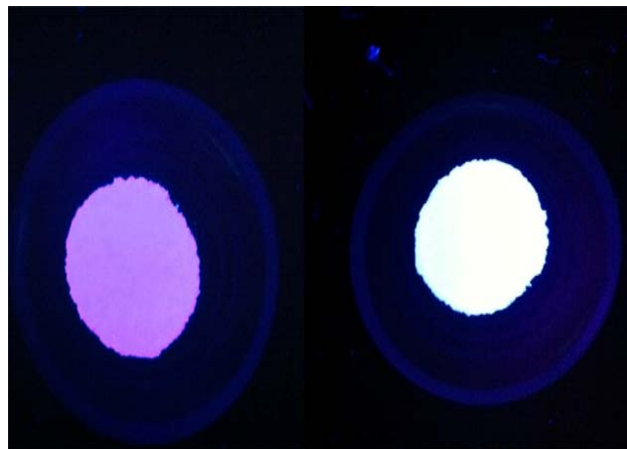


Figure 2-1. Photographs of $CaAl_2Si_2O_8:5\%Eu$ prepared in air excited at 254 nm (pink color) and 356 nm (white color)

2. Experimental part

2.1. Synthesis process

Materials were prepared via ceramic routes in air with the target $M_{1-3x/2}Al_2Si_2O_8:xEu^{3+}$ and $M_{1-x}Al_2Si_2O_{8+0.5x}:xEu^{3+}$ compositions. Namely, precursors were weighted in stoichiometric amounts. Basically, calcium carbonate ($CaCO_3$ 99.997% Alfa Aesar), strontium carbonate ($SrCO_3$ 99.997% Alfa Aesar), barium carbonate ($BaCO_3$ 99.997% Alfa Aesar), silica (SiO_2 99.99% Chempur), γ -alumina (Al_2O_3 99.997% Alfa Aesar) and europium oxide (Eu_2O_3 99.99%), were weighted in the appropriate proportions without further purification. Doping rates varied from 0.5 to 13 mol % for the $CaAl_2Si_2O_8$ and $SrAl_2Si_2O_8$ matrixes (the substitutions are much higher when prepared under Ar/H_2 atmosphere, see below), and from 0.5% to 9% for the $BaAl_2Si_2O_8$ matrix. Starting materials were placed in silicon nitride container 65% filled with ethanol and ball milled with a Fritsch Pulverisette 7 for about two hours to ensure a complete mixture. Then, after drying in an oven at around 150°C, blends were calcined at 1350°C under air for 50 h for CASO and BASO, and 20 h for SASO, respectively. The air atmosphere is replaced by reducing conditions (argon/hydrogen

(95/5%)) and the target composition is M_{1-x}Al₂Si₂O₈:xEu²⁺ when the “only” stabilization of Eu²⁺ cations is desired. To make it simple, MAl₂Si₂O₈ (M = Ca, Sr, Ba), CaAl₂Si₂O₈, SrAl₂Si₂O₈ and BaAl₂Si₂O₈ samples will be named hereafter MASO, CASO, SASO and BASO, respectively. In all these materials, the rare earth cations (Eu²⁺, Eu³⁺) are expected to substitute for the alkaline earth cations (M²⁺) in the host lattice for steric reasons [3, 21].

Let us note that when Eu³⁺ cations are inserted in the matrices, we can *a priori* envision two different kinds of compositions for our samples to respect the charge balance, namely, the formula of M_{1-3x/2}Al₂Si₂O₈:xEu³⁺ and M_{1-x}Al₂Si₂O_{8+0.5x}:xEu³⁺, respectively. The former will be privileged in the discussions even if results will be systematically acquired on both prepared series of samples.

2.2 Optical measurements

The photoluminescence (PL) and PL excitation (PLE) spectra for all the phosphors were obtained with a Spex Fluorolog-3 spectrofluorometer (Instruments Jobin Yvon) equipped with a 450-W Xe light source and double excitation monochromators. The luminescence decay curve was obtained from a Lecroy Wave Runner 6100 digital oscilloscope (1GHz) using a tunable laser (pulse width = 4 ns, gate = 50 ns) as excitation source (continuum sunlite OPO). The Commission International de l'Eclairage (CIE) chromaticity coordinates for all samples were determined by a Laiko DT-100 color analyzer equipped with a CCD detector. All of the measurements were performed at room temperature. The spectra decomposition and emission decay fit were accomplished with the Origin8.1 software (originLab Corporation, U.S.A) using Gaussian curves.

2.3. Structural characterization

The phase purity and the crystal structure were examined by powder X-ray diffraction (XRD) with a Bruker AXS D8 advanced automatic diffractometer with Cu K-L3 radiation (germanium monochromator) operating at 40 kV and 40 mA. Structure refinements were carried out with the Jana 2006 version software. The instrumental function was expressed in terms of the geometry of the diffractometer (fundamental approach) with the relevant parameters reported in **Table 2-1**.

Table 2-1. Instrumental data Used for Rietveld Refinements

Primary and second radius	217.5mm
Receiving slit length	16mm
Glancing angle	13.65 °
Source and sample length	12mm
Primary soller slit aperture	2.5°
Reception slit divergence angle	0.2 °
Receiving slit width	0.1mm

2.4. Description of $\text{MAl}_2\text{Si}_2\text{O}_8$ structures

On the basis of thermodynamic investigations, the structure of MASO feldspars is very stable [25]. Therefore they are suitable for being the host lattice of phosphors by doping with rare earth ions, such as Ce^{3+} , Mn^{2+} , $\text{Eu}^{2+/3+}$ etc (also see chapter III). In the following, we will concentrate our attentions on the luminescence properties of the three MASO phases stabled at low temperature, i.e. the celsian and anorthite forms. All of them consist of a 3D network of AlO_4 and SiO_4 tetrahedra bounded by vertices, with alkaline-earth (AE) cations housed in channels along the three directions (**Fig. 2-2**). The aluminium avoidance principle is respected, i.e. each aluminium cation is surrounded by four silicon and vice versa [27]. Ba^{2+} and Sr^{2+} cations occupied a single nine-fold coordinated site, whereas Ca^{2+} cations lie at four two-fold crystallographically independent sites exhibiting either a six-fold or a seven-fold coordination [3]. The chemical environments of Ca^{2+} in CASO, Sr^{2+} in SASO and Ba^{2+} in BASO are drawn in **Figure 2-3** with their Wyckoff positions (2i for Ca1 to Ca4 in CASO, 8f for Sr and Ba in SASO and BASO, respectively) and interatomic distances. The ionic radius of the different cations (M^{2+}) and the Al/Si distribution determines the symmetry of the host lattice [27]. The monoclinic symmetry would be favoured by the larger cations (i.e. Sr^{2+} , Ba^{2+}) contrary to the smallest one (i.e. Ca^{2+}). Due to the preferential ordering of trivalent aluminium ions in tetrahedral sites, the smaller cations would allow the structure to collapse to triclinic symmetry. Thus, CASO exhibits a triclinic structure whereas SASO and BASO crystallise with a monoclinic symmetry.

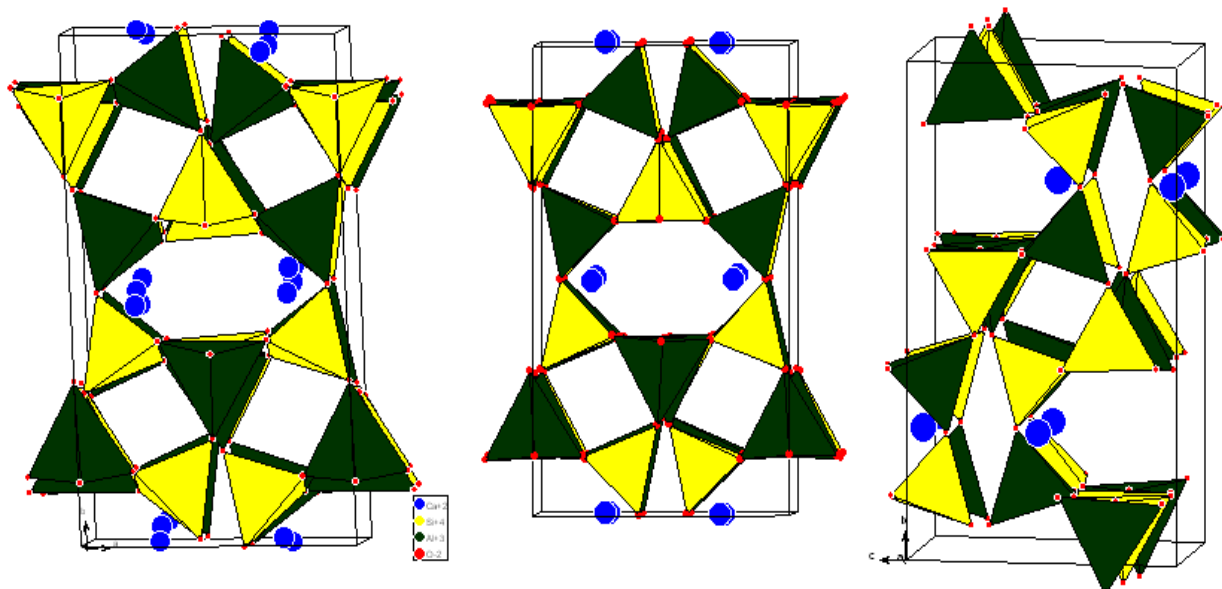
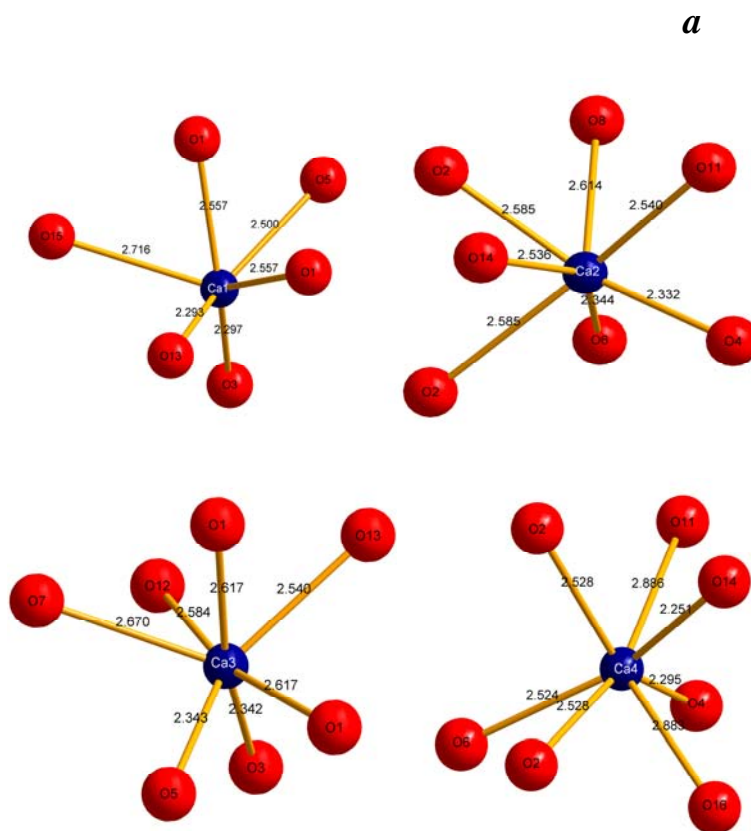


Figure 2-2. Crystal structure of CASO, SASO and BASO (from left to right). Yellow and black polyhedra correspond to SiO_4 and AlO_4 tetrahedron in CASO and BASO



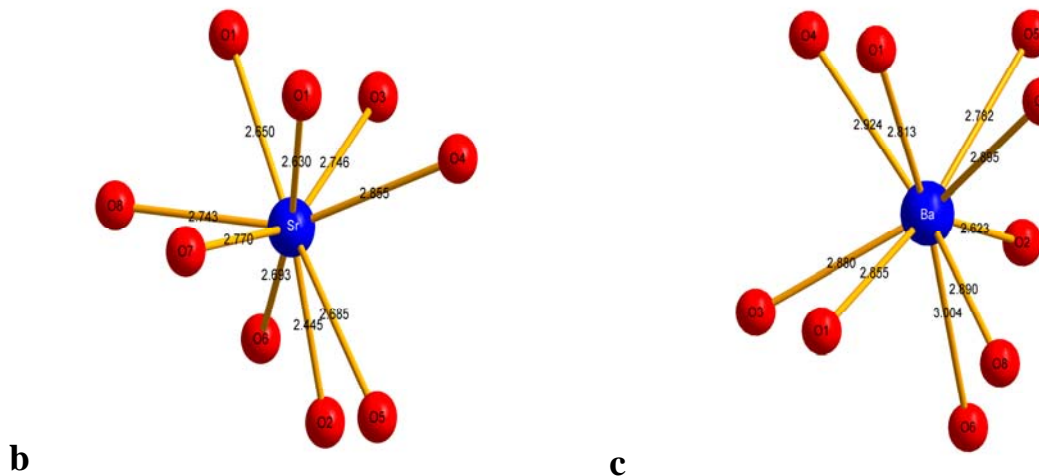


Figure 2-3. *a*, Calcium environments in CASO (Wyck.: 2*i*); *b*, Strontium environment in SASO (Wyck.: 8*i*) and *c*, Baryum environment in BASO (Wyck.: 8*f*)

3. Optical properties of MASO: Eu^{2+} in reducing atmosphere

In this part, we will focus only on the luminescent properties of MASO doped by Eu^{2+} ($\text{M} = \text{Ca}, \text{Sr}, \text{Ba}$), i.e. $\text{M}_{1-x}\text{ASO}:x\text{Eu}^{2+}$ compounds. In this way, samples were synthesized by solid-state route in reductive, i.e. an $\text{Ar} + 5\% \text{H}_2$ atmosphere (gas flow of 2 bubbles/sec) to preferentially stabilize Eu^{2+} .

X-Ray diffraction analyses confirmed that pure phases were obtained for Eu^{2+} concentrations ranging from 0.1 to 70 mol % for Eu^{2+} -doped CASO, 0.5 to 15 mol % for Eu^{2+} -doped SASO and 0.5 to 9 mol % for Eu^{2+} -doped BASO. Based on a Rietveld analysis, the full X-ray patterns of CASO: Eu^{2+} , SASO: Eu^{2+} and BASO: Eu^{2+} were assigned with the ICDD files 89-1462, 70-1862 and 38-1450, respectively. As an example, the structural parameters of the samples (at the critical dopant concentration, i.e. the higher concentration before concentration quenching) for the compositions $\text{M}_{1-x}\text{ASO}:x\text{Eu}^{2+}$ ($\text{M} = \text{Ca}, \text{Sr}, \text{Ba}$, respectively) are reported in **Table 2-2**. Furthermore, the introduction of Eu^{2+} cations in place of AE^{2+} cations leads to a small shift of the diffraction peaks because of the ionic radius difference. The shift turns to be toward high 2θ angles when $r(\text{M}^{2+}) < r(\text{Eu}^{2+})$ and toward low 2θ angles when $r(\text{M}^{2+}) > r(\text{Eu}^{2+})$. Except when explicitly mentioned, all the samples discussed in this part are all impurity-free.

Table 2-2. Structural parameters for $M_{1-x}ASO:xEu^{2+}$ ($x = 7\%, 1\%$ and 5% for $M = Ca, Sr, Ba$, respectively) determined by Rietveld refinement of powder XRD data at room temperature

Formula	$Ca_{0.93}Eu_{0.07}Al_2Si_2O_8^1$	$Sr_{0.99}Eu_{0.01}Al_2Si_2O_8$	$Ba_{0.95}Eu_{0.05}Al_2Si_2O_8$
Cryst. syst	Triclinic	Monoclinic	Monoclinic
Space group	P-1	I2/c	I2/c
a (Å)	8.1852(3)	8.3902(2)	8.6147(2)
b (Å)	12.8803(4)	12.9794(3)	13.0684(2)
c (Å)	14.1814(4)	14.2687(3)	14.4005(1)
α (deg)	93.1462(30)	90	90
β (deg)	115.7511(20)	115.3261(20)	115.1246(10)
γ (deg)	91.2223(20)	90	90
$V(\text{\AA}^3)$	1341.75(10)	1402.93(10)	1469.84(10)
Z	8	8	8
Number of cationic sites	4	1	1
CN	6 and 7	9	9
$d_{\text{calcd}}(\text{g/cm}^{-3})$	2.7534(2)	3.1028(2)	3.3910(1)
R_p (%)	12.41	12.89	12.68
R_{wp} (%)	16.52	16.88	15.94
GOF	1.48	1.54	1.62

¹ According to Angel et al., the anorthite form of $CaAl_2Si_2O_8$ may crystallize also in the I-1 space group with similar cell parameters than those reported in Table 2. Then the multiplicity of the Wyckoff sites occupied by calcium cations is doubled compared to P-1 SG but the occupancy rate is about 50%. So far, based on X-ray patterns collected in laboratory, we couldn't distinguish between the two models and we systematically privileged the P-1 SG.

3.1. $\text{Ca}_{1-x}\text{Al}_2\text{Si}_2\text{O}_8:\text{xEu}^{2+}$

3.1.1. Structural investigation

The structure refinement of the $\text{C}_{0.95}\text{Eu}_{0.05}\text{Al}_2\text{Si}_2\text{O}_8$ sample is depicted in **Figure 2-4**. The other members of the $\text{Ca}_{1-x}\text{Eu}_x\text{Al}_2\text{Si}_2\text{O}_8$ compounds (at least $x < 0.7$) evidence similar patterns. Namely, no peaks can be associated to any by-product. Samples are pure and a solid solution exists from $x = 0$ to $x = 0.7$. It may also be noticed that the Rietveld refinement is far to be satisfactory. This is attributed in part to the low symmetry of the structure with cell parameters large enough to induce peaks overlaps. Let us mention that attempt to refine the $\text{CaAl}_2\text{Si}_2\text{O}_8$ structure in an I-1 space group does not improve the reliability factors and the pattern matching.

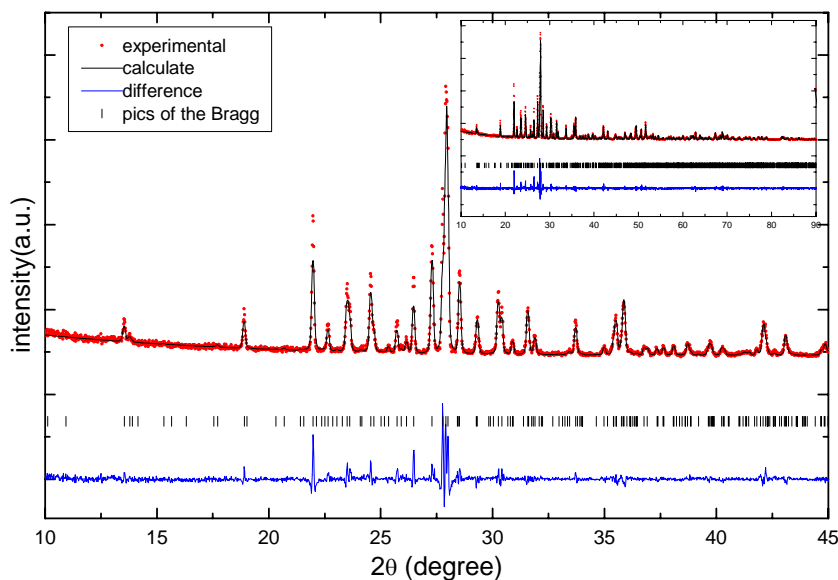


Figure 2-4. Observed, calculated and difference X-ray diffraction pattern of $\text{C}_{0.95}\text{Eu}_{0.05}\text{ASO}$ compound in the 10-45 2θ range (in inset is given the whole pattern)

The lattice parameters of $\text{C}_{1-x}\text{Eu}_x\text{Al}_2\text{Si}_2\text{O}_8$ ($x = 0$ to 70%) samples calculated from XRD data are also displayed in **Figure 2-5**. Due to the ionic radius difference between Eu^{2+} and Ca^{2+} , cell parameters and volume increase with the amount of Eu^{2+} ions. From **Figure 2-5**, one can see that the solid solution respects the Vegard's law for Eu^{2+} concentration up to a 70% substitution rate. Beyond, the $\text{Ca}_{1-x}\text{Eu}_x\text{Al}_2\text{Si}_2\text{O}_8$ compound ($x > 0.7$) coexists with the monoclinic $\text{Eu}_{0.92}\text{Al}_{1.76}\text{Si}_{2.24}\text{O}_8$ compound (ICDD # 80-0408).

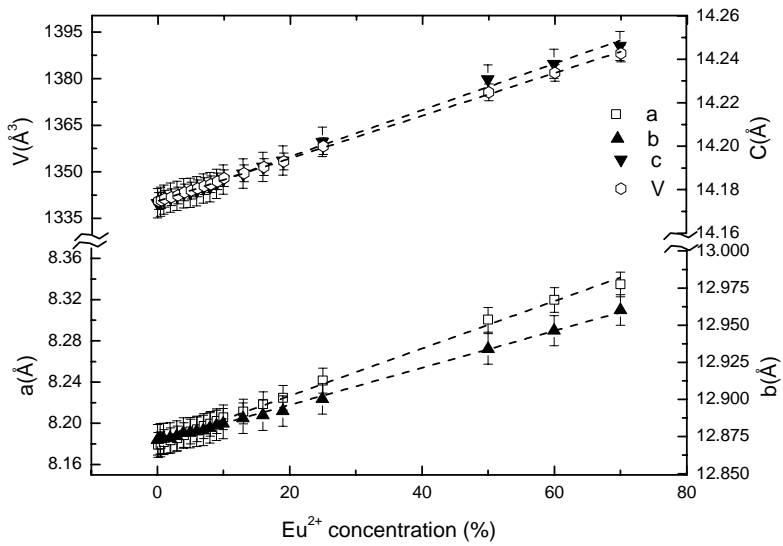


Figure 2-5. Evolution of the cell parameters of $\text{Ca}_{1-x}\text{Eu}_x\text{ASO}$ with $x = 0$ to 70%

3.1.2. Photoluminescence properties

The PLE and the PL spectra of the $\text{C}_{1-x}\text{Eu}_x\text{Al}_2\text{Si}_2\text{O}_8$ samples monitored at $\lambda_{\text{em}} = 420 \text{ nm}$ and $\lambda_{\text{ex}} = 320 \text{ nm}$ respectively are displayed in **Figure 2-6**. PLE spectrum is composed of a very broad band which can be deconvoluted in two contributions, one centred at around 320 nm, the other at about 287 nm. This absorption band is associated with $\text{Eu}^{2+}-4f^7 \rightarrow 4f^65d^1$ electronic transitions where the d block is split due to the ligand field. The intense broad emission bands, that peaks between 420-475 nm versus the Eu concentration, are associated with $4f^65d^1 \rightarrow 4f^7(^8S_{7/2})$ radiative transition of Eu^{2+} [1, 3]. The broad emission bands are due to the allowed character of the $5d \rightarrow 4f$ transitions but also to the existence of 4 alkaline earth sites available for the activator. As one can see in **Figure 2-6** the higher the Eu concentration, the longer the emission wavelength is. This shift could be related to an increase of the ET from one Eu to another when Eu concentration increases. Practically, it is very interesting to notice that a white-bluish luminescence was observed by naked eyes for any Eu^{2+} -doped CASO compositions because of large emission bands located in the visible range. The calculated CIE chromatic coordinates for $\text{Ca}_{0.98}\text{Eu}_{0.02}\text{Al}_2\text{Si}_2\text{O}_8$ compound is (0.1706, 0.1197) under $\lambda_{\text{ex}} = 320 \text{ nm}$. Let notice that even if Clabau et al. detected Eu^{3+} species in this material by Mossbauer spectroscopy [3], no trace of Eu^{3+} cations was detected by luminescence emission. Actually, different reasons can be assumed to explain the lack of the emission lines

from Eu^{3+} : 1) the 4f-4f emissions from the Eu^{3+} cations are forbidden as electric dipole transitions and are several orders of magnitude less intense than the spin and parity allowed $5d \rightarrow 4f$ transitions of Eu^{2+} , 2) the contents of Eu^{3+} ions are quite low compared to those of Eu^{2+} , 3) excitation at 320 nm is not well appropriate for favoring the 4f-4f transitions of Eu^{3+} .

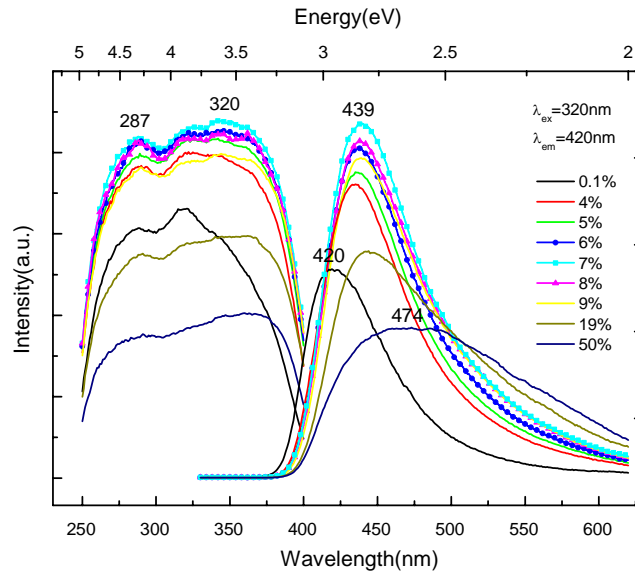


Figure 2-6. Excitation and emission spectra of $\text{Ca}_{1-x}\text{Eu}_x\text{ASO}$ ($x = 0.1\%$ to 50%) collected at room temperature, $\lambda_{ex} = 320\text{nm}$ and $\lambda_{em} = 420\text{nm}$

Moreover, we can observe that quenching of emission intensity occurs when the dopant concentration x exceeds 0.07 in $\text{Ca}_{1-x}\text{Eu}_x\text{Al}_2\text{Si}_2\text{O}_8$ compounds. This phenomenon is due to a non-radiative ET from one Eu^{2+} ion to another. Based on the **Equation (2-1)** [21, 28, 29]:

$$R_c = 2 \left[\frac{3V}{4\pi X_c N} \right]^{1/3} \quad (2-1)$$

where V is the unit-cell volume of the sample $\text{C}_{1-x}\text{Eu}_x\text{Al}_2\text{Si}_2\text{O}_8$ (1341.75 \AA^3 for $\text{C}_{0.93}\text{Eu}_{0.07}\text{ASO}$ as shown in **Table 2-2**) and N is the number of formula units per unit cell ($N = 8$ for $\text{MAl}_2\text{Si}_2\text{O}_8$ materials), X_c is the critical concentration (0.07)), the mean separation R_c between Europium activators can be calculated. Thus, R_c for $\text{C}_{0.93}\text{Eu}_{0.07}\text{Al}_2\text{Si}_2\text{O}_8$ is estimated at about 16.60 \AA . We can also observe from the **Figure 2-6** that the radiative emission from Eu^{2+} prevailed when $R(\text{Eu}^{2+}-\text{Eu}^{2+}) > R_c$ (the Eu^{2+} dopant concentration lower than 7%), whereas energy transfer between Eu^{2+} dominated when $R(\text{Eu}^{2+}-\text{Eu}^{2+}) < R_c$ (higher than 7%). Note that, as mentioned in the introduction chapter, non-radiative ET at work between ions

for such distances correspond to multipole-multipole interactions, exchange mechanism being not effective beyond a few angstroms [30].

As mentioned above CASO host lattice exhibits 4 crystallographic sites for Ca²⁺ in which Eu²⁺ can be placed. Consequently, the intense broad emission band should be deconvoluted into four contributions. However, any attempt to fit the emission band by four Gaussian curves remained unsuccessful. This result can be explained by the slight energy difference between the different Ca²⁺ sites, especially the sites with the same CN (= 7). Then according to literature [3, 31], broad bands can only be decomposed into two contributions, one for the 6-coordinated site (noted Ca(1)) and another one for the three 7-coordinated sites (noted Ca(2), Ca(3) and Ca(4)). Our emission spectrum in this study has been actually decomposed by two Gaussian contributions, as one can see in **Figure 2-7** for the C_{0.999}Eu_{0.001}ASO compound. At very first glance, Eu²⁺ cations at Ca(2) to Ca(4) sites (with CN = 7) are expected to give emissions at shorter wavelengths than Eu²⁺ at Ca(1) site. Actually, Eu-O distances at Ca(1) site are shorter than the Eu-O distances at Ca(2)-Ca(4) sites that impacts the crystal field and the splitting of the d-bloc for the Eu cations. Therefore, Eu(1) (when substituted in the Ca(1) site) results in the longer wavelength band while the other sites show the shorter wavelength band. As one can see in **Figure 2-7**, the locations of the decomposed curves originated from the two types of Eu²⁺ sites are in good agreement with the principle of crystal field energy level as mentioned above. For low Eu concentration, the emission at high energy is more intense than the one at low energy because there are more CN = 7 sites than CN = 6 ones at the disposal of Eu²⁺ cations.

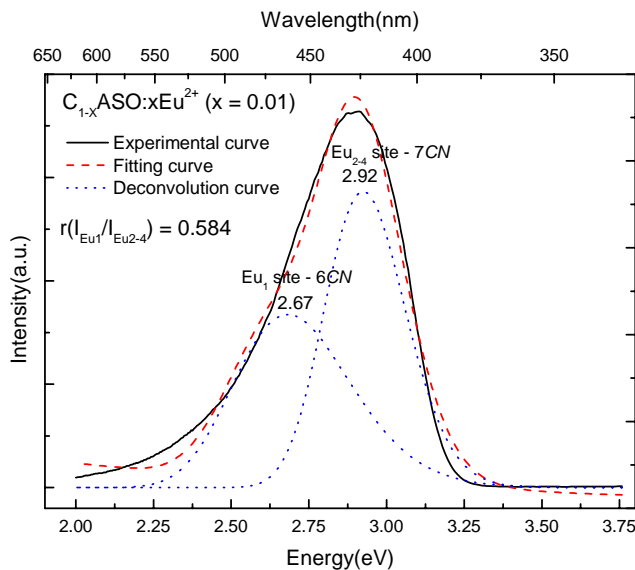


Figure 2-7. The $\text{C}_{1-x}\text{Eu}_x\text{ASO}$ ($x = 1\%$) emission spectra decomposed into two components using Gaussian functions (three 7-coordinated sites at the higher energy and 6- at the lower energy).

Deconvolutions have been also performed for other different Eu^{2+} concentrations. Results are reported in **Table 2-3**. The two different emission bands are approximately centred around 2.63 eV (472 nm) and 2.86 eV (433 nm) for $CN = 6$ and $CN = 7$, respectively. The intensity of the emission band from Eu^{2+} ions located in the 6-coordinated site (Ca(1)) increases with Eu^{2+} concentration while the emission from Eu^{2+} ions located in the Ca(2) to Ca(4) sites decreases. This trend can be explained by an ET. We might also suggest that Eu^{2+} cations at the Ca(1) sites are (much) less stable than Eu^{2+} at Ca(2), Ca(3) and Ca(4) sites. Thus, 7-fold coordinated sites would be occupied preferentially when europium atoms are inserted in the host lattice.

Table 2-3. Ratio of the emission intensity between the peak related to the 7-coordinated sites ($I_{[7]}$) and the one associated to the 6- coordinated site ($I_{[6]}$) for $\text{C}_{1-x}\text{Eu}_x\text{ASO}$ compounds

x	$E_{[6]}$ (eV)	$E_{[7]}$ (eV)	$I_{[6]}/I_{[7]}$
0.001	2.67 (464 nm)	2.92 (424 nm)	0.584
0.05	2.62 (473 nm)	2.86 (433 nm)	0.655
0.09	2.61 (475 nm)	2.84 (436 nm)	0.872
0.19	2.60 (476 nm)	2.82 (439 nm)	1.170

At this stage, let us mention that the decay times of Eu²⁺ cations in Eu doped CASO with x ranging from 0.5 to 50% have been measured. The evolution of the intensity vs. time once excitation stopped is given in **Figure 2-8** ($I = I_0 \exp(-t/\tau)$ according to [21, 32]). Surprisingly, whatever the substitution rate, the lifetimes associated with the Eu²⁺ 4f⁶5d¹ → 4f⁷ radiative transition are almost the same, namely, 0.65 μs. This value agrees with data reported in the literature [21] (0.73 μs) and is characteristic of Eu²⁺ cations. Therefore, we may be surprised that the value of τ is not impacted by the occurrence of ET when Eu concentration increases.

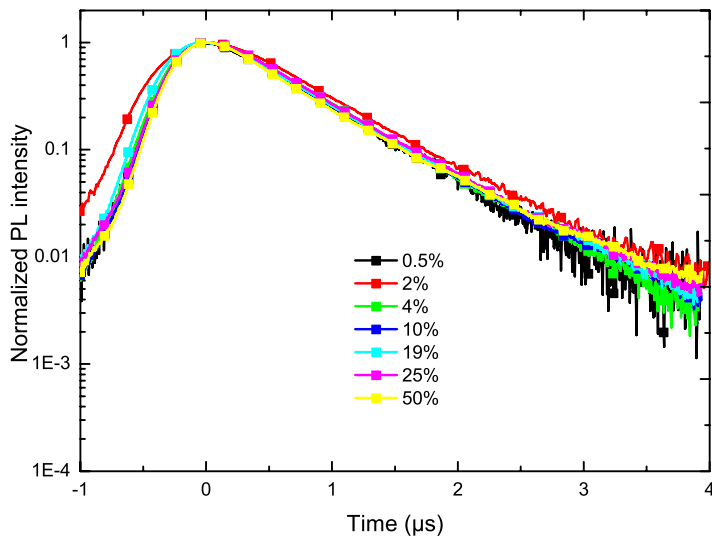


Figure 2-8. Photoluminescence decay curve of $C_{1-x}Eu_xASO$ ($x = 0.5\%$ to 50% , $\lambda_{em} = 420nm$ and $\lambda_{ex} = 265 nm$)

At the end, as discussed in previous works, a little amount of residual Eu³⁺ is still present in the CASO:Eu²⁺ phosphor even synthesized in reductive atmosphere. This residue turns out to be very difficult to detect by optical emission spectra. In fact, it is well-known that for Eu³⁺ ions, the valence electrons are shielded by the 5s and 5p outer electrons. Thus, the f-f transitions of trivalent lanthanides are weakly affected by ligand ions in the crystals [11, 19]. This means that properties of the emission spectra (the wavelength, the sharpness of the band doped with trivalent rare-earth elements (i.e. Eu³⁺) are similar with each other no matter what kind of phosphor is involved. Moreover, in most cases for Eu³⁺ doped phosphors (at low symmetry site for Eu³⁺), the predominant transition ($^5D_0 \rightarrow ^7F_2$) of the emission band is located at approximately 611 nm (see below for materials prepared in air). Based on the above consideration, we also depict the excitation spectra monitored at $\lambda_{em} = 611$ nm for the samples

$\text{C}_{1-x}\text{Eu}_x\text{Al}_2\text{Si}_2\text{O}_8$ synthesised in reductive atmosphere. Then, as observed in **Figure 2-9**, two weak f-f absorption peaks located at around 393 and 463 nm can be detected (${}^7\text{F}_0 \rightarrow {}^5\text{L}_0$ and ${}^7\text{F}_0 \rightarrow {}^5\text{D}_2$, respectively). On the basis of these luminescent results and the Mossbauer spectra from the literature [3], we can confirm that both Eu^{2+} (majority) and Eu^{3+} ions co-exist in the CASO matrix even synthesized in reducing atmosphere in this study. It is worthy to note that the spectra shape PLE of $\text{C}_{1-x}\text{Eu}_x\text{ASO}$ monitored at 611 nm has a similar appearance than CASO:Eu²⁺ monitored at 420 nm (**Figure 2-6**) with characteristic f-f line peaks (at 393 and 463 nm for instance) in addition. Therefore, we can suppose that Eu²⁺ co-doped with Eu³⁺ in the CASO matrix can impact the CIE parameters because of ET from Eu²⁺ to Eu³⁺.

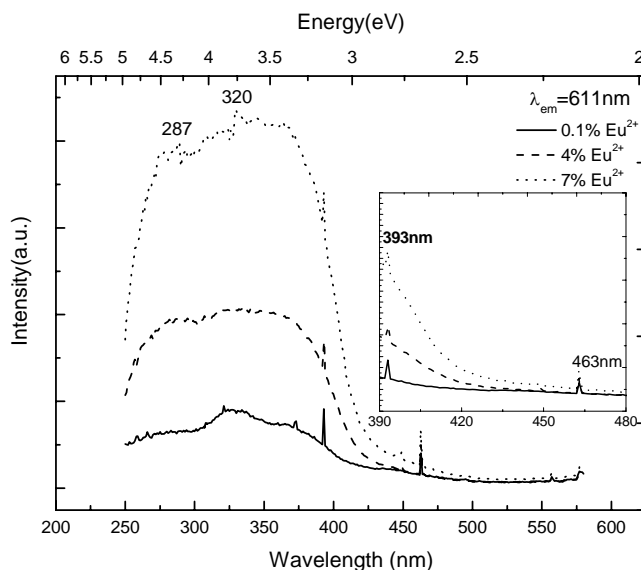


Figure 2-9. Excitation spectra of the $\text{C}_{1-x}\text{Eu}_x\text{ASO}$ ($x = 0.1\%$, 4% and 7%) monitored at 611 nm, inset is the enlarger spectra between the wavelength 390 and 480 nm

3.2. $\text{Sr}_{1-x}\text{Al}_2\text{Si}_2\text{O}_8:\text{xEu}^{2+}$

3.2.1. Structural investigation

Figure 2-10 displays the XRD pattern of $\text{Sr}_{0.99}\text{Eu}_{0.01}\text{Al}_2\text{Si}_2\text{O}_8$ after Rietveld refinement. For any materials with x lower than 15%, no by-product was detected. Moreover, although Eu²⁺ substituted for Sr²⁺ cation in the SASO matrix, there is almost no significant change in the XRD patterns going from the undoped host lattice to the doped host lattice. This originates from the fact that the radii difference between Sr²⁺ and Eu²⁺ is quite small (Eu²⁺ = 1.30 Å,

$\text{Sr}^{2+} = 1.31 \text{ \AA}$ when $CN = 9$). The evolution of the lattice parameters and volume cell of doped SASO samples issued from an X-ray analysis are shown in **Figure 2-11** for different Eu²⁺ concentrations ranging from 0.5% to 15%.

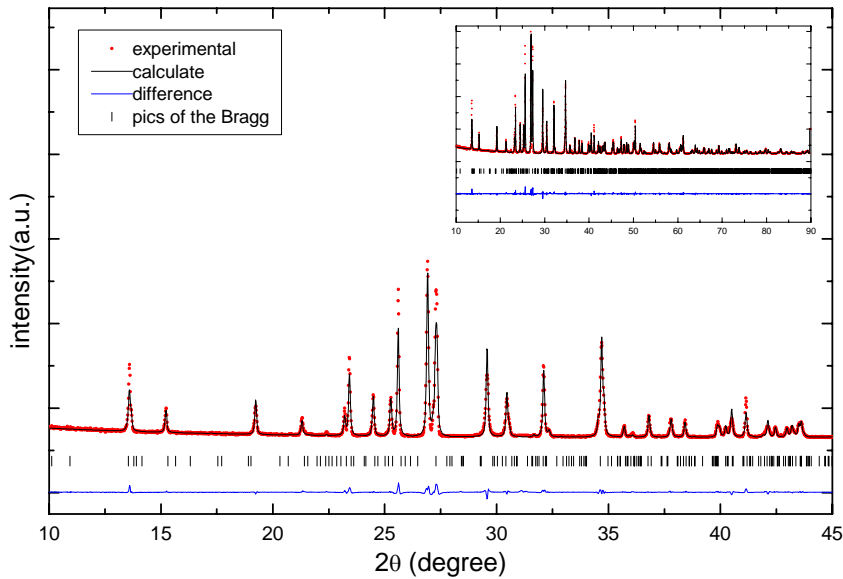


Figure 2-10. Observed, calculated and difference X-ray diffraction patterns of an $S_{0.99}\text{Eu}_{0.01}\text{ASO}$ compound in the 10–45 2θ range (in inset is given the total pattern)

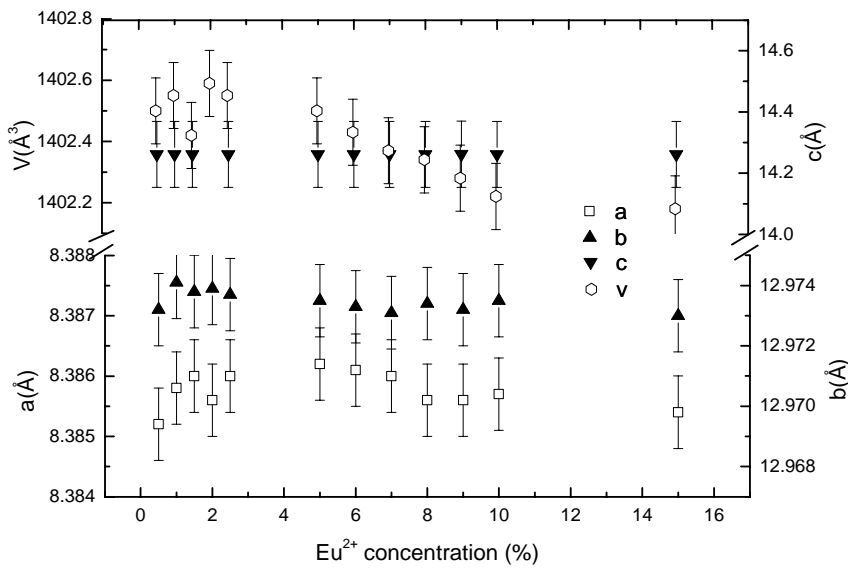


Figure 2-11. Evolution of $\text{Sr}_{1-x}\text{Eu}_x\text{ASO}$ cell parameters with $x = 0.5\%$ to 15%. Errors bars are equal to three times the standard deviation.

3.2.2. Photoluminescence properties

The photoluminescence excitation (monitored at $\lambda_{\text{em}} = 404$ nm) and emission (monitored at $\lambda_{\text{ex}} = 310$ nm) spectra of $\text{S}_{1-x}\text{Eu}_x\text{Al}_2\text{Si}_2\text{O}_8$ samples synthesised in reducing atmosphere are displayed in **Figure 2-12**. Similarly to CASO:Eu²⁺, PLE spectra of SASO:Eu²⁺ is composed of two broad bands located at 266 nm and 310 nm. As previously seen, the presence of these two bands is due to the splitting of the 5d block of Eu²⁺ cations caused by the ligand field. The allowed $4f^65d^1 \rightarrow 4f^7$ emission transition of Eu²⁺ is located at 404 nm for low concentration in Eu but is also red shifted when europium concentration increases. This red shift goes along with broadening of the emission peak and a decrease of intensity for x higher than 1% as shown in **Figure 2-12**.

As mentioned before, there is only one crystallographic site for Sr²⁺ in the SASO host matrix and consequently only one site is supposed to house Eu²⁺ cations. Thus, emission should be simulated by one Gaussian curve only. However, as one can see in **Figure 2-12**, emission band gets a strong asymmetry which involves some difficulties in the deconvolution with only one Gaussian curve. This asymmetry supposes that there is not a unique environment for Sr²⁺ cations. Actually, the presence of different environments could be explained by the existence of defects located in the surrounding of Eu²⁺ ions. If we suppose that a small amount of Eu³⁺ is present (see below), defects could be vacancies ($V_{\text{Sr}}^{/\!/}$) necessary to accommodate the charge balance when one Eu³⁺ cation substitutes one Sr²⁺ ion.

Let notice that self ET takes place for x higher than 1%, which indicates that ET is favoured in the SASO compared to the CASO matrix (quenching at 7%). Using **Equation 2-1**, a critical distance (R_c) of ~ 32.24 Å is calculated ($V = 1402.93$ Å³, $N = 8$ and $X_c = 0.01$).

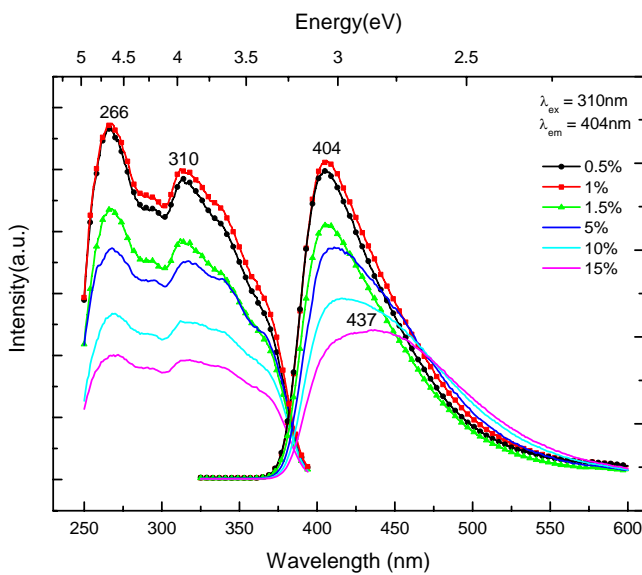


Figure 2-12. Excitation and emission spectra of Sr_{1-x}Eu_xASO ($x = 0.5\%$ to 15%) collected at room temperature, $\lambda_{ex} = 310$ nm and $\lambda_{em} = 404$ nm

Figure 2-13 shows the excitation spectra of Sr_{1-x}Eu_xAl₂Si₂O₈ compounds monitored at 611 nm corresponding to the 4f-4f ($^5D_0 \rightarrow ^7F_2$) transition (at low symmetry site for Eu³⁺ doped in SASO) as previous discussed. The presence of Eu³⁺ can be observed by photoluminescence in the Sr_{1-x}Eu_xASO compounds. Actually, the sharp peaks based on the broad excitation spectra of Eu²⁺ are characteristic to Eu³⁺ transitions and are located at 393 nm ($^7F_0 \rightarrow ^5L_0$), 463 nm ($^7F_0 \rightarrow ^5D_2$), 530 nm ($^7F_0 \rightarrow ^5D_1$) and 576 nm ($^7F_0 \rightarrow ^5D_0$). Similarly, the spectra shape PLE of Sr_{1-x}Eu_xASO monitored at 611 nm has the spectral shapes PLE of both SASO:Eu²⁺ and SASO:Eu³⁺ (the typical excitation bands located at 393 and 463 nm). We can also suppose that Eu³⁺ doped in the SASO matrix accompanied with Eu²⁺ can improve the luminescent properties of Eu³⁺ because of the ET from Eu²⁺ to Eu³⁺.

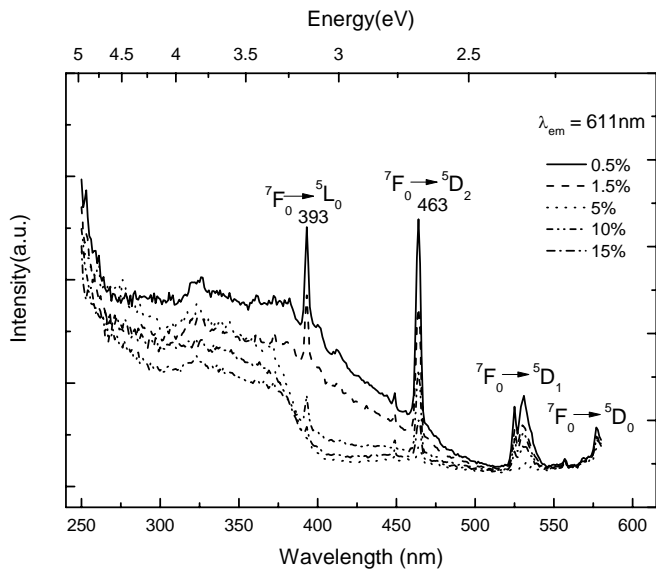


Figure 2-13. Excitation spectra of $\text{Sr}_{1-x}\text{Eu}_x\text{ASO}$ ($x = 1\%$ to 15%) monitored at 611 nm

3.3. $\text{Ba}_{1-x}\text{Al}_2\text{Si}_2\text{O}_8:\text{xEu}^{2+}$

3.3.1. Structural investigation

In the Eu^{2+} doped BASO series, europium atoms occupy Ba sites as usual. The purity of all prepared materials was systematically checked through X-ray powder diffraction. No side product was observed at least up to a substitution rate of 9%. The Rietveld refinement of the $\text{Ba}_{0.95}\text{Eu}_{0.05}\text{Al}_2\text{Si}_2\text{O}_8$ phase is given in **Figure 2-14** as example. The evolution of lattice parameters with Eu^{2+} concentration is depicted in **Figure 2-15**. As expected, the doping with Eu^{2+} induces a shrink of the cell because of the radius difference between Eu^{2+} ($r = 1.30\text{ \AA}$) and Ba^{2+} ($r = 1.47\text{ \AA}$) in a 9-fold coordination.

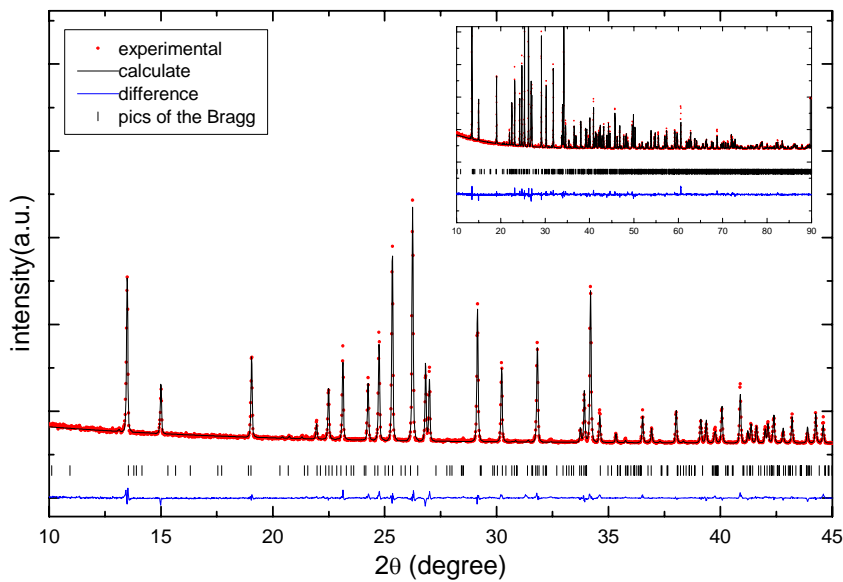


Figure 2-14. Observed, calculated and difference X-ray diffraction patterns of an $B_{0.95}Eu_{0.05}ASO$ compound in the 10-45 2θ range (in inset is given the total pattern)

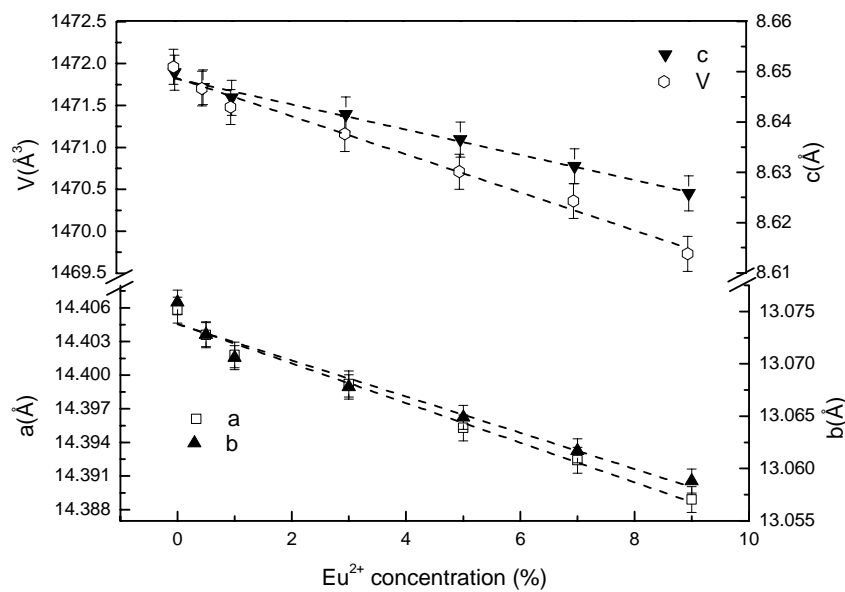


Figure 2-15. Evolution of $Ba_{1-x}Eu_xAl_2Si_2O_8$ cell parameters ($x = 0$ to 9%)

3.3.2. Photoluminescence properties

In **Figure 2-16** are shown the PLE and PL spectra of $\text{Ba}_{1-x}\text{Eu}_x\text{Al}_2\text{Si}_2\text{O}_8$ samples ($x = 0.5\%$ to 9%). Excitation spectra are composed of a broad band from 250 nm to 400 nm with two maximum peaks at 265 nm and 335 nm. The emission spectrum consists of a quite broad band lying from 350 nm to 600 nm with a maximum at around 440 nm. Similarly, the intense broad emission band centred at 435 nm can be attributed to the typical $4f^65d^1 \rightarrow 4f^7$ (${}^8\text{S}_{7/2}$) transition of Eu^{2+} . From **Figure 2-16**, the concentration quenching can be determined at $x = 5\%$ of phosphors in $\text{Ba}_{1-x}\text{Eu}_x\text{Al}_2\text{Si}_2\text{O}_8$. Excitation bands can be attributed to the transitions from ground state of Eu^{2+} (${}^8\text{S}_{7/2}$) to the different components of $4f^65d^1$ state created by the crystal field splitting. By employing the parameters from **Table 2-2** into **Eq.2-1**, the critical distance (R_c) for the compounds $\text{Ba}_{1-x}\text{Eu}_x\text{Al}_2\text{Si}_2\text{O}_8$ is then calculated to be $\sim 19.15\text{\AA}$. There is no sharp peaks (generated from Eu^{3+} transitions) in the excitation spectra for the compounds $\text{Ba}_{1-x}\text{Eu}_x\text{Al}_2\text{Si}_2\text{O}_8$ ($x = 0.5\%$ to 9%) by monitoring at 611 nm. In some extent, we can conclude that Eu^{3+} ions are much more difficult to stabilize in BASO than in CASO and SASO due to a too large difference in atomic radii between Eu^{3+} and Ba^{2+} .

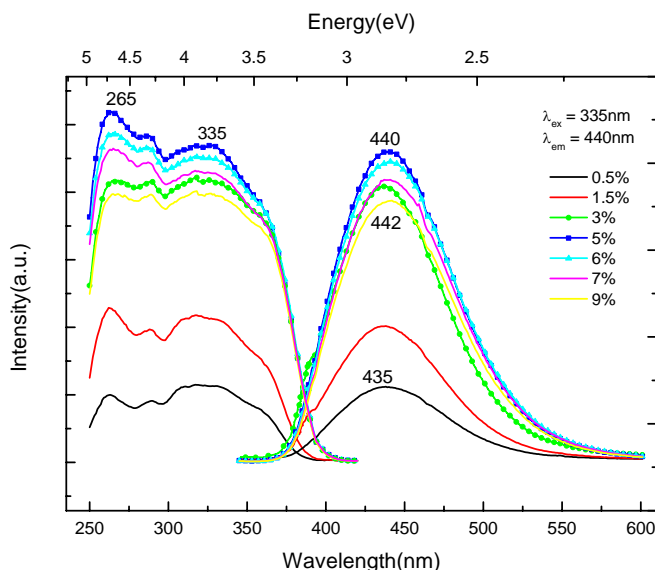


Figure 2-16. Excitation and emission spectra of $\text{Ba}_{1-x}\text{Eu}_x\text{ASO}$ ($x = 0.5\%$ to 9%) collected at room temperature, $\lambda_{\text{ex}} = 335\text{ nm}$ and $\lambda_{\text{em}} = 440\text{ nm}$

3.4. Comparison between Eu²⁺-doped CASO, SASO and BASO synthesized in reducing atmosphere

Excitation and emission spectra of $M_{0.95}Eu_{0.05}Al_2Si_2O_8$ materials are gathered in **Figure 2-17**. Clearly, the PLE spectra are quite similar for the three materials and a regular trend is observed going from CASO, to SASO and BASO: the excitation is shifted towards higher energies from Ca to Ba. At first sight, this agrees with a decrease of the covalency of the Eu-O bonds from CASO, to SASO and BASO. Namely, the smaller the size of the alkaline earth, the higher the ligand field splitting of the d states of europium, the lower the absorption 4f → 5d threshold [25]. Let notice that this simple concept is valid to account for the observed blue shift only if the barycentre of Eu d-block, as well the position in energy of the f-block, is not affected by the host lattice.

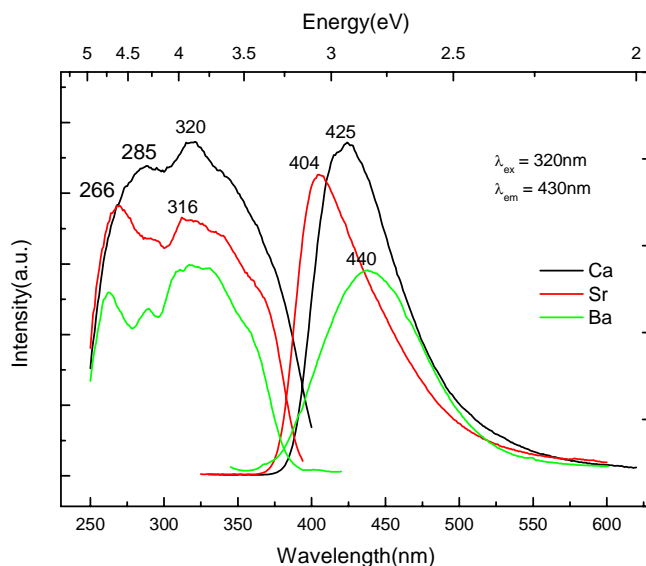


Figure 2-17. Excitation and emission spectra at $\lambda_{ex} = 320$ nm of $M_{1-x}Eu_xAl_2Si_2O_8$ ($x = 0.005$) collected at room temperature

Let us now consider the position of the emission peaks from Ca to Ba. In contrast with excitation, the evolution in the position of emission wavelength is quite erratic. As one can see **Figure 2-17**, the maximum of the broad and intense emission is located at 425 nm (2.91 eV), 404 nm (3.06 eV) and 440 nm (2.80 eV) for $Ca_{0.95}Eu_{0.05}Al_2Si_2O_8$, $Sr_{0.95}Eu_{0.05}Al_2Si_2O_8$, and $Ba_{0.95}Eu_{0.05}Al_2Si_2O_8$, respectively. Namely, as previously mentioned, the higher the coordination number, the lower the ligand field and consequently the lower the emission wavelength. In parallel, for a given coordination, the 5d-Eu block splitting decreases with

increasing the size of the alkaline earth. Thus the Eu^{2+} emission should shift to shorter wavelengths when the ionic radius of the cation increases, i.e. in the sequence $\text{Ca} < \text{Sr} < \text{Ba}$. Based on this argument, the blue shift observed from Ca to Sr is justified (**Figure 2-18**).

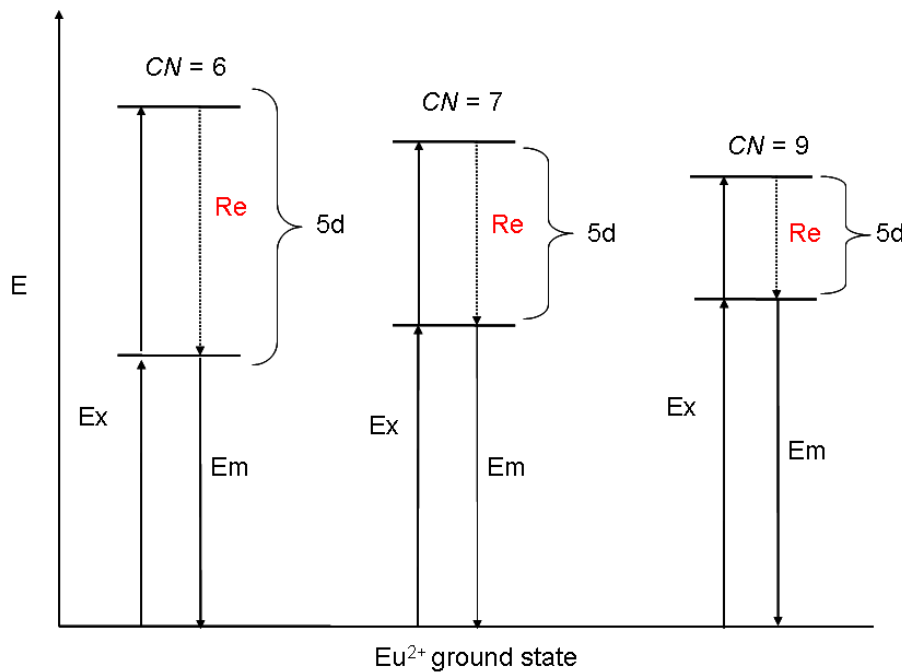


Figure 2-18. Schematic diagram of Eu^{2+} energy levels for different CN (= 6, 7 in CASO and 9 in SASO matrix). Ex, Em and Re stand for excitation, emission and relaxation processes, respectively

At the opposite, the higher emission wavelength of Eu^{2+} in BASO (centred at ~ 440 nm) remains unexplained. However, we can observe that the Stock shift is much more important for BASO (1.11 eV) than for CASO (0.96 eV) and SASO (0.86 eV) (commonly, the Stock shift decreases from Ca to Sr and Ba for isostructural compounds). The Stock shift is associated with changing in the Eu-O equilibrium distances. As there are evidences now [33-35] that this distance is shorter in the excited state than in the ground one for Eu^{2+} cation (stronger bonding in the excited state than in the ground state), we can suggest that Eu^{2+} cations at Ba sites may gain much more in stability in the excited state than Sr via a possible change in the coordination environment of Eu in the photogenerated state (**Figure 2-19**).

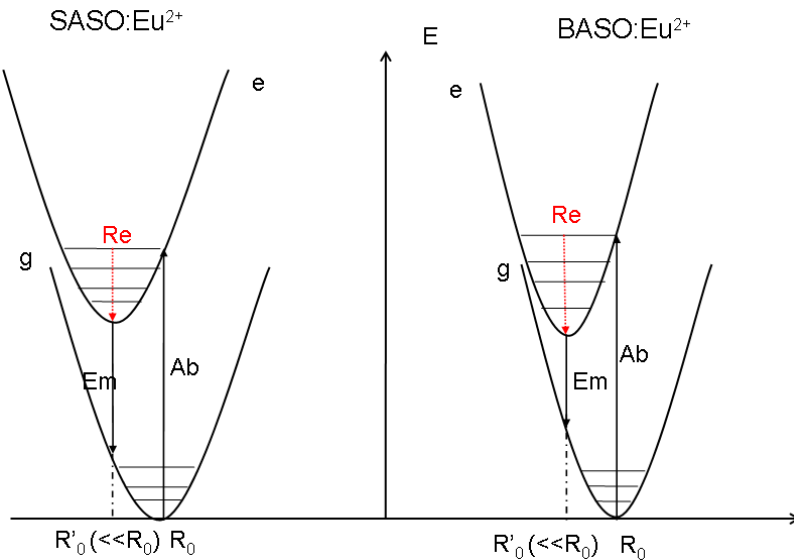


Figure 2-19. Single configurational coordinate diagram for SASO and BASO doped with Eu²⁺. Ab- absorption, Em-Emission, the equilibrium distance R_0 (ground state) and R_0' (excited state), Re- Relaxation (small in SASO and large in BASO due to the changes in the Eu-O equilibrium distances)

Concerning Eu³⁺ cations occurrence in MASO:Eu prepared in Ar/H₂, let us remind that a bundle of f-f lines characteristic of the presence of Eu³⁺ can be observed on excitation spectra monitored at $\lambda_{\text{ex}} = 611\text{nm}$ for CASO and SASO only (**Figures 2-9 and 2-13**). In principle, there are overlaps between the emission and the excitation bands of Eu²⁺ and Eu³⁺ suggesting the possibility of ET from Eu²⁺ to Eu³⁺. In addition, the amount of Eu³⁺ cations appears to be larger in CASO and SASO than in BASO. This may be related to steric reasons, the radius of Ba being too large and leading to the stabilization of the trivalent europium cations in the Ba based host lattice.

4. Optical properties of MASO:Eu³⁺/Eu²⁺ materials prepared in air

So far we have discussed only about Eu²⁺ doped MASO materials prepared in reductive atmosphere, i.e. materials where Eu³⁺ cations were expected to be present only as traces. In this section, we will focus on the luminescence properties of the samples synthesized in air condition. Thus, concentrations of Eu³⁺ should be much higher. Consequently, due to the differences in charge and size with alkaline-earth cation, materials should contain defects (e.g. appearance of vacancies, local distortions, etc). During the synthesis process, two formulas were considered to end at the correct charge balance, namely $M_{1-3x/2}Eu_xAl_2Si_2O_8$ and $M_{1-x}Eu_xAl_2Si_2O_{8+0.5x}$. The formulas suppose that all Eu atoms are fully oxidized into Eu³⁺ cations.

On one hand, we envisioned that defects are M^{2+} vacancies (two Eu^{3+} ions replace three M^{2+} sites). On the other hand we suppose that additional oxygen anions are inserted to counterbalance the one by one $\text{AE}^{2+}/\text{Eu}^{3+}$ substitution. Although the two serials of samples ($\text{M}_{1-3x/2}\text{Eu}_x\text{Al}_2\text{Si}_2\text{O}_8$ and $\text{M}_{1-x}\text{Eu}_x\text{Al}_2\text{Si}_2\text{O}_{8+0.5x}$) are strictly weighed in the appropriate proportions, the final samples would not fully agree with the two aforementioned formulas since synthesis in air will lead to the stabilization of both Eu^{2+} and Eu^{3+} cations (see below).

As for MASO: Eu^{2+} materials, we will discuss alternatively the optical properties of “ Eu^{3+} ” doped CASO, SASO and BASO. For all investigated samples, no long persistent luminescence is observed with naked eyes in contrast with CASO: Eu^{2+} for instance. The fluorescence of materials is white-pink, in agreement with the coexistence of Eu^{2+} and Eu^{3+} cations [4]. The Kroger-Vink notation of defects was chosen to be used throughout the entire section [36].

4.1. CASO: $\text{Eu}^{2+}/\text{Eu}^{3+}$

4.1.1. Structural investigation

Similarly, the XRD analysis was performed to determine the chemical purity and phase homogeneity of all samples. CASO compounds doped with $\text{Eu}^{2+}/\text{Eu}^{3+}$ synthesised in air ($\text{C}_{1-3x/2}\text{Al}_2\text{Si}_2\text{O}_8$ and $\text{C}_{1-x}\text{Al}_2\text{Si}_2\text{O}_{8+0.5x}$, compositions with x ranging from 0.5% to 13%) were obtained as a single phase (CASO, ICDD # 89-1462) (no side product). Against any expectations, the evolution of lattice parameters with the $\text{Eu}^{2+}/\text{Eu}^{3+}$ concentrations were investigated but no significant evolution was found. In fact a very slight increase is notified which is estimated at less than 0.2% in the range of 0-13% substitution rate. In the case of the hypothetical $\text{M}_{1-3x/2}\text{Eu}_x\text{Al}_2\text{Si}_2\text{O}_8$ formula, this means that the expected decrease associated to the $\text{Ca}^{2+} \rightarrow \text{Eu}^{3+}$ substitution induced by the appearance of calcium vacancies could be counterbalanced by the presence of Eu^{2+} ($r(\text{Eu}^{2+}) > r(\text{Ca}^{2+})$ and $r(\text{Eu}^{3+}) \sim r(\text{Ca}^{2+})$). In the case of the $\text{M}_{1-x}\text{Eu}_x\text{Al}_2\text{Si}_2\text{O}_{8+0.5x}$, a much more significant change in the cell volume would be expected. This suggests, as already mentioned and as expected, that the $\text{M}_{1-3x/2}\text{Eu}_x\text{Al}_2\text{Si}_2\text{O}_8$ formula has to be privileged over the $\text{M}_{1-x}\text{Eu}_x\text{Al}_2\text{Si}_2\text{O}_{8+0.5x}$ one. **Figure 2-20** shows the X-ray diffraction pattern of a $\text{Eu}^{2+}/\text{Eu}^{3+}$ (5%)-doped $\text{C}_{1-3x/2}\text{Al}_2\text{Si}_2\text{O}_8$ compound in the [10-45] 20

range. Due to the same reasons as for the CASO compounds doped with Eu²⁺ ions, the observed and the calculated patterns do not fit well.

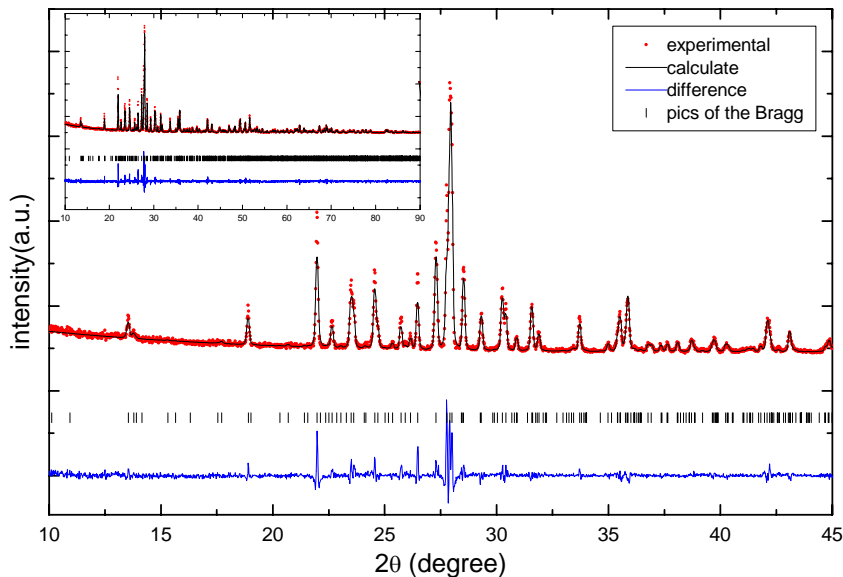


Figure 2-20. Observed, calculated and difference X-ray diffraction patterns of $C_{1-3x/2}ASO:xEu^{2+/3+}$ ($x = 5\%$) compound in the $10-45$ 2θ range, inset is given the total pattern

4.1.2. Excitation and emission spectra of Eu²⁺ in CASO:Eu^{2+/3+} compounds synthesized in air conditions

Figures 2-21a and **2-21b** show the excitation and emission spectra of the samples synthesized in air monitored at typical Eu²⁺ optical transitions, namely, $\lambda_{ex} = 320$ nm and $\lambda_{em} = 425$ nm for both compounds $C_{1-3x/2}Al_2Si_2O_8:xEu$ and $C_{1-x}Al_2Si_2O_{8+0.5x}:xEu$ ($x = 0.5\%$ to 13%). From **Figures 2-21a** and **2-21b**, the photoluminescence excitation spectra monitored at 425nm (Eu²⁺ emission) in CASO:Eu^{2+/3+} shows an optimal excitation $4f \rightarrow 5d$ band centred at 320 nm with a shoulder at 287nm, while the emission band located at around 425nm is due to the typical transition of Eu²⁺ from the 4d excited state to the $4f^7$ ground state. Then, we can assume that Eu²⁺ ions are present in the host matrix when synthesis is performed in air conditions.

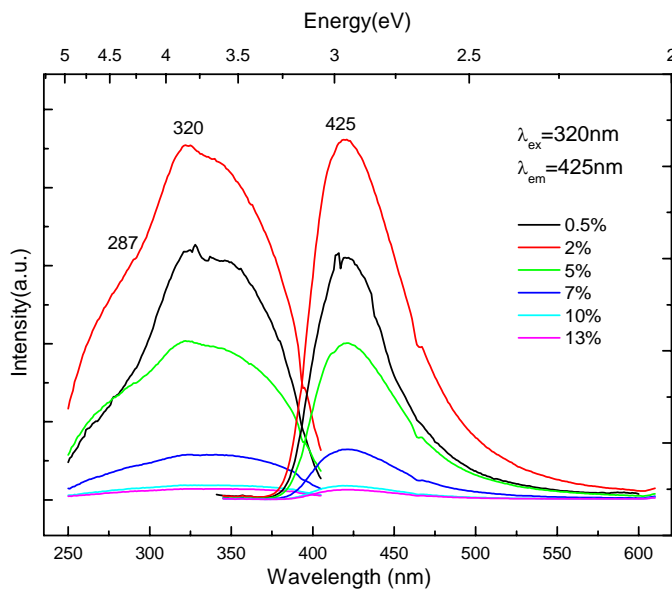


Figure 2-21a. The excitation and emission spectra of Eu^{2+} in $\text{C}_{1-3x/2}\text{ASO}:x\text{Eu}$ synthesized in air

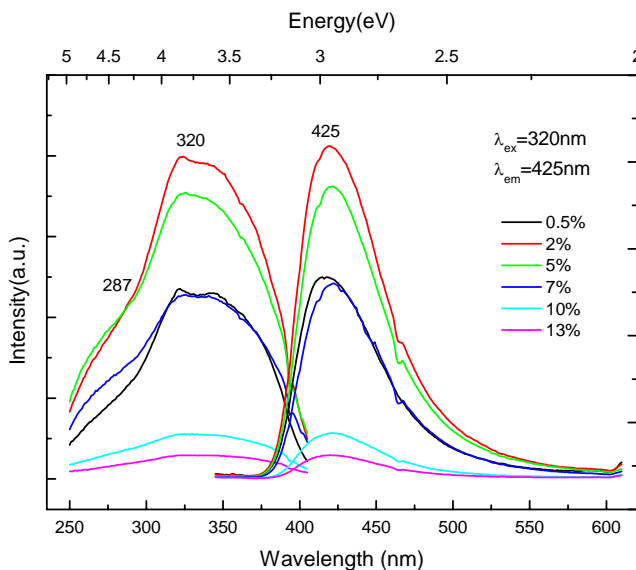


Figure 2-21b. The excitation and emission spectra of Eu^{2+} in $\text{C}_{1-x}\text{ASO}_{8+0.5x}:x\text{Eu}$ synthesized in air

From the observation of **Figures 2-21a** and **2-21b**, it is striking to notice that the intensity of the Eu²⁺ emission centred at ~ 425 nm begins decreasing at a dopant rate of about 2% for $\text{C}_{1-3x/2}\text{Al}_2\text{Si}_2\text{O}_8:x\text{Eu}$ and $\text{C}_{1-x}\text{Al}_2\text{Si}_2\text{O}_{8+0.5x}:x\text{Eu}$ materials. Note here that this value includes both Eu²⁺ and Eu³⁺ cations. Hence, the real contents of Eu²⁺ ions in each sample is significantly less than 2%, that is a value much lower than the critical concentration determined for $\text{C}_{1-x}\text{Al}_2\text{Si}_2\text{O}_8:x\text{Eu}^{2+}$ prepared in Ar/H₂ atmosphere (critical concentration of $\sim 7\%$). This could be explained by the occurrence of the ET from Eu²⁺ to Eu³⁺ (decrease of the

emission intensities of Eu²⁺ before reaching the Eu²⁺-Eu²⁺ critical concentration) and transfer from Eu²⁺ towards defect (V_{Ca} and/or O_i).

In order to investigate the chromaticity of the phosphors as a function of dopant contents, we calculated the CIE (x, y) parameters of the samples at $\lambda_{ex} = 320$ nm. Data are reported in **Figure 2-22**. As we can see, all the samples are located in the blue area of the horseshoe shaped diagram. Nevertheless, we may observe a slight shift of the CIE (x, y) parameters towards pink region when Eu concentration increases, which indicate Eu²⁺ → Eu³⁺ s or Eu²⁺ → defects transfers. This effect remains quite limited at this excitation wavelength.

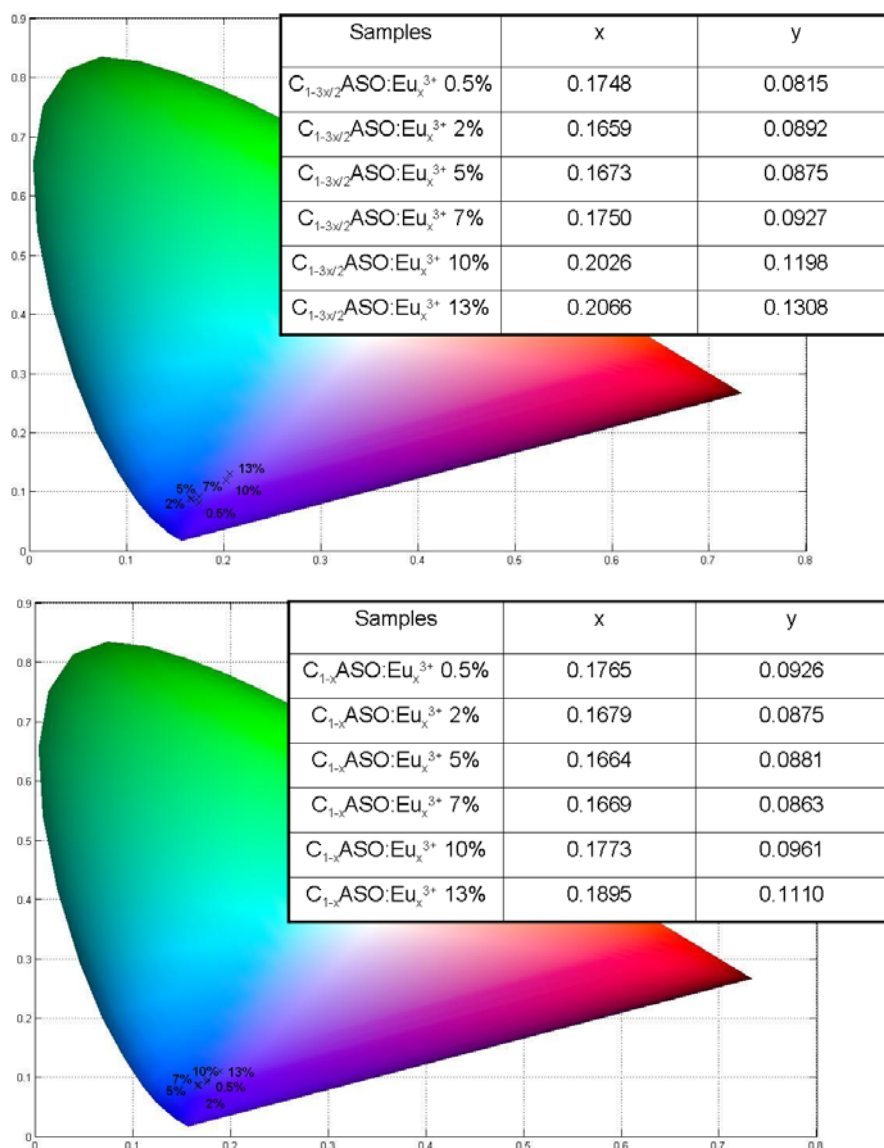


Figure 2-22. Above, CIE chromaticity for $C_{1-3x/2}Eu_xASO$ and below, CIE chromaticity for $C_{1-x}Eu_xASO_{8+0.5x}$ ($x = 0.5$ to 13%) under $\lambda_{ex} = 320\text{nm}$

4.1.3. Excitation spectra of Eu^{3+} in the CASO:Eu matrix synthesized in air

As we previously mentioned, since the valence electrons of Eu^{3+} are shielded by the 5s and 5p outer electrons, the 4f-4f transitions of Eu^{3+} are weakly affected by the crystal field. Therefore, optical spectra of most phosphors doped with Eu^{3+} are similar to those expected for free ions. Thus, we can expect that the position of the narrow Eu^{3+} excitation bands would be located at the same place in the CASO matrix whatever the doping Eu concentration. **Figure 2-23** shows the photoluminescence excitation spectra for Eu-doped CASO, under both formulas and for different Eu concentrations, excitation being monitored at 611 nm corresponding to the predominant transition of Eu^{3+} , namely ${}^5\text{D}_0 \rightarrow {}^7\text{F}_2$ transition. One can see from **Figure 2-23** that the PLE spectra consists of several sharp excitation bands corresponding to the typical intra-4f transitions of Eu^{3+} ions and a $\text{O}^{2-} \rightarrow \text{Eu}^{3+}$ charge transfer band (CTB) located in the UV range. Here, it is very interesting to notice that the broad CTB overlap with the weaker bands located at about 320 nm for CASO: $\text{Eu}^{2+/3+}$. Actually, as mentioned before, the 320 nm band is corresponding to the Eu^{2+} excitation transition $4\text{f}({}^8\text{S}_{7/2}) \rightarrow 4\text{f}^6 5\text{d}^1$. The weak excitation bands of Eu^{2+} indicate not only the presence of Eu^{2+} cations but also the existence of ET from Eu^{2+} ions of 5d level to the Eu^{3+} ions of 4f levels (spectra monitored at 611 nm). The sharp excitation bands relative to the 4f transitions centred at 361, 382, 393, 413, 463, 530 and 576 nm can be attributed to the ${}^7\text{F}_0 \rightarrow {}^5\text{D}_4$, ${}^7\text{F}_0 \rightarrow {}^5\text{L}_7$, ${}^7\text{F}_0 \rightarrow {}^5\text{L}_0$, ${}^7\text{F}_0 \rightarrow {}^5\text{D}_3$, ${}^7\text{F}_0 \rightarrow {}^5\text{D}_2$, ${}^7\text{F}_0 \rightarrow {}^5\text{D}_1$ and ${}^7\text{F}_0 \rightarrow {}^5\text{D}_0$ transitions [16, 18], respectively. These Eu^{3+} sharp excitation bands indicate that violet and blue laser diodes/LEDs are efficient pumping sources to obtain a red emission from Eu^{3+} doping, which could be useful for white light devices.

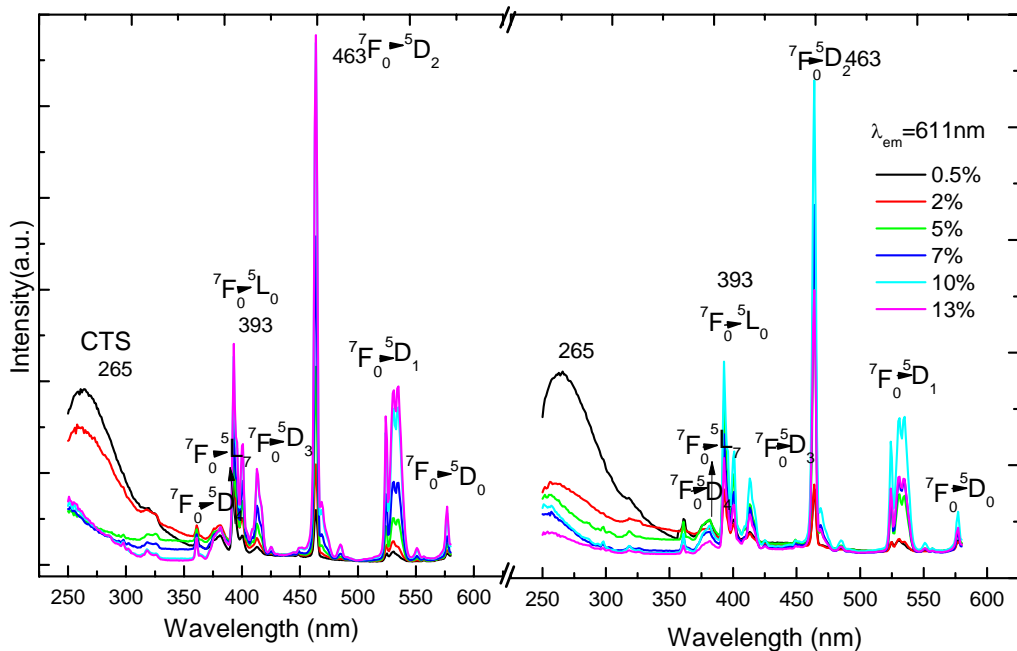


Figure 2-23. Left, excitation spectra of $C_{1-3x/2}ASO:xEu^{3+}$ and right, excitation spectra of $C_{1-x}ASO_{8+0.5x}:xEu^{3+}$ ($x = 0.5$ to 13%), monitored at 611nm

Furthermore, it is worthy to notice that the main difference between the samples in the two different formulas deals with the excitation intensities of the 4f-4f transitions of Eu³⁺. The excitation band intensity of the $Ca_{1-x}Eu_xAl_2Si_2O_{8+0.5x}$ samples starts to decrease for a concentration beyond 10% (Figure 2-23, right), whereas it gradually increases (up to 13%) for the $C_{1-3x/2}Eu_xAl_2Si_2O_8$ formula.

4.1.4. Emission spectra of Eu³⁺ in the CASO:Eu matrix synthesized in air

It is well-known that the characteristic sharp emission bands of Eu³⁺ strongly depend on its local environment in the host lattice. The orange emission associated to the $^5D_0 \rightarrow ^7F_1$ transition (normally located at around 585 nm) corresponds to a magnetic-dipole transition with the selection rule, $\Delta J = 0, \pm 1$ and is non sensitive to the crystal field symmetry around the Eu³⁺ ion. In contrast, the red emission from the $^5D_0 \rightarrow ^7F_2$ transition (normally located at around 610 nm) belongs to a hypersensitive transition with the selection rule, $\Delta J = 0, \pm 2$, and is strongly influenced by the outside surrounding environment. According to these statements, the red emission is dominant when Eu³⁺ is located at a low symmetry site (without inversion

centre) and the orange emission is more intense than the red one when Eu^{3+} is placed in a high symmetry site (with inversion centre).

Figure 2-24 shows the emission spectra of the samples $\text{C}_{1-3x/2}\text{Eu}_x\text{Al}_2\text{Si}_2\text{O}_8$ and $\text{Ca}_{1-x}\text{Eu}_x\text{Al}_2\text{Si}_2\text{O}_{8+0.5x}$ ($x = 0.5\%$ to 13%) monitored at 463 nm (${}^5\text{D}_0 \rightarrow {}^7\text{F}_2$, predominant transition of Eu^{3+}) for different Eu concentrations. The position and shape of the Eu^{3+} emission bands do not change with Eu concentration. For each composition, the strongest emission peak is located at 611 nm and attributed to the ${}^5\text{D}_0 \rightarrow {}^7\text{F}_2$ transition. Other peaks located at 570 - 579 , 580 - 604 , 638 - 661 and 679 - 715 nm are assigned to the ${}^5\text{D}_0 \rightarrow {}^7\text{F}_0$, ${}^5\text{D}_0 \rightarrow {}^7\text{F}_1$, ${}^5\text{D}_0 \rightarrow {}^7\text{F}_3$ and ${}^5\text{D}_0 \rightarrow {}^7\text{F}_4$ transitions of the Eu^{3+} ions [16, 18], respectively. As the red emission generated from the ${}^5\text{D}_0 \rightarrow {}^7\text{F}_2$ transition predominates in the emission spectra, one can suppose that Eu^{3+} cations occupy sites having no inversion centre in the CASO matrix, as expected for Eu housed in both the 6-fold Ca1 and 7-fold Ca2,3,4 sites. As previously seen for excitation spectra, similarly, a quenching of Eu^{3+} emission can be also only observed for the $\text{C}_{1-x}\text{Eu}_x\text{Al}_2\text{Si}_2\text{O}_{8+0.5x}$ formula when the doping rate reaches 10% . Therefore, one can suppose that for the same doping rate, $\text{C}_{1-3x/2}\text{Eu}_x\text{Al}_2\text{Si}_2\text{O}_8$ samples contain less Eu^{3+} ions than samples under the other formula and consequently, the $\text{C}_{1-3x/2}\text{Eu}_x\text{Al}_2\text{Si}_2\text{O}_8$ samples would have more Eu^{2+} ions than in the $\text{C}_{1-x}\text{Eu}_x\text{Al}_2\text{Si}_2\text{O}_{8+0.5x}$ for a given Eu concentration. The insets show the peaks of the Eu^{3+} ${}^5\text{D}_0 \rightarrow {}^7\text{F}_2$ transitions.

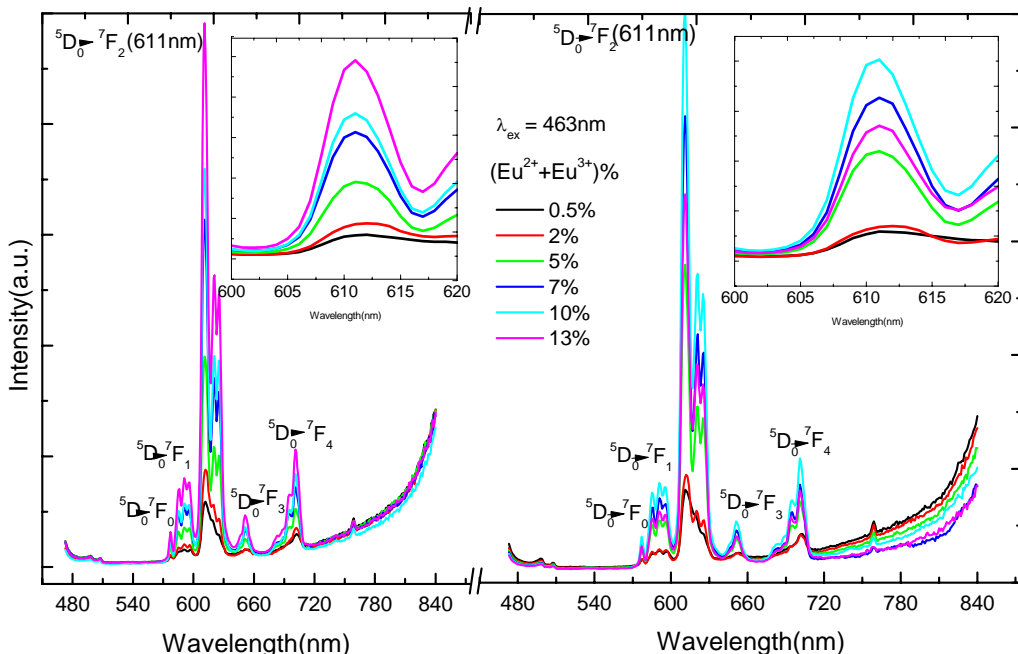


Figure 2-24. (Left) emission spectra of $\text{C}_{1-3x/2}\text{ASO}:x\text{Eu}^{3+}$, and (right) emission spectra of $\text{C}_{1-x}\text{ASO}:x\text{Eu}^{3+}$ ($x = 0.5$ to 13%), excited at 463 nm

Figure 2-25 shows the emission spectra of Eu doped in both compositions ($C_{1-3x/2}Eu_xAl_2Si_2O_8$ and $Ca_{1-x}Eu_xAl_2Si_2O_{8+0.5x}$ ($x = 0.5\%$ to 13%)) monitored at $\lambda_{ex} = 393$ nm which is the second predominant transition of Eu³⁺ ($^7F_0 \rightarrow ^5L_0$) and which can also, in some extent, excite Eu²⁺ transition. Emission spectra are composed of a broad band located at 425 nm (generated from Eu²⁺) together with sharp transitions associated with 4f-4f transitions of Eu³⁺. The strongly change of the emission intensities of Eu²⁺ is probably due to the ET from Eu²⁺ to Eu³⁺. The insets show the enlarged emission bands of the transition Eu³⁺ from the $^5D_0 \rightarrow ^7F_2$.

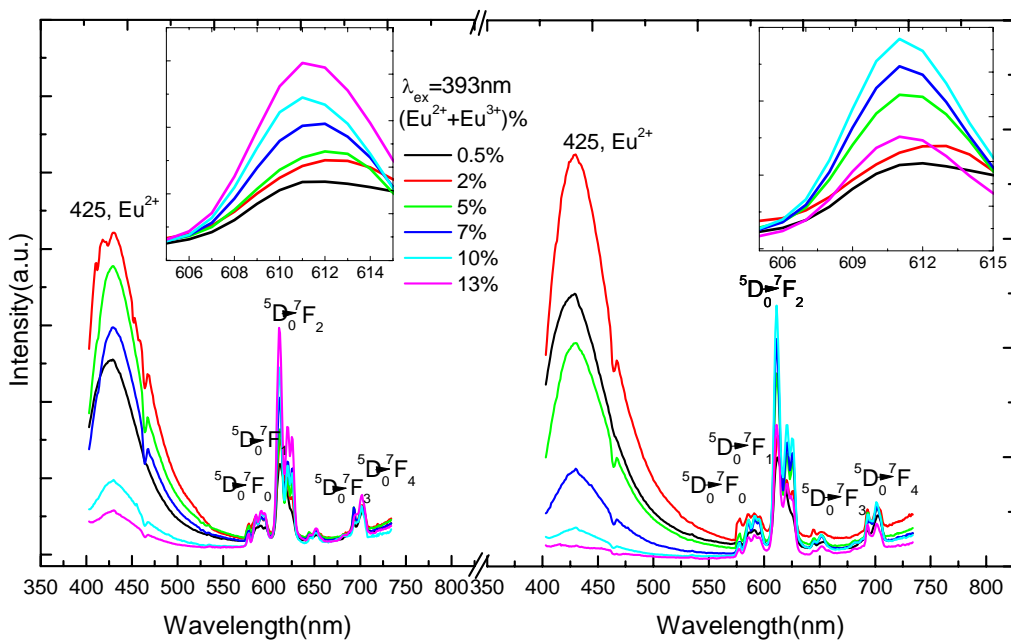


Figure 2-25. Left, emission spectra of $C_{1-3x/2}ASO:xEu^{3+}$, and right, emission spectra of $C_{1-x}ASO:xEu^{3+}$ ($x = 0.5$ to 13%), excited at 393nm .

Figure 2-26 shows the CIE chromaticity coordinates for the same samples under a 393nm excitation wavelength. The CIE coordinates of the $C_{1-3x/2}Eu_xAl_2Si_2O_8$ samples are more deeply in the pink area when compared to the same dopant rate samples under the $C_{1-x}Eu_xAl_2Si_2O_{8+0.5x}$ formula ($x = 0.5$ to 13%). This can be due to more Eu²⁺ ions in the $C_{1-3x/2}Eu_xAl_2Si_2O_8$ compounds than in $C_{1-x}Eu_xAl_2Si_2O_{8+0.5x}$ ones leading to more ET in the former samples. Note here, this could be also related to the presence of a higher content of Eu³⁺ cation which can be directly excited at 393 nm .

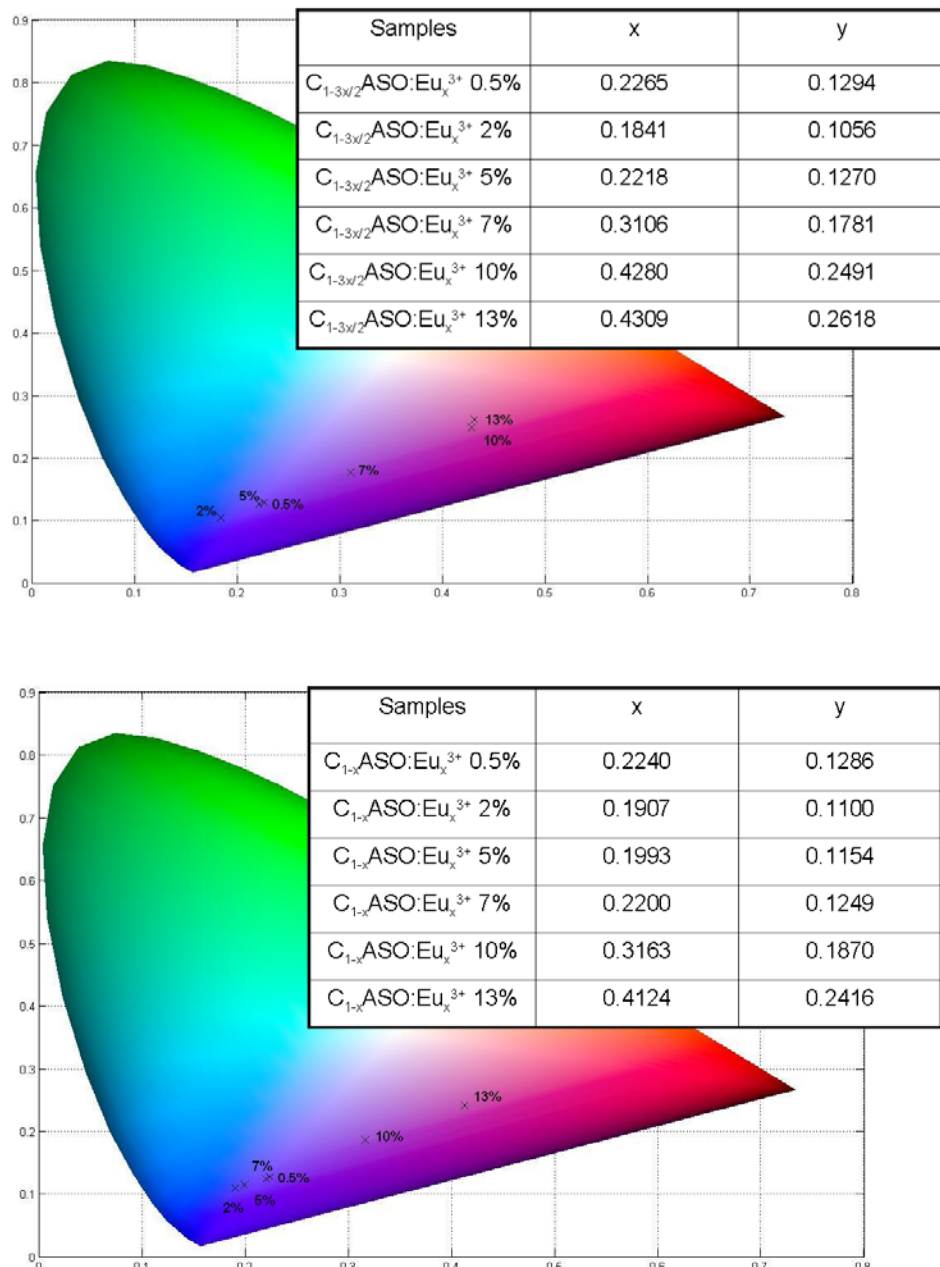


Figure 2-26. Above, CIE chromaticity for $\text{C}_{1-3x/2}\text{Eu}_x\text{ASO}$ and below, CIE chromaticity for $\text{C}_{1-x}\text{Eu}_x\text{ASO}_{8+0.5x}$ ($x = 0.5$ to 13%) under $\lambda_{ex} = 393\text{nm}$

Figure 2-27 shows the photoluminescence emission spectra for an excitation located in the charge transfer band ($\lambda_{ex} = 265\text{nm}$) of the CASO samples under the two different formulas ($\text{C}_{1-3x/2}\text{Eu}_x\text{Al}_2\text{Si}_2\text{O}_8$ and $\text{C}_{1-x}\text{Eu}_x\text{Al}_2\text{Si}_2\text{O}_{8+0.5x}$, $x = 0.5\%$ to 13%). The broad band centered at about 425 nm and the sharp peaks located in the longer wavelength are with no doubt attributed to the transition of Eu^{2+} ($4f^65d \rightarrow 4f^7$) and the interconfigurational (${}^5D_0 \rightarrow {}^7F_j$) transition of Eu^{3+} , respectively. Eu^{2+} emission intensity is higher when compared to the Eu^{3+} peak intensity even if there is only a low Eu^{2+} concentration because Eu^{2+} emission results from allowed transitions. Furthermore, the evolution of Eu^{2+} emission intensity varies with

the same tendency as previously described due to either the increase of Eu²⁺ concentration and/or an ET from Eu²⁺ to Eu³⁺ (V_{Ca} and/or O_i). In addition, Eu³⁺ emission intensities decrease due to the excitation CTB decrease as shown in **Figure 2-27** following with the Eu dopant concentrations.

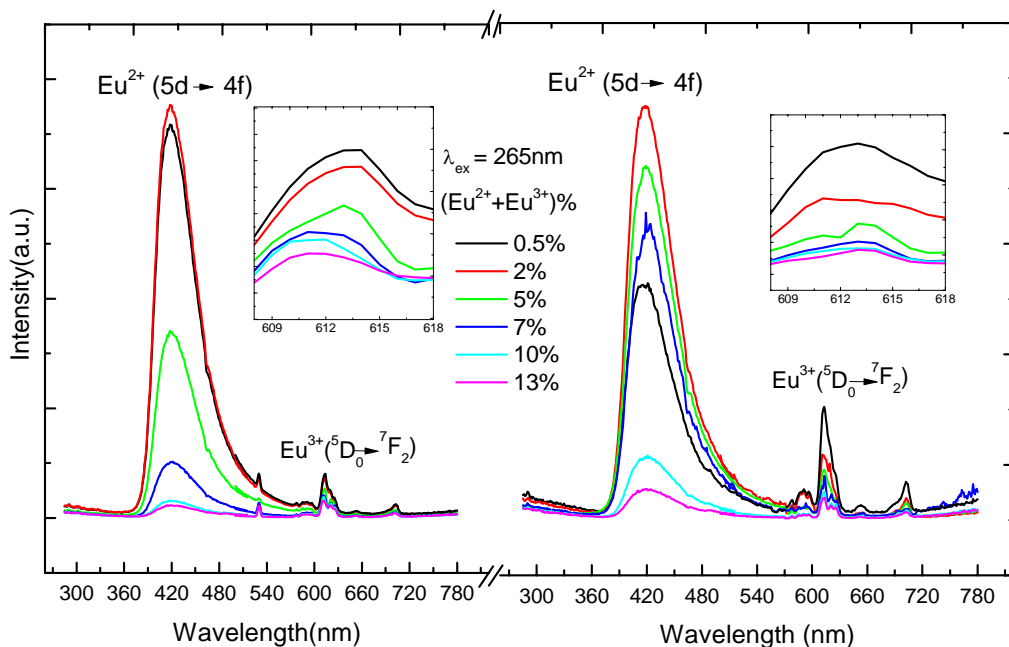


Figure 2-27. Left, emission spectra of $C_{1-3x/2}ASO:xEu^{3+}$, and right, emission spectra of $C_{1-x}ASO:xEu^{3+}$ ($x = 0.005-0.13$), excited at 265nm. The insets show the peaks of the $^5D_0 \rightarrow ^7F_2$ Eu^{3+} transitions.

4.2. SASO:Eu²⁺/Eu³⁺

4.2.1. Structural investigation

The X-ray diffraction patterns for all SASO materials synthesized in air conditions fit well with the standard ICDD file N° 70-1862. No secondary phase was detected. Moreover, for the SASO host lattice, the substitution of Eu for strontium involves a regular decrease of the cell volume, as one can see in **Figure 2-28**. The shrink of the lattice is due to the radius difference between strontium and europium ($r(Sr^{2+}) \sim r(Eu^{2+}) > r(Eu^{3+})$) suggesting that much more Eu³⁺ cations are incorporated in the matrix than in the materials synthesised in reducing atmosphere. **Figure 2-29** shows the X-ray diffraction pattern of a Eu^{2+/3+} (5%)-doped $S_{1-3x/2}Al_2Si_2O_8$ compound in the [10-45] 2θ range.

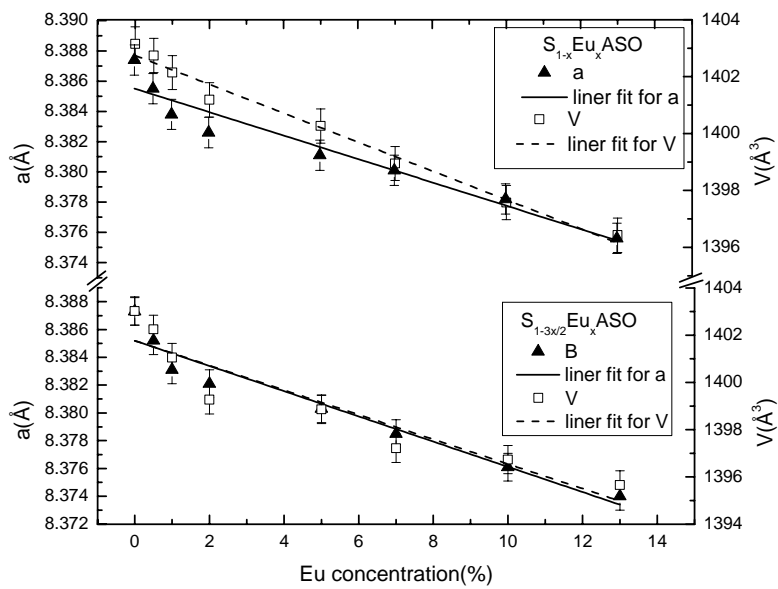


Figure 2-28. $\text{Eu}^{2+}/\text{Eu}^{3+}$ concentration dependence of unit cell for $\text{S}_{1-3x/2}\text{Eu}_x\text{Al}_2\text{Si}_2\text{O}_8$ and $\text{S}_{1-x}\text{Eu}_x\text{Al}_2\text{Si}_2\text{O}_{8+0.5x}$ ($x = 0.5$ to 13%)

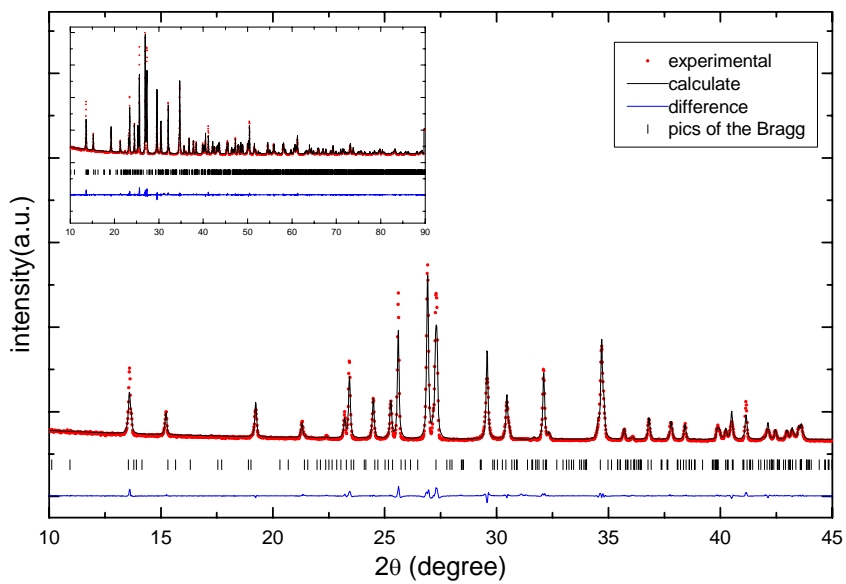


Figure 2-29. Observed, calculated and difference X-ray diffraction patterns of $\text{S}_{1-3x/2}\text{ASO}: x\text{Eu}^{2+/3+}$ ($x = 5\%$) compound in the 10-45 2θ range, inset is given the total pattern

4.2.2. Excitation and emission spectra of Eu²⁺ in SASO:Eu^{2+/3+} compounds synthesized in air conditions

Figures 2-30a and **2-30b** show the excitation and emission spectra of the samples synthesized in air monitored at typical Eu²⁺ transitions, namely, $\lambda_{\text{ex}} = 310 \text{ nm}$ and $\lambda_{\text{em}} = 404 \text{ nm}$ for $S_{1-3x/2}Al_2Si_2O_8:xEu$, and $S_{1-x}Al_2Si_2O_{8+0.5x}:xEu$, respectively. These spectra are quite similar to those collected for SASO:Eu²⁺ and fully confirm the presence of Eu²⁺ in materials prepared in air.

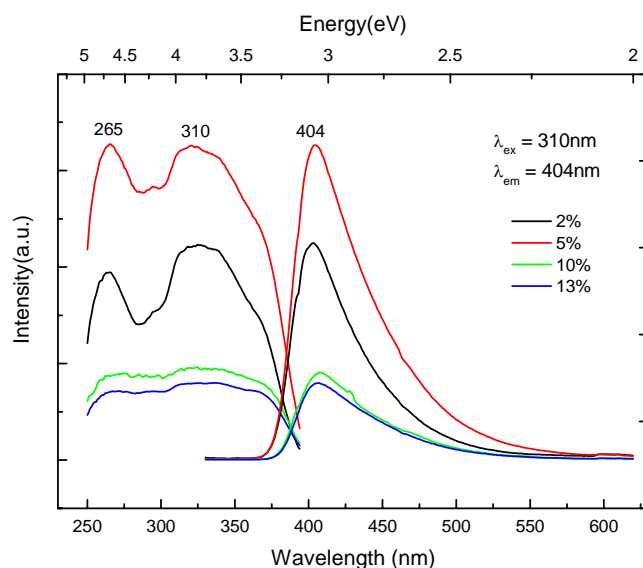


Figure 2-30a. The excitation and emission spectra of Eu²⁺ in $S_{1-3x/2}ASO:xEu$ synthesized in air

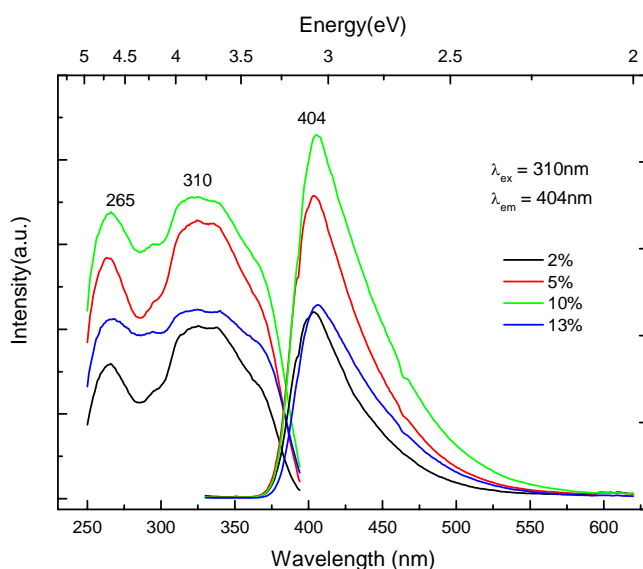


Figure 2-30b. The excitation and emission spectra of Eu²⁺ in $S_{1-x}ASO_{8+0.5x}:xEu$ synthesized in air

From the optical spectra in **Figures 2-30a** and **2-30b**, it can be determined that the intensities of the emission bands originated from the Eu^{2+} are continuous increasing till 5% and 10% for $\text{S}_{1-3x/2}\text{Al}_2\text{Si}_2\text{O}_8:\text{xEu}$ and $\text{S}_{1-x}\text{Al}_2\text{Si}_2\text{O}_{8+0.5x}:\text{xEu}$, respectively. As previously seen, the critical Eu^{2+} concentration in the SASO matrix synthesised in reducing atmosphere is $\sim 1\%$. Consequently, this suggests that a very large part of Eu cations are present under the Eu^{3+} form in material prepared in air. Furthermore, the ratio of Eu^{2+} and Eu^{3+} is different in $\text{S}_{1-3x/2}\text{Al}_2\text{Si}_2\text{O}_8:\text{xEu}$ and $\text{S}_{1-x}\text{Al}_2\text{Si}_2\text{O}_{8+0.5x}:\text{xEu}$ even if the dopant rate of Eu cations and the synthesis condition are identical. Actually, we might speculate that for a given Eu concentration, more Eu^{2+} cations are present in $\text{S}_{1-3x/2}\text{Al}_2\text{Si}_2\text{O}_8:\text{xEu}$ than in $\text{S}_{1-x}\text{Al}_2\text{Si}_2\text{O}_{8+0.5x}:\text{xEu}$ if we account only for Eu^{2+} - Eu^{2+} energy transfers.

4.2.3. Excitation spectra of Eu^{3+} in the SASO:Eu matrixes synthesized in air

Figure 2-31 shows the PLE spectra for Eu-doped SASO under both formulas and for different Eu concentration ($\lambda_{\text{em}} = 611$ nm corresponding to the predominant transition of Eu^{3+}). The CTB in each sample are due to the charge transfer between the completely filled 2p orbitals of O^{2-} and the 5d orbitals of Eu^{3+} . The sharp excitation bands relative to the 4f transitions of Eu^{3+} centred at 362, 384, 393, 411, 463, 532 and 577 nm can be attributed to the $^7\text{F}_0 \rightarrow ^5\text{D}_4$, $^7\text{F}_0 \rightarrow ^5\text{L}_7$, $^7\text{F}_0 \rightarrow ^5\text{L}_0$, $^7\text{F}_0 \rightarrow ^5\text{D}_3$, $^7\text{F}_0 \rightarrow ^5\text{D}_2$, $^7\text{F}_0 \rightarrow ^5\text{D}_1$ and $^7\text{F}_0 \rightarrow ^5\text{D}_0$ transitions, respectively. Similarly, the CTB overlaps with the excitation spectra (located at 310 nm) generated from Eu^{2+} in each samples. The excitation peaks from Eu^{2+} ions in each compound indicate that the presence of ET from Eu^{2+} ions 5d level to the Eu^{3+} ions 4f levels.

As shown in **Figure 2-31**, the main difference between both serials compounds also deals with the intensities of the 4f-4f transitions from Eu^{3+} . The Eu^{3+} excitation band intensity of the $\text{S}_{1-x}\text{Eu}_x\text{Al}_2\text{Si}_2\text{O}_{8+0.5x}$ samples starts to decrease for a concentration beyond 10%, whereas it gradually increases (up to 13%) for the $\text{S}_{1-3x/2}\text{Eu}_x\text{Al}_2\text{Si}_2\text{O}_8$ formula.

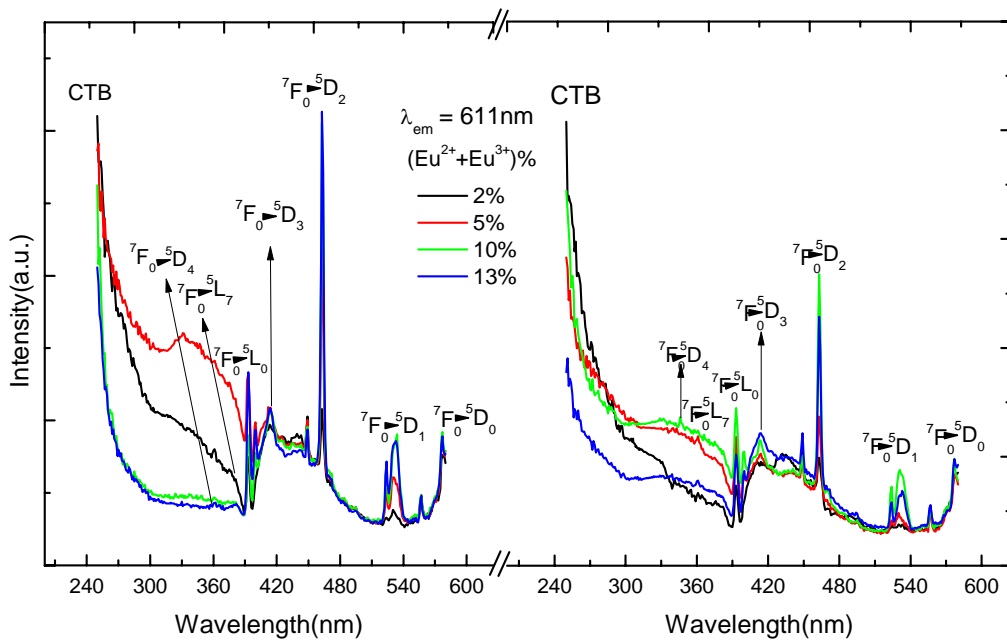


Figure 2-31. Left, excitation spectra of $S_{1-3x/2}ASO:xEu^{3+}$, and right, excitation spectra of $S_{1-x}ASO_{8+0.5x}:xEu^{3+}$ ($x = 2$ to 13%), monitored at 611 nm.

4.2.4. Emission spectra of Eu³⁺ in the SASO:Eu matrix synthesized in air

Figure 2-32 shows the emission spectra ($\lambda_{ex} = 463$ nm, $^5D_0 \rightarrow ^7F_2$, predominant transition of Eu³⁺) of the $S_{1-3x/2}Eu_xAl_2Si_2O_8$ and $S_{1-x}Eu_xAl_2Si_2O_{8+0.5x}$ ($x = 2\%$ to 13%). The insets represent the peaks of the Eu³⁺ transitions from the $^5D_0 \rightarrow ^7F_2$. One can notice that because of the weak intensity of Eu³⁺ emission bands and the background contribution originated from the setup, intensities of all emission bands seem to increase following the wavelength. As we expect, the band positions are the same as in the Eu doped CASO matrix due to the valence electrons of Eu³⁺ are shielded by the 5s and 5p outer electrons and thus, the f-f transitions of Eu³⁺ are weakly affected by the crystal field. The most intense emission is associated with the $^5D_0 \rightarrow ^7F_2$ transition red emission and supposed that Eu³⁺ cations occupy sites with no inversion centre. One can see clearly from the insets of **Figure 2-32**, the quenching of Eu³⁺ emission can be observed for the group of samples under the formula $S_{1-x}Eu_xAl_2Si_2O_{8+0.5x}$. Hence, for the same Eu dopant rate, $S_{1-3x/2}Eu_xAl_2Si_2O_8$ samples contain less Eu³⁺ ions than samples under the other formula because the intensities of the Eu³⁺ emissions continuously increase (no reach of the critical concentration) in $S_{1-3x/2}Eu_xAl_2Si_2O_8$. Consequently, in the opposite, the $S_{1-3x/2}Eu_xAl_2Si_2O_8$ samples would have more Eu²⁺ ions than in the $S_{1-x}Eu_xAl_2Si_2O_{8+0.5x}$ which also can be observed from the **Figure 2-30**.

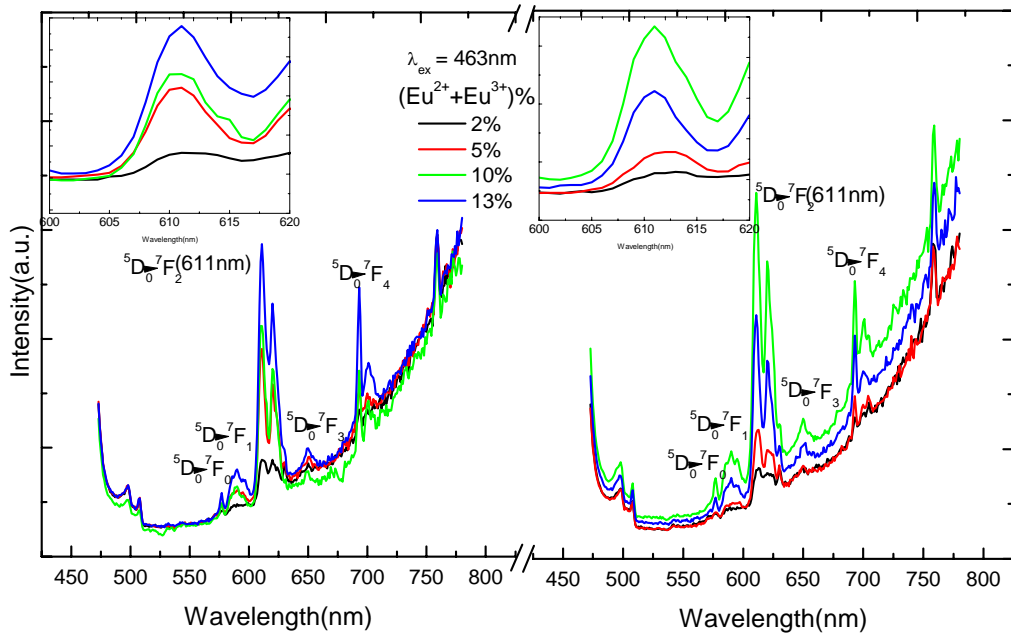


Figure 2-32. Left, emission spectra of $S_{1-3x/2}ASO:xEu^{3+}$, and right, emission spectra of $S_{1-x}ASO_{8+0.5x}:xEu^{3+}$ ($x = 2$ to 13%), excited at 463 nm

Figure 2-33 shows the PL spectra monitored at the charge transfer band ($\lambda_{ex} = 265\text{ nm}$). Due to the lower intensities of Eu³⁺ emission bands in the SASO matrix as compared to the CASO matrix, it is difficult to observe the emission bands originated from Eu³⁺ (the Eu³⁺ emission bands are shown in the inset of the **Figure 2-33**). The CTB decreases for high Eu concentration in the SASO matrix and consequently, the Eu³⁺ emission intensities decrease when monitored at charge transfer band.

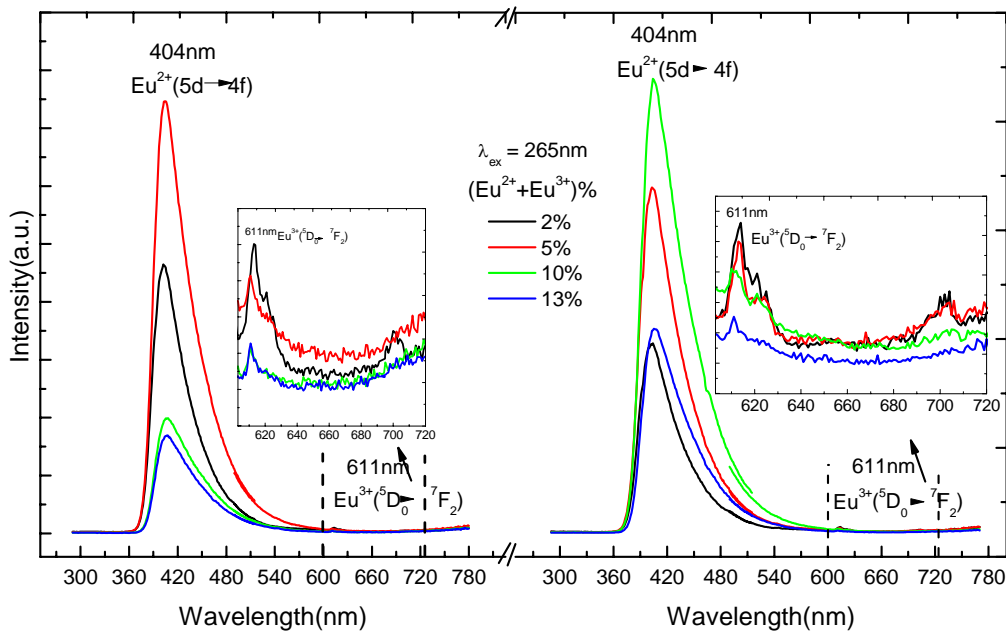


Figure 2-33. Left, emission spectra of $S_{1-3x/2}ASO:xEu^{3+}$, and right, emission spectra of $S_{1-x}ASO_{8+0.5x}:xEu^{3+}$ ($x = 2$ to 0.13%), excited at 265 nm

4.3. BASO:Eu²⁺/(Eu³⁺)

4.3.1. Structural investigation

In an oxidative treatment atmosphere, the barium cation in the BASO structure can be substituted by europium as the same as for CASO and SASO matrixes. The XRD patterns of the samples agree well with ICDD 38-1450, which correspond to a monoclinic BASO. Although Eu²⁺ (and together with little amount of Eu³⁺) substituted for Ba²⁺ sites, there is no significant change in the XRD patterns compared to that of the ICDD card as well as to the simulated XRD patterns. This indicates that the phosphor samples were also well synthesized by the solid-state reaction method. Furthermore, the evolution of the crystal structure parameters following the dopant concentration of Eu is shown in the **Figure 2-34**. The decrease of the parameters are due to the decrease of the ionic radii along the sequence Ba²⁺ > Eu²⁺ > Eu³⁺. Furthermore, **Figure 2-35** shows the X-ray diffraction pattern of a Eu^{2+/3+} (5%) doped $B_{1-3x/2}Al_2Si_2O_8$ compound in the 10-45 2θ range.

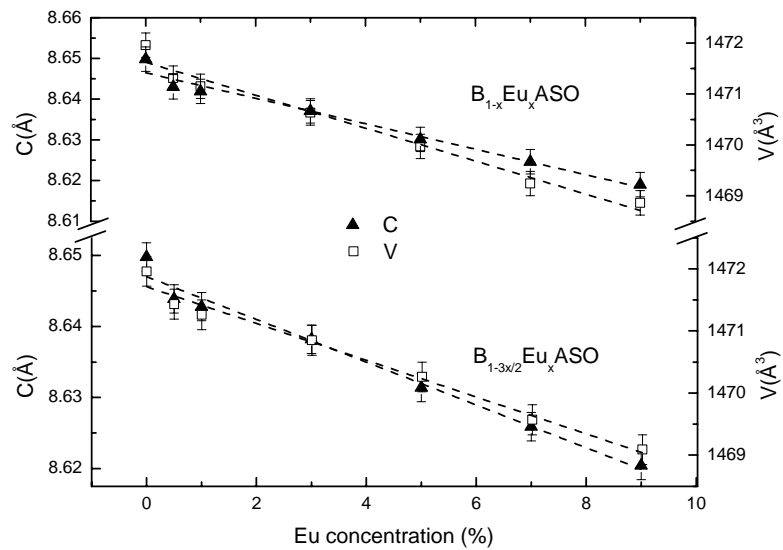


Figure 2-34. $\text{Eu}^{2+}/\text{Eu}^{3+}$ concentration dependence of unit cell for $\text{B}_{1-3x/2}\text{Eu}_x\text{Al}_2\text{Si}_2\text{O}_8$ and $\text{B}_{1-x}\text{Eu}_x\text{Al}_2\text{Si}_2\text{O}_{8+0.5x}$ ($x = 0.5\%$ to 9%)

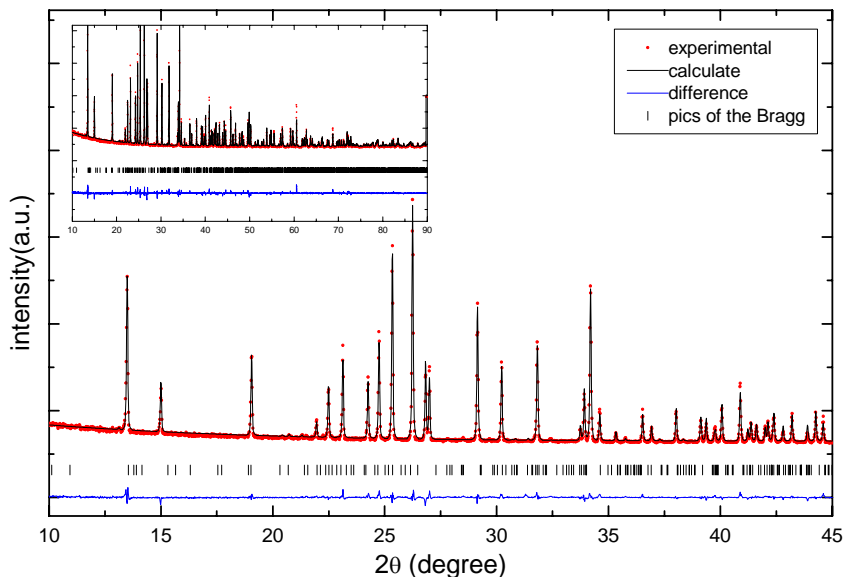


Figure 2-35. Observed, calculated and difference X-ray diffraction patterns of $\text{B}_{1-3x/2}\text{ASO}: x\text{Eu}^{2+/3+}$ ($x = 5\%$) compound in the 10-45 2θ range, inset is given the total pattern

4.3.2. Luminescent properties of BASO:Eu²⁺/(Eu³⁺)

The PLE spectra for the Ba_{1-3x/2}Eu_xAl₂Si₂O₈ and Ba_{1-x}Eu_xAl₂Si₂O_{8+0.5x} samples were also determined, emission wavelength being also settled at 611nm ($^5D_0 \rightarrow ^7F_2$ transition, the predominant transition). However, no excitation bands of Eu³⁺ were observed (thus, the figure is not shown here). This suggests that if Eu³⁺ cations are present, there are in very small amount.

Figure 2-36 shows the photoluminescence emission spectra monitored at $\lambda_{ex} = 393\text{nm}$. No emission bands corresponding to the 4f-4f transition of Eu³⁺ can be observed whereas a broad band relative to Eu²⁺ and located at 440 nm is present in each sample. Interestingly, the transitions of the Eu²⁺ PLE and PL are the same as those obtained when the samples are synthesized in reductive atmosphere. This confirms that almost all the Eu³⁺ ions are transform into the divalent Eu²⁺ state. The same observations can be done from emission spectra at $\lambda_{ex} = 274\text{ nm}$ reported in **Figure 2-37**.

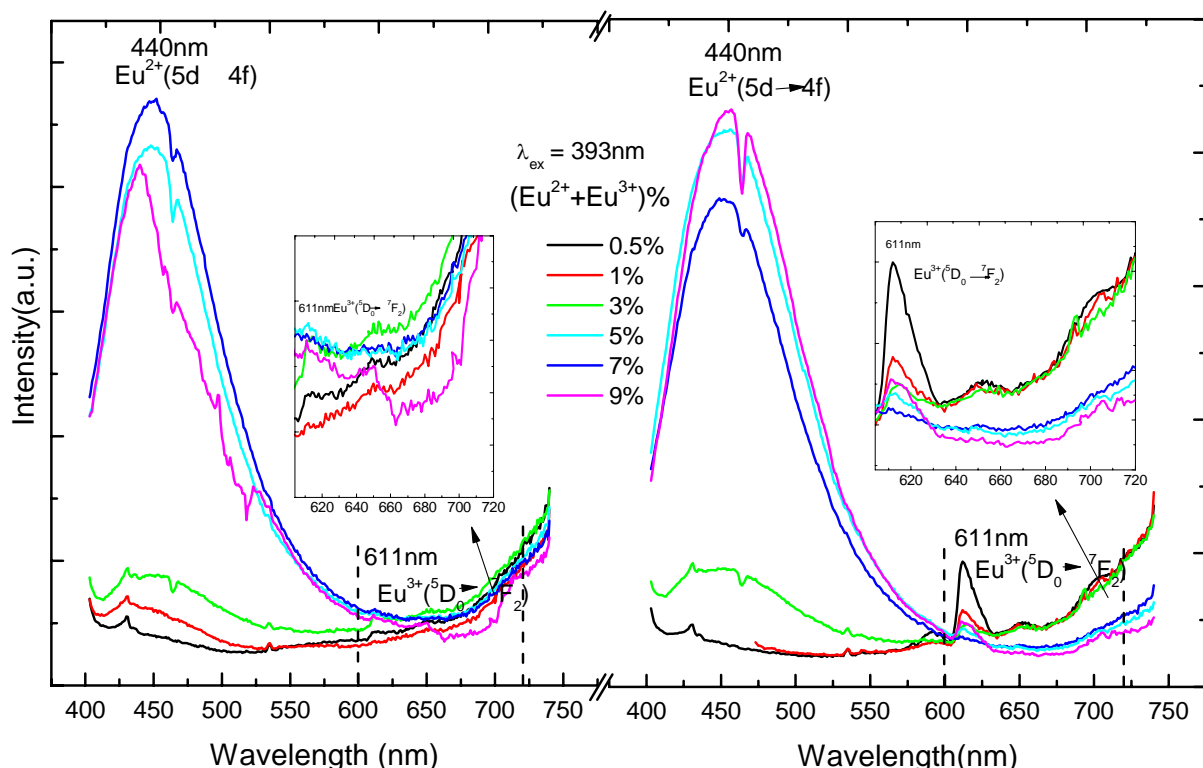


Figure 2-36. Left, emission spectra of $B_{1-3x/2}ASO:xEu^{3+}$, right, emission spectra of $B_{1-x}ASO_{8+0.5x}:xEu^{3+}$ ($x = 0.5$ to 9%), excited at 393 nm, the inset is the enlarged emission band from 600 nm to 720 nm

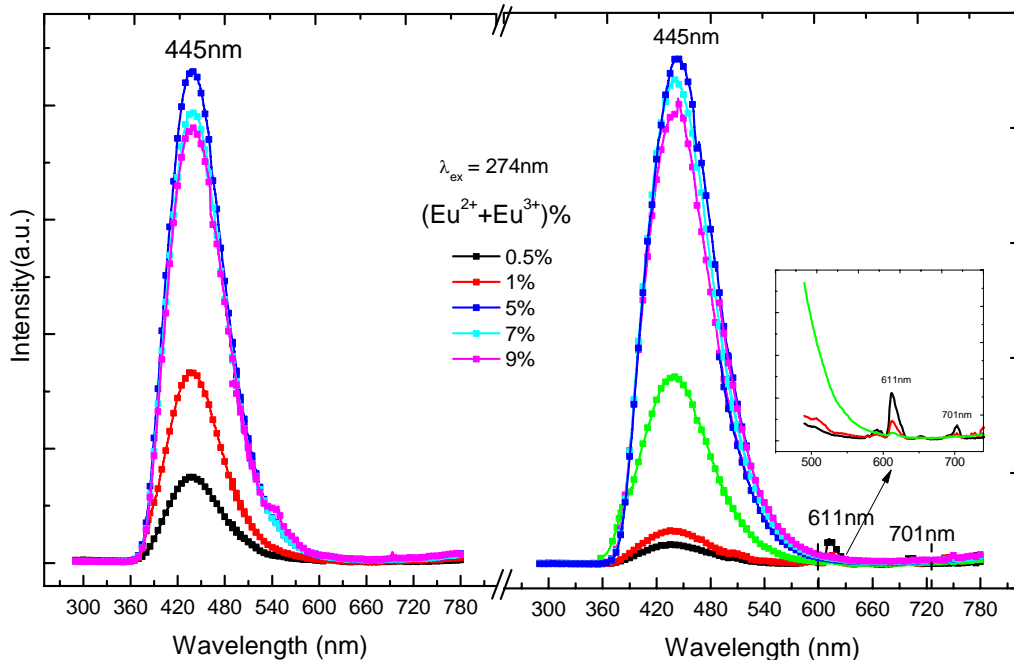


Figure 2-37. Left, emission spectra of $\text{B}_{1-3x/2}\text{ASO}:x\text{Eu}^{3+}$, and right, emission spectra of $\text{B}_{1-x}\text{ASO}:x\text{Eu}^{3+}$ ($x = 0.5$ to 9%), excited at 274 nm

By far, the optical spectra of the materials $\text{M}_{1-3x/2}\text{Al}_2\text{Si}_2\text{O}_8:\text{xEu}^{3+}$ and $\text{M}_{1-x}\text{Al}_2\text{Si}_2\text{O}_{8+0.5x}:\text{xEu}^{3+}$ are all shown in section 4. The former series of compounds considered the creation of cationic vacancies of M^{2+} while the latter supposed additional oxygen ion O^{2-} sited in interstitial sites to respect the charge balance. Nevertheless, it has to be noted that none of the aforementioned formulas would fit with the real compositions of prepared materials in air since Eu^{2+} and Eu^{3+} cations coexist in these compounds and the ratio of Eu^{2+} strongly increases from Ca to Ba host lattices.

5. Stabilization of Eu^{3+} ions higher in CASO and SASO than in BASO

When Eu^{2+} and/or Eu^{3+} are incorporated into the MASO host lattices, the Eu ion could be located, in a first approach, at all cationic sites, i.e. at the AE^{2+} sites but also at the Al^{3+} and Si^{4+} ones. Obviously, on the basis of geometrical reasons (namely size and coordination number), it is impossible for Eu ion to be housed at the Al^{3+} or Si^{4+} tetrahedral sites. As lanthanides have the propensity to migrate towards the AE sites, how can we explain the ability of the MASO materials to stabilize both Eu^{2+} and Eu^{3+} cations when prepared in air?

Commonly, according to investigation on BaAlO₄:Eu [10], NaCaPO₄:Eu [37], etc, four conditions are necessary to favour the abnormal reduction of Eu³⁺ into Eu²⁺ when solids are prepared in non-reducing atmosphere with Eu³⁺ containing precursors. They are listed below [25, 38, 39]:

- 1) no oxidizing ions must be present in the host lattice
- 2) the Eu³⁺ dopant ion has to replace a divalent cation, i.e. alkaline earth ion M²⁺
- 3) the substituted cation is supposed to have a similar radius as that of Eu²⁺ divalent ions
- 4) the host lattice must be appropriate, that is built upon tetrahedral anion groups as BO₄, SiO₄, PO₄, or AlO₄.

In the case of MASO, the four criteria are fulfilled. Therefore, the reduction process of Eu³⁺ changing into Eu²⁺ can happen in the MASO matrixes. For sure, the conversion degree will strongly depend on the nature of the alkaline earth, and in particular the gap in size between the radii of Eu²⁺, Eu³⁺ and M²⁺ cations.

As aforementioned, the emission spectrum associated to Eu³⁺ ions are more and more weak going from CASO to BASO. This result means that the Eu³⁺ ions in the MASO matrix are much more difficult to stabilize for the Ba derivative than the Ca one when synthesized in air. We can explain this trend by considering the radius percentage difference between M²⁺, Eu²⁺ and Eu³⁺. Normally, it is well accepted that a tolerable percentage difference in ion radii between doped and substituted ions must not exceed $\pm 30\%$ [38, 40]. The different percentage can be calculated by the following **Equation (2-2)**:

$$D_r = 100 \times [R_m(CN) - R_d(CN)] / R_m(CN) \quad (2-2)$$

where D_r is the radius percentage difference, CN stands for the coordination number, $R_m(CN)$ is the radius of the host cation (M²⁺) and the $R_d(CN)$ is the radius of dopant ion (Eu²⁺ and Eu³⁺). The calculations of the radius percentage difference between the doped ions and the possible substituted ions in MASO matrix are summarized in **Table 2-4**.

Table 2-4. Ionic radii D_r between the doped and the substituted ions

Dopant ions	$R_d(\text{CN})$	$D_r = 100 \times [R_m(\text{CN}) - R_d(\text{CN})] / R_m(\text{CN})$ (%)			
		Ca^{2+} (1.00(6))	Ca^{2+} (1.06(7))	Sr^{2+} (1.31(9))	Ba^{2+} (1.47(9))
Eu^{3+}	0.947(6)	5.3%			
	1.01(7)		4.72%		
	1.12(9)			14.50%	23.81%
Eu^{2+}	1.17(6)	-17%			
	1.20(7)		-13.21%		
	1.30(9)			0.76%	11.56%

From horizontal comparison from Ca to Ba, the radius percentage differences between the M^{2+} and Eu^{3+} significantly increase from approximately 5% (Ca^{2+} - Eu^{3+}) to 24% (Ba^{2+} - Eu^{3+}), a value close to the 30% limit. This is sufficient to explain why the trivalent state of europium is much more difficult to stabilize in BASO than in SASO or CASO. Furthermore, the radius percentage differences between the M^{2+} and Eu^{2+} are all far away below the limit especially for the SASO matrix (0.76% compared to 30%). This suggests that Eu^{2+} are, *a priori*, stable in the three MASO materials. However, from vertical comparison for SASO matrix, owing to the radius percentage differences between the Sr^{2+} and Eu^{3+} which is also not very high (14.50%), we can indicate that a considerable amount of Eu^{3+} ions can exist in the matrix. As for the CASO matrix both for the two different crystallographic sites ($\text{CN} = 6$ and 7), we can induce that there would be much more amount of Eu^{3+} ions in this matrix due to the radius percentage different value for Ca^{2+} - Eu^{3+} which is much smaller than the value of Ca^{2+} - Eu^{2+} . Oppositely, for BASO matrix, almost all the Eu^{3+} ions are likely to transform to Eu^{2+} due to the same reason. Based on above facts, we can understand the change in optical properties (ration $\text{Eu}^{2+}/\text{Eu}^{3+}$) in the MASO series going from Ca to Ba.

6. The Eu³⁺ to Eu²⁺ reduction mechanism in MASO (M = Ca to Ba) host lattice and the ET from Eu²⁺ to Eu³⁺

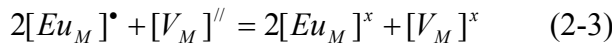
6.1. The mechanism of the abnormal reduction of Eu³⁺ to Eu²⁺ in MASO

Commonly, it is well accepted within the community that the stabilization of Eu²⁺ cations is triggered in reducing conditions, while Eu³⁺ cations are naturally stabilized in air or in pure oxygen. From this postulate, the reciprocal is often deduced, that synthesis in air will conduct systematically to the stabilization of Eu³⁺ cations only, while the use of Ar/H₂ atmosphere will lead to the systematic reduction of Eu³⁺ into Eu²⁺. In fact, such assertions have to be modulated as discussed below. In this section, we will try to determine the mechanism about the “abnormal” reduction of Eu³⁺ to Eu²⁺ occurring in the MASO host lattice when synthesised in air condition with Eu³⁺ containing precursors as Eu₂O₃. We do here the hypothesis that Eu³⁺ cations are first inserted in the host lattice, and that the latter reorganizes its composition to favour the appearance of Eu²⁺ ions.

In principle, the reduction of Eu³⁺ cations into Eu²⁺ ones require electron transfers from chemical elements of the host lattice towards the rare earth. In the MASO matrixes, no element can be reduced. Thus, we may wonder where the electrons come from and how they are transferred to the doped Eu³⁺ ions in the MASO matrix. From a chemistry point of view, when dopant is inserted in place of alkaline earth elements under the divalent state (Eu²⁺), overall charge compensation in the MASO lattice is fulfilled by a one to one substitution (M²⁺-Eu²⁺). In contrast, for Eu³⁺ cations at the M²⁺ sites, charge compensation requires changing in composition of the host lattice, which is appearance of cationic vacancies or oxygen atoms at interstitial sites. These two types of charge rearrangements can be schematized as followed:



Let consider the former case that we privileged. One alkaline earth vacancy defect V_M^{II} with two negative charges is generated as well as two substituting defects with a net +1 charge. In some extent, we can regard one vacancy V_M^{II} (with two negative charges) as an electron donor and similarly, the two positive Eu_M^{\bullet} defects as electron acceptors. As a result, under thermal stimulus, the negative charges of the vacancy defects of V_M^{II} would be transferred to the Eu^{3+} sites and would reduce them to the divalent state of Eu^{2+} . The whole process can be expressed by the following **Equation (2-3)**:



By considering this model, highly used in the glass community [41], we can suppose that if more V_M^{II} are created, more Eu^{3+} ions will be present, and higher will be their propensity to be reduced into the divalent state (Eu^{2+}). Based on this postulate, more vacancies (V_M^{II}) are created in $\text{M}_{1-3x/2}\text{Eu}_x\text{Al}_2\text{Si}_2\text{O}_8$ than in $\text{M}_{1-x}\text{Eu}_x\text{Al}_2\text{Si}_2\text{O}_{8+0.5x}$ for identical Eu dopant concentrations. Consequently, more Eu^{2+} cations are expected to be stabilized in $\text{M}_{1-3x/2}\text{Eu}_x\text{Al}_2\text{Si}_2\text{O}_8$ than in $\text{M}_{1-x}\text{Eu}_x\text{Al}_2\text{Si}_2\text{O}_{8+0.5x}$ at a given Eu concentration which are in good agreement with the observations (see **Figures 2-21** and **2-30**).

To confirm the hypothesis that an increase of V_M^{II} in the host lattice would facilitate the reduction of Eu^{3+} to Eu^{2+} , we prepared a series of materials with different codopants in the CASO series and analyse their optical properties. The chosen co-dopants were K^+ , La^{3+} and Zr^{4+} . Materials were prepared in the same conditions as reported for CASO: $\text{Eu}^{2+}/\text{Eu}^{3+}$. The used precursors were K_2CO_3 (Aldrich, 99.9%), La_2O_3 (S.M, 99.9%), and ZrO_2 (Ventron, 99.9%), for K, La and Zr, respectively. In that context, we prepared $\text{Ca}_{0.90}\text{Eu}_{0.05}\text{K}_{0.05}\text{Al}_2\text{Si}_2\text{O}_8$ (0 $V_{\text{Ca}}^{\text{II}}$ per Eu atom), $\text{Ca}_{0.85}\text{Eu}_{0.05}\text{La}_{0.05}\text{Al}_2\text{Si}_2\text{O}_8$ (1 $V_{\text{Ca}}^{\text{II}}$ per Eu atom), $\text{Ca}_{0.825}\text{Eu}_{0.05}\text{Zr}_{0.05}\text{Al}_2\text{Si}_2\text{O}_8$ (1.5 $V_{\text{Ca}}^{\text{II}}$ per Eu atom) compounds that we compared with $\text{Ca}_{0.925}\text{Eu}_{0.05}\text{Al}_2\text{Si}_2\text{O}_8$ (0.5 $V_{\text{Ca}}^{\text{II}}$ per Eu atom). As $r(\text{K}^+) = 1.37 \text{ \AA}$ when $CN = 6$ and 1.38 \AA when $CN = 7$, $r(\text{La}^{3+}) = 1.032 \text{ \AA}$ when $CN = 6$ and 1.10 \AA when $CN = 7$, $r(\text{Zr}^{4+}) = 0.72 \text{ \AA}$ when $CN = 6$ and 0.78 \AA when $CN = 7$, all these ions are more likely to replace the Ca^{2+} ions in the CASO matrix for steric reason as usual. **Figure 2-38** displays the photoluminescence spectra of the

four materials ($\lambda_{\text{ex}} = 393 \text{ nm}$) while **Table 2-5** reports informations related to the nature of the substitution and the intensity ratio between Eu²⁺ and Eu³⁺. In this table R is defined as the ratio of the number of effective electrons on negative defects (total negative net charge on defects) and the number of expected Eu³⁺ ions to be reduced.

Table 2-5. Evolution of the Eu²⁺/Eu³⁺ ratio versus the number of V_{Ca} vacancies per Eu in $\text{Ca}_{0.90}\text{Eu}_{0.05}\text{K}_{0.05}\text{Al}_2\text{Si}_2\text{O}_8$, $\text{Ca}_{0.925}\text{Eu}_{0.05}\text{Al}_2\text{Si}_2\text{O}_8$, $\text{Ca}_{0.85}\text{Eu}_{0.05}\text{La}_{0.05}\text{Al}_2\text{Si}_2\text{O}_8$, $\text{Ca}_{0.825}\text{Eu}_{0.05}\text{Zr}_{0.05}\text{Al}_2\text{Si}_2\text{O}_8$ materials

Substitution reaction	Positive defect	Negative defect	$R^{(*)}$	$I(\text{Eu}^{2+}/\text{Eu}^{3+})^{(*)}$
$2 \text{Ca}^{2+} \rightarrow \text{Eu}^{3+} + \text{K}^+ (0 V_{\text{Ca}}^{\parallel}/\text{Eu})$	$[\text{Eu}_{\text{Ca}}]^\bullet$	$[\text{K}_{\text{Ca}}]'$	$\leq 1/1=1$	0.216
$3\text{Ca}^{2+} \rightarrow 2\text{Eu}^{3+} + \text{V}_{\text{Ca}} (0.5 V_{\text{Ca}}^{\parallel}/\text{Eu})$	$2[\text{Eu}_{\text{Ca}}]^\bullet$	$[\text{V}_{\text{Ca}}]^{\parallel}$	$2/2=1$	0.287
$3\text{Ca}^{2+} \rightarrow \text{Eu}^{3+} + \text{La}^{3+} + \text{V}_{\text{Ca}} (1 V_{\text{Ca}}^{\parallel}/\text{Eu})$	$[\text{Eu}_{\text{Ca}}]^\bullet$ $[\text{La}_{\text{Ca}}]^\bullet$	$[\text{V}_{\text{Ca}}]^{\parallel}$	$2/1=2$	0.374
$7\text{Ca}^{2+} \rightarrow 2\text{Eu}^{3+} + 2\text{Zr}^{4+} + 3\text{V}_{\text{Ca}} (1.5 V_{\text{Ca}}^{\parallel}/\text{Eu})$	$2[\text{Eu}_{\text{Ca}}]^\bullet$ $2[\text{Zr}_{\text{Ca}}]^{..}$	$3[\text{V}_{\text{Ca}}]^{\parallel}$	$6/2=3$	0.8995

(*) R is ratio of the number of effective electrons on negative defects and the number of Eu³⁺ ions to be reduced and

b is the intensity ratio between Eu²⁺ and Eu³⁺ ($I_{\text{Eu}^{2+}}^{\max}/I_{\text{Eu}^{3+}}^{\max}$)

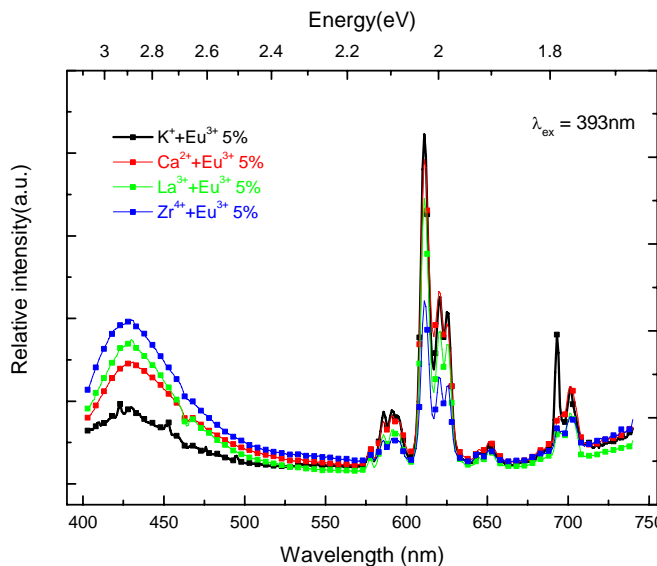


Figure 2-38. Emission spectra of co-doped samples of CASO: 0.05Eu³⁺, 0.05Mⁿ⁺ from which the $I(\text{Eu}^{2+}/\text{Eu}^{3+})$ in Table 2-5 was calculated, monitored at $\lambda_{\text{ex}} = 393\text{nm}$

From **Figure 2-38**, it appears obvious that the intensity of the Eu^{2+} -5d \rightarrow 4f transition increases along the $\text{K} < \text{Ca} < \text{La} < \text{Zr}$ sequence. At the opposite, the inverse trend is observed for the evolution of the intensity of the Eu^{3+} -4f \rightarrow 4f transitions. Thus, according to the results reported in **Table 2-5**, the increase of R favors the reduction of Eu^{3+} into Eu^{2+} . Namely, following the sequence $\text{K}^+ < \text{Ca}^{2+} < \text{La}^{3+} < \text{Zr}^{4+}$, the ratio of initial Eu^{3+} ions which undergoes a reduction increases.

Furthermore, the PLE and PL spectra of these four samples were also monitored at $\lambda_{\text{em}} = 420$ and $\lambda_{\text{ex}} = 320$ (typical optical values for the allowed transitions of Eu^{2+} doped in CASO matrix) as shown in **Figure 2-39**. For a fix dopant rate ($x = 5\%$), the intensity of Eu^{2+} excitation and emission increases when more vacancies are created. The above results further confirm that the higher the charge of the codopant, the more alkaline earth vacancies, the higher the degree of reductibility of Eu^{3+} cations, and the higher the $\text{Eu}^{2+}/\text{Eu}^{3+}$ ratio.

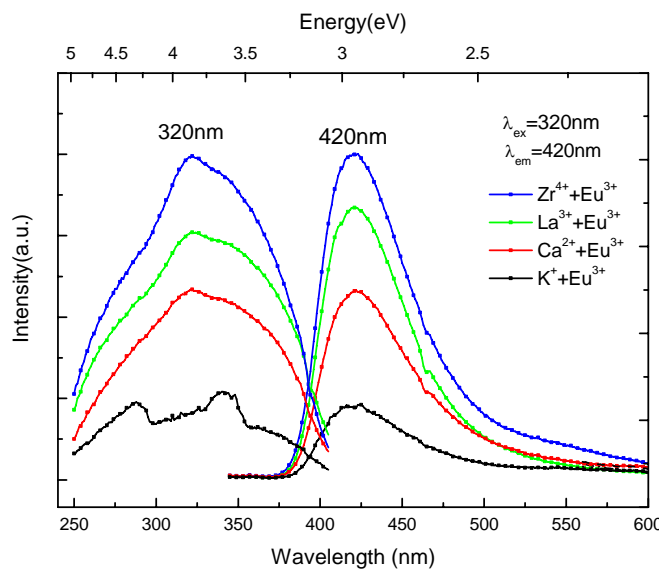


Figure 2-39. Excitation and emission spectra of the four codoped samples monitored at $\lambda_{\text{ex}} = 320$ and $\lambda_{\text{em}} = 420$ nm

At this stage based on the optical properties, we may wonder what is the electronic factor governing this phenomenon. As aforementioned, there are V_M^{\parallel} defects in the $\text{M}_{1-3x/2}\text{Eu}_x\text{Al}_2\text{Si}_2\text{O}_8$. This defect is made up of AE vacancies, which are void surrounded by oxygen ions (**Figure 2-40**). Of course, for electrostatic reasons, we may expect that this negatively charged defect will be located in the neighborhood of Eu^{3+} cations, considered as positively charged defects. Namely, V_M^{\parallel} will induce localized energy levels located between

the valence band and the conduction band of the CASO host lattice. *A priori*, these donor levels are built upon O orbitals (lone pairs) pointing towards the vacancy and are thus expected to be positioned just above the valence band. The higher the $V_M^{\parallel\parallel}$ concentration, the more disperse the defect band, and the higher the capacity of the materials to reduce Eu^{3+} cations into Eu^{2+} ones. This phenomenon is schematized in **Figure 2-41**.

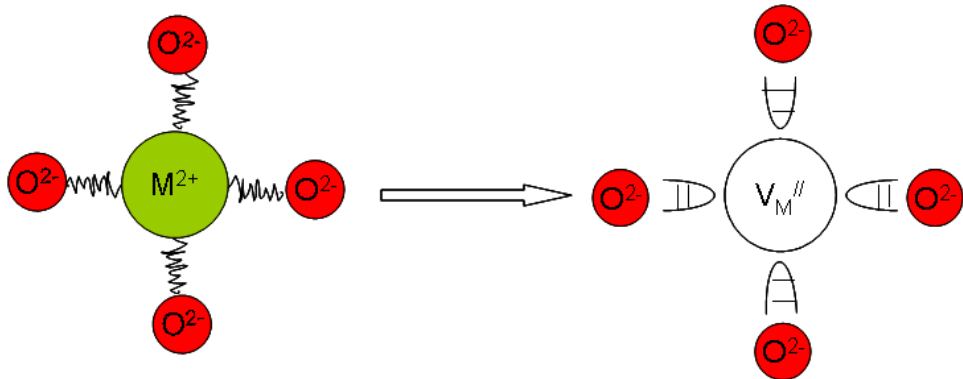


Figure 2-40. Schematic diagram of the environments around the M^{2+} in CASO matrix before and after doping Eu^{3+} ions (\subset stands for the lone pair pointing towards the vacancy)

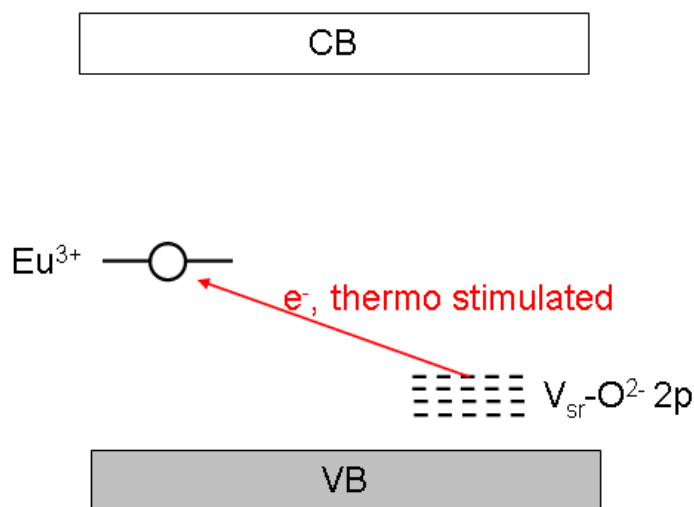


Figure 2-41. Mechanism proposed in the present work for abnormal reduction of Eu^{3+} to Eu^{2+} in the MASO matrix

Let notice here that depletion of the V_M^{\parallel} levels at the benefit of the appearance of Eu^{2+} may be temperature dependant. Namely, we may envision a thermo stimulated phenomenon which favours the hoping of an electron from the vacancy towards a Eu^{3+} site.

To confirm this hypothesis, we also measured the emission intensities generated from Eu^{2+} and Eu^{3+} in the $\text{C}_{1-3x/2}\text{Eu}_x\text{Al}_2\text{Si}_2\text{O}_8$ ($x = 13\%$) under different temperatures, respectively. As one can clearly see **Figure 2-42**, the emission intensities from the Eu^{3+} decreases when the temperature increases while the emission intensities associated with Eu^{2+} cations is enhanced. Obviously, this phenomenon can be explained by changing in the different amount of Eu^{2+} and Eu^{3+} ions in the $\text{C}_{1-3x/2}\text{Eu}_x\text{Al}_2\text{Si}_2\text{O}_8$ ($x = 13\%$) following the temperature.

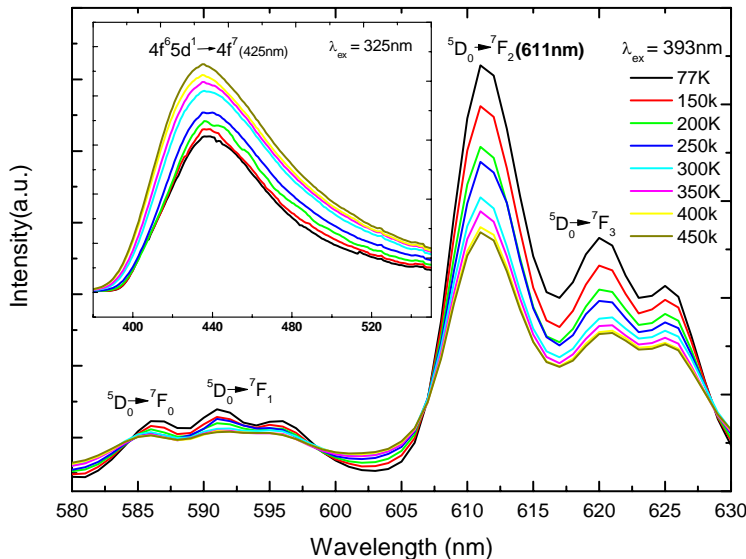


Figure 2-42. Temperature dependence of emission spectra for $\text{C}_{1-3x/2}\text{Eu}_x\text{ASO}$ ($x = 13\%$) sample under $\lambda_{\text{ex}} = 393 \text{ nm}$. The inset shows the relative intensity of the same sample under $\lambda_{\text{ex}} = 325 \text{ nm}$

6.2. The mechanism of ET from Eu^{2+} to Eu^{3+} in the MASO

Based on above experimental results, the energy level diagram of the Eu^{2+} and Eu^{3+} ions and its possible pathway for the ET from the Eu^{2+} to Eu^{3+} ions are schematically drawn in **Figure 2-43**. In this study, we measured the fluorescence properties of the Eu^{3+} corresponding to the transitions from the lowest excited ${}^5\text{D}_0$ level to ${}^7\text{F}_j$ levels under the excitation corresponding to the ${}^7\text{F}_0 \rightarrow {}^5\text{D}_2$ transition. As previously observed, the fluorescence is

associated with the non-radiative relaxation of the excited Eu³⁺ ion in the higher excited states to the ⁵D₀ level and the radiative transition into the ground ⁷F_j levels. Moreover, with the co-existence of Eu²⁺, as one can see **Figure 2-43**, the emission spectra of the Eu²⁺ (4f⁶5d¹ (e_g) → 4f⁷) is overlapped with the excitation spectra of Eu³⁺ (⁷F_j → ⁵D₄, ⁵D₃ till ⁵D₀). Thus, the ET from Eu²⁺ to Eu³⁺ is considered as follows: the excited Eu²⁺ in the 4f⁶5d¹ (e_g) level partly radiatively relaxes to the ground state ⁸S_{7/2}, and the rest part of the energy causes the excitation of Eu³⁺ ion.

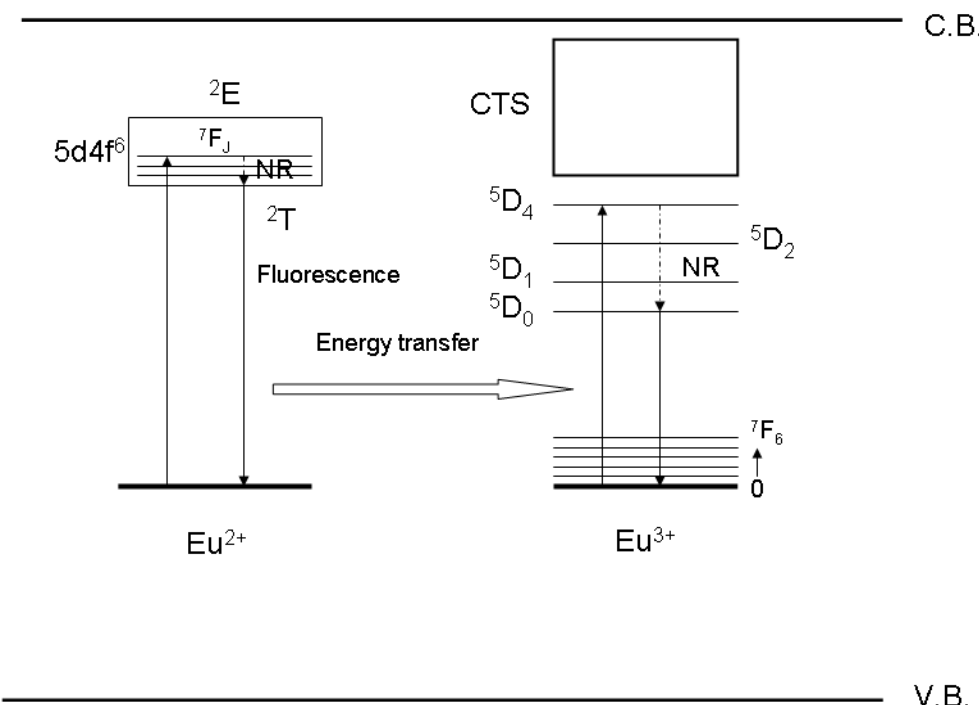


Figure 2-43. A schematic diagram of the induced luminescence from CASO resulting from radiative energy transfer from Eu²⁺ to Eu³⁺

So far, I propose in this study the existence of Eu²⁺ → Eu³⁺ ET. Do this ET really exist or is there excitation of both Eu³⁺ and Eu²⁺ cations at specific wavelengths when f → f and 4d → 5f transitions are observed? ET can only occur if there is overlap between the emission spectrum of the sensitizer (here Eu²⁺) and the excitation spectrum of the activator (here Eu³⁺) [21, 28, 29]. Such a condition is respected for CASO and SASO as depicted in **Figures 2-44** and **2-45**. For BASO, we didn't detect the presence of Eu³⁺ cations (see above). Consequently, ET should occur via multipole interactions. Do we have proofs of such transfers? **Figure 2-44a** represents the excitation spectra for Eu doped CASO prepared in air and in 5% Ar/H₂, respectively. The emission of Eu²⁺ cations only at around 425 nm is triggered by excitation of

CASO:Eu at 287 and 320 nm. Clearly, the excitation spectrum of CASO:Eu^{2+/3+} monitored at 611 nm, i.e. a characteristic lines of Eu³⁺ 4f-4f transitions, evidences a peak at 320 nm. Consequently, we can conclude that we can induce emission of Eu³⁺ via the excitation of Eu²⁺, what imply ET from Eu²⁺ cations towards Eu³⁺ ones. This is also asserted via the collect of the excitation spectrum of CASO:Eu prepared in reducing atmosphere (containing slight amount of Eu³⁺ cations) when monitored at 611 nm. For SASO:Eu, the same reasoning can be applied (see **Figure 2-45a**). Another indication of Eu^{2+ → Eu³⁺ transfers in CASO and SASO concerns the evolution of the emission spectra monitored at 393 nm for CASO:Eu^{2+/3+} and SASO:Eu^{2+/3+} (**Figures 2-46** and **2-47** respectively) where the Eu²⁺-4d → 5f transitions decrease at the benefit Eu³⁺-4f → 4f transitions when Eu concentration increases. At the end, the variation of the decay times collected for CASO:Eu^{2+/3+} samples agree with ET.}

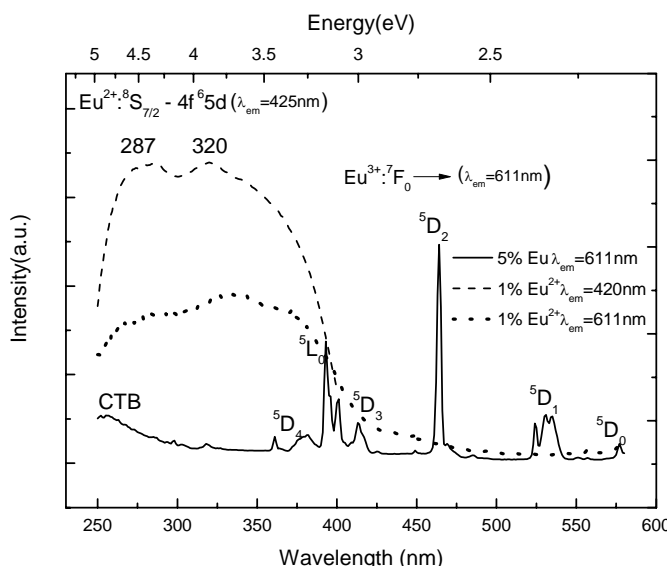


Figure 2-44a. Excitation spectra $\text{C}_{1-3x}/2\text{ASO}:x\text{Eu}^{3+}$ ($x = 0.05$) of the A (Eu^{3+}) emission (monitored at $\lambda_{em} = 611 \text{ nm}$, solid line), which include the S (Eu^{2+}) absorption (located at $\sim 320 \text{ nm}$) and A absorption bands. The dotted line (excitation spectra monitored at $\lambda_{em} = 425 \text{ nm}$ of the sample $\text{C}_{1-x}\text{Eu}_x\text{ASO}$, $x = 0.01$) and dashed line (excitation spectra monitored at $\lambda_{em} = 611 \text{ nm}$ of the same sample $\text{C}_{1-x}\text{Eu}_x\text{ASO}$, $x = 0.01$) are also shown for comparison

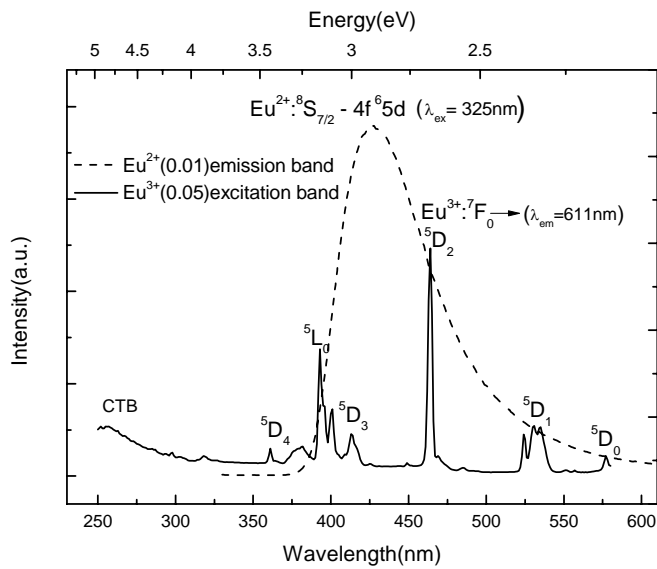


Figure 2-44b. Overlap of Eu²⁺ luminescence spectrum ($\lambda_{ex} = 320\text{nm}$) with Eu³⁺ excitation spectrum for CASO matrix as-prepared Eu-doped samples under formula $C_{1-3x/2}\text{ASO}:xEu^{3+}$ ($x = 0.05$) and $C_{1-x}\text{ASO}:xEu^{2+}$ ($x = 0.01$)

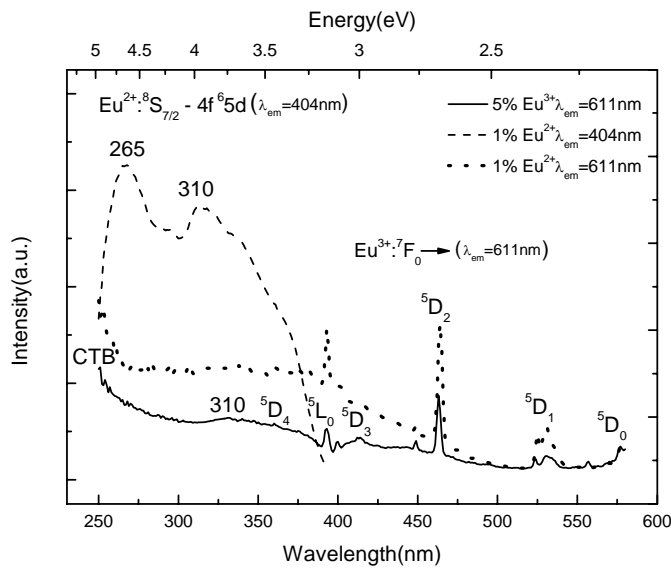


Figure 2-45a. Excitation spectra ($S_{1-3x/2}\text{ASO}:xEu^{3+}$ ($x = 0.05$)) of the A (Eu³⁺) emission (monitored at $\lambda_{em} = 611\text{ nm}$, solid line), which include the S (Eu²⁺) absorption (located at $\sim 310\text{ nm}$) and A absorption bands. The dotted line (excitation spectra monitored at $\lambda_{em} = 404\text{ nm}$ of the $S_{1-x}\text{Eu}_x\text{ASO}$, $x = 0.01$) and dashed line (excitation spectra monitored at $\lambda_{em} = 611\text{ nm}$ of the $S_{1-x}\text{Eu}_x\text{ASO}$, $x = 0.01$) are also shown for comparison

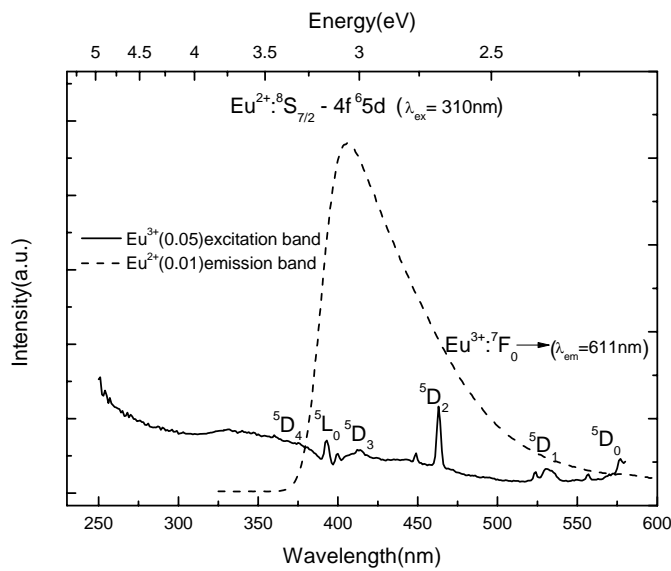


Figure 2-45b. Overlap of Eu^{2+} luminescence spectrum ($\lambda_{\text{ex}} = 310\text{nm}$) with Eu^{3+} excitation spectrum for SASO matrix as-prepared Eu-doped samples under formula $\text{S}_{1-3x/2}\text{ASO}:x\text{Eu}^{3+}$ ($x = 0.05$) and $\text{S}_{1-x}\text{ASO}:x\text{Eu}^{2+}$ ($x = 0.01$)

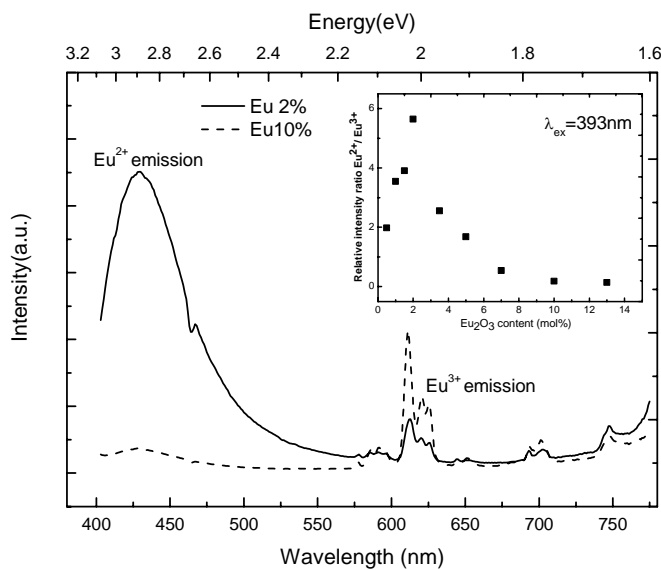


Figure 2-46. Evolution of the luminescence spectra ($\lambda_{\text{ex}} = 393\text{nm}$) on Eu concentration, samples under the formula $\text{C}_{1-3x/2}\text{ASO}:x\text{Eu}^{3+}$ ($x = 0.005$ to 0.13). In inset, the intensity ratio $\text{Eu}^{2+}/\text{Eu}^{3+}$ as a function of Eu_2O_3 content

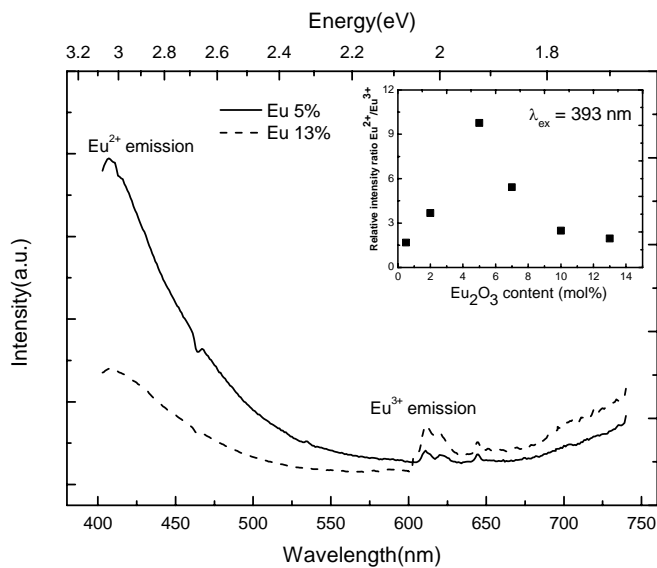


Figure 2-47. Evolution of the luminescence spectra ($\lambda_{\text{ex}} = 393\text{nm}$) on Eu concentration, samples under the formula $S_{1-3x/2}\text{ASO}:xEu^{3+}$ ($x = 0.005$ to 0.13). In inset, the intensity ratio $\text{Eu}^{2+}/\text{Eu}^{3+}$ as a function of Eu_2O_3 content

The room-temperature decay curves are shown in **Figure 2-48** for x ranging from 0.5% to 13%. In contrast to CASO:Eu²⁺ prepared in reducing atmosphere (see Figure 2-8) where lifetime remains constant whatever the Eu concentrations, we notice here a decrease of τ from 0.65 μs to 0.26 μs going from $\text{Ca}_{0.9925}\text{Eu}_{0.0050}\text{Al}_2\text{Si}_2\text{O}_8$ to $\text{Ca}_{0.805}\text{Eu}_{0.13}\text{Al}_2\text{Si}_2\text{O}_8$. Again this suggests some ET from Eu²⁺ to Eu³⁺. The same observation can be done for $\text{C}_{1-x}\text{Eu}_x\text{ASO}_{8+0.5x}:xEu$ compositions (see **Figure 2-48** and **Table 2-6**).

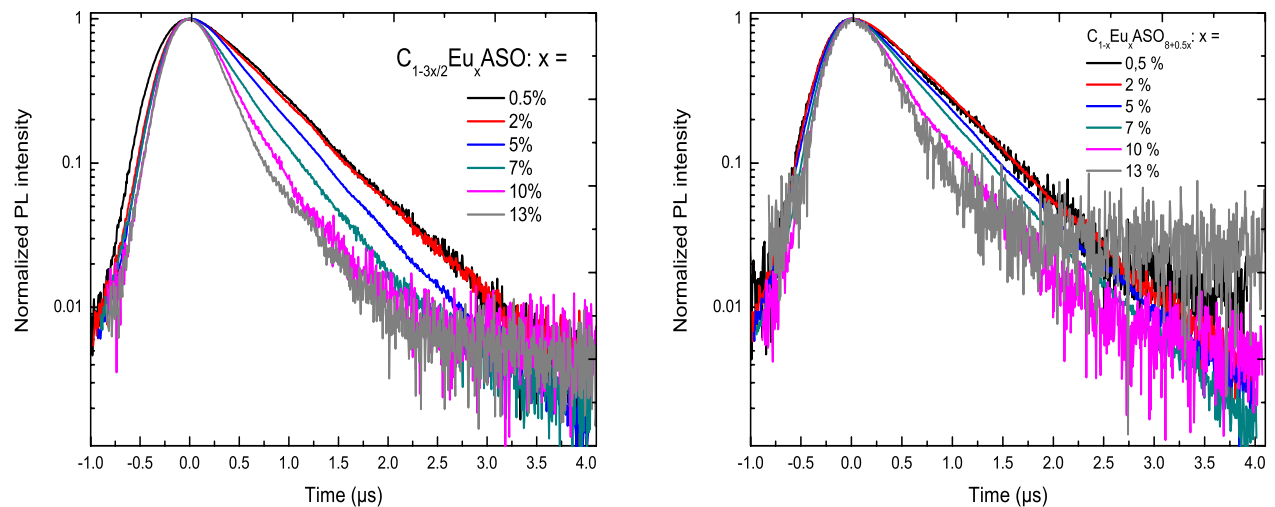


Figure 2-48. $4f^65d$ emission decay curve acquired at room temperature for $\text{C}_{1-3x/2}\text{Eu}_x\text{ASO}$ and $\text{C}_{1-x}\text{Eu}_x\text{ASO}_{8+0.5x}$ ($x = 0.5\%$ to 0.13%), monitored the emission at 420nm and with excitation at 400nm (data collected on $I = I_0 \exp(-t / \tau)$)

Table 2-6. Lifetimes of the emission decay of Eu^{2+} (monitored at 420nm) in the two groups of samples

Eu concentration	$\text{C}_{1-x}\text{Eu}_x\text{ASO}_{8+0.5x}$	$\text{C}_{1-3x/2}\text{Eu}_x\text{ASO}$
0.5%	$0.65\ \mu\text{s}$	$0.65\ \mu\text{s}$
2%	$0.64\ \mu\text{s}$	$0.64\ \mu\text{s}$
5%	$0.52\ \mu\text{s}$	$0.58\ \mu\text{s}$
7%	$0.42\ \mu\text{s}$	$0.53\ \mu\text{s}$
10%	$0.32\ \mu\text{s}$	$0.40\ \mu\text{s}$
13%	$0.26\ \mu\text{s}$	$0.29\ \mu\text{s}$

Generally, the ET efficiency from a sensitizer (Eu^{2+}) to activator (Eu^{3+}) can be expressed by the following **Equation (2-4)** [21, 32, 42, 43]:

$$\eta_T = 1 - \frac{I_S}{I_{S0}} \approx 1 - \frac{\tau_s}{\tau_{s0}} \quad (2-4)$$

where τ_s and τ_{s0} are the decay lifetimes of the sensitizer (Eu^{2+}) in the presence and absence of the activator (Eu^{3+}), respectively. Here, τ_{s0} is the intrinsic decay time of Eu^{2+} emission when

CASO is only doped by Eu²⁺, namely 0.65 μs. τ_s is the decay time of the sensitizer (Eu²⁺) in the presence of an activator (Eu³⁺), i.e. the decay time of Eu²⁺ of samples prepared in air. The collected values are shown in **Table 2-6**. Thus, the ET efficiency of Eu²⁺-Eu³⁺ in CASO host lattice is calculated for the samples under the different formulas (**Figure 2-49**). The η_T increases gradually with Eu concentration. Moreover, η_T is systematically higher for C_{1-3x/2}Eu_xAl₂Si₂O₈ than C_{1-x}Eu_xAl₂Si₂O_{8+0.5x} for a given x value.

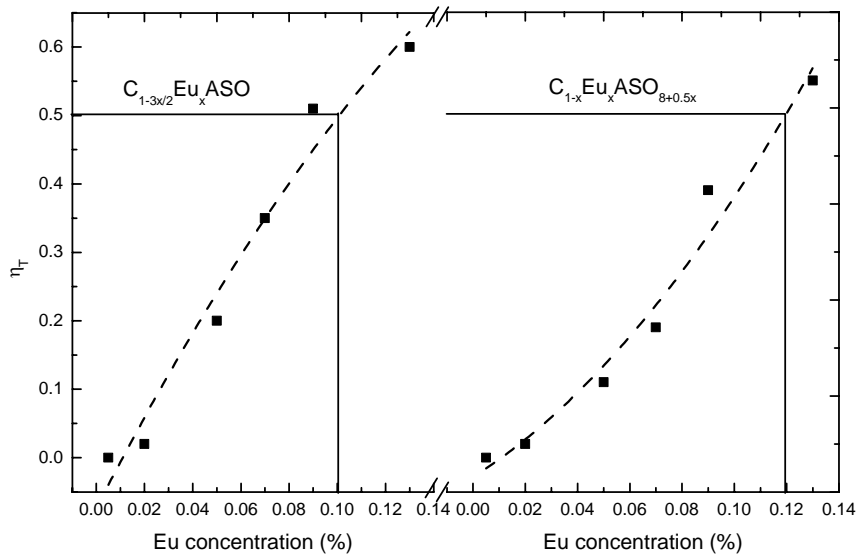


Figure 2-49. ET efficiency for Eu²⁺ to Eu³⁺ under the formula C_{1-3x/2}Eu_xASO (left) and C_{1-x}Eu_xASO_{8+0.5x} (right), x = 0.5% to 13%

As suggested by Blasse [28, 42, 43], the average separation $R(\text{Eu}^{2+}-\text{Eu}^{3+})$ can be expressed by **Equation (2-1)**, Where R corresponds to the mean separation between the nearest Eu²⁺ and Eu³⁺ ions at the critical concentration, x is the total concentration of Eu²⁺ and Eu³⁺. Thus, $R(\text{Eu}^{2+}-\text{Eu}^{3+})$ (in Å) were determined to be 40.00, 25.20, 18.57, 16.60, 14.74 and 13.50 corresponding to x = 0.005, 0.02, 0.05, 0.07, 0.1 and 0.13, respectively, in both of the two group of samples. Moreover, as one can see in **Figure 2-49**, the critical concentrations at which the ET efficiency fixed at 0.5 [29] are about 0.102 and 0.120 under the formula C_{1-3x/2}Eu_xAl₂Si₂O₈ and C_{1-x}Eu_xAl₂Si₂O_{8+0.5x}, respectively. Thus, if we define that the critical concentration x_c are the concentration at while η_T equal 0.5, the critical distance (R_c) of the ET is calculated to be about 14.64Å and 13.87Å for C_{1-3x/2}Eu_xAl₂Si₂O₈ and C_{1-x}Eu_xAl₂Si₂O_{8+0.5x}, respectively.

The resonant ET mechanism may consist of two types: 1) exchange interaction and 2) multipolar interaction. It is known that if ET belongs to the exchange interaction, the critical distance between the sensitizer and activator should be shorter than $\sim 5 \text{ \AA}$ [5, 30]. In our case, the critical distance between Eu^{2+} and Eu^{3+} are 14.64 and 13.87 \AA under the two different formulas, respectively. Therefore, the ET mechanism should be under the second case, namely, multipolar interaction. Moreover, the ET mechanism between Eu^{2+} and Eu^{3+} in $\text{C}_{1-3x/2}\text{Eu}_x\text{Al}_2\text{Si}_2\text{O}_8$ and $\text{C}_{1-x}\text{Eu}_x\text{Al}_2\text{Si}_2\text{O}_{8+0.5x}$ are controlled by electric multipole-multipole interactions according to Dexter theory [21, 28, 29, 32], which follows the ET **Equation (2-5)** given below:

$$\frac{\tau_{S0}}{\tau_S} \propto C^{\alpha/3} \quad (2-5)$$

where τ_{S0} and τ_S are the luminescence decay times of Eu^{2+} cations in the absence and presence of Eu^{3+} , respectively. C is the sum of Eu^{2+} and Eu^{3+} contents. The α parameter equals to 6, 8 and 10 corresponding to dipole-dipole, dipole-quadrupole and quadrupole-quadrupole interactions, respectively. The τ_{S0}/τ_S vs $C^{\alpha/3}$ curves are represented in **Figure 2-50a** ($\alpha = 6$), **2-50b** ($\alpha = 8$), **2-50c** ($\alpha = 10$) and **Figure 2-51a** ($\alpha = 6$), **2-51b** ($\alpha = 8$), **2-51c** ($\alpha = 10$), for the $\text{C}_{1-3x/2}\text{Eu}_x\text{Al}_2\text{Si}_2\text{O}_8$ and $\text{C}_{1-x}\text{Eu}_x\text{Al}_2\text{Si}_2\text{O}_{8+0.5x}$ formulas, respectively.

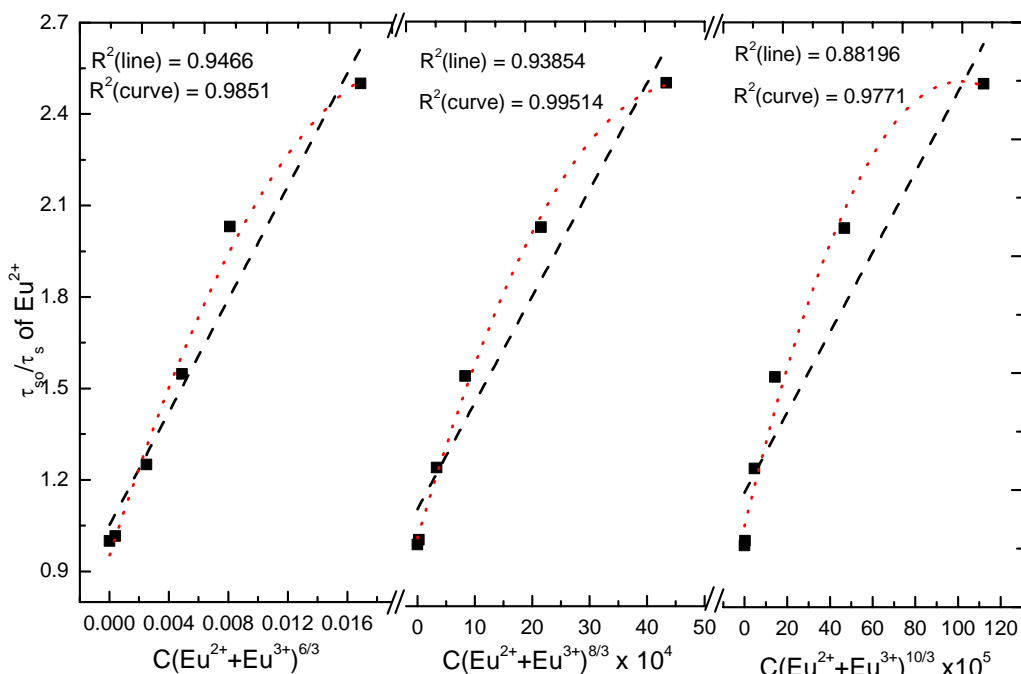


Figure 2-50a, 2-50b, 2-50c (from left to right). Dependence of τ_{S0}/τ_S of Eu^{2+} on a) $\alpha = 6$, b) $\alpha = 8$ and c) $\alpha = 10$ for the samples under the formula $\text{C}_{1-3x/2}\text{Eu}_x\text{ASO}$, $x = 0.5\%$ to 13%

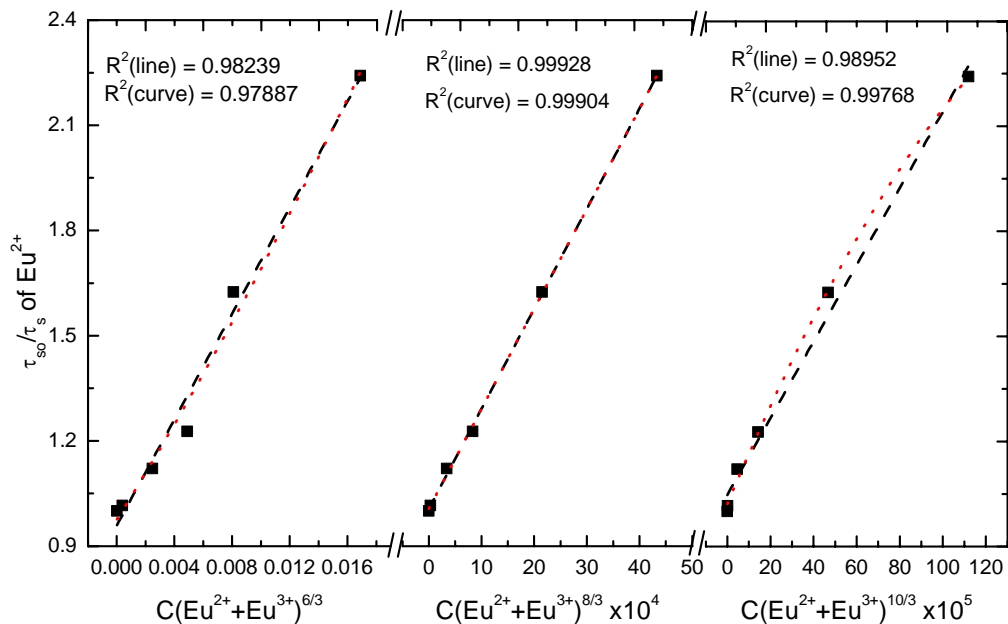


Figure 2-51a, 2-51b, 2-51c (from left to right). Dependence of τ_{s0}/τ_s of Eu²⁺ on a) $a = 6$, b) $a = 8$ and c) $a = 10$ for the samples under the formula $C_{1-x}Eu_xASO_{8+0.5x}$, $x = 0.5\%$ to 13%

As shown in **Figures 2-50a** and **2-51b**, these curves would indicate that the ET from Eu²⁺ to Eu³⁺ occurs rather via a dipole-dipole mechanism under the formula $C_{1-3x/2}Eu_xAl_2Si_2O_8$ and dipole-quadrupole mechanism under the formula $C_{1-x}Eu_xAl_2Si_2O_{8+0.5x}$. Therefore, the electric dipole-dipole interaction predominates in the ET mechanism from the Eu²⁺ to Eu³⁺ ions in $C_{1-3x/2}Eu_xAl_2Si_2O_8$ and dipole-quadrupole reaction predominates under the $C_{1-x}Eu_xAl_2Si_2O_{8+0.5x}$ samples. At this stage, we do not fully understand why the dipole-quadrupole mechanism is not obtained for both groups of samples as expected. Supplementary experiments are in progress to address this observation.

Concluding remarks

In summary, we have demonstrated the possibility to "co-dope" $\text{MAl}_2\text{Si}_2\text{O}_8$ (M = Ca, Sr, Ba) aluminosilicates host lattices by both Eu^{3+} and Eu^{2+} via high temperature solid-state reactions in air. The "only" Eu^{2+} -doped $\text{MAl}_2\text{Si}_2\text{O}_8$ has to be prepared in reducing atmosphere. These materials, with a very low concentration of residual Eu^{3+} cations (at least for the Ca and Sr derivatives) exhibit a bluish white luminescence centred at around 425 nm, 404 nm and 440 nm due to the allowed $4f^65d^1 \rightarrow 4f^7$ (${}^8S_{7/2}$) radiative transition for M from Ca to Ba, respectively. The irregular evolution of the emission wavelength going from CASO to SASO and BASO could be assigned to a modification of the local chemical environment of Eu^{2+} cations once excited in the BASO host lattice.

For materials prepared in air, Eu^{2+} and Eu^{3+} cations coexist, at least for the Ca and Sr derivatives. For the BASO phases, it appears quite difficult to stabilize the more oxidized form of Eu^{3+} mainly because of the difference in radius between the alkaline earth and the rare earth. In addition, the concentration of Eu^{2+} at the expense of Eu^{3+} cations can be privileged via the codoping with a M⁴⁺ cation (Zr⁴⁺ for instance). This could open up the door to the synthesis of Eu^{2+} containing phosphors in air in the next future.

As expected, the position and shape of the Eu^{3+} emission bands are not impacted by the nature of host lattice. For CASO and SASO compositions, the strongest f-f emission peaks located at around 611 nm are attributed to the ${}^5D_0 \rightarrow {}^7F_2$ transition and can be sensitized by ET from Eu^{2+} . This lead to the addition of red contribution to the bluish one observed for only Eu^{2+} doped materials. We expected to take benefit of these observations to generate new phosphors in the future with a control of the CIE (x, y) parameter and to tune white emission from cold to warm.

References

1. V. Bachmann, C. Ronda, O. Oeckler, W. Schnick and A. Meijerink, *Chemistry of Materials* **21** (2008) (2), p. 316.
2. F. Clabau, X. Rocquefelte, S. Jobic, P. Deniard, M.-H. Whangbo, A. Garcia and T. Le Mercier, *Solid State Sciences* **9** (2007) (7), p. 608.
3. F. Clabau, A. Garcia, P. Bonville, D. Gonbeau, T. Le Mercier, P. Deniard and S.p. Jobic, *Journal of Solid State Chemistry* **181** (2008) (6), p. 1456.
4. G.g. Denis, P. Deniard, E. Gautron, F.d.r. Clabau, A. Garcia and S.p. Jobic, *Inorganic Chemistry* **47** (2008) (10), p. 4226.
5. P. Joung Kyu, K. Jae Myung, O. Eun Suk and K. Chang Hae, *Electrochemical and Solid-State Letters* **8** (2005) (1), p. H6.
6. S.M. Lee and K.C. Choi, *Opt. Express* **18** (2010) (12), p. 12144.
7. T. Kida, M.M. Rahman and M. Nagano, *Journal of the American Ceramic Society* **89** (2006) (5), p. 1492.
8. X.Y. Chen, Z. Li, S.P. Bao and P.T. Ji, *Optical Materials* **34** (2011) (1), p. 48.
9. F. Clabau, X. Rocquefelte, S. Jobic, P. Deniard, M.H. Whangbo, A. Garcia and T. Le Mercier, *Chemistry of Materials* **17** (2005) (15), p. 3904.
10. M. Peng and G. Hong, *Journal of Luminescence* **127** (2007) (2), p. 735.
11. M.L. Debasu, D. Ananias, A.G. Macedo, J. Rocha and L.s.D. Carlos, *The Journal of Physical Chemistry C* **115** (2011) (31), p. 15297.
12. T. Endo, T. Masuda, H. Takizawa and M. Shimada, *Journal of Materials Science Letters* **11** (1992) (19), p. 1330.
13. S.A. Lourenco, N.O. Dantas, E.O. Serqueira, W.E.F. Ayta, A.A. Andrade, M.C. Filadelpho, J.A. Sampaio, M.J.V. Bell and M.A. Pereira-da-Silva, *Journal of Luminescence* **131** (2011) (5), p. 850.
14. C.-C. Wu, K.-B. Chen, C.-S. Lee, T.-M. Chen and B.-M. Cheng, *Chemistry of Materials* **19** (2007) (13), p. 3278.
15. A. Cho, S.Y. Kim, M. Lee, S.-J. Kim, C.-H. Kim and C.-H. Pyun, *Journal of Luminescence* **91** (2000) (3-4), p. 215.
16. M.D. Chambers, P.A. Rousseve and D.R. Clarke, *Journal of Luminescence* **129** (2009) (3), p. 263.
17. G. Blasse, *Chemistry of Materials* **1** (1989) (3), p. 294.
18. G. Seeta Rama Raju, H.C. Jung, J.Y. Park, B.K. Moon, R. Balakrishnaiah, J.H. Jeong and J.H. Kim, *Sensors and Actuators B: Chemical* **146** (2010) (1), p. 395.
19. Y.-C. Chang, C.-H. Liang, S.-A. Yan and Y.-S. Chang, *The Journal of Physical Chemistry C* **114** (2010) (8), p. 3645.
20. D.L. MacAdam, *Color measurements*, Springer, Berlin, Heidelberg (1985).
21. W.-J. Yang, L. Luo, T.-M. Chen and N.-S. Wang, *Chemistry of Materials* **17** (2005) (15), p. 3883.
22. J. Edmond, A. Abare, M. Bergman, J. Bharathan, K. Lee Bunker, D. Emerson, K. Haberern, J. Ibbetson, M. Leung, P. Russel and D. Slater, *Journal of Crystal Growth* **272** (2004), p. 242.
23. C.C. Lin and R.-S. Liu, *The Journal of Physical Chemistry Letters* **2** (2011) (11), p. 1268.
24. S. Sapru and K.L. Tan, *physica status solidi (b)* **125** (1984) (2), p. K161.
25. C. Zhang, J. Yang, C. Lin, C. Li and J. Lin, *Journal of Solid State Chemistry* **182** (2009) (7), p. 1673.

26. M. Nogami, T. Yamazaki and Y. Abe, *Journal of Luminescence* **78** (1998) (1), p. 63.
27. R.A. McCauley, *Journal of Materials Science* **35** (2000) (15), p. 3939.
28. C.-H. Huang, T.-M. Chen, W.-R. Liu, Y.-C. Chiu, Y.-T. Yeh and S.-M. Jang, *ACS Applied Materials & Interfaces* **2** (2010) (1), p. 259.
29. N. Guo, Y. Huang, H. You, M. Yang, Y. Song, K. Liu and Y. Zheng, *Inorganic Chemistry* **49** (2010) (23), p. 10907.
30. B.C.G. Blass, Editor, *Luminescent materials*, Springer-Verlag (1994).
31. J.K. Park, J.M. Kim, E.S. Oh and C.H. Kim, *Electrochim. Solid State Lett.* **8** (2005) (1), p. H6.
32. L. Sung Hun, P. Je Hong, S. Se Mo, K. Jong Su and P. Hong Lee, *Applied Physics Letters* **89** (2006) (22), p. 221916.
33. B. Zoila and S. Luis, *The Journal of Chemical Physics* **119** (2003) (7), p. 3785.
34. A. Meijerink and G. Blasse, *Journal of Luminescence* **43** (1989) (5), p. 283.
35. R. Fernando, S. Luis and B. Zoila, *The Journal of Chemical Physics* **122** (2005) (23), p. 234507.
36. A. Chroneos, M.J.D. Rushton, R.W. Grimes and J.M.K. Editor-in-Chief: Rudy, *Comprehensive Nuclear Materials*, Elsevier, Oxford (2012), pp. 47-64.
37. B.K. Grandhe, V.R. Bandi, K. Jang, S.-S. Kim, D.-S. Shin, Y.-I. Lee, J.-M. Lim and T. Song, *Journal of Alloys and Compounds* **509** (2011) (30), p. 7937.
38. L. Bitao, W. Yuhua, Z. Jun, Z. Feng and W. Zhaofeng, *Journal of Applied Physics* **106** (2009) (5), p. 053102.
39. Z. Pei, Q. Zeng and Q. Su, *Journal of Solid State Chemistry* **145** (1999) (1), p. 212.
40. A.M. Pires and M.R. Davolos, *Chemistry of Materials* **13** (2000) (1), p. 21.
41. E. Malchukova and B. Boizot, *Materials Research Bulletin* **45** (2010) (9), p. 1299.
42. B. Wang, L. Sun, H. Ju, S. Zhao, D. Deng, H. Wang and S. Xu, *Journal of Sol-Gel Science and Technology* **50** (2009) (3), p. 368.
43. R. Pang, C. Li, L. Shi and Q. Su, *Journal of Physics and Chemistry of Solids* **70** (2009) (2), p. 303.

Chapter III : Optical characterization of $M_{1-y-3x/2}Al_2Si_2O_8$: xCe^{3+} , yMn^{2+} ($M = Ca, Sr$) with efficient energy transfers for generation of white-light-emitting diodes

Among materials doped with rare-earth ions, Ce^{3+} activated phosphors have been extensively applied in the field of lighting, display, and scintillation. Here we specifically investigated the capability of Ce^{3+} cations to transfer energy towards Mn^{2+} in the host lattice $MAI_2Si_2O_8$ ($M = Ca, Sr$) to shift the emission spectra from cold to warm light.

1. Introduction

Because of its versatile spectroscopic properties, the Ce^{3+} ion has been used as a sensitizer in ET processes taking place in diverse crystals. In the same manner as the Eu^{2+} cations, Ce^{3+} ions are characterized by parity- and spin-allowed electron transitions which occur between 4f- and 5d-orbitals. As expected, the optical properties are strongly affected by the crystal field strength of the host matrix and emission may range from UV to visible [1-5]. In the same way, Mn^{2+} doped luminescent materials are known to always show broadband emissions from 500 to 700 nm depending on the crystal field of the host materials [6-10]. Actually, Mn^{2+} has the 3d^5 configuration with a 6A^1 ground state. Generally, Mn^{2+} activated phosphors are divided into two classes [11-13]: those are emitting green emission and those are emitting between yellow and red emission. In octahedral surroundings (large crystal field), the emission is usually located at longer wavelength than in tetrahedral surroundings (smaller crystal field). In many cases, the emission arises from the $4\text{T}_1(4\text{G})$ level, which shifts to lower energies for higher crystal field strengths. Although these doped Mn^{2+} luminescent materials could be the good candidates for green to red phosphors, their disadvantage is that the d-d transitions of Mn^{2+} ions are strongly parity forbidden, and therefore, the ions are difficult to pump [14, 15]. Ye et al. and Kim et al. have observed effective ET from Eu^{2+} to Mn^{2+} in $\text{BaMg}_2\text{Si}_2\text{O}_7$ [16] and $\text{Ba}_3\text{MgSi}_2\text{O}_8$ [7], respectively, where Mn^{2+} shows red emissions. As the same as for the Eu^{2+} ions, we can imagine that Ce^{3+} ions could also be as an effective sensitizer of the Mn^{2+} activators when gathered in one matrix. Till up now, Ce^{3+} has been studied in few Mn^{2+} doped hosts such as MgSiN_2 [17], BaAl_2O_4 [18] and $\text{Ca}_9\text{Y}(\text{PO}_4)_7$ [19] to improve the emission intensity of Mn^{2+} . To the best of our knowledge, the luminescence properties of $\text{MAl}_2\text{Si}_2\text{O}_8:\text{Ce}^{3+},\text{Mn}^{2+}$ have not been yet reported in the literature. In this study, thus, we have reported an emission-tunable white emitting phosphor, $\text{MAl}_2\text{Si}_2\text{O}_8:\text{Ce}^{3+}, \text{Mn}^{2+}$ (hereafter abbreviated MASO: Ce, Mn). We have also systematically investigated the ET mechanism between Ce^{3+} and Mn^{2+} based on the evolution of the emission intensities versus the doping rates.

2. Experimental section

2.1. Synthesis and optical measurements

Strontium carbonate ($SrCO_3$ Alfa Aesar, 4N), Calcium carbonate ($CaCO_3$ Alfa Aesar, 4N), Silica (SiO_2 Chempur, 4N), Alumina- γ (Al_2O_3 Alfa Aesar, 4N), Cerium carbonate ($Ce_2(CO_3)_3$ Alfa Aesar, 4N), Manganese oxide (MnO Alfa Aesar, 4N), Cerium oxide (CeO_2 , Alfa Aesar, 4N) and Manganese carbonate ($MnCO_3$ Aldrich, 4N) were employed as raw materials. The pristine $Ce_2(CO_3)_3$ and MnO , and CeO_2 and $MnCO_3$ materials were used to (co)-doped the CASO and SASO host lattices, respectively. Precursors were weighed in stoichiometric amounts and alkaline-earth (AE) cations were expected to be substituted for the Ce^{3+} or/and Mn^{2+} in the host lattice for steric reasons. Celsian SASO: Ce^{3+} , Mn^{2+} and anorthite CASO: Ce^{3+} , Mn^{2+} were obtained after heating the starting materials in alumina crucibles in a reductive atmosphere ($Ar + 5\%H_2$) at $1350^\circ C$ for 20h and 50h, respectively. Several series of powder samples of the phosphors under the MASO structure with compositions $M_{1-3x/2}ASO: xCe^{3+}$ ($x = 0.001$ to 0.25), $M_{1-x}ASO: xMn^{2+}$ ($x = 0.005$ to 0.15), $Ca_{0.865-y}ASO: 0.09Ce^{3+}, yMn^{2+}$, $Sr_{0.895-y}ASO: 0.07Ce^{3+}, yMn^{2+}$ ($y = 0.01$ to 0.15) and $M_{0.91-3x/2}ASO: xCe^{3+}, 0.09Mn^{2+}$ ($x=0.01$ to 0.15) were prepared. Starting materials were ball milled with a Fritsch Pulverisette 7 for two hours in silicon nitride container $\sim 65\%$ filled with ethanol before synthesised for speeding up the sluggish phase transformation. The optical measurements were performed in the same way as introduced in chapter II.

2.2. Structure characterization

The purity of all the prepared materials was systematically checked by XRD at room temperature (RT). For all the samples, no characteristic peaks of the precursors were observed after a full pattern matching analysis, which reveals that dopants are completely dissolved in investigated samples. Typical XRD patterns of MASO, $M_{1-3x/2}ASO:xCe^{3+}$ ($x = 0.09$ and 0.07 for CASO and SASO, respectively), $M_{1-x}ASO:xMn^{2+}$ ($x = 0.09$ and 0.06 for CASO and SASO, respectively) and $M_{1-y-3x/2}ASO:xCe^{3+}, yMn^{2+}$ ($x = 0.09$, $y = 0.06$ and $x = 0.07$, $y = 0.06$ for CASO and SASO, respectively) are displayed in **Figure 3-1**. All the XRD patterns are in good agreement with the ICDD standard card No.89-1462 (CASO) and No. 70-1862 (SASO). Moreover, when doping by Ce^{3+} or/and Mn^{2+} in MASO, a small shift of the diffraction peaks

is also observed because of the variation of the lattice parameters as a result of the difference in ionic radius of Ce^{3+} and/or Mn^{2+} with respect to M^{2+} [20].

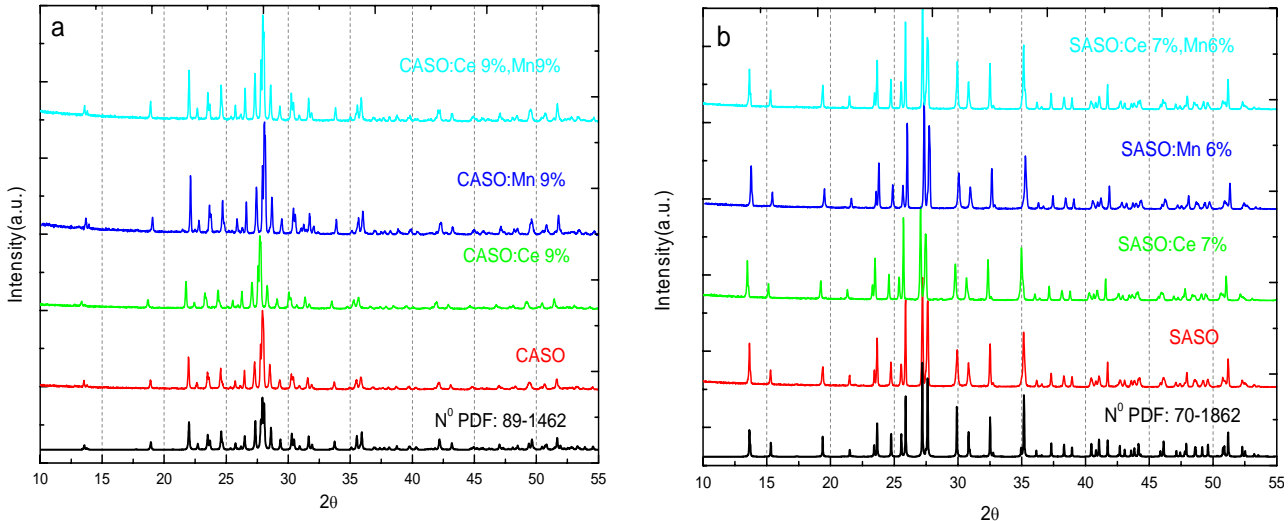


Figure 3-1. a) XRD patterns for different (co-)doped CASO samples, and b) XRD profiles for SASO samples

Due to steric reasons already discussed in the previous chapter, the AE cations can be substituted for Ce, Mn or both. In **Figure 3-2** are reported the evolution of refined lattice volume for CASO and SASO matrixes with different dopant concentrations (Ce^{3+} and Mn^{2+} separately). For the CASO matrix, the slight difference of ionic radii between Ce^{3+} and Ca^{2+} ($r(\text{Ce}^{3+}) = 1.01 \text{ \AA}$ and $r(\text{Ca}^{2+}) = 1.00 \text{ \AA}$ when $CN = 6$, $r(\text{Ce}^{3+}) = 1.07 \text{ \AA}$ and $r(\text{Ca}^{2+}) = 1.06 \text{ \AA}$ when $CN = 7$) leads to a continuous increase of the lattice volume. At the opposite, a shrink of the cell volume is observed when Ca^{2+} cations are replaced by Mn^{2+} ones ($r(\text{Mn}^{2+}) = 0.67 \text{ \AA}$ and 0.90 \AA when $CN = 6$ and 7 , respectively). In the SASO host lattice, the substitution of Sr^{2+} by Ce^{3+} or Mn^{2+} ($r(\text{Sr}^{2+}) = 1.31 \text{ \AA}$, $r(\text{Ce}^{3+}) = 1.20 \text{ \AA}$ and $r(\text{Mn}^{2+}) = 0.96 \text{ \AA}$ when $CN = 9$) leads to a regular decrease of lattice volume. All these results indicate that in all cases, a solid solution is formed because the evolution of the cell parameters regularly evolves with dopant ions concentration.

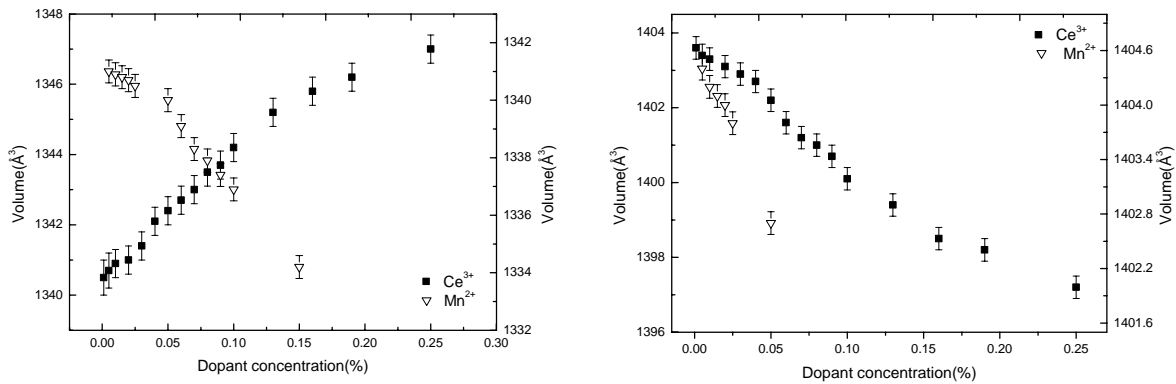


Figure 3- 2 . (left) The variations in the lattice volume with Ce^{3+} and Mn^{2+} concentrations in CASO and (right) in SASO

3. Fluorescence of MASO doped with Ce^{3+}

3.1. Fluorescence of $C_{1-3x/2}ASO: xCe^{3+}$ ($x = 0.1\%$ to 25%)

Figure 3-3 shows the photoluminescence excitation (PLE) spectra of $C_{1-3x/2}ASO: xCe^{3+}$ ($x = 1\%$ and 10%) monitored at 356 nm which corresponds to the main emission band of Ce^{3+} ion (see below). The PLE is composed of two excitation bands peaking at 250 nm and 294 nm . These bands correspond to the transitions from the ground $4f$ ($^2F_{5/2}$) level to the $5d$ block separated in several components due to the ligand field splitting [21] (the $^2F_{7/2}$ level of Ce^{3+} cations cannot be occupied at room temperature and do not have to be considered for PLE due to the fact that the spin-orbit splitting ($\sim 1860\text{ cm}^{-1} = 231\text{ meV} \approx 0.25\text{ eV}$) is far large than $K_B T$ (26 meV) at room temperature.). Absorption bands are quite large hindering to distinguish $4f \rightarrow 5d$ transitions issued from Ce ions at the six-fold and seven-fold sites.

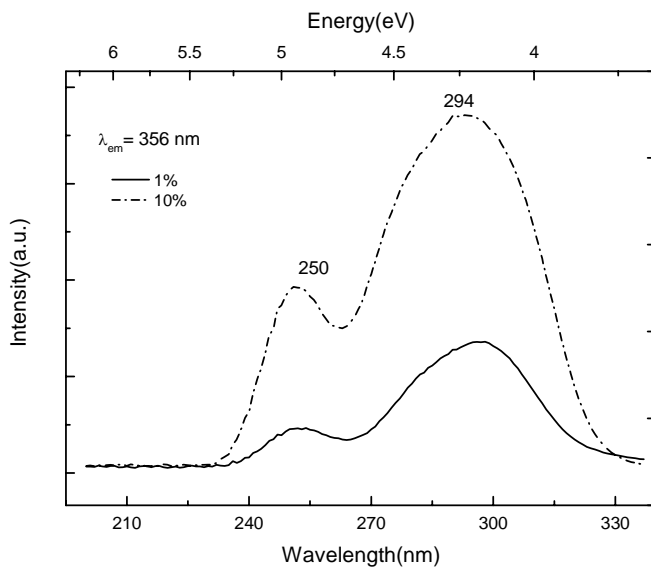


Figure 3- 3. Room temperature excitation spectra of $\text{C}_{1-3x/2}\text{ASO}: \text{xCe}^{3+}$ ($x = 1\%$ and 10%) monitored at $\lambda_{\text{em}}=356 \text{ nm}$

Emission spectra of $\text{C}_{1-3x/2}\text{ASO}: \text{xCe}^{3+}$ are depicted in **Figure 3-4**. PL emission spectra are composed of two broad bands located at 356 and 430 nm respectively. One can also notice a slight shoulder around 340 nm which progressively disappears when the cerium content increases. As Ce^{3+} may occupy two types of crystal sites, at least two types of emissions should be observed. Moreover each cerium cation is expected to lead to two emission bands separated by about 0.25 eV due to the spin-orbit coupling of the $4f^1$ ground state of Ce^{3+} (5d \rightarrow $^2\text{F}_{5/2}$ and 5d \rightarrow $^2\text{F}_{7/2}$ transitions). At this stage, considering the crystal field effect, we can suspect that Ce^{3+} ions that are housed at the Ca(2) to Ca(4) sites (7-coordinated sites) give rise to the short-wavelength bands (340 nm) while the Ce^{3+} cations at the Ca(1) site (6-coordinated site) lead to the long-wavelength emission band (356 nm).

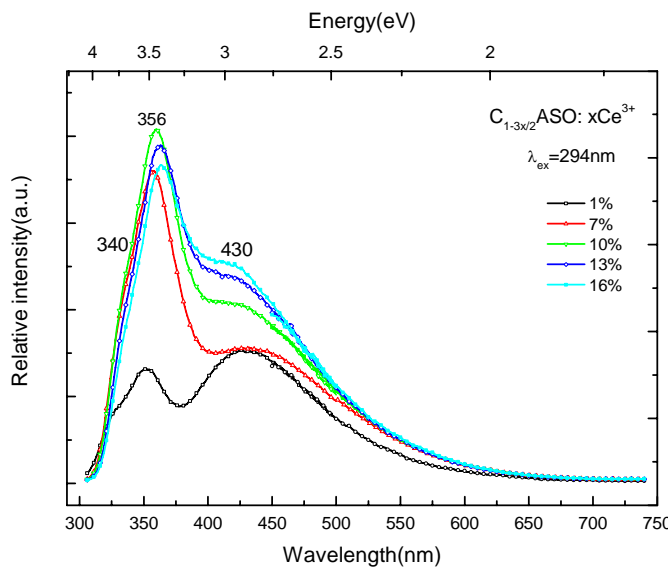


Figure 3-4. Room temperature emission spectra of $C_{1-3x/2}ASO: xCe^{3+}$ ($x = 1\%$ to 16%) monitored at $\lambda_{exc}=294$ nm.

In **Figure 3-5** is reported the evolution of the maximum intensity of the excitation band ($\lambda_{em} = 356$ nm) and of emission band ($\lambda_{exc} = 294$ nm) versus the doping concentration. Hence, it is possible to assess the quenching concentration to be around 9% of Ce^{3+} .

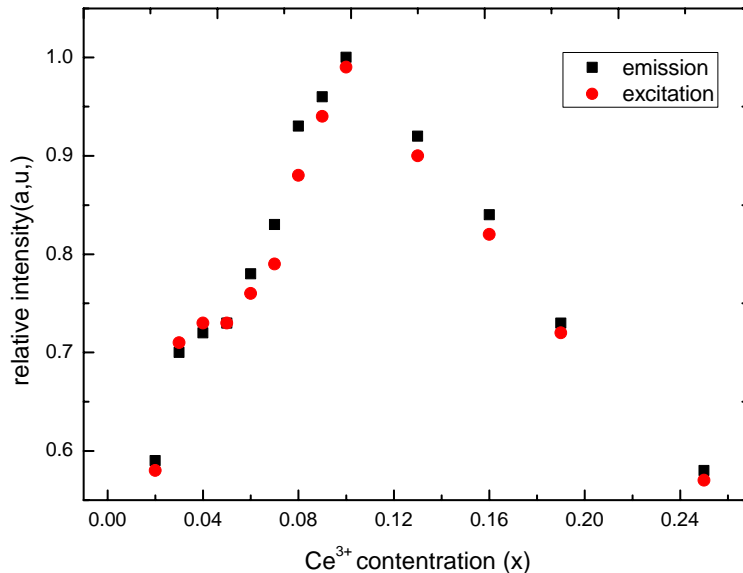


Figure 3-5. Dependence of the relative excitation ($\lambda_{em}= 356$ nm) and emission ($\lambda_{ex}= 294$ nm) intensities of $C_{1-3x/2}ASO: xCe^{3+}$ ($x = 1\%$ to 25%)

The critical distance (R_c) for ET in $\text{C}_{1-3x/2}\text{ASO}:x\text{Ce}^{3+}$ can be calculated from the structural parameters such as unit-cell volume (V) and number of total Ce^{3+} sites per unit cell (N), together with x_c the quenching concentration as expressed by the following **Equation (3-1)** [19, 22]:

$$R_c = 2 \left(\frac{3V}{4\pi x_c N} \right)^{1/3} \quad (3-1)$$

here R_c corresponds to the mean separation between the nearest Ce^{3+} ions at the critical concentration. Using $V = 1343.74\text{\AA}^3$, $N = 8$, and $x_c = 0.09$, the critical transfer distance of Ce^{3+} in $\text{C}_{1-3x/2}\text{ASO}:x\text{Ce}^{3+}$ is determined to be $\sim 15.28\text{\AA}$.

As two emission broad bands are observed instead of the four expected bands, we performed a decomposition of emission spectra into Gaussian components. Decompositions have been carried out for all samples and for both excitation wavelengths. In **Figure 3-6** and **Figure 3-7** is reported an example for the emission spectra relative to the sample doped by 9% Ce^{3+} and monitored at $\lambda_{\text{exc}} = 294 \text{ nm}$ and $\lambda_{\text{exc}} = 250 \text{ nm}$, respectively.

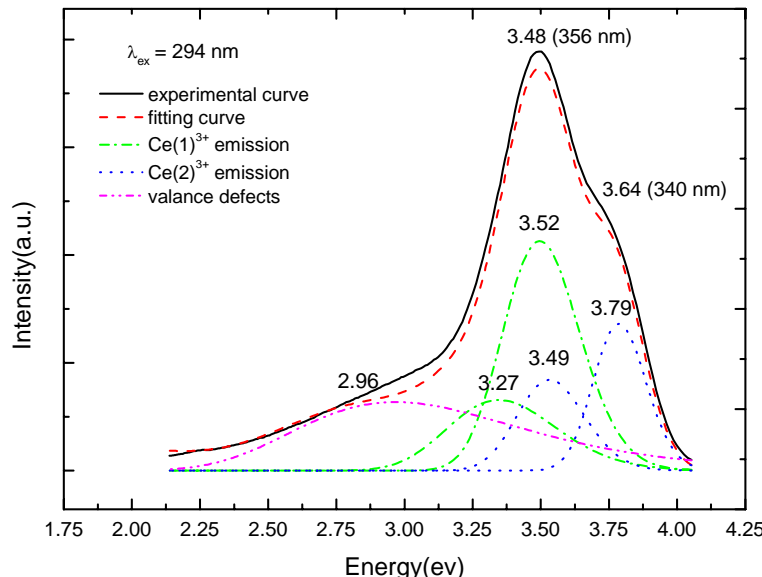


Figure 3-6. Emission spectra of $\text{C}_{1-3x/2}\text{ASO}:x\text{Ce}^{3+}$ ($x = 9\%$) with decomposition in Gaussian curves under $\lambda_{\text{ex}} = 294 \text{ nm}$;

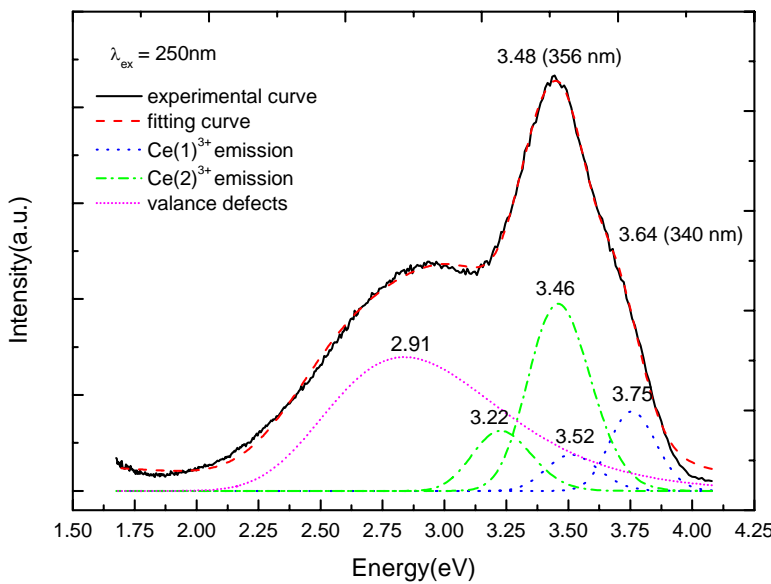


Figure 3-7. Emission spectra of $C_{1-3x/2}ASO : xCe^{3+}$ ($x = 9\%$) with decomposition in Gaussian curves under $\lambda_{ex} = 250\text{ nm}$.

Deconvolutions can be achieved by using five bands for CASO:Ce³⁺ whatever the excitation wavelength. These bands are located at 3.79 eV (327 nm), 3.52 eV (352 nm), 3.49 eV (355 nm), 3.27 eV (379 nm) and 2.96 eV (430 nm) for $\lambda_{ex} = 294\text{ nm}$ and at 3.75 eV (331 nm), 3.52 eV (352 nm), 3.46 eV (358 nm), 3.22 eV (385 nm) and 2.91 eV (426 nm) for $\lambda_{ex} = 250\text{ nm}$ as one can see **Figures 3-6** and **3-7**. Emissions located at 3.79 eV (3.75 eV for $\lambda_{ex} = 250\text{ nm}$) and 3.49 eV (3.52 eV for $\lambda_{ex} = 250\text{ nm}$) can be associated to the presence of Ce³⁺ in one kind of crystallographic sites while the emissions at 3.52 eV (3.46 eV for $\lambda_{ex} = 250\text{ nm}$) and 3.27 eV (3.22 eV for $\lambda_{ex} = 250\text{ nm}$) correspond to the other sites. Reporting to the crystal field effect which speculates that the higher coordination the shorter the wavelength of the emission because of a lower crystal field splitting. Therefore, emission peaks at 3.79 eV (327 nm) and 3.49 eV (355 nm) can be attributed to Ce₂, Ce₃ and Ce₄ ($CN = 7$), whereas the peaks at 3.52 eV (352 nm) and 3.27 eV (379 nm) should correspond to Ce₁ ($CN = 6$). However, this hypothesis must be moderated by the existence of counter-examples [23].

At present, it is worthy to notice that the additional peaks located at $\sim 2.96\text{ eV}$ (430 nm) have been always observed whatever the Ce³⁺ concentrations in the CASO and the excitation values. This kind of bands cannot originate from the transitions of Ce³⁺ ion doped in CASO matrix because: 1) all the four different crystallographic sites of Ca²⁺ ions are occupied by Ce³⁺ and the emission bands are all located in the 300-380 nm range from, 2) the smallest

energy difference between the 2.96 eV emission band and the Ce_1 (3.27 eV, 3.52 eV) is much bigger than 0.25 eV (~ 0.31 eV). This means that this band cannot originate from the transition of the spin-orbit splitting of the ground state of Ce^{3+} . Furthermore, as previously investigated in the literature [9, 24, 25], the emission band from Eu^{2+} ion in Eu-doped CASO is located at ~ 425 nm. However, this possible pollution by Eu^{2+} ions can also be excluded because the decay time relative to the emission band at around 430 nm is equal to 22 ns which is not characteristic of the Eu^{2+} ion and does not correspond at all to the decay time of 0.65 μs measured in CASO: Eu^{2+} (see chapter II). Let us notice at this stage that syntheses were actually carried out in new alumina crucibles with high purity precursors and systematically led to materials exhibiting this broad emission band at around 430 nm.

Actually, because of the different charge between the Ce^{3+} and Eu^{2+} and to maintain the charge balance, two Ce^{3+} ions are needed to compensate three Ca^{2+} ions. Hence, one vacancy defect $V_{\text{Ca}}^{\parallel\parallel}$ with two negative charges and two positive defects of $\text{Ce}_{\text{Ca}}^{\bullet}$ will be created when two Ce^{3+} cations are introduced in the host lattice in place of Ca^{2+} ions according to the **Equation (3-2)**:



Thus, we can suggest that this broad emission band at around 420 nm is due to the perturbed levels of the vacancy ions ($V_{\text{Ca}}^{\parallel\parallel}$) in the neighbourhood of $\text{Ce}_{\text{Ca}}^{\bullet}$. In this way, it can also explain that the strength of such a band should naturally increase with cerium concentration in the CASO matrix (by creates more $V_{\text{Ca}}^{\parallel\parallel}$ vacancies), which is observed in **Figure 3-4**.

Furthermore, **Figure 3-8** illustrates the excitation spectra of the $\text{C}_{1-3x/2}\text{ASO}:x\text{Ce}^{3+}$ ($x = 1\%$ and 10%) monitored at $\lambda_{\text{em}} = 430$ nm. By comparison with **Figure 3-3**, one can notice that the profiles of the spectra are slightly different but that absorption takes place in the same energy range. Apparently, no additional excitation transition band is associated with the emission band at 420 nm. This phenomenon suggests that the additional emission bands are related to defects involved $V_{\text{Ca}}^{\parallel\parallel}$ vacancies.

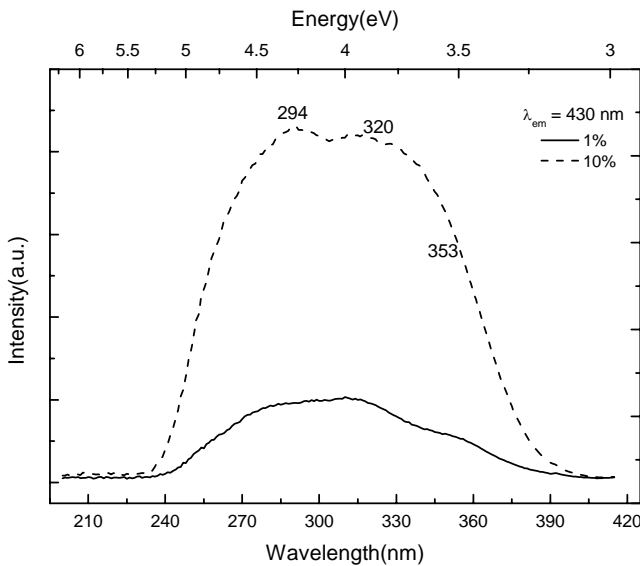
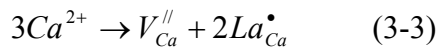


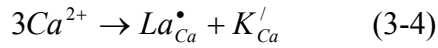
Figure 3-8. Excitation spectra of $C_{1-3x/2}ASO: xCe^{3+}$ ($x = 1\%$ and 10%) under $\lambda_{em} = 430$ nm.

Moreover, we can verify this hypothesis by doping the CASO matrix with La^{3+} , La^{3+} and K^+ , and Ce^{3+} and K^+ ions. **Figure 3-9** depicts the fluorescence spectra of CASO matrix doped with different ions. Namely, chemical compositions are $Ca_{0.925}La_{0.05}Al_2Si_2O_8$, $Ca_{0.925}Ce_{0.05}Al_2Si_2O_8$, $Ca_{0.9}K_{0.05}La_{0.05}Al_2Si_2O_8$ and $Ca_{0.925}K_{0.05}Ce_{0.05}Al_2Si_2O_8$ (prepared in the same conditions). Due to steric reasons ($r(K^+) = 1.38 \text{ \AA}$ and 1.46 \AA , $r(La^{3+}) = 1.03 \text{ \AA}$ and 1.10 \AA when $CN = 6$ and 7 , respectively) all dopants occupy Ca^{2+} sites as usual. The emission spectrum of the un-doped CASO host lattice was also collected under $\lambda_{ex} = 294$ nm as shown in **Figure 3-9**. No emission band from the host lattice is observed what clearly indicates that the additional band (420 nm) can also not originate from the CASO matrix itself.

When only doped with La^{3+} ions, one can see a unique broad emission peak seated at around 430 nm. Thus, this band can be associated without doubt to V_{Ca}^{II} defects since La^{3+} ions cannot lead to emission [26]. The process can be expressed by the following **Equation (3-3)**:



Meanwhile, let us notice that the fluorescence properties of $C_{1-3x/2}ASO: xLa^{3+}$ ($x = 5\%$) sample is quite different from the $C_{1-2x}ASO: xLa^{3+}, xK^+$ ($x = 5\%$) sample co-doped with K^+ . In the latter case, the strong decrease of the 430 nm emission band reflects the fact that the V_{Ca}^{II} vacancies are vanished which can be expressed by the **Equation (3-4)**:



In a similar way when we also co-doped CASO: Ce^{3+} with K^+ , ($2\text{Ca}^{2+} \rightarrow \text{Ce}^{3+} + \text{K}^+$), the emission peak at around 430 nm tends to disappear. This confirms definitely that the peak located around 430 nm is originated from the vacancy defects ($V_{\text{Ca}}^{\prime\prime}$).

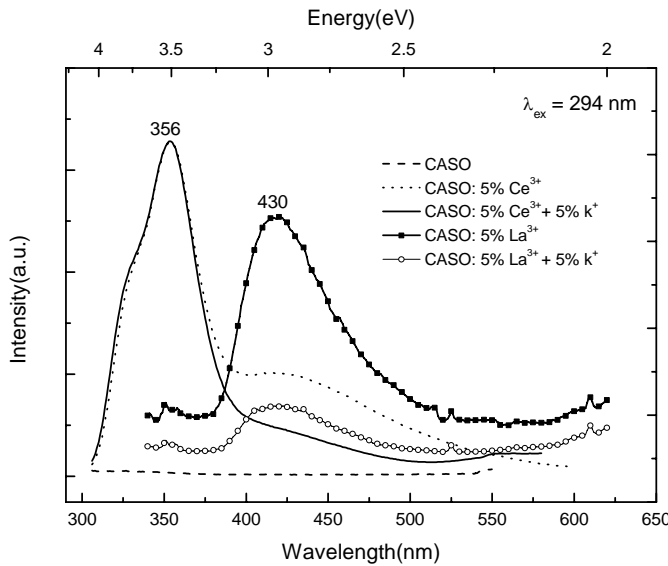


Figure 3-9. Emission spectra of CASO, CASO:Ce, CASO:Ce+K, CASO:La, CASO:La+K monitored at $\lambda_{\text{ex}} = 294\text{nm}$.

3.2 Fluorescence of $\text{S}_{1-3x/2}\text{ASO: xCe}^{3+}$ ($x = 0.1\%$ to 25%)

Then, we performed the same investigation on the SASO matrix. **Figure 3-10** shows the photoluminescence excitation spectra of $\text{S}_{1-3x/2}\text{ASO: xCe}^{3+}$ ($x = 2\%$ and 10%) monitored at $\lambda_{\text{em}} = 348\text{ nm}$. One can notice that spectra are similar with those obtained for CASO:Ce $^{3+}$.

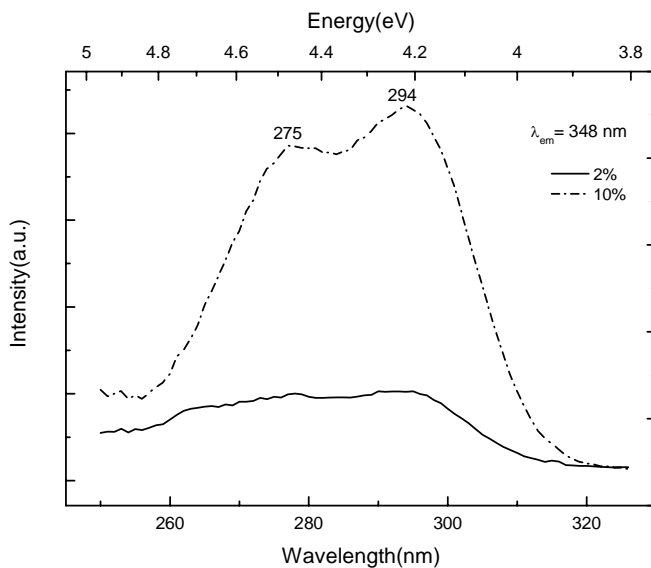


Figure 3-10. Excitation spectra of $S_{1-3x/2}ASO: xCe^{3+}$ ($x = 2\%$ and 10%) monitored at $\lambda_{em} = 348$ nm.

As previously discussed, there is only one alkaline-earth cation site in the SASO matrix. Thus, the double excitation band of Ce³⁺ ions can only be assigned to 4f → 5d transitions with splitting of 5d bloc into two components due to the crystal field. Decomposition of the excitation spectrum ($\lambda_{em} = 348$ nm) was performed with Gaussian functions (**Figure 3-11**). The appearance of multiple contributions can be attributed to $^2F_{5/2} \rightarrow 5d$ transitions with different sub-levels of the Ce³⁺ 5d orbitals. As aforementioned, excitation from the $^2F_{7/2}$ state can be ignored at room temperature. Five contributions that we related to transitions from the 4f bloc towards the 5d orbitals of Ce³⁺ can be observed.

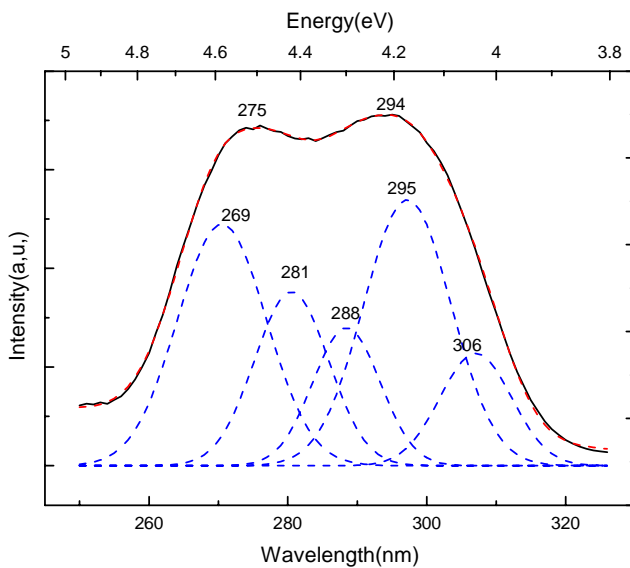


Figure 3-11. Excitation spectra of $\text{S}_{1-3x/2}\text{ASO}: \text{xCe}^{3+}$ ($x = 7\%$), and peak deconvolution of excitation bands are indicated as dotted lines under $\lambda_{em} = 348 \text{ nm}$

The emission spectra of $\text{S}_{1-3x/2}\text{ASO}: \text{xCe}^{3+}$ samples monitored at 294 nm are reported in **Figure 3-12**. In addition to two well-shaped emission peaks at 321 nm and 348 nm related to Ce^{3+} cations, an unexpected broad band is also observed at $\sim 400 \text{ nm}$ which present similar features with that 430 nm in CASO.

The intensities of the emission from Ce^{3+} increase from 0.1% till 7%. Then the emission intensities start decreasing due to the concentration quenching. Thus, the critical concentration x_c is estimated around 7%. The associated critical distance (R_c) for ET can also be calculated by the **Equation (3-1)** and is determined to be $\sim 22.81 \text{ \AA}$.

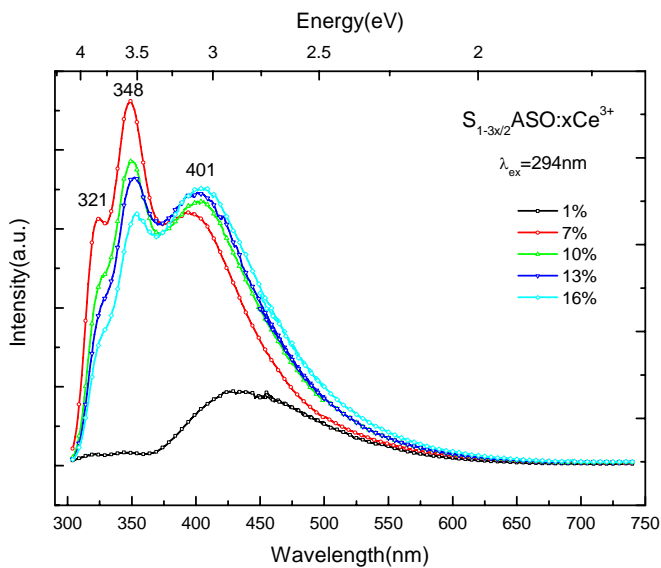


Figure 3-12 . Influence of doping concentration on the emission spectra of $S_{1-3x/2}ASO:xCe^{3+}$ samples under $\lambda_{ex} = 294$ nm.

Like for the CASO matrix, a decomposition of emission spectra into Gaussian functions has also been carried out for two distinct excitation wavelengths (**Figures 3-13 and 3-14**). An example is given by the 7% Ce^{3+} doped SASO sample.

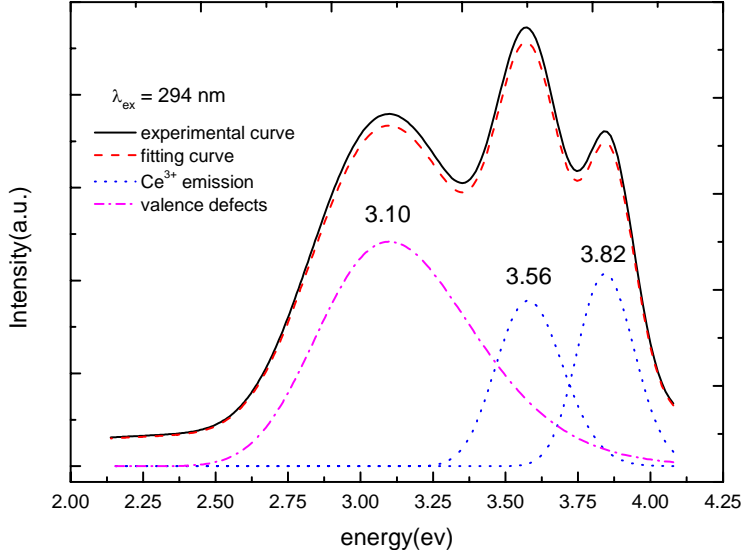


Figure 3-13 . Emission spectra of $S_{1-3x/2}ASO :xCe^{3+}$ ($x = 7\%$) with decomposition in Gaussian curves under $\lambda_{ex} = 294$ nm.

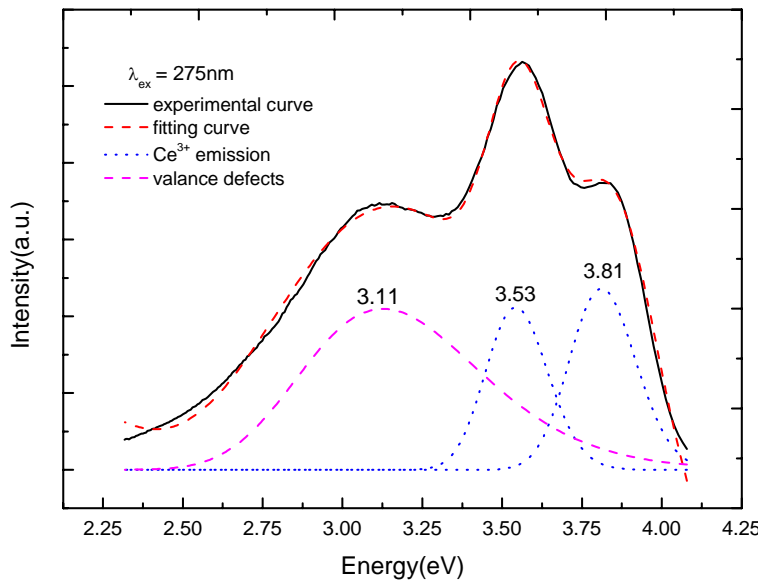
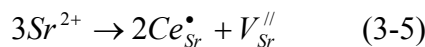


Figure 3-14. Emission spectra of $\text{S}_{1-3x/2}\text{ASO} : x\text{Ce}^{3+}$ ($x = 7\%$) with decomposition in Gaussian curves under $\lambda_{\text{ex}} = 275\text{nm}$.

The asymmetric emission band is fitted by the sum of three components. In the higher energy range, the two bands are accounting for the transition from the lowest-lying excited d-state to the $^2\text{F}_{5/2}$ and $^2\text{F}_{7/2}$ ground state. In the lower energy range, the additional band is likely due to the vacancies of $V_{\text{Sr}}^{/\!/}$ when doped trivalent Ce^{3+} substituted the divalent Sr^{2+} ion as expressed by the **Equation (3-5)**:



Just in passing, let us notice for this sample that the $5\text{d} \rightarrow ^2\text{F}_{7/2}$ band is much more intense than expected for isolated Ce^{3+} activator (normally the intensity ratio between $5\text{d} \rightarrow ^2\text{F}_{7/2}$ and $5\text{d} \rightarrow ^2\text{F}_{5/2}$ is about $1/2$ [27]). This accounts for emission-reabsorption phenomena which strongly impact the intensity of the $5\text{d} \rightarrow ^2\text{F}_{7/2}$ and $5\text{d} \rightarrow ^2\text{F}_{5/2}$ transition, the former increasing at the expense of the latter.

Figure 3-15 shows the excitation spectra of the samples $\text{S}_{1-3x/2}\text{ASO} : x\text{Ce}^{3+}$ ($x = 2\%$ and 10%) monitored at $\lambda_{\text{em}} = 401\text{ nm}$, the "defect" emission band. **Figure 3-15** turns out to be very similar with **Figure 3-11**, except the addition of an extra "band" located at 348 nm. This

means that the "defect" can be excited at the same energies than Ce^{3+} dopant, and in addition at the emission wavelength of Ce^{3+} in SASO.

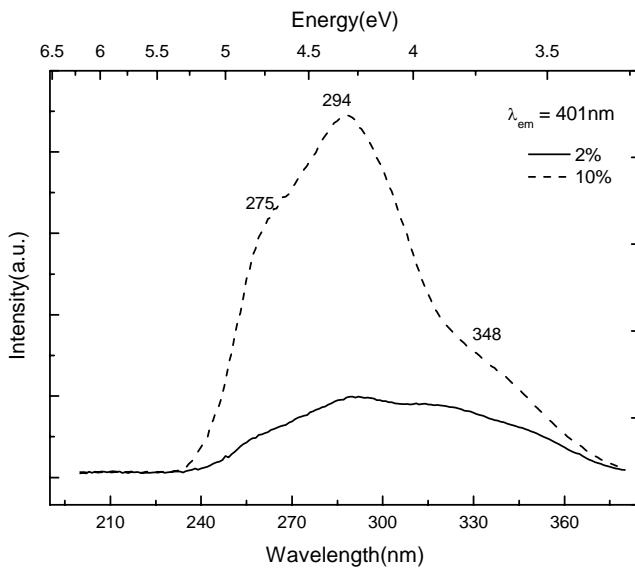


Figure 3-15. Excitation spectra of the samples $S_{1-3x/2}ASO: xCe^{3+}$ ($x = 2\%$ and 10%) under $\lambda_{em} = 400$ nm.

Moreover, **Figure 3-16** shows the emission spectra of SASO, $S_{1-3x/2}ASO: xCe^{3+}$, $S_{1-2x}ASO: xCe^{3+}, xK^+$, $C_{1-3x/2}ASO: xLa^{3+}$ and $S_{1-2x}ASO: xLa^{3+}, xK^+$, respectively with $x = 0.05$ under $\lambda_{ex} = 294$ nm. Again, as for the CASO derivatives, the additional "defect" band tends to decrease in intensity when K^+ cations are co-inserted in the host lattice with La^{3+} or Ce^{3+} cations to eliminate the V_{Sr}^{II} vacancies. Thus, we can again confirm that the additional band in the 400 nm region is also due to the presence of V_{Sr}^{II} vacancies as followed by the **Equation (3-6):**



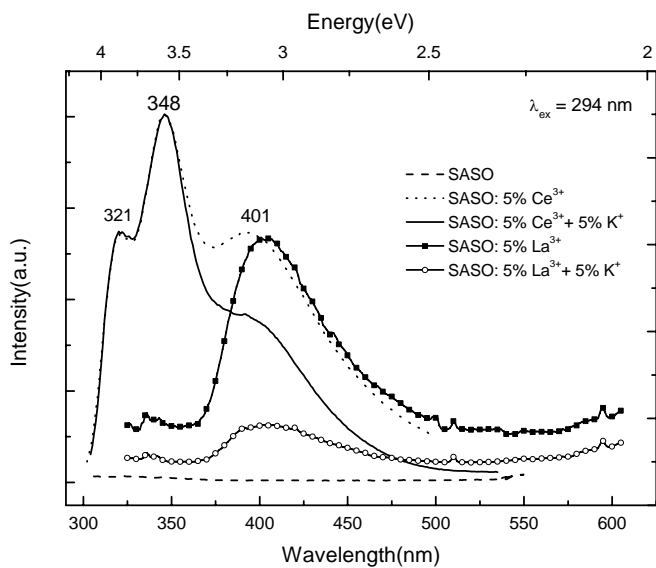


Figure 3-16. Emission spectra of SASO, $S_{1-3x/2}\text{ASO}:x\text{Ce}^{3+}$, $S_{1-2x}\text{ASO}:x\text{Ce}^{3+}$, $x\text{K}^+$, $C_{1-3x/2}\text{ASO}:x\text{La}^{3+}$ and $S_{1-2x}\text{ASO}:x\text{La}^{3+}$, $x\text{K}^+$, respectively, under $\lambda_{\text{ex}} = 294 \text{ nm}$.

On the basis of the peak deconvolution result and the transition paths described above, an energy level scheme for Ce^{3+} in $S_{1-3x/2}\text{ASO}:x\text{Ce}^{3+}$ can be proposed in **Figure 3-17**. Let us notice that the SASO host lattice exhibits an optical gap of $\sim 4 \text{ eV}$ according to Clabau et al [24]. This means that the "defect" emission could be triggered via excitation of Ce^{3+} as well the host lattice itself.

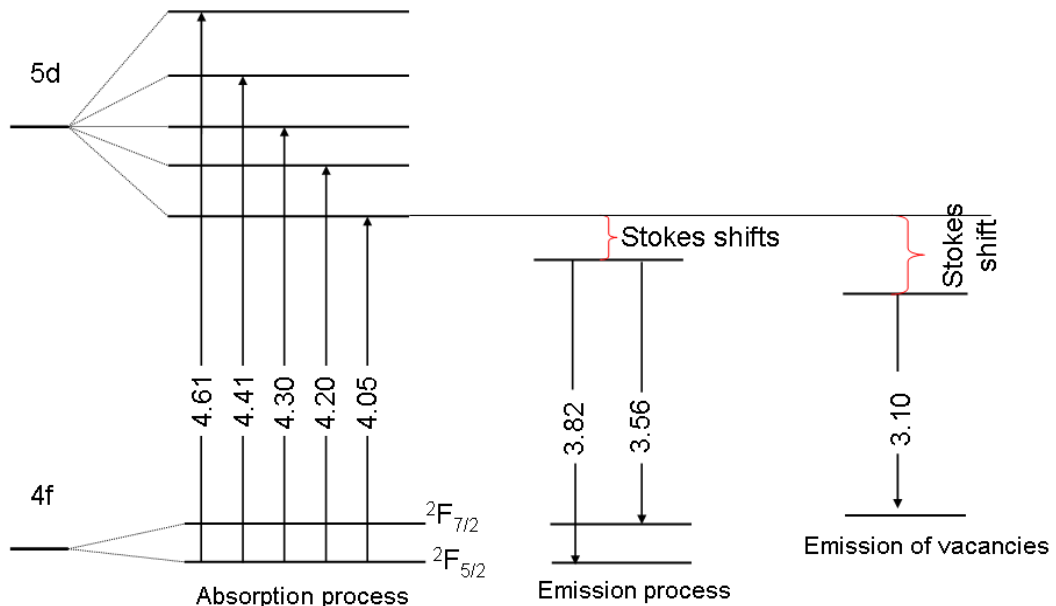


Figure 3-17. Proposed energy level scheme for Ce 4f and 5d levels and $V_{\text{Sr}}^{1/2}$ vacancies in $S_{1-3x/2}\text{ASO}:x\text{Ce}^{3+}$. Numbers shown over the arrows indicate the corresponding transition energies in eV

3.3 Comparison of CASO: xCe^{3+} and SASO: xCe^{3+} fluorescences

At present, we can notice that emission peaks of Ce^{3+} doped SASO phosphors are all shift toward the higher energy side compared to the Ce^{3+} doped CASO (340 nm and 356 nm in CASO, 321 nm and 348 nm in SASO, respectively). This blue shift behaviour can be explained by the different effect of the crystal field in CASO and SASO matrixes [28, 29]. As the ionic radius (Ca^{2+} , Sr^{2+}) and structure are quite different (coordination of 6 and 7 of Ce in CASO, and 9 in SASO), the crystal field intensity around Ce^{3+} in CASO, SASO decreases from Ca to Sr. Therefore, the lowest 5d levels of Ce^{3+} in CASO matrix would become lower in energy than the ones of SASO matrix. The crystal field splitting of 5d levels for Ce^{3+} and the excitation and emission processes are shown in a schematic way as one can see in **Figure 3-18**. The emission of the defects related to AE vacancies are modified as expected due to the change in the structure and composition.

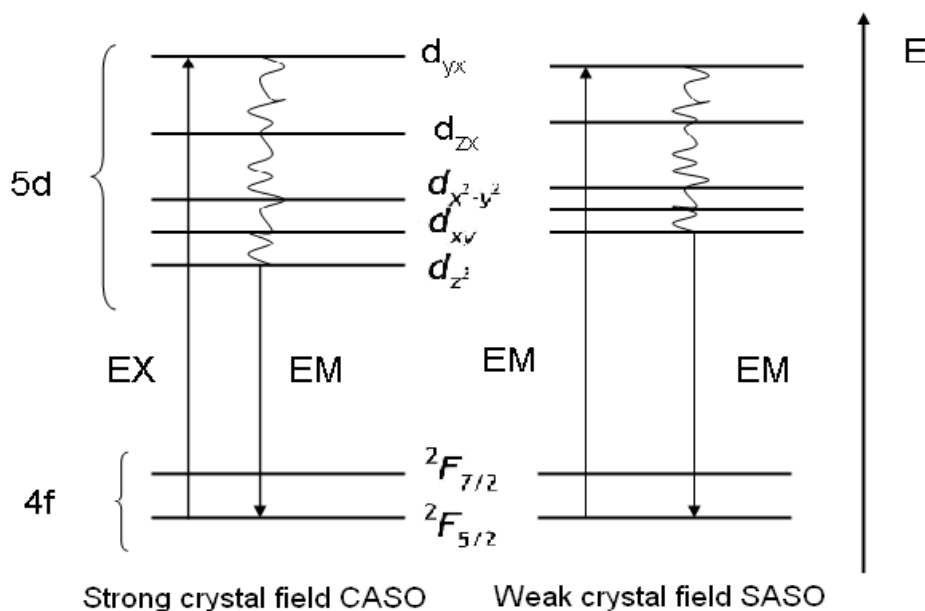


Figure 3-18. Schematic diagram for Ce^{3+} energy levels in CASO and SASO crystal fields

4. Fluorescence of MASO doped with Mn^{2+}

4.1. Fluorescence of $\text{C}_{1-x}\text{ASO:xMn}^{2+}$ ($x = 0.5\% \text{ to } 15\%$)

The PL and PLE for purely Mn^{2+} activated CASO are represented in **Figure 3-19**. The PLE spectrum consists of several weak bands in the UV and visible regions. These bands are assigned to the spin-forbidden transitions within the $3d^5$ electron configurations of the Mn^{2+} ions. As the d-d transitions of Mn^{2+} are forbidden in spin and parity, those transitions are difficult to pump and emission intensity is usually very weak. According to the Orgel diagram for divalent Mn^{2+} [30], the excitation spectrum consists of several bands centered at ~ 339 , 353 , 403 , 416 , and 470 nm which would correspond to the transitions from the ground state of ${}^6\text{A}_1({}^6\text{S})$ to the sub-levels of ${}^4\text{E}({}^4\text{D})$, ${}^4\text{T}_2({}^4\text{D})$, $[{}^4\text{A}^1({}^4\text{G}), {}^4\text{E}({}^4\text{G})]$, ${}^4\text{T}_2({}^4\text{G})$, and ${}^4\text{T}_1({}^4\text{G})$, respectively. Moreover the intense broad emission band centered at ~ 568 nm is attributed to the spin-forbidden ${}^4\text{T}_1({}^4\text{G}) \rightarrow {}^6\text{A}_1({}^6\text{S})$ transition of Mn^{2+} .

Due to the photoluminescence property of Mn^{2+} ions and the low dopant concentration in the CASO matrix, it is difficult to observe the excitation and emission spectra for the $\text{C}_{0.995}\text{ASO}: 0.5\%\text{Mn}^{2+}$ sample. However, excitation and emission can be observed for higher dopant rate (**Figure 3-19**). Mn^{2+} ion in solid materials is usually characterized by a green emission in tetrahedral coordination and by a yellow-red emission in octahedral coordination [6, 7, 17-19, 31]. The emission at 568 nm suggests that Mn^{2+} cations are located at the alkaline-earth site instead of being at the Al or Si sites as already proposed by [9] for $\text{CaAl}_2\text{Si}_2\text{O}_8$. This was expected on the basis of steric considerations.

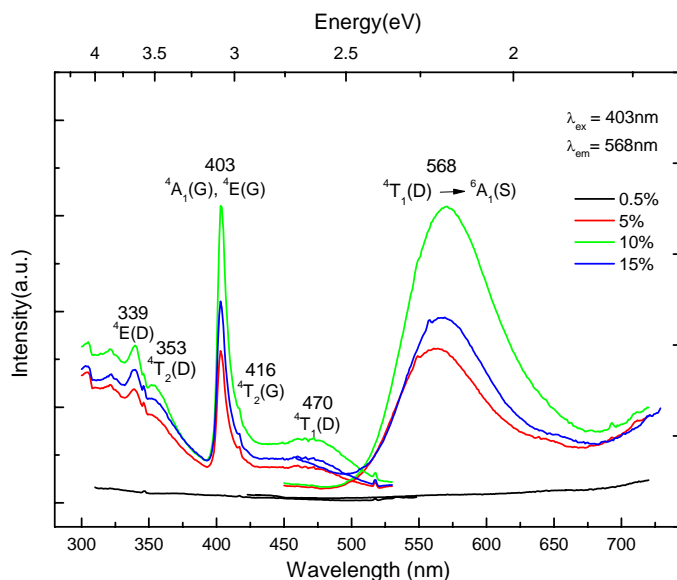


Figure 3-19. Photoluminescence excitation and emission spectra of $C_{1-x}ASO:xMn^{2+}$ ($x = 0.5\%$ to 15%).

The quenching concentration of Mn²⁺ in CASO was found to be $\sim 10\%$ mol per formula unit. Then, the critical distance R_{Mn-Mn} between nearest Mn²⁺ cations can be estimated to be around 17 Å. As shown in **Figure 3-19**, we also observed that the radiative emission from Mn²⁺ prevailed when $R_{Mn-Mn} > R_c$ ($x < 10\%$), whereas ET between Mn²⁺ and Mn²⁺ dominated when $R_{Mn-Mn} < R_c$ ($x > 10\%$). Furthermore, as the d-d transitions of Mn²⁺ ion are difficult to pump, the transitions energy between the ground state and excited sub-levels states are weak. Thus, we can suppose that the energy differences between the Mn₁ (occupying the Ca₁ site) and the other sites Mn_{2,3,4} (occupying the Ca_{2,3,4} sites) are also weak and thus not easy to distinguish. Under this consideration, we can not give proper assignments to the emission and excitation spectra of Mn²⁺. Furthermore, the large Stocks shift (0.9 eV) of Mn²⁺ center in CASO matrix indicates that a strong electron-lattice interaction occurs inducing a bad resolution of emission band of Mn²⁺.

4.2. Fluorescence of $\text{S}_{1-x}\text{ASO}:x\text{Mn}^{2+}$ ($x = 0.5\%$ to 15%)

As mentioned above, the d-d transitions of Mn^{2+} are difficult to pump. In the case of SASO, this phenomenon is particularly present. For the SASO compound, the PLE spectrum (**Figure 3-20**) consists, as expected, of several weak bands located in the UV and visible regions. Peaks at ~ 334 , 346 , 401 , 416 , and 445 nm are associated with transitions from the ground state of ${}^6\text{A}_1({}^6\text{S})$ to the sub-levels of ${}^4\text{E}({}^4\text{D})$, ${}^4\text{T}_2({}^4\text{D})$, [${}^4\text{A}_1({}^4\text{G})$, ${}^4\text{E}({}^4\text{G})$], ${}^4\text{T}_2({}^4\text{G})$, and ${}^4\text{T}_1({}^4\text{G})$, respectively. Moreover, the broad emission band centered at ~ 550 nm is attributed to the spin-forbidden ${}^4\text{T}_1({}^4\text{G}) \rightarrow {}^6\text{A}_1({}^6\text{S})$ transition of Mn^{2+} and is blue shifted compared to CASO because of a change in the coordination of the Mn^{2+} ion going from calcium to strontium based alumino-silicate phases.

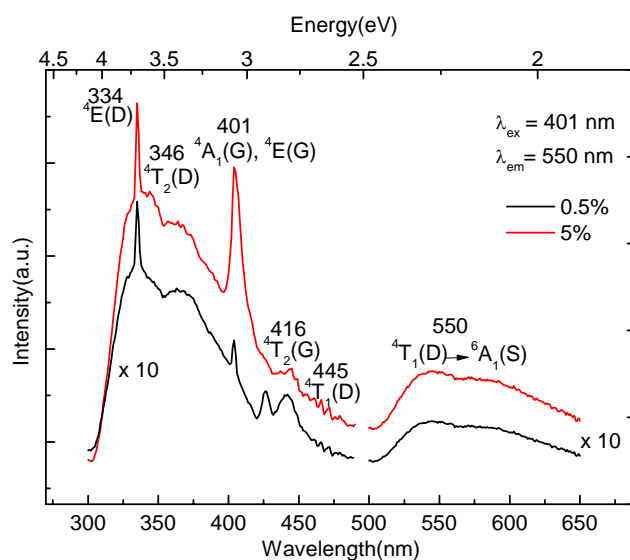


Figure 3-20 . Photoluminescence excitation and emission spectra of $\text{S}_{1-x}\text{ASO}:x\text{Mn}^{2+}$ ($x = 0.5\%$ and 5%)

5. The mechanism of the ET from Ce^{3+} to Mn^{2+} in the CASO and SASO matrixes

ET is an effective approach for enhancing and tuning the luminescence of phosphor. In this method, an activator and a sensitizer with efficient excitation properties are introduced into one matrix. When the sensitizer and the activator form small clusters in the lattice, efficient ET from the sensitizer to the activator takes place enhancing the luminescence. One of the essential conditions usually required for ET is the overlap between the sensitizer emission and the activator excitation spectra [6, 17-19, 32].

5.1. Energy transfer from Ce^{3+} to Mn^{2+} in CASO matrix

Figure 3-21 shows the spectral overlap between the photoluminescence spectrum of Ce^{3+} (solid line, $\lambda_{ex} = 294$ nm) and the photoluminescence excitation spectrum of Mn^{2+} (dashed line, $\lambda_{em} = 568$ nm) doped in CASO matrix. The comparison of the photoluminescence emission and excitation spectra for $C_{0.865}ASO:9\%Ce^{3+}$ and $C_{0.91}ASO:9\%Mn^{2+}$ phosphors reveals a light spectral overlap between the emission bands of Ce^{3+} and the V_{Ca}^{II} based "defect" band, and the main excitation band of Mn^{2+} . Therefore, it can be speculated that ET from Ce^{3+} and " V_{Ca}^{II} defects" to Mn^{2+} ions may occur through the effective resonance-type. Till up now, this kind of ET from Ce^{3+} to Mn^{2+} has also been observed in other structure hosts, such as in glaserite-type alkaline-earth silicates [33], fluoride and phosphate nanocrystals [19, 34], sulfide [31] ... There is no report on the use of Mn^{2+} and Ce^{3+} as co-dopants for improving the luminescence of MASO ($M = Ca, Sr$) based phosphors.

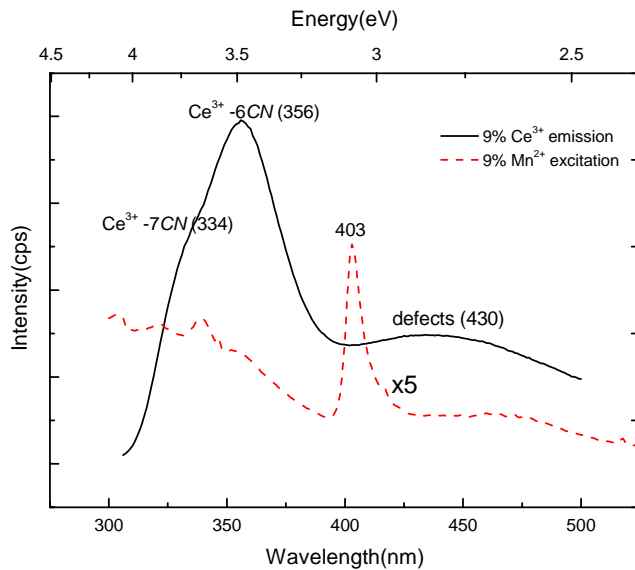


Figure 3-21. Spectral overlap between the photoluminescence spectrum of $\text{C}_{0.865}\text{ASO}:9\%\text{Ce}^{3+}$ (solid line) and photoluminescence excitation spectrum of $\text{C}_{0.91}\text{ASO}:9\%\text{Mn}^{2+}$.

Therefore, we have embarked on the investigation of the ET processes between Ce^{3+} and Mn^{2+} in the CASO matrix. **Figure 3-22** gathers the PLE of CASO: 9% Ce^{3+} monitored at 353 nm (Ce^{3+} emission), and CASO: 9% Ce^{3+} , 9% Mn^{2+} monitored at 353 nm and 568 nm (Mn^{2+} emission). It can be observed for CASO: Ce, Mn that photoluminescence excitation spectrum monitored by the Mn^{2+} emission ($\lambda_{\text{em}} = 568 \text{ nm}$, green line) has a profile very similar to that of the excitation band monitored by the Ce^{3+} emission ($\lambda_{\text{em}} = 353 \text{ nm}$, red line). This reveals that the Mn^{2+} ions can be essentially excited in the same energy range than Ce^{3+} ions. This observation, coupled with the strong decrease of the PLE going from CASO: 9%Ce (black line) to CASO: 9%Ce, 9%Mn (red line) confirms that an ET occurs from $\text{Ce}^{3+}/V_{\text{Ca}}^{\text{II}}$ to Mn^{2+} .

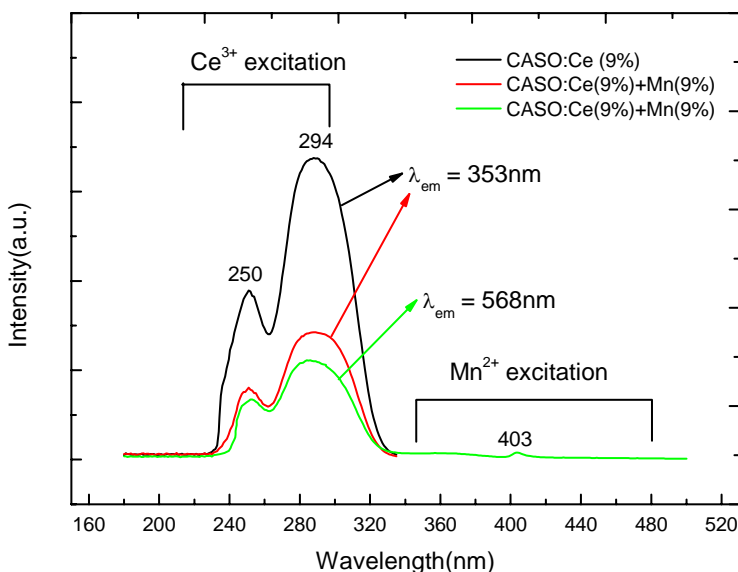


Figure 3-22 . Photoluminescence excitation of CASO:9% Ce^{3+} (black line), CASO:9% Ce^{3+} , 9% Mn^{2+} (red line) under $\lambda_{em} = 353$ nm and CASO:9% Ce^{3+} , 9% Mn^{2+} (green line) under $\lambda_{em} = 568$ nm.

Furthermore, the photoluminescence excitation spectra of the Mn^{2+} ions in the Ce^{3+} - and Mn^{2+} -co-activated sample extend from 230 to 340 nm, indicating that this phosphor could be, in principle, used in a UV white-light LED. In order to optimize the white-light-emitting performance of the phosphors, a series of samples with nominal compositions of $Ca_{0.865-y}ASO:0.09Ce^{3+}, yMn^{2+}$ were synthesized and their luminescent properties systematically investigated. **Figure 3-23** illustrates the photoluminescence emission spectra of the phosphor samples prepared with a fixed Ce^{3+} concentration (9%, the critical concentration of Ce^{3+} doped in CASO matrix) and different concentrations in Mn^{2+} (from 0 to 15%). Samples have been excited at 294 nm, which corresponds to the main excitation band of CASO: Ce, Mn. As expected, the broad violet-blue-green emission band from 320 to 500 nm is characteristic of the allowed f-d transition of the Ce^{3+} ion, accompanied by the vacancy defects emission which was created for the charge balance in the CASO matrix, whereas the intense broad yellow emission centered at 568 nm is attributed to the $^4T_1 \rightarrow ^6A_1$ forbidden transition of Mn^{2+} ions. The emission spectrum nearly covers almost the entire visible region for CASO: Ce,Mn in contrast with CASO: Ce and CASO: Mn alone. Moreover, the relative intensities of these three emissions can be varied and further combined to form pure white light in a single matrix by simply adjusting the amounts of the activators through the principle of ET. It is believed that the obtained white light would enable easy fabrication with perfect stability and color reproducibility [19, 35].

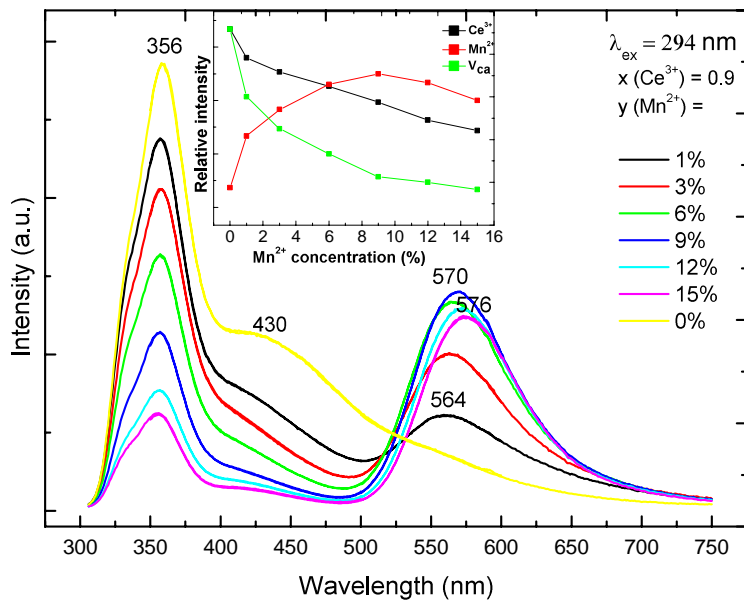


Figure 3-23. Photoluminescence spectra for $\text{C}_{0.865-y}\text{ASO}:9\%\text{Ce}^{3+},y\text{Mn}^{2+}$ phosphors versus the Mn^{2+} doping content (y), the inset shows the dependence of the relative emission intensity of Ce^{3+} (356 nm), V''_{Ca} defect (430 nm) and Mn^{2+} (570 nm) for CASO phosphors on the Mn^{2+} content, under $\lambda_{\text{ex}} = 294 \text{ nm}$.

As one can see in the inset of **Figure 3-23**, the intensity of the Ce^{3+} emission decreases monotonically with the increase of the Mn^{2+} content, whereas the Mn^{2+} emission intensity reaches a maximum at about 9% Mn^{2+} before decreasing. Note here that the intensity of bands originated from vacancies and located at $\sim 430 \text{ nm}$ also decrease when Mn^{2+} rate increases. This phenomenon indicates that the ET also occurs from these bands to Mn^{2+} ions. **Figure 3-24** illustrates possible mechanisms at work in CASO: Ce,Mn.

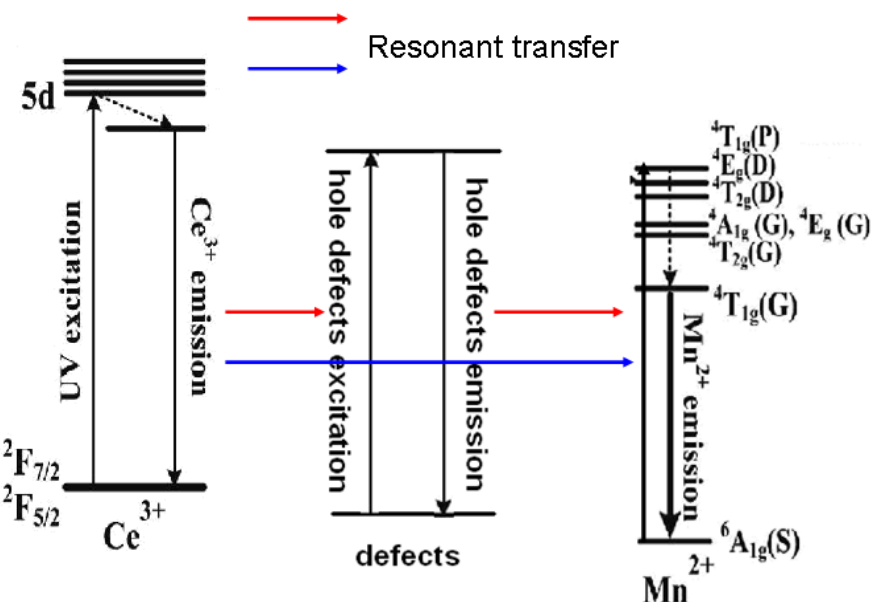


Figure 3-24. Energy level diagram of the CASO:Ce,Mn with $Ce^{3+} (V_{Ca}^{\prime\prime}) \rightarrow Mn^{2+}$ energy transfer processes

At present, we will examine the efficiency (η_T) of the ET from $Ce^{3+}/V_{Ca}^{\prime\prime}$ to Mn^{2+} . Generally, the ET efficiency from a sensitizer to activator can be expressed by the following **Equation (3-7)** [18, 19, 25, 32]:

$$\eta_T = 1 - \frac{I_s}{I_{s0}} \quad (3-7)$$

where η_T is the ET efficiency and I_0 and I_s are the luminescence intensity of a sensitizer in the absence and presence of an activator, respectively. In our case, I_{s0} is the intrinsic emission intensity of the sensitizer (Ce^{3+}) and I_s is the emission intensity of the sensitizer (Ce^{3+}) in the presence of the activator (Mn^{2+}) for identical cerium concentrations. **Figure 3-25** shows the results of ET efficiency from Ce^{3+} to Mn^{2+} calculated by the previous **Equation (3-7)** for the $C_{0.865-y}ASO: 9\%Ce^{3+}, yMn^{2+}$ ($y = 1\%$ to 15%) samples. As shown in **Figure 3-25**, the ET efficiency increases with increasing Mn^{2+} concentration. However, the slope of the emission intensity gradually decreases when Mn^{2+} concentration increases. This indicates that the quantity of energy that can transfer from Ce^{3+} to Mn^{2+} is gradually restricted for high Mn^{2+} concentration due to: 1) the fixed concentration of Ce^{3+} and 2) the concentration quenching of Mn^{2+} to a lesser extent.

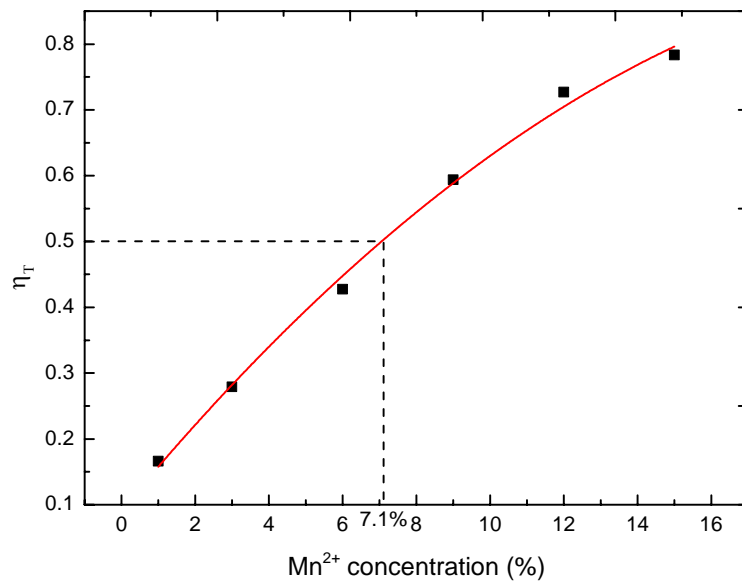


Figure 3-25. Dependence of the energy transfer efficiency η_T on the Mn^{2+} content (y) for the $\text{C}_{0.865-y}\text{ASO}:9\%\text{Ce}^{3+},y\text{Mn}^{2+}$ samples under $\lambda_{ex} = 294$ nm.

Two types of resonant ET mechanism exist. One corresponds to exchange interactions and the other to multipolar interactions [19, 25, 27]. It is well-known that if ET is based on exchange interaction, the critical distance between the sensitizer and activator should be shorter than about 10 Å. We previously saw that the critical distance can be calculated from the quenching concentration. From **Figure 3-25**, the critical concentration can be determined to be about 0.161 (= 0.09 (Ce³⁺ concentration) + 0.071 (Mn²⁺ concentration)) from the total concentration of Ce³⁺ and Mn²⁺ for which the ET efficiency is 0.5. Therefore, the critical distance R_c (Ce³⁺-Mn²⁺) was calculated to be ~15.21 Å. This value is too large to lead to exchange interaction via orbital overlaps. Consequently, the electric multipolar interaction must be considered for ET between Ce³⁺ and Mn²⁺ ions in the CASO matrix.

At present, on the basis of the Dexter's ET formula of multipolar interaction and Reisfeld's approximation, the following **Equation (3-8)** can be obtained [6, 9, 10, 19, 35]:

$$\frac{I_{S0}}{I_S} \propto C^{\alpha/3} \text{ or } \frac{\tau_{S0}}{\tau_S} \propto C^{\alpha/3} \quad (3-8)$$

where I_{S0} and I_S have the same meaning as above. C is the concentration of Mn^{2+} . α equal to 6, 8, 10 for dipole-dipole, dipole-quadrupole, quadrupole-quadrupole interactions, respectively. Plots of I_{S0}/I_S based on the above equation are shown in **Figure 3-26**. As one can see, linear behavior is only observed when $\alpha = 6$, which implies that ET from Ce^{3+} to Mn^{2+} occurred via a dipole-dipole mechanism. This is quite surprising because a dipole-quadripole interactions was expected however this was already observed in the literature for several series of materials [36]. In the present case, the same results were obtained for CASO: Ce,Mn with 1% Ce and Mn concentration between 0 and 12 %.

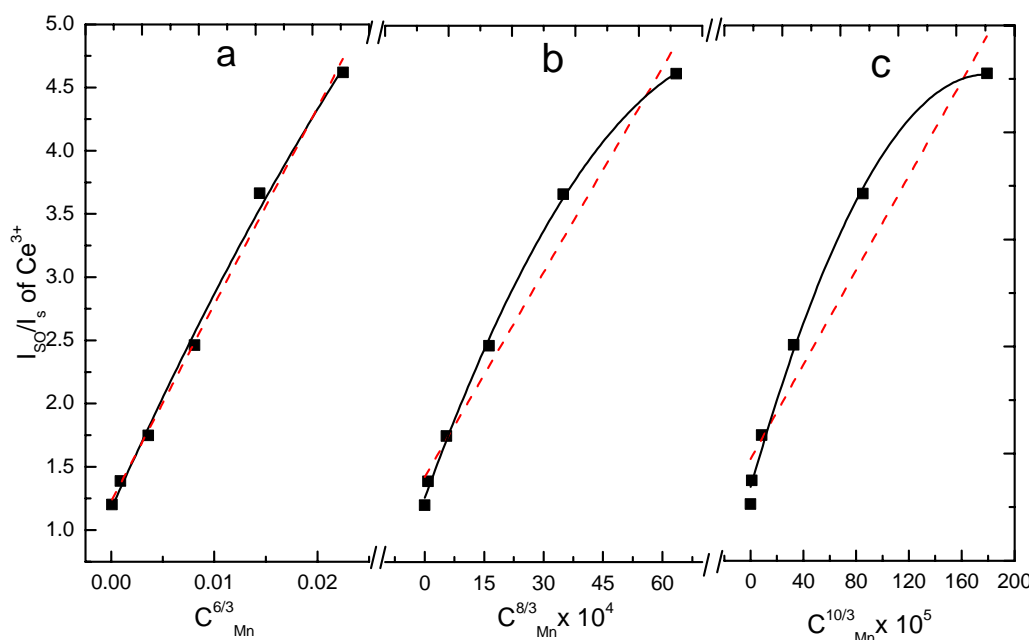


Figure 3-26. Dependence of I_{S0}/I_S of Ce^{3+} versus $\alpha = 6, 8$ and 10 for the samples $C_{0.865-y}ASO: 9\%Ce^{3+}, yMn^{2+}$.

To confirm these results based on intensity measurements only, the decay curves of the $C_{0.865-y}ASO: 9\%Ce^{3+}, yMn^{2+}$ ($y = 0$ to 15%) samples were also collected. These ones are depicted in **Figure 3-27** while decay times are reported in **Table 3-1**. For the first three samples, the decay curve was best fitted with a monoexponential function whereas for others samples the decays curves were fitted with a biexponential function.

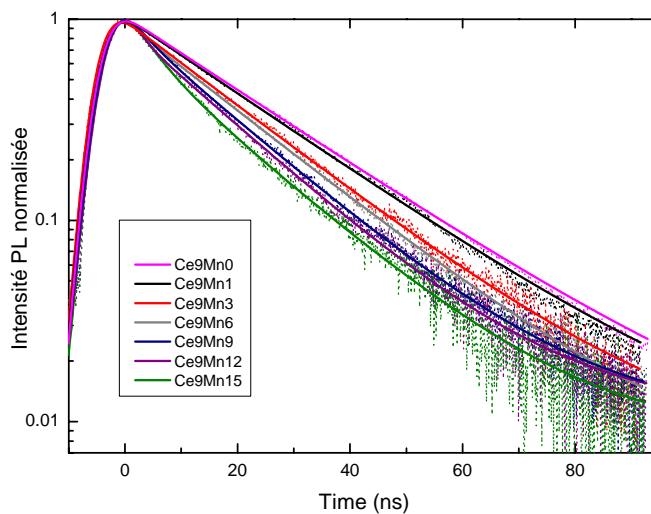


Figure 3-27. Decay curve obtained under excitation $\lambda_{\text{ex}} = 267 \text{ nm}$ and emission $\lambda_{\text{em}} = 360 \text{ nm}$ (centered at the maximum emission of Ce^{3+} in the CASO matrix). Dotted lines represent the experimental value and solid lines represent the fitting value

Table 3-1 : The results of the decay times for the samples $\text{C}_{0.865-y}\text{ASO}:9\%\text{Ce}^{3+},y\text{Mn}^{2+}$ ($y = 0$ to 15%) ($\lambda_{\text{em}} = 360 \text{ nm}$)

Phosphors	A_1	A_2	$\tau_1 \text{ (ns)}$	$\tau_2 \text{ (ns)}$	$\langle \tau \rangle \text{ (ns)}$
Ce9Mn0	-	-	23.524	-	23.524
Ce9Mn1	-	-	22.665	-	22.665
Ce9Mn3	-	-	20.280	-	20.280
Ce9Mn6	8.1	91.9	0.682	19.654	18.117
Ce9Mn9	7.0	93.0	3.067	17.963	16.920
Ce9Mn12	12.8	87.2	0.663	17.268	15.143
Ce9Mn15	17.5	82.5	4.697	17.803	12.073

From **Table 3-1** and **Figure 3-27**, one can also notice that the meantime value $\langle \tau \rangle$ decreases when the concentration of Mn increases. Thus we can further confirm that the ET from Ce^{3+} to Mn^{2+} occurs in the CASO matrix. Furthermore, we can also conclude that the ET is a resonant non-radiative transfer because the decay times of the Ce^{3+} decreases with the Mn^{2+} ion concentration. The plots of $\tau_{\text{S0}}/\tau_{\text{S}}$ that are calculated from the previous **Equation (3-8)** are reported in **Figure 3-28**. This plot also proves that the dipole-dipole interactions are at work ($\alpha = 6$) even if dipole-quadripole interactions cannot be now totally rebutted ($\alpha = 8$). Consequently, at this stage, we may wonder whether this transfer we observed is (in some extent) a Ce-Ce ET instead of a Ce-Mn one.

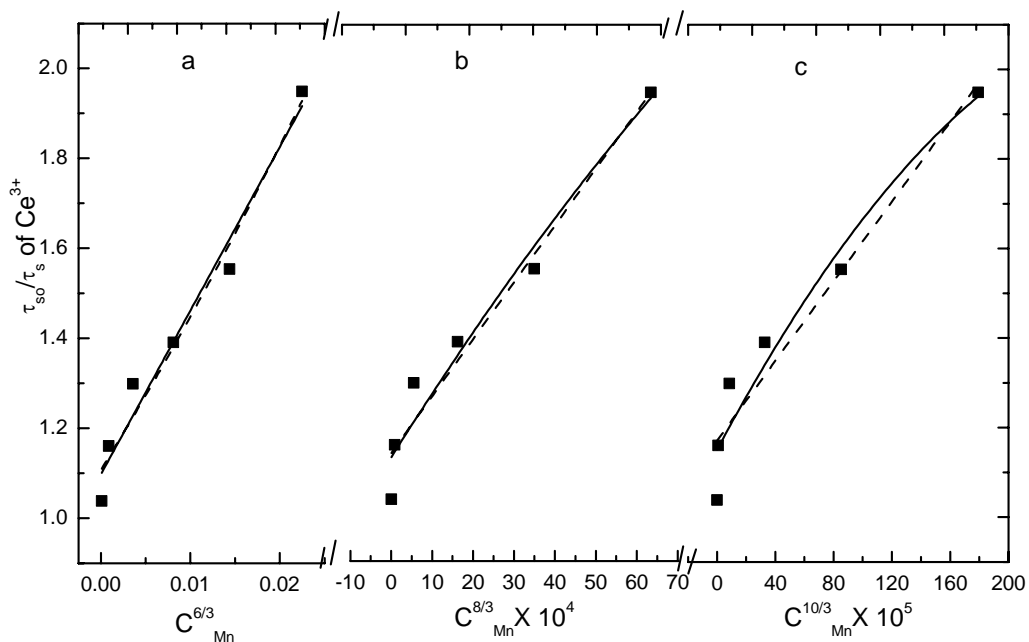


Figure 3-28. Dependence of τ_{S0}/τ_S of Ce^{3+} on $\alpha = 6, 8$ and 10 for the samples $C_{0.865-y}ASO : 9\%Ce^{3+}, yMn^{2+}$.

As mentioned above, an ET also occurs between the defects emission (V_{Ca}^{\parallel}) and the Mn^{2+} ions in the CASO matrix. The ET efficiency from V_{Ca}^{\parallel} to Mn^{2+} ions in the samples $C_{0.865-y}ASO: 9\%Ce^{3+}, yMn^{2+}$ ($y = 1\%$ to 15%) phosphors were also calculated and the results are presented in **Figure 3-29**. As one can see, the ET efficiency increases gradually with the increase of Mn^{2+} concentration. The rate of increase of the emission intensity dramatically decreases with increasing Mn^{2+} concentration and the efficiency in the V_{Ca}^{\parallel} - Mn^{2+} transfer is higher than in the Ce^{3+} - Mn^{2+} when compared to the ET from Ce^{3+} to Mn^{2+} shown in **Figure 3-25**. These phenomena in the V_{Ca}^{\parallel} - Mn^{2+} may be due to a better overlap between the emission of the V_{Ca}^{\parallel} (~ 420 nm) with the excitation of the Mn^{2+} (~ 403 nm) compared to the emission of Ce^{3+} at 356 nm.

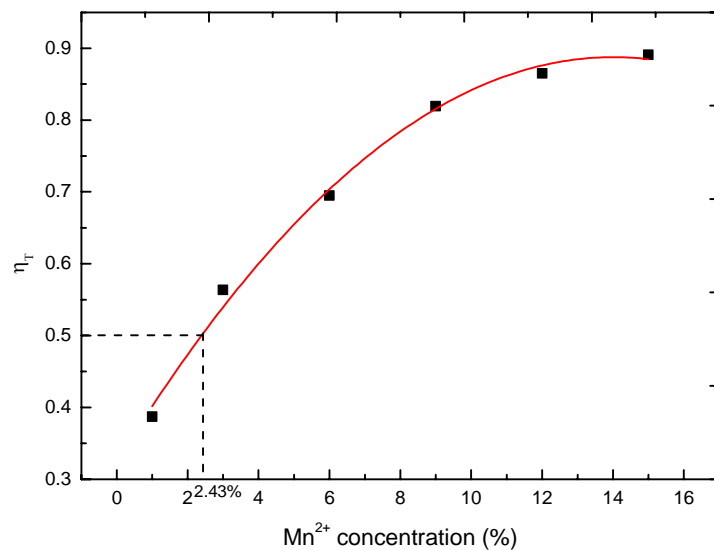


Figure 3-29. Dependence of the energy transfer efficiency η_T from $V_{\text{Ca}}^{\text{II}}$ to Mn^{2+} (on the Mn^{2+} content (y))

The critical concentration R_c ($V_{\text{Ca}}^{\text{II}}$ - Mn^{2+}) for energy transfer from $V_{\text{Ca}}^{\text{II}}$ to Mn^{2+} ions was also calculated and estimated to be around 17 Å for a $V_{\text{Ca}}^{\text{II}}$ concentration of ~ 0.045 and a quenching concentration for Mn^{2+} of 2.43%. In the same way as previously described, the mechanism of multipolar interactions can be expected. **Figure 3-23** was used to determine the intensities of the emissions from the defects ($V_{\text{Ca}}^{\text{II}}$) for samples $\text{C}_{0.865-y}\text{ASO}: 9\%\text{Ce}^{3+}, y\text{Mn}^{2+}$. For those samples, the Ce^{3+} concentration is fixed and consequently, the content of defects also ($V_{\text{Ca}}^{\text{II}}$). As one can see in **Figure 3-30**, a linear behavior is only observed when α is equal to 6, meaning that a dipole-dipole interactions also occurs between vacancies ($V_{\text{Ca}}^{\text{II}}$) and Mn^{2+} ions.

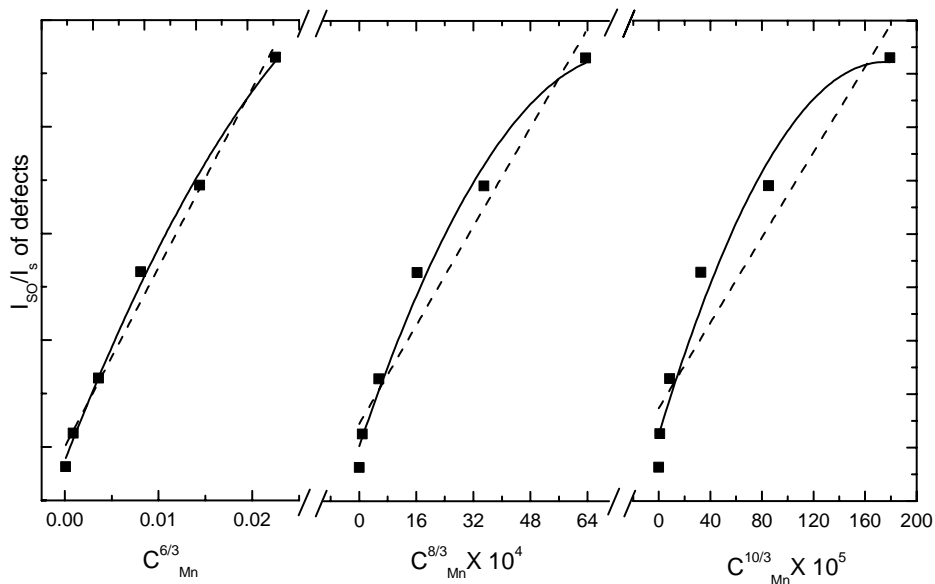


Figure 3-30. Dependence of I_{SO}/I_s of defects emission ($V_{Ca}^{||}$) versus $\alpha = 6, 8$ and 10 (fixed Ce^{3+} (thus, $V_{Ca}^{||}$), change the concentration of Mn^{2+})

5.2. Energy transfer from Ce^{3+} to Mn^{2+} in SASO matrix

In a similar way, we will discuss about the ET property in the SASO host lattice when co-doped Ce^{3+} and Mn^{2+} . As one can see in **Figure 3-31**, Mn^{2+} ion in the SASO host lattice are difficult to pump, and consequently, the excitation spectrum intensities of Mn^{2+} ion are very weak. However, as the excitation spectrum of Mn^{2+} slightly overlaps the emission spectrum of Ce^{3+} in the SASO matrix, we can also strongly suppose that there would be an ET from Ce^{3+} to Mn^{2+} when the host lattice is co-doped.

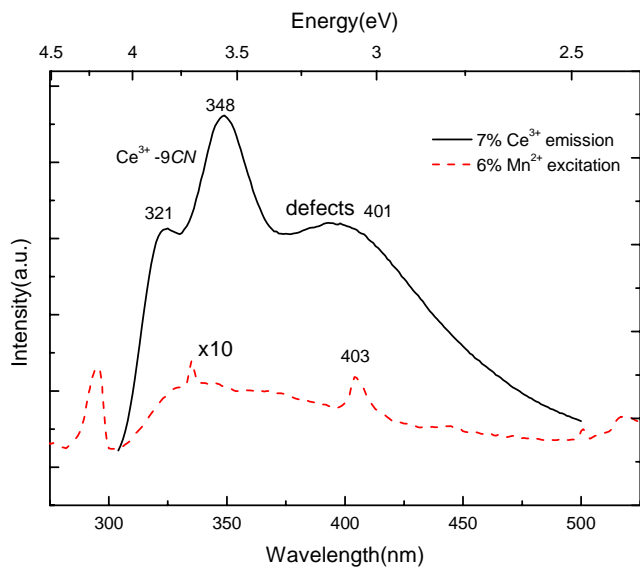


Figure 3-31. Spectral overlap between the photoluminescence spectrum of $\text{S}_{0.895}\text{ASO}:7\%\text{Ce}^{3+}$ (solid line) and photoluminescence excitation spectrum of $\text{S}_{0.94}\text{ASO}:6\%\text{Mn}^{2+}$

Co-doping Ce/Mn has also been performed in the SASO matrix. In **Figure 3-32** is depicted PLE spectra for the phosphor CASO: 7% Ce^{3+} , 6% Mn^{2+} monitored at $\lambda_{\text{em}} = 348$ nm and $\lambda_{\text{em}} = 550$ nm. One can notice that PLE spectra have the same overall profile whatever the emission wavelength and that the Mn^{2+} emission at 550 nm can be triggered via excitation in the 320-240 nm range, i.e. energy characteristic of Ce^{3+} -4f \rightarrow 5d transition. This is another clue to confirm that ET between Ce^{3+} and Mn^{2+} may occur in SASO.

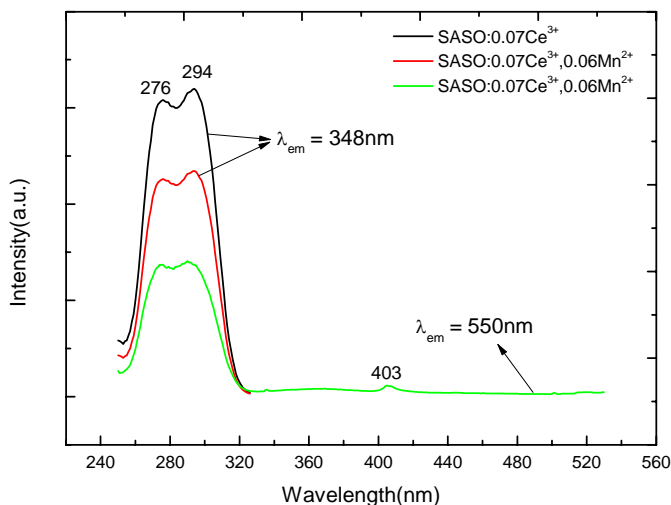


Figure 3-32 . Photoluminescence excitation of SASO:7% Ce^{3+} (black line), SASO:7% Ce^{3+} , 6% Mn^{2+} (red line) under $\lambda_{\text{em}} = 348$ nm and CASO:7% Ce^{3+} , 6% Mn^{2+} (green line) under $\lambda_{\text{em}} = 550$ nm.

Figure 3-33 shows the PLE and PL spectra for Ce^{3+} and Mn^{2+} co-activated $S_{0.895-y}ASO: 0.07Ce^{3+}, yMn^{2+}$ phosphors with different Mn^{2+} contents ($y = 0, 1\%, 3\%, 6\%, 9\%, 12\%$ and 15%). As one can see, the emission intensities of Mn^{2+} (around 550 nm) slightly increase till 6%, whereas emission bands originated from Ce^{3+} and $V_{Sr}^{''}$ defects continuously decreases with the Mn^{2+} content. **Figure 3-34** shows the dependence of the relative emission intensities of Ce^{3+} , $V_{Sr}^{''}$ and Mn^{2+} in the samples $S_{0.895-y}ASO: 0.07Ce^{3+}, yMn^{2+}$ ($y = 0$ to 15%) on y contents.

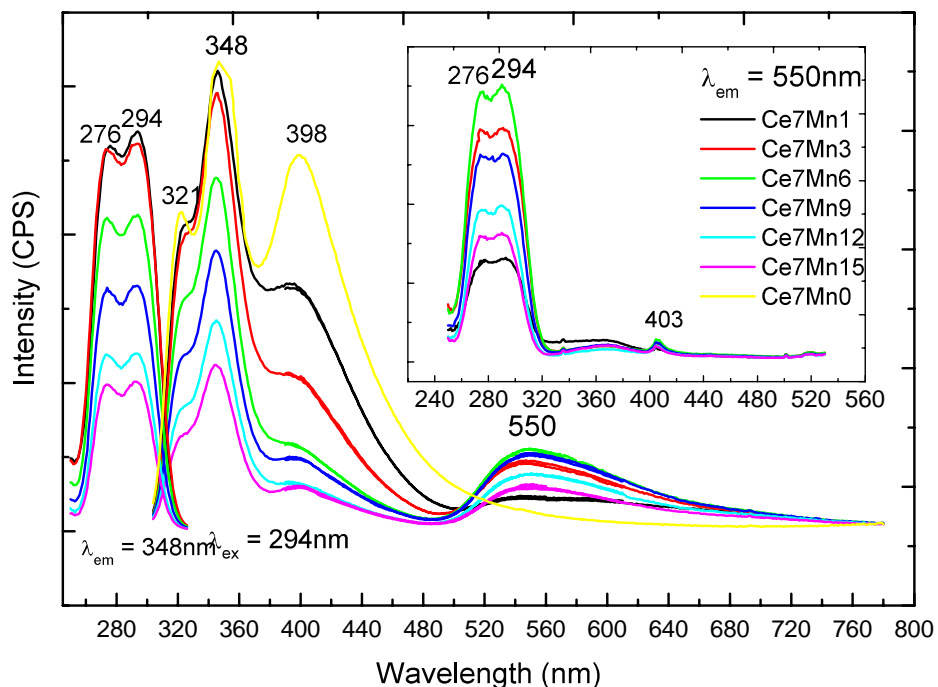


Figure 3-33 . Photoluminescence excitation and photoluminescence spectra for $S_{1-3x/2-y}ASO: xCe^{3+}, yMn^{2+}$ ($x = 7\%$, $y = 0$ to 15%) phosphors, under $\lambda_{ex} = 294\text{nm}$ and monitored at $\lambda_{em} = 348\text{nm}$ and 550nm (the inset), respectively

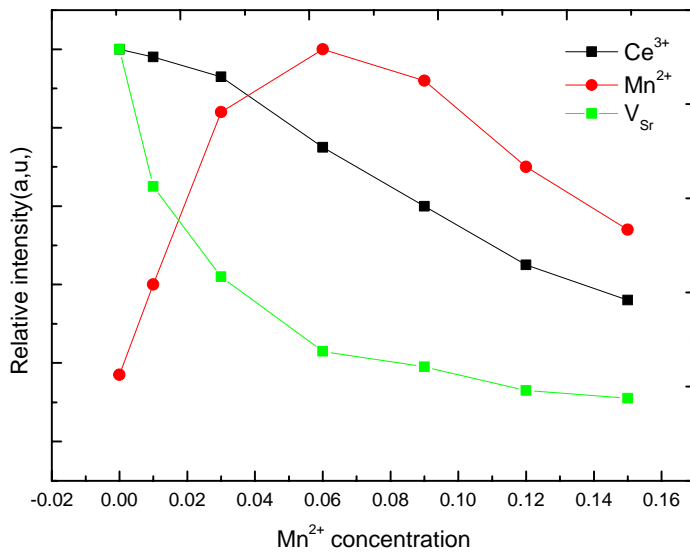


Figure 3-34. Dependence of the relative emission intensities of Ce^{3+} , $V_{\text{Sr}}^{\parallel}$ and Mn^{2+} in the samples $\text{S}_{1-3x/2-x}\text{ASO}: x\text{Ce}^{3+}, y\text{Mn}^{2+}$ ($x = 7\%$, $y = 0$ to 15%) on y contents

At present, the ET efficiency from Ce^{3+} to Mn^{2+} can be calculated as previously explained for the CASO matrix. **Figure 3-35** shows the result of ET efficiency from Ce^{3+} to Mn^{2+} for different Mn^{2+} concentration. It can be noticed that the ET efficiency increases with increasing Mn^{2+} concentration. This trend is similar to that of result portrayed for the CASO system. The critical distance was also estimated from the quenching concentration. From **Figure 3-35**, the critical concentration can be assessed to be about 0.183 (= 0.07 (Ce³⁺ concentration) + 0.113 (Mn²⁺ concentration)) from the total concentration of the Ce³⁺ and Mn²⁺ ions for which the energy transfer efficiency is 0.5 in the SASO matrix. Based on the above data, the critical distance $R_c(\text{Ce}^{3+}-\text{Mn}^{2+})$ was calculated to be ~ 15.02 Å. At this stage, we can confirm again that ET occurs via multipolar interaction..

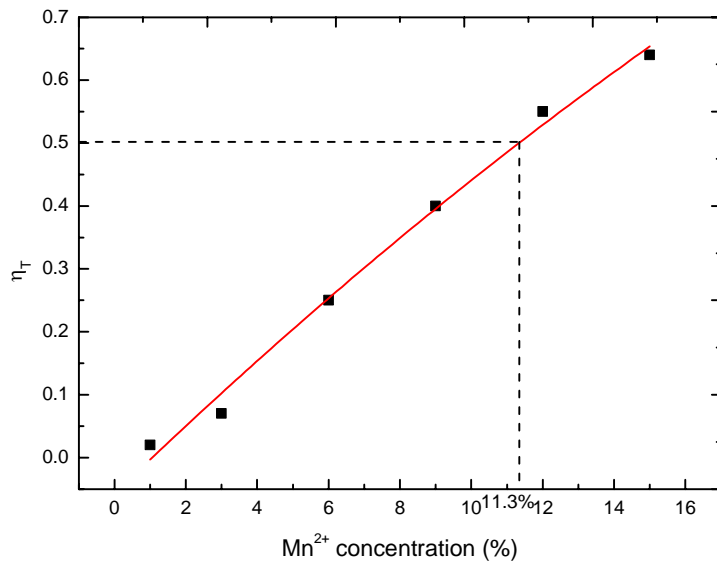


Figure 3-35. Dependence of the energy transfer efficiency η_T on the Mn^{2+} content (y) for the samples $S_{0.895-y}ASO: 7\%Ce^{3+}, yMn^{2+}$ matrix under $\lambda_{ex} = 294$ nm

The plot of I_{SO}/I_S vs C^α given in **Figure 3-36** gets a linear relationship when $\alpha = 6$. This also clearly indicates that the ET mechanism from Ce^{3+} to Mn^{2+} ions belongs to dipole-dipole interaction in nature.

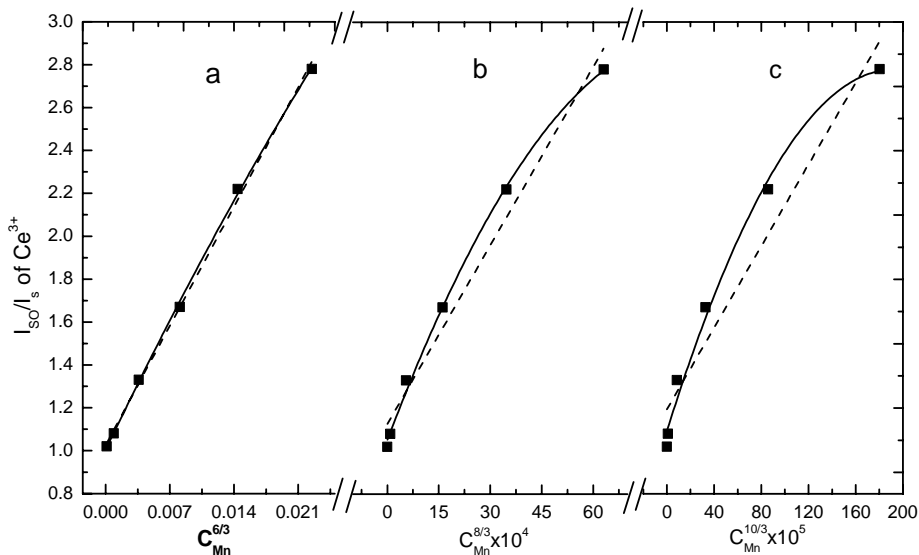


Figure 3-36 . Dependence of I_{SO}/I_S of Ce^{3+} on $\alpha = 6, 8$ and 10 (fixed Ce^{3+} , change the concentration of Mn^{2+})

As the same as for the CASO host lattice, the fluorescence decay curves of Ce^{3+} emission in the serial samples $\text{S}_{0.895-y}\text{ASO}: 0.07\text{Ce}^{3+}, y\text{Mn}^{2+}$ ($y = 0$ to 15%) were also measured (**Figure 3-37**), and the lifetime extracted via a fit of the curve with an exponential function (**Table 3-2**).

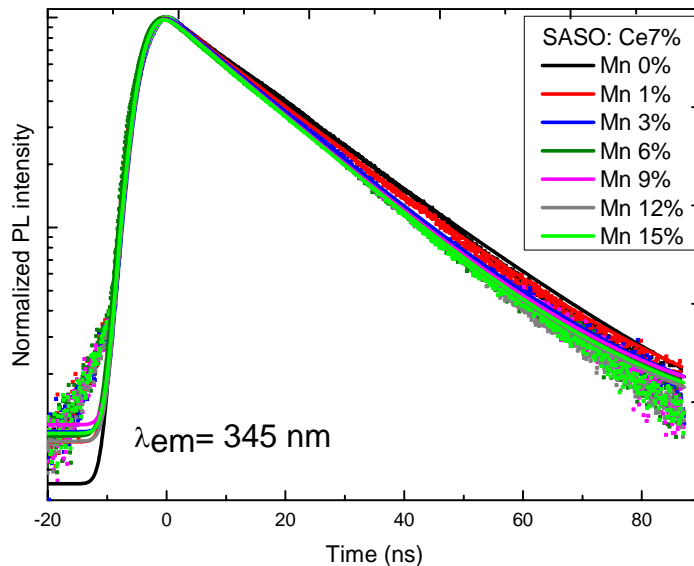


Figure 3-37. Photoluminescence decay curves of Ce^{3+} in the samples $\text{S}_{0.895-y}\text{ASO}: 0.07\text{Ce}^{3+}, y\text{Mn}^{2+}$ ($y = 0$ to 15%), under excited at 267 nm and monitored at 345 nm.

Table 3-2 . Lifetime values for the samples $\text{S}_{0.895-y}\text{ASO}: 0.07\text{Ce}^{3+}, y\text{Mn}^{2+}$ ($y = 0$ to 15%), excited at 265 nm, monitored at 345 nm

Phosphors	τ for $\lambda_{\text{em}} = 345 \text{ nm}$
$\text{S}_{0.895}\text{ASO:Ce } 7\%, \text{Mn } 0\%$	20.7 ns
$\text{S}_{0.885}\text{ASO:Ce } 7\%, \text{Mn } 1\%$	20.0 ns
$\text{S}_{0.865}\text{ASO:Ce } 7\%, \text{Mn } 3\%$	19.6 ns
$\text{S}_{0.835}\text{ASO:Ce } 7\%, \text{Mn } 6\%$	19.0 ns
$\text{S}_{0.805}\text{ASO:Ce } 7\%, \text{Mn } 9\%$	18.4 ns
$\text{S}_{0.775}\text{ASO:Ce } 7\%, \text{Mn } 12\%$	17.9 ns
$\text{S}_{0.745}\text{ASO:Ce } 7\%, \text{Mn } 15\%$	17.4 ns

Plots of $\tau_{\text{S}0}/\tau_{\text{S}}$ versus $C^{\alpha/3}$ have been also performed and are depicted in **Figure 3-38**. The linear behavior was better fitted well when $\alpha = 6$ than $\alpha = 8$ or 10, which implies that ET from Ce^{3+} to Mn^{2+} likely occurs via dipole-dipole mechanism, as suggested previously.

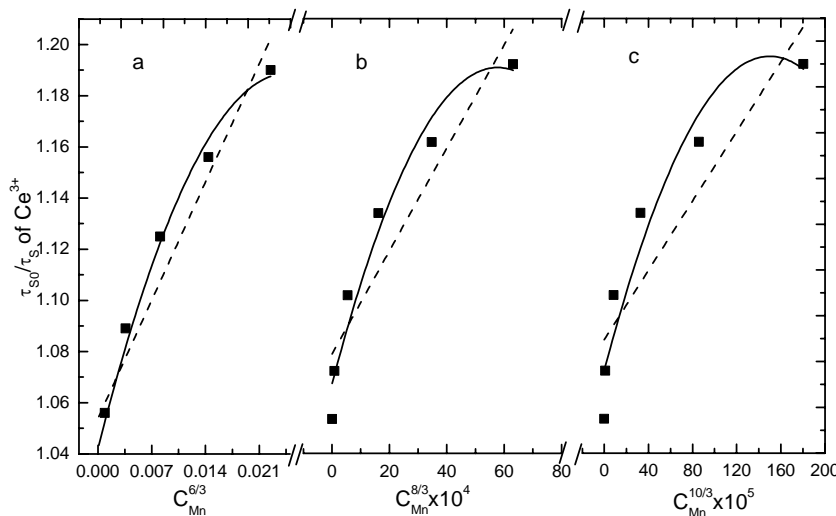


Figure 3-38. Dependence of $\tau_{S0}/\tau_S-C^{\alpha/3}$ of Ce^{3+} versus (a) $\alpha = 6$, (b) $\alpha = 8$ and (c) $\alpha = 10$ for the samples $S_{0.895-y}ASO: 0.07Ce^{3+}, yMn^{2+}$ ($y = 0$ to 15%).

Similarly, the efficiency of the ET from $V_{Sr}^{//}$ to Mn^{2+} was also calculated for different samples $S_{0.895-y}ASO: 0.07Ce^{3+}, yMn^{2+}$. At present, the concentration of $V_{Sr}^{//}$ was calculated to be ~ 0.035 which corresponds to the quantity created for a Ce^{3+} concentration equal to 7% . Thus, the x_c ($V_{Sr}^{//}$ - Mn^{2+} , critical concentration) is ~ 0.0598 ($0.035 + 0.0248$) from the total concentration of $V_{Sr}^{//}$ and Mn^{2+} ions for which the ET efficiency is equal to 0.5 (Figure 3-33). Hence, the R_c ($V_{Sr}^{//}$ - Mn^{2+}) was calculated to be ~ 17.70 Å.

The ET efficiency was found to dramatically increase with an increase of the Mn^{2+} concentration. Moreover, the efficiency in the $V_{Sr}^{//}$ - Mn^{2+} is higher than that of Ce^{3+} - Mn^{2+} . These phenomena in the $V_{Sr}^{//}$ - Mn^{2+} may be also due to the fact that the degree of the overlap between the emission of the $V_{Sr}^{//}$ (~ 404 nm) and the excitation of the Mn^{2+} (~ 403 nm) is much better than for the Ce^{3+} - Mn^{2+} system where the excitation band of Ce^{3+} (345 nm) is very separate to the emission band of Mn^{2+} (403 nm).

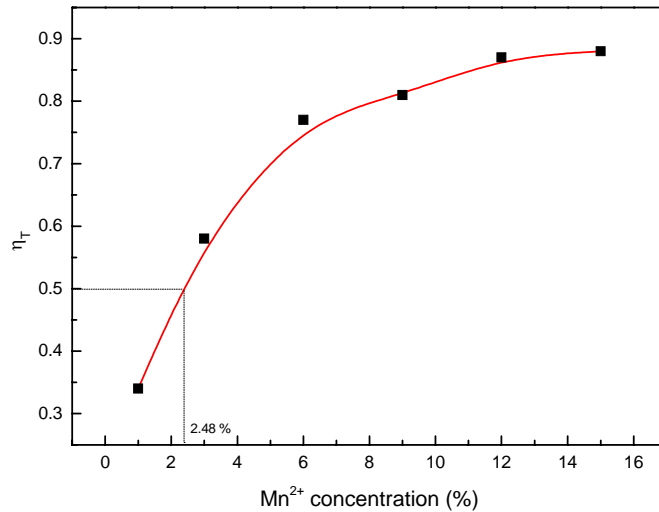


Figure 3-39. Dependence of the energy transfer efficiency η_T from $V_{\text{Sr}}^{\text{II}}$ to Mn^{2+} (on the Mn^{2+} content (y)).

As the critical distance of the ET between $V_{\text{Sr}}^{\text{II}}$ - Mn^{2+} was calculated to be $\sim 17.70 \text{ \AA}$, the ET from $V_{\text{Sr}}^{\text{II}}$ to Mn^{2+} is also through the multipolar interaction. According to the Dexter's ET formula, the mechanism of multipolar interactions can be detected between $V_{\text{Sr}}^{\text{II}}$ - Mn^{2+} . As one can see in **Figure 3-40**, the linear behavior was only observed when $\alpha = 6$. This phenomenon indicates that the ET between $V_{\text{Sr}}^{\text{II}}$ - Mn^{2+} is of the dipole-dipole mechanism type.

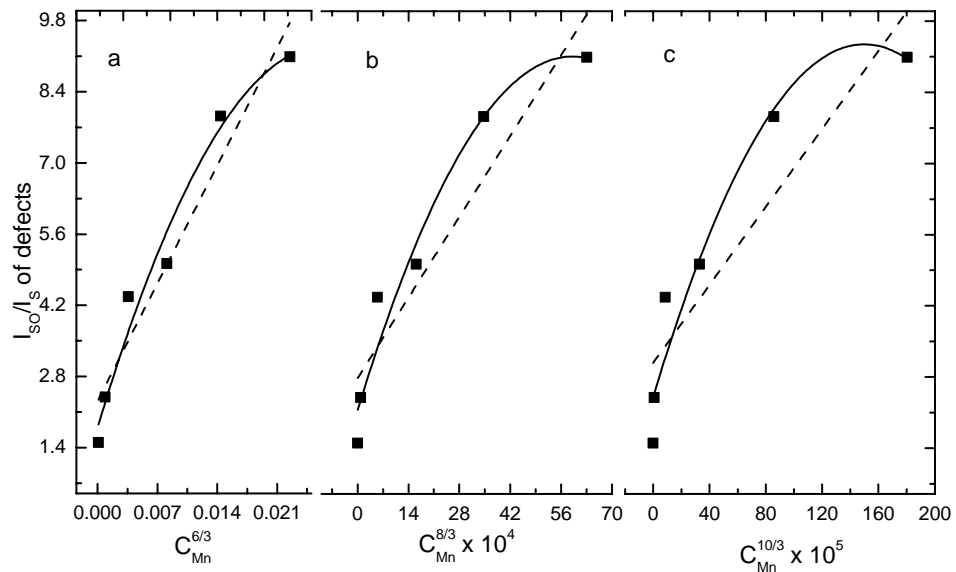


Figure 3-40. Dependence of I_{SO}/I_s of defects emission ($V_{\text{Sr}}^{\text{II}}$) versus $\alpha = 6, 8$ and 10 .

6. The CIE chromaticity coordinates of the phosphors for CASO and SASO (co)-doped with Ce^{3+} and Mn^{2+}

To quantify the optical characteristics of phosphors and to judge the impact of Mn^{2+} codoping on the generated color, the CIE (x,y) parameters of prepared materials have to be determined. These values are reported below for CASO: Ce, CASO: Ce,Mn, SASO: Ce, and SASO: Ce,Mn. All data were collected with an excitation wavelength of 294 nm.

6.1. CIE chromaticity properties of Ce^{3+} and/or Mn^{2+} (co)doped in CASO matrix

The CIE chromaticity coordinates values for the $C_{1-3x/2}ASO: xCe^{3+}$ and $C_{1-3x/2-y}ASO: xCe, yMn$ phosphors were measured. They are reported in **Tables 3-3 and 3-4**.

Table 3-3. CIE chromaticity coordinates for $C_{1-3x/2}ASO: xCe^{3+}$ ($\lambda_{ex} = 294\text{ nm}$)

Phosphors ($C_{1-3x/2}ASO: xCe^{3+}$)	CIE(x, y)
x = 0.005	(0.1976, 0.1564)
x = 0.02	(0.2162, 0.1791)
x = 0.05	(0.2148, 0.1876)
x = 0.09 (point 1 in Figures 3-41 and 3-43)	(0.2270, 0.2212)
x = 0.15	(0.2022, 0.1868)

Table 3-4. CIE chromaticity coordinates for two group of phosphors $C_{0.865-y}ASO: 0.09Ce^{3+}, yMn^{2+}$ and $C_{0.91-3x/2}ASO: xCe^{3+}, 0.09Mn^{2+}$

Phosphors $C_{0.865-y}ASO: 0.09Ce^{3+}, yMn^{2+}$			Phosphors $C_{0.91-3x/2}ASO: xCe^{3+}, 0.09Mn^{2+}$		
Concentration (%)	point	(x, y)	Concentration (%)	point	(x, y)
y = 0.01	2	(0.2968, 0.3142)	x = 0.01	2	(0.4536, 0.5194)
y = 0.015	3	(0.3176, 0.3242)	-	-	-
y = 0.02	4	(0.3416, 0.3342)	-	-	-
y = 0.03	5	(0.3577, 0.4016)	x = 0.03	3	(0.4317, 0.5027)
y = 0.06	6	(0.3982, 0.4535)	x = 0.06	4	(0.4424, 0.5085)
y = 0.09	7	(0.4272, 0.4794)	x = 0.09	5	(0.4397, 0.4931)
y = 0.12	8	(0.4414, 0.4799)	x = 0.12	6	(0.4375, 0.4844)
y = 0.15	9	(0.4551, 0.4797)	x = 0.15	7	(0.4337, 0.4720)

The $\text{C}_{1-3x/2}\text{ASO}: \text{xCe}$ series gives rise to a "blue" emission with CIE (x,y) coefficients quite similar whatever the Ce concentration. This was expected on the basis of the observation of the collected emission spectra. For sure, some modification of the CIE (x,y) parameters are observed but there are not very important.

For the $\text{C}_{0.865-y}\text{ASO}: 9\%\text{Ce}^{3+}, y\text{Mn}^{2+}$ ($y = 0$ to 15%) series, a regular shift from blue for $y = 0\%$ to white ($y = 1, 1.5$ and 2%) and to yellow ($y > 3\%$) is clearly evidenced (see **Figures 3-41 and 3-42**). This corresponds to a change from $(0.2270, 0.2212)$ to $(0.4551, 0.4797)$ of the chromatic coordinates for Mn^{2+} concentrations increasing from 0 to 15% . This clearly evidences the role of ET from Ce (and $V_{\text{Ca}}^{\prime\prime}$ defect) towards Mn^{2+} cations in these materials and the importance to control the Mn concentration to generate a white color. The white color would be obtained for a $\text{Ca}_{0.850}\text{Ce}_{0.090}\text{Mn}_{0.015}\text{Al}_2\text{Si}_2\text{O}_8$ composition, this composition being probably not optimal.

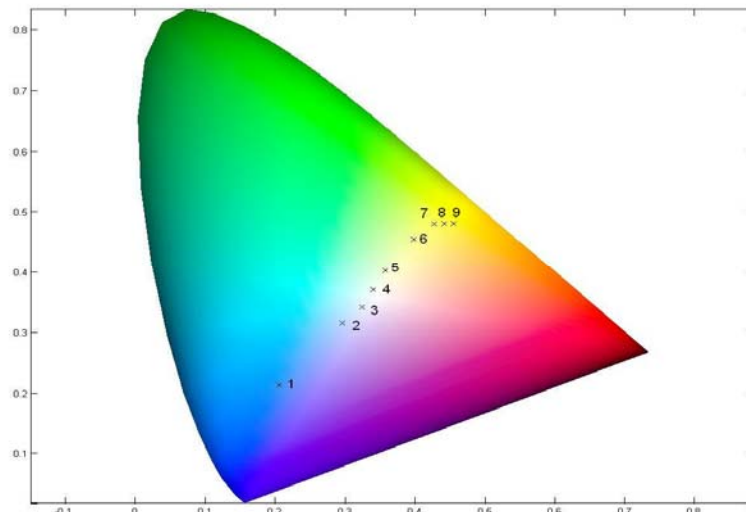


Figure 3-41 . Evolution of CIE chromaticity coordinates for $\text{C}_{0.865-y}\text{ASO}: 0.09\%\text{Ce}^{3+}, y\text{Mn}^{2+}$ excited at 294nm. The numbers from 1-9 correspond to: 1, $y = 0$; 2, $y = 0.01$; 3, $y = 0.015$; 4, $y = 0.02$; 5, $y = 0.03$; 6, $y = 0.06$; 7, $y = 0.09$; 8, $y = 0.12$; 9, $y = 0.15$.



Figure 3-42. Photographs of emission from $Ce_{0.865-y}ASO: 0.09Ce^{3+}, yMn^{2+}$ excited at 294 nm. From left to right, $y = 0$, $y = 0.02$ and $y = 0.09$

The evolution of the CIE (x,y) parameters in the $Ce_{0.91-3x/2}ASO: xCe^{3+}, 0.09Mn^{2+}$ series is reported in **Figure 3-43**. In contrast to the previous series, due to the quite high concentration in Mn, a steep jump from blue to yellow is observed going from $Ce_{1-3x/2}ASO: xCe$ to $Ce_{0.91-3x/2}ASO: xCe, 9\%Mn$. Generation of white color request a good compromise between Ce and Mn!

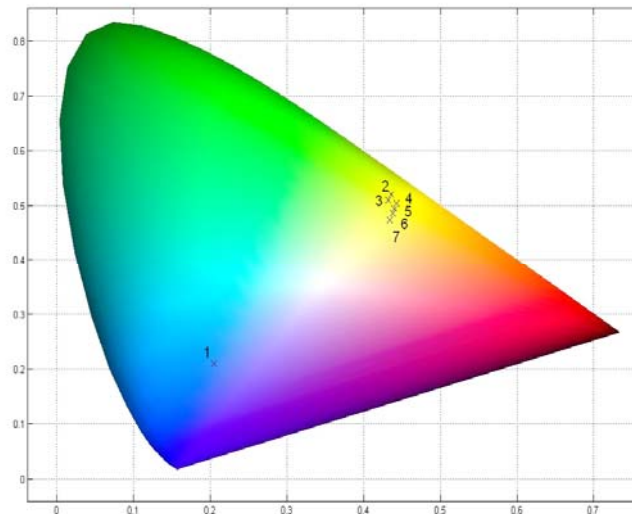


Figure 3-43. Evolution of CIE chromaticity coordinates for $Ce_{0.91-3x/2}ASO: xCe^{3+}, 0.09Mn^{2+}$ ($x = 1$ to 15%) excited at 294 nm. The numbers from 1-7 correspond to: 1, $x = 0.09Ce^{3+}$ and $y = 0$; 2, $x = 0.01$; 3, $x = 0.03$; 4, $x = 0.6$; 5, $x = 0.09$; 6, $x = 0.12$; 7, $x = 0.15$

6.2. CIE chromaticity properties of Ce^{3+} and/or Mn^{2+} (co)doped phosphors in SASO matrix

The CIE chromaticity coordinates of the phosphors $\text{S}_{1-3x/2}\text{ASO}: \text{xCe}^{3+}$ and $\text{S}_{1-3x/2-y}\text{ASO}: \text{xCe}, \text{yMn}$ series are listed in **Tables 3-5 and 3-6**.

Table 3-5. CIE chromaticity coordinates for $\text{S}_{1-3x/2}\text{ASO}: \text{xCe}^{3+}$ ($\lambda_{ex} = 294 \text{ nm}$)

Phosphors ($\text{S}_{1-3x/2}\text{ASO}: \text{xCe}^{3+}$)	CIE(x, y)
$\text{x} = 0.005$	(0.2596, 0.2348)
$\text{x} = 0.02$	(0.2562, 0.2328)
$\text{x} = 0.05$	(0.2027, 0.2023)
$\text{x} = 0.07$ (point 1 in Figure 3-44)	(0.1166, 0.1634)
$\text{x} = 0.15$	(0.1088, 0.1423)

Table 3-6. CIE chromaticity coordinates for two group of phosphors $\text{S}_{0.895-y}\text{ASO}: 0.07\text{Ce}^{3+}, \text{yMn}^{2+}$ and $\text{S}_{0.91-3x/2}\text{ASO}: \text{xCe}^{3+}, 0.06\text{Mn}^{2+}$

Phosphors $\text{S}_{0.895-y}\text{ASO}: 0.07\text{Ce}^{3+}, \text{yMn}^{2+}$			Phosphors $\text{C}_{0.91-3x/2}\text{ASO}: \text{xCe}^{3+}, 0.06\text{Mn}^{2+}$		
Concentration (%)	point	(x, y)	Concentration (%)	point	(x, y)
$y = 0.01$	2	(0.2393, 0.1835)	$x = 0.01$	1	(0.3873, 0.4951)
$y = 0.03$	3	(0.3105, 0.3260)	$x = 0.03$	2	(0.3727, 0.4424)
$y = 0.045$	4	(0.3362, 0.3442)	$x = 0.06$	3	(0.3622, 0.4225)
$y = 0.06$	5	(0.3550, 0.4140)	$x = 0.09$	4	(0.3421, 0.3959)
$y = 0.09$	6	(0.3608, 0.4182)	$x = 0.12$	5	(0.3384, 0.3806)
$y = 0.12$	7	(0.3682, 0.4332)	$x = 0.15$	6	(0.3221, 0.3463)
$y = 0.12$	8	(0.3542, 0.4125)	-	-	-

All the CIE coordinates values (x, y) are located in the blue region for $\text{S}_{1-3x/2}\text{ASO}: \text{xCe}$. Namely, the color light turns from bluish to deep blue area when Ce content increases. Therefore, as for the CASO, Mn²⁺ co-doping is needed to get white emission. Following this consideration, we have also measured the series of $\text{S}_{0.895-y}\text{ASO}: 0.07\text{Ce}^{3+}, \text{yMn}^{2+}$ (y = 0 to 15%) phosphors (see **Table 3-6**). In **Figure 3-44**, the chromaticity coordinates for $\text{S}_{0.895-y}\text{ASO}: 0.07\text{Ce}^{3+}, \text{yMn}^{2+}$ are represented for y ranging from 0 to 15%, respectively. Again, we can see that the color characteristics can be tuned continuously from blue to white and yellow to green, i.e. from (0.1166, 0.1634) to (0.3542, 0.4125), see **Figure 3-45**.

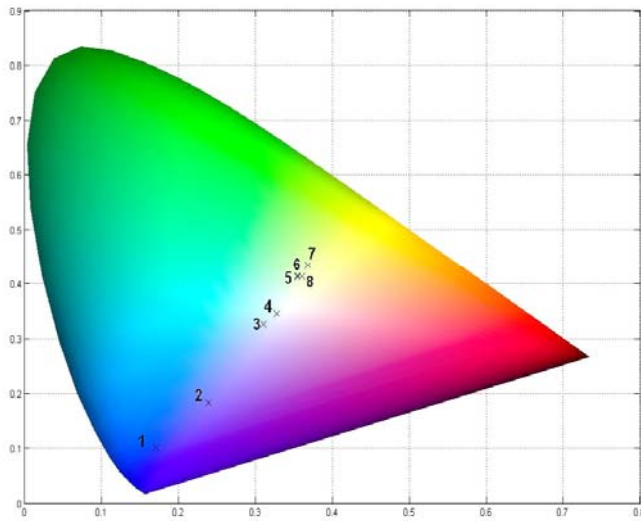


Figure 3-44. Evolution of CIE chromaticity coordinates for $S_{0.895-y}ASO: 0.07Ce^{3+}, yMn^{2+}$ ($y = 0$ to 15%) excited at 294nm. The numbers from 1-8 correspond to: 1, $y = 0$; 2, $y = 0.01$; 3, $y = 0.03$; 4, $y = 0.045$; 5, $y = 0.06$; 6, $y = 0.09$; 7, $y = 0.12$ and 8, $y = 0.15$.



Figure 3-45. Photographs of emission from $S_{0.895-y}ASO: 0.07Ce^{3+}, yMn^{2+}$ excited at 294nm. From left to right, $y = 0$, $y = 0.045$ and $y = 0.15$

For the $Sr_{0.94-3x/2}ASO: Ce^{3+}$ ($x = 1$ to 15%), $0.06Mn^{2+}$ series (see **Table 3-6**, **Figure 3-46**), white and yellow materials can also be obtained. Hence, it can be observed that white phosphor can be obtained for different Ce/Mn compositions (e.g. $S_{0.895-y}ASO: 0.07Ce, yMn$ when $y = 0.045$ ($Sr_{0.850}Ce_{0.07}Mn_{0.045}Al_2Si_2O_8$) and $S_{0.94-3x/2}ASO: xCe^{3+}, 0.06Mn^{2+}$ when $x = 0.12$ ($Sr_{0.73}Ce_{0.12}Mn_{0.09}Al_2Si_2O_8$)).

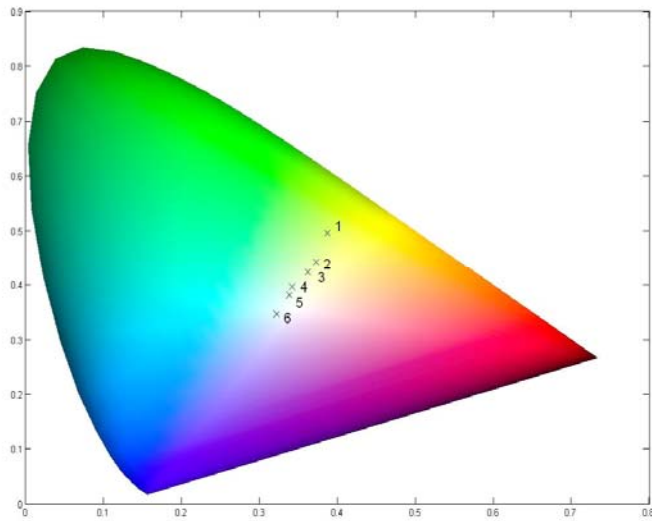


Figure 3-46. Evolution of CIE chromaticity coordinates for $\text{S}_{0.94-3x/2}\text{ASO}: x\text{Ce}^{3+}, 0.06\text{Mn}^{2+}$ ($x = 1$ to 15%) excited at 294 nm. The numbers from 1-6 correspond to: 1, $x = 0.01$; 2, $y = 0.03$; 3, $y = 0.06$; 4, $y = 0.09$; 5, $y = 0.12$ and 6, $y = 0.15$

Concluding remarks

In conclusion, color-tunable Ce^{3+} and Mn^{2+} co-doped $MAI_2Si_2O_8$ ($M = Ca, Sr$) aluminosilicates phosphors have been prepared by the traditional solid-state method, and their luminescence properties have also been investigated in details. PL spectra reveal that MASO: Ce^{3+} phosphors exhibit a strong blue emission bands due to Ce^{3+} -intralattice allowed transitions from the bottom of the 4d-bloc towards the $^2F_{5/2}$ and $^2F_{7/2}$ states. At room temperature, the critical concentrations for Ce^{3+} in CASO and SASO matrixes are estimated to be around 9% and 7%. Systematically, the cerium emissions are accompanied with an additional broad band located at ~ 430 nm and ~ 400 nm for CASO and SASO host lattices, respectively. This band must be linked to alkaline metal vacancies V_M^{II} which appear under the M^{2+}/Ce^{3+} substitutions according to the formal reaction: $3M^{2+} \rightarrow 2Ce_M^\bullet + V_M^{II}$. The intensity of these bands strongly decreases when CASO: Ce and SASO: Ce materials are co-doped with an alkali metal ($2M^{2+} \rightarrow Ce_M^\bullet + Li_M^+$) to restrain the number of cationic vacancies (V_M^{II}).

Meanwhile, the examination of MASO: Ce^{3+}, Mn^{2+} PL spectra clearly revealed the possible pumping Mn^{2+} cations via $Ce^{3+} \rightarrow Mn^{2+}$ and " V_M^{II} defect" $\rightarrow Mn^{2+}$ ET. This leads to the addition of a yellow contribution to the nominal blue luminescence of MASO: Ce. Thus, through the proper choice of Ce and Mn contents, it is possible to tune the color of the prepared phosphors at will. Namely, the emission color of the obtained phosphors can be easily modulated from blue to white by simply adjusting the amount of Ce^{3+} and Mn^{2+} . In that context, it is worth mentioning that the CIE values of compositions as $C_{0.85}ASO: 0.09Ce^{3+}, 0.015Mn^{2+}$ (0.3176, 0.3242) and $S_{0.85}ASO: 0.07Ce^{3+}, 0.045Mn^{2+}$ (0.3362, 0.3442) are quite close to the expected white color (1/3, 1/3). However, we may regret that Mn^{2+} substitution reinforce the yellow rather than the red component, the latter being preferred to generate warm light. In any case, prior to any application as potential white-light-emitting UV-LED devices, the behaviour of CASO: Ce,Mn and SASO: Ce,Mn will have to be tested in temperature. The internal quantum yield will also have to be determined.

References

1. U. Caldino, *Journal of Physics: Condensed Matter* **15** (2003).
2. Y. Hua, S. Xu, D. Deng, S. Zhao, H. Wang and L. Huang, *Optics Communications* **284** (2010) (1), p. 27.
3. B. Wang, L. Sun and H. Ju, *Solid State Communications* **150** (2010), p. 1460.
4. E.J. Bosze, G.A. Hirata, L.E. Shea-Rohwer and J. McKittrick, *Journal of Luminescence* **104** (2003), p. 47.
5. D. Jia, R.S. Meltzer, W.M. Yen, W. Jia and X. Wang, *Applied Physics Letters* **80** (2002) (9), p. 1535.
6. S. Ye, Z.-S. Liu, X.-T. Wang, J.-G. Wang, L.-X. Wang and X.-P. Jing, *Journal of Luminescence* **129** (2009) (1), p. 50.
7. J.S. Kim, P.E. Jeon, J.C. Choi, H.L. Park, S.I. Mho and G.C. Kim, *Applied Physics Letters* **84** (2004) (15), p. 2931.
8. S.H. Lee, J.H. Park, S.M. Son, J.S. Kim and H.L. Park, *Applied Physics Letters* **89** (2006) (22), p. 221916.
9. W.-J. Yang, L. Luo, T.-M. Chen and N.-S. Wang, *Chemistry of Materials* **17** (2005) (15), p. 3883.
10. B. Wang, L. Sun, H. Ju, S. Zhao, D. Deng, H. Wang and S. Xu, *Journal of Sol-Gel Science and Technology* **50** (2009) (3), p. 368.
11. K.N. Shinde, I.M. Nagpure, A.B. Fulke and S.J. Dhoble, *Luminescence* **26** (2010) (5), p. 363.
12. M.J.J. Lammers and G. Blasse, *physica status solidi (b)* **127** (1985) (2), p. 663.
13. S.C. Gedam, S.J. Dhoble and S.V. Moharil, *Journal of Luminescence* **124** (2007) (1), p. 120.
14. D. Talapatra and R.K. Mukherjee, *physica status solidi (b)* **155** (1989) (2), p. 541.
15. H.J.W.M. Hoekstra, P.R. Boudewijn, H. Groenier and C. Haas, *Physica B+C* **121** (1983), p. 62.
16. S. Ye, J. Zhang, X. Zhang, S. Lu, X. Ren and X.-j. Wang, *Journal of Applied Physics* **101** (2007) (6), p. 063545.
17. C. Kulshreshtha, J.H. Kwak, Y.-J. Park and K.-S. Sohn, *Opt. Lett.* **34** (2009) (6), p. 794.
18. N. Suriyamurthy and B.S. Panigrahi, *Journal of Luminescence* **127** (2007) (2), p. 483.
19. C.-H. Huang, T.-W. Kuo and T.-M. Chen, *ACS Applied Materials & Interfaces* **2** (2010) (5), p. 1395.
20. R. Shannon, *Acta Crystallographica Section A* **32** (1976) (5), p. 751.
21. W.B. Im, N.N. Fellows, S.P. DenBaars, R. Seshadri and Y.-I. Kim, *Chemistry of Materials* **21** (2009) (13), p. 2957.
22. G. Blesse, *Philips Res. Rep.* **24** (1969), p. 131.
23. G. Denis, P. Deniard, E. Gautron, F. Clabau, A. Garcia and S. Jobic, *Inorganic Chemistry* **47** (2008) (10), p. 4226.
24. F.d.r. Clabau, A. Garcia, P. Bonville, D. Gonbeau, T. Le Mercier, P. Deniard and S.p. Jobic, *Journal of Solid State Chemistry* **181** (2008) (6), p. 1456.
25. J.K. Park, J.M. Kim, E.S. Oh and C.H. Kim, *Electrochim. Solid State Lett.* **8** (2005) (1), p. H6.
26. R. Ghildiyal, C.-H. Hsu, H.-Y. Chang, S. Kumar and C.-H. Lu, *Journal of Luminescence* **132** (2012) (1), p. 185.
27. B.C.G. G.Blass, Editor, *Luminescent materials*, Springer-Verlag (1994).

28. C. Zhang, J. Yang, C. Lin, C. Li and J. Lin, *Journal of Solid State Chemistry* **182** (2009) (7), p. 1673.
29. S. Ye, F. Xiao, Y.X. Pan, Y.Y. Ma and Q.Y. Zhang, *Materials Science and Engineering: R: Reports* **71** (2010) (1), p. 1.
30. L.E. Orgel, *J. Chem. Phys* **23** (1955), p. 1004.
31. S.-H. Yang, Y.-J. Lial, N.-J. Cheng and Y.-H. Ling, *Journal of Alloys and Compounds* **489** (2010) (2), p. 689.
32. K.Y. Jung and J.H. Kim, *Journal of Luminescence* **128** (2008) (12), p. 2004.
33. Y. Yonesaki, T. Takei, N. Kumada and N. Kinomura, *Journal of Solid State Chemistry* **183** (2010) (6), p. 1303.
34. S.C. Sen and H.N. Bose, *Zeitschrift für Physik A Hadrons and Nuclei* **201** (1967) (4), p. 368.
35. N. Guo, Y. Huang, H. You, M. Yang, Y. Song, K. Liu and Y. Zheng, *Inorganic Chemistry* **49** (2010) (23), p. 10907.
36. K.H. Kwon, W.B. Im, H.S. Jang, H.S. Yoo and D.Y. Jeon, *Inorganic Chemistry* **48** (2009) (24), p. 1152.

General conclusion

The CIE (x,y) coefficient of Eu²⁺ and Ce³⁺ doped MAI₂Si₂O₈ materials can be impacted via the insertion of Eu³⁺ and Mn²⁺ cations in the host lattice due the appearance of energy transfers. This changes the luminescence from white bluish to white and pink or yellow according to the concentration in dopants and codopants. Clearly this evidences that the emission spectra can almost be adapted at wish via the insertion of the appropriate activators. Nevertheless, prior to any applications of such materials, tests have to be initiated concerning their stability towards thermal quenching and their ability of generate color with a high efficiency (external quantum yield).

For Ce³⁺ doped MASO (M= Ca, Sr), a peak related to defects is systematically observed. More specifically, this emission band, broader than the ones associated to Ce³⁺-5d → 4f transitions and located at longer wavelength, is related to the occurrence of alkaline metal vacancies V_M^{II} requested to respect the charge balance (i.e. $3M^{2+} \rightarrow 2Ce_M^{\bullet} + V_M^{II}$). The intensity of this band can be modulated and its contribution almost annihilates when alkaline metals are used as co-dopants (i.e. $2M^{2+} \rightarrow Ce_M^{\bullet} + A_M^{'}$ with A = K for instance). Nevertheless, this band may be of interest since it encroaches on the visible spectrum and can serve as potential springboard for energy transfer from the sensitizers (e.g. Ce³⁺) to the activators (e.g. Mn²⁺). According to the desired luminescence spectrum, this "defect" band will have to be privileged or cancelled.

A major point of my investigations concerns also the possible stabilization of Eu²⁺ cations in aluminosilicates when materials are prepared in air. Commonly, Eu³⁺ species are expected to be formed in oxidizing conditions, while the stabilization of Eu²⁺ cations requests reducing conditions. In fact, the substitution in air of trivalent europium cations for alkaline earth (M) triggers the formation of V_M^{II} vacancies that play the role of electron donor towards Eu_M^{\bullet} defects. The higher the concentration of V_M^{II} , the easier the reduction of Eu³⁺ into Eu²⁺. Consequently, the codoping with tetravalent chemical elements (e.g. transition element) may help a lot in increasing the concentration of Eu²⁺ cations at the expense of Eu³⁺ ions. For sure, we will take advantages of this observation in the future to prepare materials.

So far, our investigations have focused only on the $MAl_2Si_2O_8$ host lattices. For sure, many other compounds could also lead to white luminescence. In that context, materials of the $M_{13-x}Al_{22-2x}Si_{10+2x}O_{66}$ ($M = Sr, Ba$) series doped with Eu^{2+} or Ce^{3+} and codoped with transition elements appear appropriate to access to warm white light for instance. Formally, the already strong similarity between the emission spectrum of $Ba_{10.4}Sr_{2.6}Al_{22}Si_{10}O_{66}:Eu1\%$ and that of a YAG:Ce –GaN LED light device is striking and suggests that co-doping could significantly improved the chromatic rendering index. In the present case codoping will have to be tested for different Sr/Ba compositions. Many other aluminosilicate derivatives could be also investigated...

Annexes

Appendix 1

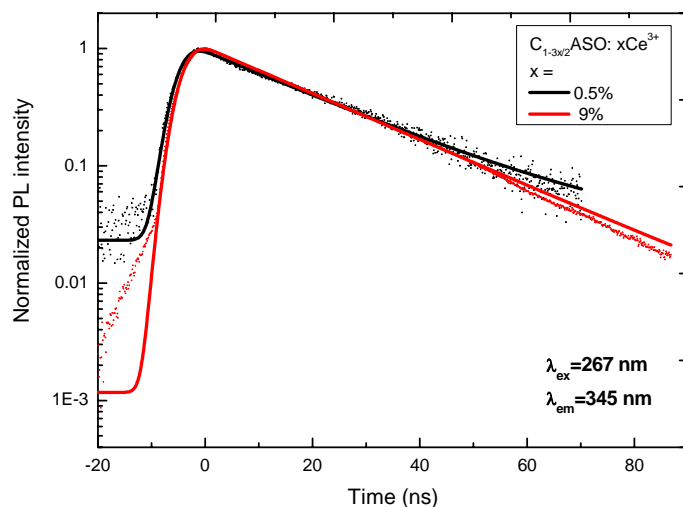


Figure 1a. Photoluminescence decay curve of Ce^{3+} in formula $\text{C}_{1-3x/2}\text{ASO}:x\text{Ce}^{3+}$ ($x = 0.5\%, 9\%$, excited at 267 nm , monitored at 345 nm)

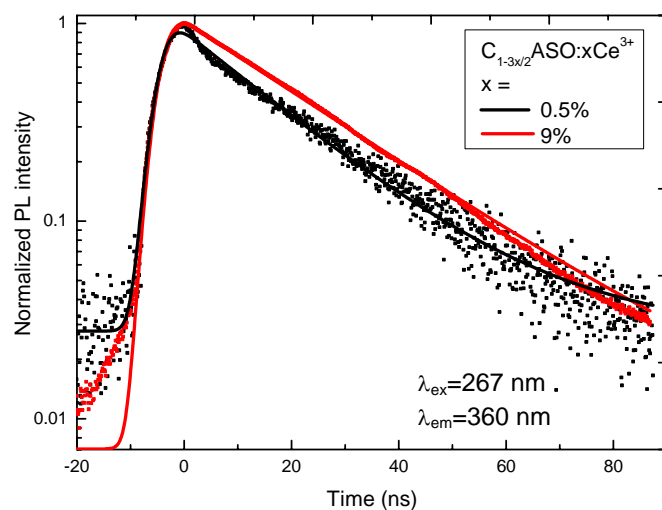


Figure 1b. Photoluminescence decay curve of Ce^{3+} in formula $\text{C}_{1-3x/2}\text{ASO}:x\text{Ce}^{3+}$ ($x = 0.5\%, 9\%$, excited at 267 nm , monitored at 360 nm)

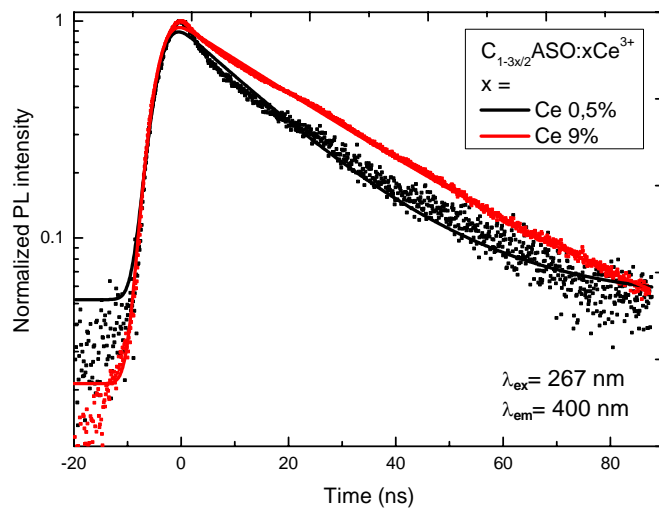


Figure 1c. Photoluminescence decay curve of Ce^{3+} in formula $\text{C}_{1-3x/2}\text{ASO}:x\text{Ce}^{3+}$ ($x = 0.5\%, 9\%$, excited at 265nm , monitored at 400nm)

Table 1. The results of the decay times for the sample $\text{C}_{1-3x/2}\text{ASO}:x\text{Ce}^{3+}$ ($\lambda_{\text{ex}} = 267 \text{ nm}$)

Samples	τ for $\lambda_{\text{em}} = 345 \text{ nm}$	τ for $\lambda_{\text{em}} = 360 \text{ nm}$	τ for $\lambda_{\text{em}} = 400 \text{ nm}$
$x = 0.5\%$	22.4 ns	19.4 ns	18.1 ns
$X = 9\%$	22.0 ns	24.1 ns	27.0 ns

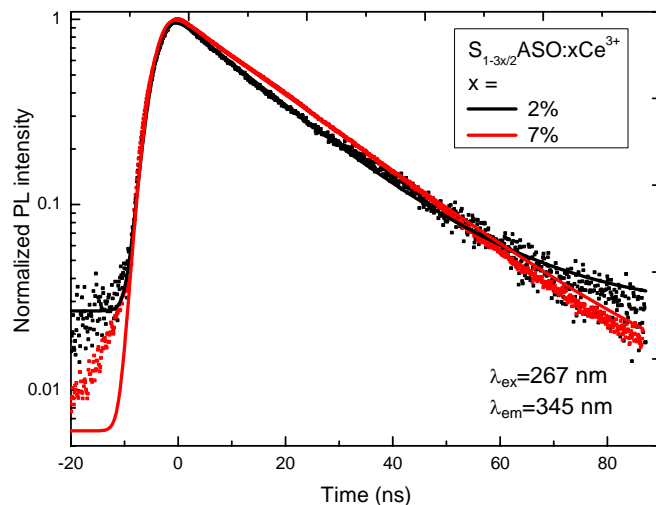


Figure 2a. Photoluminescence decay curve of Ce^{3+} in formula $\text{S}_{1-3x/2}\text{ASO}:x\text{Ce}^{3+}$ ($x = 2\%, 7\%$, excited at 265nm , monitored at 345nm)

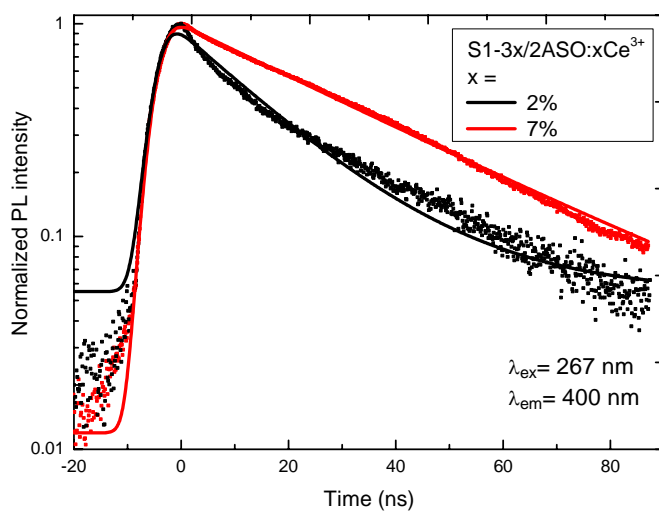


Figure 2b. Photoluminescence decay curve of Ce^{3+} in formula $S_{1-3x/2}ASO:xCe^{3+}$ ($x = 2\%, 7\%$, excited at 265nm , monitored at 400nm)

Table 2. The results of the decay times for the sample $S_{1-3x/2}ASO:xCe^{3+}$ ($\lambda_{ex} = 267\text{ nm}$)

Samples	τ for $\lambda_{em} = 345\text{ nm}$	τ for $\lambda_{em} = 400\text{ nm}$
$x = 2\%$	17.9 ns	18.3 ns
$x = 7\%$	20.7 ns	35.2 ns

Appendix 2

Table 1. EDX results for sample $C_{0.85}ASO: 10\%Ce^{3+}$

Element	Norm (%)	Prec.	Atomic (%)	Line
Ca	20.04	1.41	7.82	K line
Sr	0	0	0	K line
Al	16.29	0.59	14.46	K line
Si	18.12	0.71	15.44	K line
Mn	0	0	0	K line
Eu	0	0	0	K line
Ce	4.43	0.75	0.76	K line
O	41.12	0	61.52	K line
Total:100, Goodness of fit: 4.11				

Table 2. EDX results for sample $C_{0.715}ASO: 19\%Ce^{3+}$

Element	Norm (%)	Prec.	Atomic (%)	Line
Ca	17.57	1.26	7.90	K line
Sr	0	0	0	K line
Al	15.64	0.57	14.27	K line
Si	17.73	0.68	15.54	K line
Mn	0	0	0	K line
Eu	0	0	0	K line
Ce	8.94	0.94	1.57	K line
O	40.12	0	61.73	K line
Total:100.01, Goodness of fit: 4.33				

Table 3. EDX results for sample $C_{0.775}ASO: 9\%Ce^{3+}, 9\%Mn^{2+}$

Element	Norm (%)	Prec.	Atomic (%)	Line
Ca	19.97	1.34	7.64	K line
Sr	0	0	0	K line
Al	15.94	0.56	14.21	K line
Si	18.12	0.68	15.51	K line
Mn	1.07	0.26	0.47	K line
Eu	0	0	0	K line
Ce	4.00	0.68	0.69	K line
O	40.90	0	61.48	K line
Total:100, Goodness of fit: 4.35				

Table 4. EDX results for sample $S_{0.85}\text{ASO}: 10\%\text{Ce}^{3+}$

Element	Norm (%)	Prec.	Atomic (%)	Line
Ca	0	0	0	K line
Sr	33.76	1.90	10.88	K line
Al	13.84	0.71	14.49	K line
Si	13.05	0.76	13.12	K line
Mn	0	0	0	K line
Eu	0	0	0	K line
Ce	4.96	1.03	1.00	K line
O	34.24	0	60.43	K line
Total:100, Goodness of fit: 2.10				

Table 5. EDX results for sample $S_{0.715}\text{ASO}: 19\%\text{Ce}^{3+}$

Element	Norm (%)	Prec.	Atomic (%)	Line
Ca	0	0	0	K line
Sr	30.09	1.69	9.62	K line
Al	13.83	0.67	14.36	K line
Si	13.72	0.72	13.69	K line
Mn	0	0	0	K line
Eu	0	0	0	K line
Ce	7.63	1.07	1.53	K line
O	34.73	0	60.82	K line
Total:100, Goodness of fit: 2.45				

Appendix 3

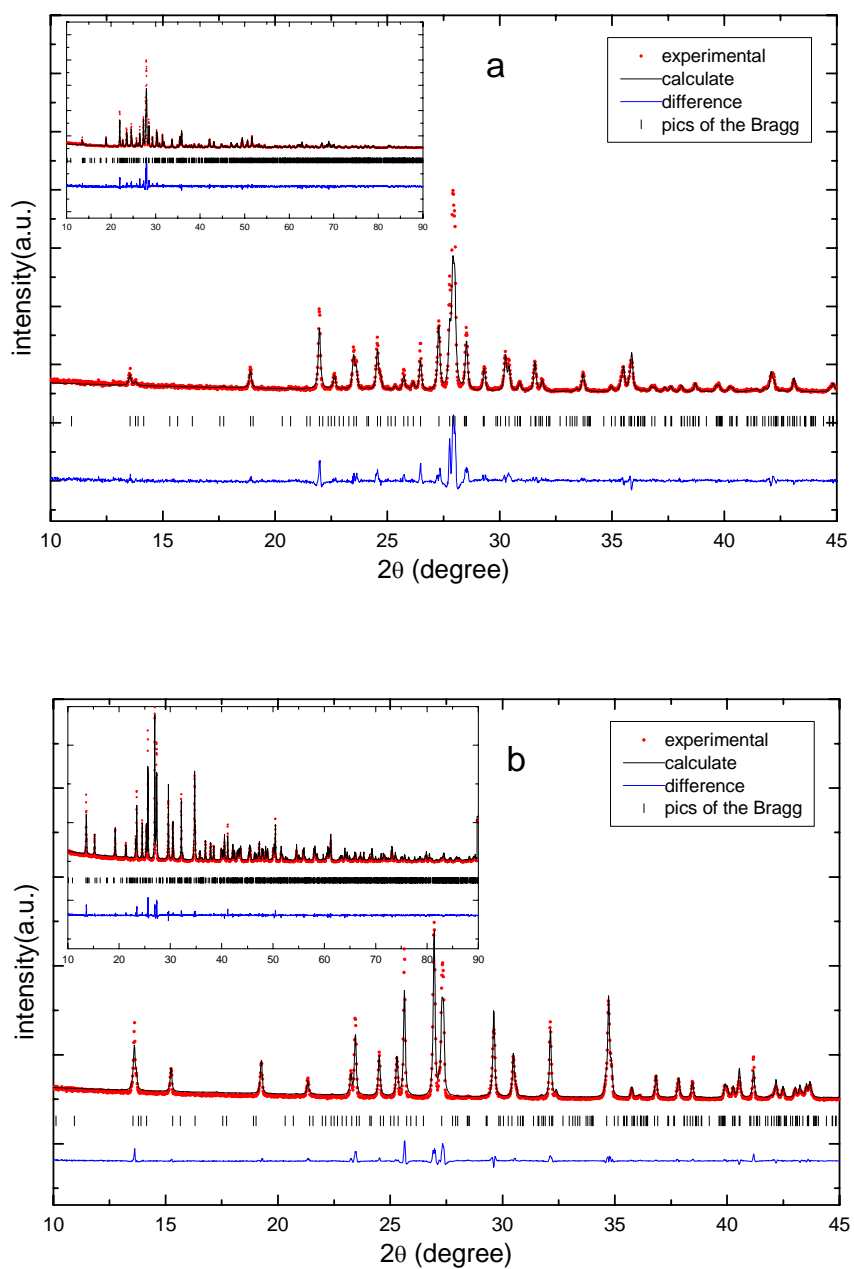


Figure 1. a, Observed, calculated and difference X-ray diffraction pattern of Ce (9%) and Mn (9%) codoped CASO compound in the [10-45] 2θ range (in set is given the total pattern), and b, the pattern of Ce (7%) and Mn(6%) codoped SASO compound

Table 1. Crystallographic details for the (co-)doped samples on CASO matrix

Formula	$\text{Ca}_{0.91}\text{Mn}_{0.09}\text{Al}_2\text{Si}_2\text{O}_8$	$\text{Ca}_{0.865}\text{Ce}_{0.09}\text{Al}_2\text{Si}_2\text{O}_8$	$\text{Ca}_{0.775}\text{Ce}_{0.09}\text{Mn}_{0.09}\text{Al}_2\text{Si}_2\text{O}_8$
Formula weight (g/mol)	2236.36	2286.26	2373.11
Cryst syst	Anorthic(triclinic)	Anorthic(triclinic)	Anorthic(triclinic)
Space group	I-1	I-1	I-1
a (Å)	8.1721(3)	8.1917(3)	8.1778(3)
b (Å)	12.8683(4)	12.8763(5)	12.8695(4)
c (Å)	14.1643(5)	14.1741(5)	14.1628(5)
α (deg)	93.348(3)	93.069(3)	93.312(3)
β (deg)	115.769(2)	115.688(2)	115.716(2)
γ (deg)	91.156(2)	91.212(3)	91.135(2)
$V(\text{\AA}^3)$	1337.39(10)	1343.74(10)	1339.01(10)
Z	8	8	8
$D_{\text{calcd}}(\text{g/cm}^{-3})$	2.7629(2)	2.7493(3)	2.7590(2)
$R_p(\%)$	10.79	11.10	12.58
$R_{\text{wp}}(\%)$	13.56	14.50	16.08
GOF	1.50	1.33	1.59

Table 2. Crystallographic details for the (co-)doped samples on SASO matrix

Formula	$\text{Sr}_{0.94}\text{Mn}_{0.06}\text{Al}_2\text{Si}_2\text{O}_8$	$\text{Sr}_{0.895}\text{Ce}_{0.07}\text{Al}_2\text{Si}_2\text{O}_8$	$\text{Sr}_{0.835}\text{Ce}_{0.07}\text{Mn}_{0.06}\text{Al}_2\text{Si}_2\text{O}_8$
Formula weight (g/mol)	2589.27	2609.82	2595.17
Cryst syst	Based-centered monoclinic	Based-centered monoclinic	Based-centered monoclinic
Space group	I2/c	I2/c	I2/c
a (Å)	8.3807(1)	8.3812(2)	8.3809(1)
b (Å)	12.9694(2)	12.9722(3)	12.9702(2)
c (Å)	14.2563(2)	14.2591(3)	14.2574(3)
α (deg)	90	90	90
β (deg)	115.380(1)	115.360(2)	115.371(2)
γ (deg)	90	90	90
$V(\text{\AA}^3)$	1338.19(20)	1339.01(10)	1338.54(20)
Z	8	8	8
$D_{\text{calcd}}(\text{g/cm}^{-3})$	3.0846(1)	3.0880(1)	3.0853(1)
$R_p(\%)$	16.77	15.96	16.46
$R_{\text{wp}}(\%)$	21.27	20.46	20.83
GOF	2.49	2.25	2.36

Table 3. Atomic parameters for $Ca_{0.775}Ce_{0.09}Mn_{0.09}Al_2Si_2O_8$ and $Sr_{0.835}Ce_{0.07}Mn_{0.06}Al_2Si_2O_8$ (Nominal composition)

atom	Wyckoff	Coordinate number	X	Y	z	occupancy	U_{iso}
$Ca_{0.775}Ce_{0.09}Mn_{0.09}Al_2Si_2O_8$							
Ca1	2i	6	0.273(3)	0.982(2)	0.087(2)	0.474(3)	0.01(1)
Ca2	2i	7	0.280(4)	0.023(3)	0.548(3)	0.532(2)	0.02(1)
Ca3	2i	7	0.774(3)	0.542(1)	0.551(1)	0.525(2)	0.03(1)
Ca4	2i	7	0.722(5)	0.514(4)	0.056(3)	0.464(2)	0.04(1)
Si1	2i	4	-0.002(3)	0.158(2)	0.110(2)	1.00	0.04(1)
Si2	2i	4	0.014(3)	0.821(2)	0.617(2)	1.00	0.02(1)
Si3	2i	4	0.694(4)	0.103(2)	0.659(2)	1.00	0.06(1)
Si4	2i	4	0.668(4)	0.882(2)	0.172(2)	1.00	0.07(1)
Al1	2i	4	0.007(3)	0.160(2)	0.608(2)	1.00	0.02(1)
Al2	2i	4	0.994(3)	0.813(2)	0.112(2)	1.00	0.02(1)
Al3	2i	4	0.670(3)	0.117(2)	0.158(2)	1.00	0.03(1)
Al4	2i	4	0.680(3)	0.874(2)	0.682(2)	1.00	0.01(1)
$Sr_{0.835}Ce_{0.07}Mn_{0.06}Al_2Si_2O_8$							
Sr1	8f	7	0.272(1)	0.003(1)	0.066(1)	0.952(1)	0.01(1)
Si(Al)1	8f	4	0.004(1)	0.176(1)	0.110(1)	1.00	0.02(1)
Si(Al)2	8f	4	0.003(2)	0.178(1)	0.617(2)	1.00	0.01(1)
Si(Al)3	8f	4	0.682(2)	0.111(2)	0.174(3)	1.00	0.03(1)
Si(Al)4	8f	4	0.679(3)	0.109(2)	0.670(2)	1.00	0.02(1)

Appendix 4

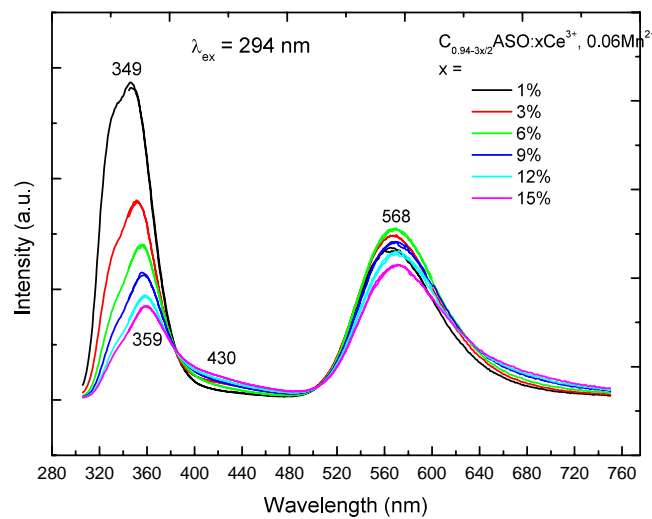


Figure 1. Photoluminescence spectra for $C_{0.94-3x/2}ASO : xCe^{3+}, 0.06Mn^{2+}$ monitored at $\lambda_{ex} = 294 \text{ nm}$

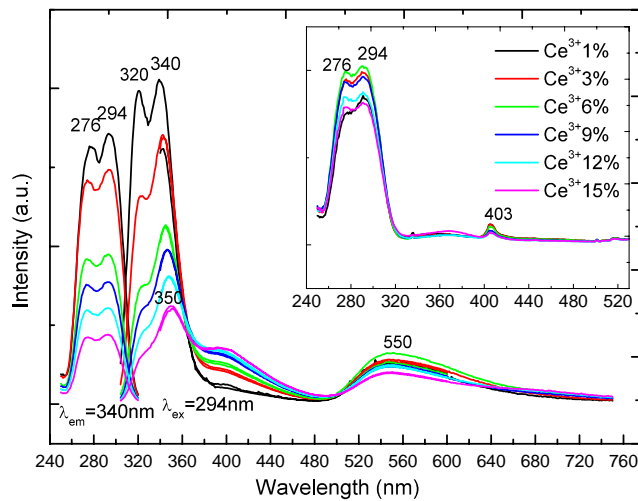


Figure 2. Photoluminescence spectra for $S_{0.94-3x/2}ASO : xCe^{3+}, 0.06Mn^{2+}$ monitored at $\lambda_{ex} = 294 \text{ nm}$

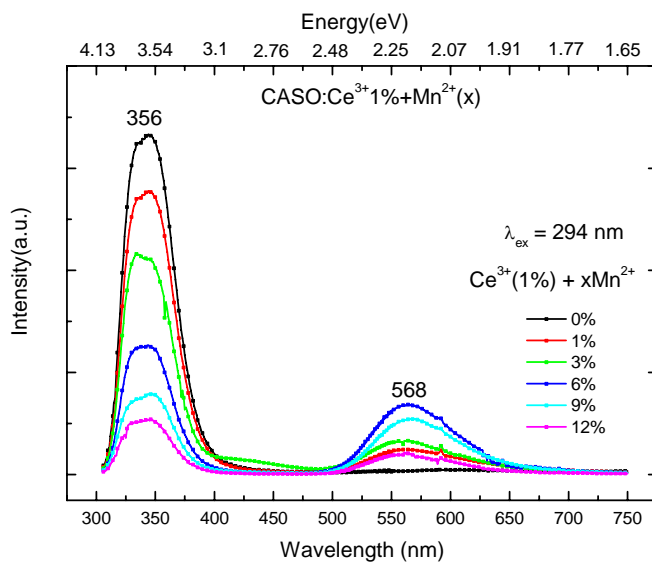


Figure 3. Photoluminescence spectra for $C_{0.985-y}\text{ASO} : 1\%\text{Ce}^{3+}, y\text{Mn}^{2+}$ phosphors on the Mn^{2+} doping content (y)

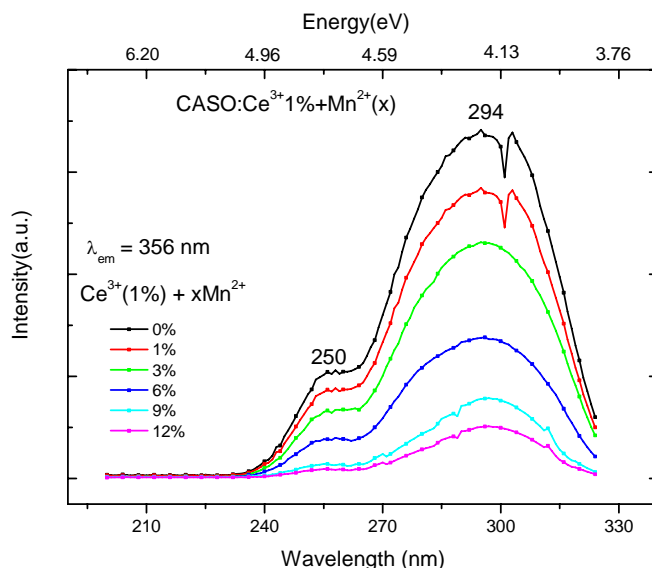


Figure 4. Excitation spectra of $C_{0.985-y}\text{ASO} : 1\%\text{Ce}^{3+}, y\text{Mn}^{2+}$ phosphors monitored at $\lambda_{\text{em}} = 356 \text{ nm}$

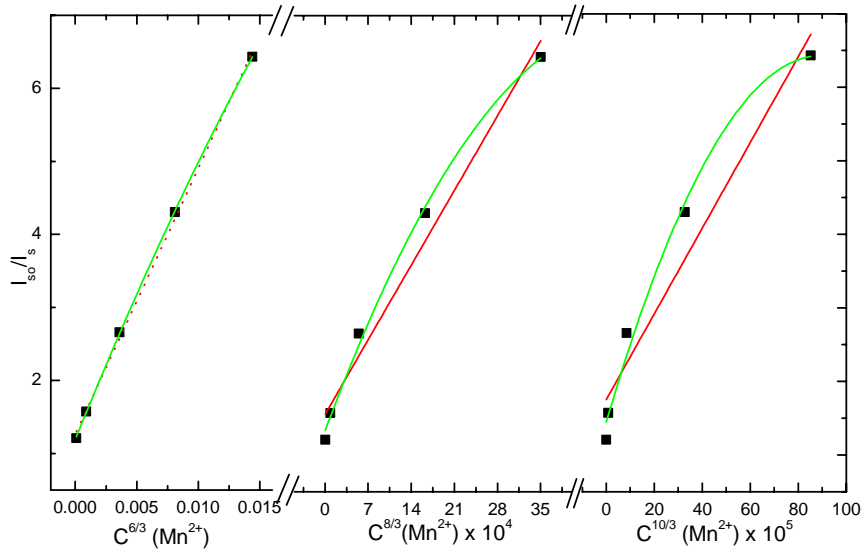


Figure 5. Dependence of I_{so}/I_s of Ce^{3+} on $\alpha = 6, 8, 10$ for the sample $C_{0.985-y}\text{ASO} : 1\%\text{Ce}^{3+}, y\text{Mn}^{2+}$

Pour espérer résoudre les problèmes de réchauffement de la planète, il devient urgent de promouvoir toute action susceptible de conduire à des économies d'énergie. A ce jour, 20% de la production d'électricité sont dédiés à l'éclairage. Dès lors, dans un contexte où la demande en énergie va croissante en relation avec une population mondiale toujours plus importante, la découverte de nouvelles sources lumineuses s'avère être primordiale pour favoriser la diminution de la consommation d'énergie électrique, tout en respectant au maximum les nouveaux impératifs environnementaux via l'augmentation de la fiabilité des dispositifs, leur temps de vie et l'innocuité des produits commercialisés. Seul un nombre très restreint de matériaux luminescents peut aujourd'hui répondre aux exigences précitées. Pourtant les dispositifs à base de diodes électroluminescentes sont appelés à remplacer les sources d'éclairages classiques à court terme. Cette thèse a pour objectif l'élaboration de luminophores blancs excitables dans l'UV. Notre attention s'est portée sur l'étude d'aluminosilicates de formulation $MAI_2Si_2O_8$ ($M = Ca, Sr, Ba$) dopés avec des ions Eu^{2+} , Eu^{3+} , Ce^{3+} et Mn^{2+} cations qui jouent le rôle d'activateur, de sensibilisateur ou de sensibilisateur et d'activateur. Le transfert d'énergie du cérium vers le manganèse a été mis en évidence et permet l'obtention d'une couleur plus chaude qu'avec la phase au cérium seul. Par ailleurs, la possibilité de stabiliser de façon concomitante des ions Eu^{2+} et Eu^{3+} dans le réseau hôte au travers de synthèse à l'air est démontrée, la concentration en Eu^{2+} pouvant être partiellement contrôlée au travers d'un choix approprié d'un co-dopant.

To address issues of global warming, promotion of energy-saving actions has become an urgent duty. Nowadays, approximately 20% of global electricity consumption is used for illumination only. In a context where the ever-increasing energy demand is coupled with a regular population growth, it is of prime importance to discover new light sources that could offer benefits in terms of electrical energy consumption, luminous efficiency, but also maintenance, reliability, lifetime, environmental protection, etc. So far only a very limited number of phosphors can fulfil the requirements for white-light LED applications, i.e. a high quantum yield, a high colour quality, a long stability. Hence, white light emitting diodes receive a strong incentive with the expectation to replace conventional and fluorescent lamps for general lighting applications in the near future. This thesis aims exclusively at the development of a next generation of LED sources based on the association of a near UV-LED chip with an innovative inorganic single phase white emitting phosphor. We will focus our attention on the optical properties of (co)doped $MAI_2Si_2O_8$ phosphors ($M= Ca, Sr, Ba$) where Eu^{2+} , Eu^{3+} , Ce^{3+} and Mn^{2+} cations can play the role of activator, sensitizer, or both sensitizer and activator. In particular, we evidence that Mn^{2+} cations can be pumped via energy transfers to give rise to a warmer light compared to Ce only based materials, while Eu^{2+} and Eu^{3+} can be stabilized naturally in $MAI_2Si_2O_8$ host lattices when prepared in air with a partial control of the Eu^{2+} concentration via the use of appropriate codopants.